# Development of a High Flux Neutron Radiation Detection System For In-Core Temperature Monitoring

by

Thifhelimbilu Daphney Singo

*Dissertation presented for the degree of Doctor of Philosophy at Stellenbosch University*

Department of Physics,
Stellenbosch University,
Private Bag X1, Matieland 7602,
South Africa

Promoters:

Dr. Paul Papka
Prof. Shaun M. Wyngaardt
*Department of Physics*

Mr. Robert T. Dobson
*Department of Mechanical & Mechatronic Engineering*

Dr. Frederick D. Smit
*Department of Nuclear Physics,*
*iThemba Labs,*
*P. O. Box 722,*
*Somerset West 7129,*
*South Africa*

March 2012

# Declaration

By submitting this thesis/dissertation electronically, I declare that the entirety of the work contained therein is my own, original work, that I am sole author thereof (save to the extent explicitly otherwise stated), that reproduction and publication thereof by Stellenbosch University will not infringe any third party rights and that I have not previously in its entirety or part in part submitted it for obtaining any qualification.

March 2012

# Abstract

## Development of a High Flux Neutron Radiation Detection System For In-Core Temperature Monitoring

T.D. Singo

*Department of Physics,*
*Stellenbosch University,*
*Private Bag X1, Matieland 7602,*
*South Africa*

Dissertation: PhD (Physics)

March 2012

The objective of this research was to develop a neutron detection system that incorporates a mass spectrometer to measure high neutron flux in a nuclear reactor environment. This system consists of slow and fast neutron detector elements for measuring fluxes in those energy regions respectively. The detector should further be capable of withstanding the harsh conditions associated with a high temperature reactor. This novel detector which was initially intended for use in the PBMR reactor has possible applications as an in-core neutron and indirect temperature-monitoring device in any of the HTGR.

Simulations of a generic HTGR core model were performed in order to obtain the neutron energy spectrum with emphasis on the behavior of three energy regions, slow, intermediate and fast neutrons within the core at different temperatures. The slow neutron flux which has the characteristic of a Maxwell-Boltzmann distribution were found to shift to larger values of neutron flux at higher energies as the fuel temperature increased, while fast neutron flux spectra remained relatively constant. In addition, the results of the fit of the slow neutron flux with a modified Maxwell-Boltzmann equation confirmed that in the presence of the neutron source, leakage and absorption, the effective neutron temperatures is above the medium temperatures. From these results, it was clear that the detection system will need to monitor both slow and fast neutron flux. Placing neutron detectors inside the reactor core, that are sensitive to a particular energy range of slow and fast neutrons, would thus provide information about the change of temperature in the fuel and hence act as an in-core temperature monitor.

A detection mechanism was developed that employs the neutron-induced break-up reaction of $^{6}$Li and $^{12}$C into $\alpha$-particles. These materials make excellent neutron converters without interference due to $\gamma$-rays, as the contributions from $^{6}$Li($\gamma$,np)$^{4}$He and $^{12}$C($\gamma$,3$\alpha$) reactions are negligible. The mass spectrometer measures the $^{4}$He partial pressure as a function of time under high vacuum with the help of pressure gradient provided by a high-vacuum turbomolecular pump and a positive-displacement fore-vacuum pump connected in series. A cryogenic trap, which contains a molecular sieve made of pellets 1.6 mm in diameter, was also designed and manufactured to remove impurities which cause a background in the lighter mass region of the spectrum.

The development and testing of the high flux neutron detection system were performed at the iThemba Laboratory for Accelerator Based Sciences (LABS), South Africa. These tests were carried out with a high energy proton beam at the D-line neutron facility, and with a fast neutron beam at the neutron radiation therapy facility. To test the principle and capability of the detection system in measuring high fluxes, a high intensity 66 MeV proton beam was used to produce a large yield of $\alpha$-particles. This was done because the proton inelastic scattering cross-section with $^{12}$C nuclei is similar to that of neutrons, with a threshold energy of about 8 MeV for both reactions. Secondly, the secondary fast neutrons produced from the $^{9}$Be(p,n)$^{9}$B reaction were also measured with the fast neutron detector.

The response of this detection system during irradiation was found to be relatively fast, with a rise time of a few seconds. This is seen as a sharp increase in the partial pressure of $^{4}$He gas as the proton or neutron beam bombards the $^{12}$C material. It was found that the production of $^{4}$He with the proton beam was directly proportional to the beam intensity. The number of $^{4}$He atoms produced per second was deduced from the partial pressure observed during the irradiation period. With a neutron beam of $10^{10}$ s$^{-1}$ irradiating the detector, the deduced number of $^{4}$He atoms was $10^{9}$ s$^{-1}$. When irradiation stops, the partial pressure drops exponentially. This response is attributed to a small quantity of $^{4}$He trapped in the present design.

Overall, the measurements of $^{4}$He partial pressure produced during the tests with proton and fast neutron beams were successful and demonstrated proof of principle of the new detection technique. It was also found that this system has no upper neutron flux detection limit; it can be even higher than $10^{14}$ n·cm$^{-2}$·s$^{-1}$. The lifetime of this detection system in nuclear reactor environment is practically unlimited, as determined by the known ability of stainless steel to keeps its integrity under the high radiation levels. Hence, it is concluded that this high flux neutron detection system is excellent for neutron detection in the presence of high $\gamma$-radiation level and provides real-time flux measurements.

# Uittreksel

## Ontwikkeling van 'n Hoë Vloed Neutron Stralingsdetektor Stelsel vir In-Kern Temperatuur Monitering

*("Development of a High Flux Neutron Radiation Detection System For In-Core Temperature Monitoring")*

T.D. Singo

*Departement Fisika,*
*Stellenbosch Universiteit,*
*Privaatsak X1, Matieland 7602,*
*Suid Afrika*

Proefskrif: PhD (Fisika)

Maart 2012

Die doel van hierdie navorsing was om 'n neutrondetektorstelsel te ontwikkel wat hoë neutronvloed binne in 'n kernreaktor kan meet. Die stelsel bevat twee aparte detektorelemente sodat die termiese sowel as snelneutronvloed gemeet kan word. Die detektor moet verder in staat wees om die strawwe toestande, kenmerkend aan 'n hoë temperatuur reaktor, te kan weerstaan. Die innoverende detektorstelsel, oorspronklik geoormerk vir gebruik in die PBMR reaktor, het toepassingsmoontlikhede as in-kern neutron- sowel as indirekte temperatuurmonitor.

Simulasies van 'n generiese model van 'n HTGR reaktorkern is uitgevoer ten einde die neutronenergiespektrum in die kern by verskillende temperature te bekom met klem op die gedrag van neutrone in drie energiegroepe: stadig (termies), intermediêr en snel (vinnig). Daar is bevind dat die stadige neutrone, wat 'n Maxwell-Boltzman verdeling toon, in intensiteit toeneem en dat die piek na hoër energie verskuif met toename in temperatuur, terwyl die vinnige neutronspektrum relatief onveranderd bly. 'n Passing van die stadige spektrum op 'n gemodifiseerde Maxwell-Boltzmann verdeling het bevestig dat die effektiewe neutrontemperatuur weens die teenwoordigheid van bronterme, verliese en absorpsie, hoër as die temperatuur van die medium is. Hierdie resultate maak dit duidelik dat die detektorstelsel beide die stadige sowel as die

vinnige neutronvloed moet kan waarneem. Deur detektorelemente wat sensitief is vir die onderskeie spekrale gebiede in die reaktorhart te plaas, kan informasie bekom word wat tot in-kern temperatuur herleibaar is sodat die stelsel inderdaad as indirekte temperatuurmonitor kan dien.

Die feit dat alfa-deeltjies geproduseer word in neutron-geïnduseerde opbreekreaksies van $^{6}$Li en $^{12}$C is as die basis van die nuwe opsporingsmeganisme aangewend. Hierdie materiale funksioneer uitstekend as neutron-selektiewe omsetters in die teenwoordigheid van gamma-strale aangesien laasgenoemde se bydraes tot helium produksie via die $^{6}$Li($\gamma$,np)$^{4}$He en $^{12}$C($\gamma$,3$\alpha$) reaksies, weglaatbaar is. Die massaspektrometer meet die tydgedrag van die 4He parsiële druk binne 'n hoogvakuum wat met behulp van 'n seriegeskakelde kombinasie van 'n turbomolekulêre en positiewe-verplasingsvoorpomp verkry word. 'n Koueval met 'n molekulêre sif, bestaande uit 1.6 mm diameter korrels, is ontwerp en vervaardig om onsuiwerhede te verwyder wat andersins as agtergrond by die ligter gedeelte van die massaspektrum sou wys.

Die ontwikkeling en toetsing van die hoëvloed detektorstelsel is te iThembaLABS (iThemba Laboratories for Accelerator Based Sciences) gedoen. Dit is uitgevoer deur gebruik te maak van die hoë energie protonbundel van die D-lyn neutronfasiliteit asook van die bundel vinnige neutrone by die neutronterapiefasiliteit. Om die beginsel en vermoë te toets om by 'n hoë neutronvloed te kan meet, is van die intense 66 MeV protonbudel gebruik gemaak om 'n hoë opbrengs alfa-deeltjies te verkry. Dit is gedoen omdat die reaksiedeursnit vir onelastiese verstrooiing van protone vanaf $^{12}$C kerne soortgelyk is aan die van neutrone, met 'n drumpelenergie van 8 MeV vir beide reaksies. Tweedens is die sekondêre vinnige neutrone afkomstig van die $^{9}$Be(p,n)$^{9}$B reaksie ook met die neutrondetektor gemeet.

Daar is bevind dat die reaksietyd van die deteksiestelsel tydens bestraling relatief vinnig is, soos gekenmerk deur 'n stygtyd van etlike sekondes. Laasgenoemde manifesteer as 'n toename in die parsiële druk van die $^{4}$He sodra die proton- of neutronbundel op die $^{12}$C teiken inval. Daar is verder bevind dat die $^{4}$He produksie direk eweredig aan die bundelintensiteit is. Vir 'n neutronbundel van nagenoeg $10^{10}$ s$^{-1}$, invallend op die neutrondetektor, is vanaf die gemete parsiële druk afgelei dat die produksie van $^{4}$He atome sowat $10^{9}$ s$^{-1}$ beloop.

In die geheel beoordeel, was die meting van die 4He parsiële druk tydens die toetse met vinnige protone en neutrone suksesvol en het dit die nuwe meetbeginsel bevestig. Dit is verder bevind dat die meetstelsel nie 'n beperking op die boonste neutronvloed plaas nie, maar dat dit vloede van selfs hoër as $10^{14}$ s$^{-1}$ kan hanteer. Die leeftyd van die detektorstelsel in die reaktor is prakties onbeperk en onderhewig aan die bevestigde integriteit van vlekvrystaal onder hoë bestraling. Die gevolgtrekking is dus dat die nuwe detektorstelsel uitstekend geskik is vir die in-tyd meting van 'n baie hoë vloed van neutrone ook in die teenwoordigheid van intense gammabestraling.

# Dedication

*I would like to dedicate this work to my mother, Mrs Nyawasedza Fhulufhedzani Singo.*

# Acknowledgements

I thank God for all the blessings, with him all things are possible.

I would like to extend my gratitude to PBMR and Necsa, for the funding that made it possible for me to study for this degree.

J'aimerais tout particulièment remercier mon superviseur, Dr. Paul Papka, qui m'a patiemment guidée du début jusqu'à la fin de cette thèse. To my co-promoters, Dr Shaun M. Wyngaardt, Dr Frederick D. Smit and Mr Rorbert T. Dobson, I thank you all for your support. Dr Peane Maleka, thank you for your help with the MCNP code. I would like to also thank Mr Peter Blaine for the English proofreading. I gratefully acknowledge the collaborators of this project, Dr A. Buffler and R. Nchodu. I am grateful to the support I received from the following: the technical staff in the workshop, the accelerator division, radioisotope production and everyone at iThemba LABS. My sincere gratitude to the iThemba LABS neutron radiation therapy staff, Mr Jaime Nieto-Camero and Mr Julyan Symons, for providing the beam time.

Mon amour Dr Remy Bucher, je suis très reconnaissante et honorée d'avoir rencontré un homme merveilleux comme toi. Merci beaucoup pour les discussions fructueuses et enrichissantes. Ndi livhuwa vhabebi vhanga, dzi khaladzi na mukomana wanga kha thikhedzo na thuthuthuwedzo ye vha nnekedza ndi sa hangwi dzi khonani dzanda.

# Contents

# List of Figures

# List of Tables

# List of Abbreviation

| Acronym | Definition |
|---|---|
| amu | atomic mass unit |
| Å | Ångström = $10^{-10}$ m |
| CFD | Computational Fluid Dynamics |
| ECU | Electronics Count Unit |
| Eskom | Electricity Supply Commission of South Africa |
| eV | electron Volt |
| HTGR | High Temperature Gas-cooled Reactor |
| HTR | High Temperature Reactor |
| iThemba LABS | iThemba Laboratory for Accelerator Based Sciences |
| kPa | kilo Pascal=101 325 Pa |
| MCNP | Monte Carlo N-Particle Code |
| MCNP 5 | Monte Carlo N-Particle Code version 5 |
| MCNPX 2.6 | Monte Carlo N-Particle X code version 2.6 |
| MeV | Mega electron Volts ($10^6$ eV) |
| MICROMEGAS | Micro MEsh Gaseous Structure |
| MPFD | Micro Pocket Fission Detector |
| $MW_{th}$ | Megawatt thermal |
| Necsa | South African Nuclear Energy Corporation |
| PBMR | Pebble Bed Modular Reactor |
| RGA | Residual Gas Analyzer |
| RPV | Reactor Pressure Vessel |
| RSICC | Radiation Safety Information Computational Center |
| R/h | Rontgen per hour |
| SCC | Separated Sector Cyclotron |
| TRIGA | Training Research Isotope General Atomics |
| TRISO | Triple Coated Isotropic Particle |
| XSDIR | Cross-section Data Library |
| wt% | weight-percent |
| ZAID | Atomic number Z, mass number A, and library specifier ID |

# Chapter 1

# Introduction

The measurements of neutron flux in High Temperature Gas-cooled Reactor (HTGR) nuclear reactors are a challenging task because of the extremely harsh environmental conditions under which the detector has to operate, e.g. high temperature and radiation dose. It is even more challenging if the detector is expected to be stable and work for long periods of time. It is known that fast neutrons found in the reactor have the most significant structural effects on the conventional detector material and the detection signal [Eis09]. To overcome this challenge, it is required to design a special neutron radiation detection device that is stable, and can work for long period under these environmental conditions providing a real-time data reading system. Also, the neutron converter material should be highly sensitive to neutron energy, and the detection technique should have inherent $\gamma$-ray discrimination.

The use of a mass spectrometer to analyze the residual gas in the vacuum system has been widespread in various fields of physics, but it has not been incorporated into the detection of high neutron flux. This device, when used with a neutron-converting material such as $^{6}$Li and $^{12}$C, can measure high flux of slow and fast neutrons, respectively, in a high $\gamma$-radiation background with almost zero sensitivity to $\gamma$-rays. This is possible if the neutron conversion materials are less (at least 4 orders of magnitude less than neutron-induced break-up reactions) sensitive to $\gamma$-rays. Thus, the neutron detector has inherent $\gamma$ discrimination. Also, the reaction product from the neutron interaction should be able to diffuse out of the material in the form of a gas, and the measurements should be performed under high vacuum.

This work focuses on developing a high flux neutron detection system that incorporates a highly sensitive atomic mass spectrometer (Residual Gas Analyzer (RGA)) and vacuum pumps. This neutron detector employs the light element neutron-induced break-up reactions of $^{6}$Li and $^{12}$C to detect slow and fast neutron flux. Due to the special design features of the detection system and the stainless steel materials used, the detector will measure high neutron flux in real time and withstand high radiation level.

The HTGR is a Generation IV reactor type which has the special distin-

guishing feature of a large negative temperature coefficient of reactivity caused by Doppler broadening of the resonance absorption cross-section. This is as a result of a change in the temperature of the fuel in the core. Since the Doppler broadening effect is dependent on the temperature of the fuel and affects the reactivity, the neutron flux is expected to evolve with temperature changes. It is the aim of this work, to find a technique that can relate measured neutron flux ratio, using two energy groups, with the temperature of the core for in-core temperature monitoring as a function of time. This system could be the solution to problems experienced when using temperature detection devices that are sensitive to the extremely harsh nuclear environment found in such an HTGR reactor. The detector will be more suitable to work for long periods in such an environment, while offering real-time neutron flux monitoring. This information can be used to optimize plant control.

## 1.1 Research background

Electricity Supply Commission (Eskom), the state utility of South Africa, generates more than 95% of the electricity in South Africa, and over 90% of this capacity is provided by large coal-fired stations and 5% by the nuclear power station at Koeberg near Cape Town. The nuclear power station generates about 1800 MW of energy [Nic96]. A large portion of the electricity is used by the South African mining and heavy metal (steel, ferrochrome, aluminum, etc.) industries. Since the fall of apartheid (in 1994), black communities also have access to electricity, and the number of industries has been increasing, which results in an ever-increasing demand for electricity. Consequently, Eskom considered a future expansion of the nuclear energy-generation option. It looked at various options, such as a High Temperature Reactor (HTR) as a possible supplement to the existing pressurized water reactors for the Eskom grid. In 1996, an investigation led to the selection of a direct-cycle HTR power plant based on the German fuel design [AVR90]. The choice was made for the HTR because it is designed to eliminate or be resistant to nuclear accidents such as core melting. Some other characteristics of the direct cycle are a high efficiency for the conversion of a heat to electricity, which is ideal because the project was designed for electricity generation. The heat produced through a heat exchanger can be directly used for industrial purposes.

The Pebble Bed Modular Reactor (PBMR) company started in 1999 and aimed to provide new reactor technology development in South Africa. In support of the design and the passive safety case of the PBMR, various analysis groups were tasked to resolve and provide insight on some specific nuclear physics characteristics of the reactor. Also because the structure of the reactor core and the requirements on the points for temperature measurements in the PBMR are different from those in conventional water-cooled reactors, new temperature-measuring devices had to be developed. Conse-

quently, two projects were proposed at Stellenbosch University: the development of a temperature-monitoring device that can be used in the PBMR core and possibly trace the movement of the fuel spheres. The first research project was "In-core temperature measurement for the PBMR using fiber-Bragg Gratings" [Dev09], and the present one, "In-core temperature measurements for the PBMR using a neutron detection system". A neutron detection system is developed to measure the neutron flux within or outside the reactor core. The neutron energy profile within the core contains information about the neutron-induced reaction rate, which is sensitive to the temperature of the fuel and moderator. The core or fuel temperature information can be extracted by having a neutron detector that is sensitive to a particular energy range (slow and fast neutrons) of the energy spectrum.

The current status of the PBMR project is that the construction of a prototype plant has been postponed indefinitely due to financial constraints. The reason for this is that Eskom, the primary customer, has reported losses and has no money for the expansion program. The South African government has also stopped funding the project and the company has scaled down to an intellectual property holding company.

The current project was proposed for the PBMR reactor before it collapsed and a lot of research had been done on this project, therefore it was decided to continue to use the model of the PBMR reactor. This is because the technique of measuring the neutron flux within the reactor core for neutron spectroscopy and, as a results, monitor the temperature of the core, could also be used effectively in other nuclear reactor designs and is not restricted only to the PBMR. The PBMR has been decommissioned in South Africa, although similar projects are currently ongoing with the China High Temperature Reactor 10 Mega Watt thermal $MW_{th}$(HTR-10) [Zha02] and the Japan High Temperature Test Reactor (HTTR) 30 Mega Watt thermal $MW_{th}$.

Previously, thermocouples [Pol91, Man93, Bec07] have been used as in-core instrumentation to measure the temperature of different components of the reactor, such as the moderator and coolant. Thermocouples have been used in several high-temperature reactors, such as HTR-10 [Zha02], the European High Temperature Reactor Technology Network (HTR-TN) project [Lau09] and Fort St. Vrain, Colorado (330 $MW_e$) [Fran82]. They consist of two dissimilar metals that produce a voltage when joined together at one end of a thermocouple. Thermocouples can be used to measure temperature up to 2873 K and may be brought into direct contact with the object being measured. However, there are a few challenges that could be experienced when using the thermocouples for temperature measurements. The challenges are de-calibration processes in high temperature reactor environments, which include: temperature-voltage relation changes in high-neutron fluxes caused by transmutation [Bri82], the relation between the process temperature and the thermocouple signal is not linear, and temperature measurements with thermocouples require two temperatures to be measured, one point as the reference

temperature and the temperature at the object. However, thermocouples can not be placed directly on the fuel elements in the core to obtain the fuel temperature while operating. Hence, an alternative fuel temperature-monitoring device had to be developed.

The neutron detection devices, such as the fission chambers [Fan04, Dou05] and the self-powered neutron detector [Lee99], have been developed to measure the neutron flux in reactor cores as a method of monitoring the reactor power level. These devices can be manufactured in small sizes to fit into the space allocated in the reactor core. However, their electric power and the signal cable from the device to the computer requires special insulation material in order to withstand the high temperature in the HTR cores. Also, the electronic devices coupled to the detector for converting and amplifying the radiation signal to a digital signal could easily damaged by fast neutrons. The gas-filled counters and scintillators employs a neutron detection method where the $\gamma$-ray discrimination over the neutron signal becomes challenging, especially, in high energy and intense $\gamma$-radiation. This makes them less suitable for the extremely harsh conditions in the HTR reactor core.

In this research we propose a new design of neutron detection where the material used is radiation resistant, the electronic devices and power cables are not placed in the high-radiation environments, and the neutron-induced reaction is insensitive to $\gamma$-rays, which offers inherent $\gamma$-ray discrimination. In the next section we discuss the motivation behind developing this high flux neutron detection system as an in-core radiation instrument.

## 1.2 Motivation for and aims of this project

The temperature in the nuclear reactor should be monitored constantly during operation and at shutdown, in order to avoid the situation where the fuel elements reach their melting point of around 3073 K. Fuel cells subjected to a temperature sufficiently high enough to induce centerline melting, experience a significantly high probability of failure. Failure is referred to as a loss in the expected functional behavior of a fuel element caused by a change in its physical properties. This could compromise the safety of the reactor.

The HTR reactor are designed to operate at a very high temperature. For example, the PBMR was a 400 $\mathrm{MW_{th}}$ helium-cooled graphite-moderated reactor [Sen06, Hon07] with a helium gas outlet temperature estimated to be about 1223 K compared to a conventional water-cooled reactor, which operates at a temperature between 548 and 588 K. With the 400 $\mathrm{MW_{th}}$ thermal reactor power, the neutron production rate from prompt fission is

$$m = \frac{P_{\mathrm{th}} \times \eta}{E_f} = 3.1920 \times 10^{19} \quad \mathrm{n{\cdot}s^{-1}}, \tag{1.1}$$

where $P_{\text{th}}$ is the thermal power produced by the reactor, $E_f$ is the average energy released $\approx$ 200 MeV per fission, and $\eta = 2.5$ is the average prompt fission neutron yield per fission event.

The fission energy is deposited within the fuel in the form of heat, causing the fuel temperature to increase. An increase in fuel temperature causes the thermal motion of the nuclei to increase. Hence, $^{238}$U, which forms a large part of the fuel, absorbs neutrons in a wide energy range. This results in more intermediate energy neutrons being absorbed before they are thermalized to cause another fission in $^{235}$U. Having less thermal neutrons will result in less fission reaction hence, less fast neutrons. This effect is known as the Doppler broadening mechanism, absorption of intermediate energy neutrons in the resonance region of $^{238}$U, and it is the inherent safety feature of the Generation-IV HTR fuel technology. Given the high radiation levels in the reactor and the high operating temperature, it will be ideal to develop a device that is radiation resistant and could make use of the ambient radiation to provide indirect information about the temperature of the core.

This project focuses on developing a technique to indirectly monitor the fuel temperature by characterizing the neutron flux in the core. This measurement technique is used because the characteristics of the radiation produced in the core are temperature dependent.

The objectives of this research were the following:

- To develop a simplified Monte Carlo N-Particle (MCNP) model of the Generation-IV HTR reactor core with the objective to obtain a neutron flux profile at different operating temperatures and to understand how the neutron energy spectrum (slow and fast neutron fluxes) is influenced by the change of temperature in the core.
- To find neutron-induced break-up reactions with cross-sections higher than of photodissociation reactions thus rendering the contribution from the $\gamma$-rays insignificant. The cross-section should also be sensitive to a certain neutron energy region, e.g. slow or fast neutron flux.
- To develop a neutron detection system capable of measuring and withstanding the high neutron flux produced in the reactor core.
- To carry out experimental tests of the newly developed neutron detection system.
- To monitor the reaction rates as the temperature increases by counting the resulting activities.

## 1.3 Outline of this work

This work presents the design and verification results of the development of a high neutron flux detection system. The review of one of the Generation-IV

high temperature reactor, PBMR reactor, is performed in Chapter 2, with a discussion of the characteristics and safety features of this reactor. In Chapter 3, neutron transport theory is reviewed in order to understand the mechanism by which neutrons are gained and lost in the reactor volume. An MCNP code based on the stochastic transport method is used to solve the neutron transport equation numerically. The purpose of the simulation was to generate the typical neutron flux profile that a high flux neutron detection system will be measuring. This is discussed together with the results of the simulation of the reactor operating at different temperatures. A good fit of the neutron spectra to the Maxwell-Boltzmann distribution and the effective neutron temperatures were obtained.

This led to the design of the slow and fast neutron detectors of the high flux neutron detection system. However, the conversion of neutrons into charged particles requires knowledge of the different types of neutron interactions with nuclei, the cross-section as a function of neutron energy, the characteristics of the different moderators and the slowing down of neutrons in an absorbing material near the resonance energy range. These topics are discussed in Chapter 4. Chapter 5 looks at previously developed neutron detectors, such as proportional gas counters, scintillators and Bonner sphere neutron detectors. Their properties and limitations regarding measurements in the nuclear reactor core are discussed. The newly developed neutron detector, its characteristics, equipment and neutron flux measurement optimization are discussed in Chapter 6. The experimental procedure for the high energy proton beam and the fast neutron beam measurements with the high flux neutron detection system and the results, are presented in Chapter 7. Conclusion and outlook are found in Chapter 8.

# Chapter 2

# Nuclear reactor

A nuclear reactor is a device designed and built for the production of energy from nuclear fission reactions, and the energy produced is used for the generation of electricity, using the steam turbines. Different types of nuclear reactors such as Generation I, II, III, III+ and IV have been used to provide power for the past 80 years. However, the types of reactor of interest in the present work is Generation IV, and we discuss its features with reference to the design of the PBMR reactor.

Generation IV nuclear reactors are a set of nuclear reactor designs currently being researched that are intended for future use in nuclear power plants. Generation III reactor properties are common in Generation IV reactors, which have the following additional features: more energy yield from the same amount of nuclear fuel, enhanced operational safety, minimal waste and proliferation resistance [Sla04]. The safety features originate from the design of the PBMR core, which is made to handle high temperatures, and the fuel technology, Triple Coated Isotropic Particle (TRISO) fuel particles, in which the fuel pebble is designed to survive high temperatures while retaining the fission products. The Doppler broadening mechanism, which creates a negative feedback mechanism as the fuel temperature increases, makes this reactor intrinsically safe, as it does not require active safety control. Some other characteristics are a high efficiency for the conversion of heat to electricity and the direct use of heat produced through a heat exchanger for industrial purposes.

## 2.1 Nuclear reactor fuel and criticality

In a nuclear reactor, the geometry, as well as the distribution of fuel materials within the reactor is of importance for the reactor to achieve criticality. The nuclear criticality is a steady state self-sustained chain fission reaction that is desired by the plant regulator for constant power output. The fuel consists of a fissile material, in which a small portion is enriched in $^{235}$U that propagates

the fission reaction, and about 90% is $^{238}$U that controls the reactivity of the reactor through the Doppler broadening mechanism at higher temperatures. The portion size determines the ability of the reactor to control itself without the need of external active safety controls.

There are three states of operation of the nuclear reactor, namely critical, subcritical or supercritical. These conditions are determined by the extent of neutron multiplication as the next generation neutrons are produced through nuclear fission. If the previous number of thermal neutrons in the reactor was represented by $N_i$, and their absorption by fissile material produced a certain number $N_{i+1}$, which represents the number of thermal neutrons in the present generation. The effective multiplication factor $k_{eff}$ is defined as the ratio of the number of thermal neutrons in the present generation to the number of thermal neutrons in the previous generation, that is

$$k_{eff} = \frac{N_{i+1}}{N_i} \tag{2.1}$$

- The system is critical if $k_{eff} = 1$, exactly. This implies that on average one of the fission neutrons emitted causes another nucleus to fission. In this condition the reactor can sustain itself.

- Supercritical is when $k_{eff} > 1$. This implies that on average more than one fission event occurs per fission neutron produced. The reactor is continuously increasing in power, which can have a bad effect on the safety of the reactor. The effect of this supercritical condition is discussed in the next section that deals with the effect of fuel temperature change on reactivity.

- Subcritical is when $k_{eff} < 1$. This condition occurs when on average less than one fission event occurs per fission neutron produced. The reactor is continuously decreasing in power.

The multiplication factor $k$ of the reactor is defined by the six-factor formula as

$$k = \Lambda_f \Lambda_{th} p f \eta \epsilon, \tag{2.2}$$

where

- $\Lambda_f$ and $\Lambda_{th}$ are the fast and thermal neutron non-leakage factors,

- $p$ is the probability that the neutrons will escape resonance capture as they slow down to thermal energies,

- $f$ represents the fraction of the $N_i$ thermal neutrons that will be absorbed in the fissionable material known as the thermal utilization factor,

- $\eta$ represents the average number of neutrons produced per thermal neutron capture and it is known as the reproduction factor,

- $\epsilon$ is the ratio of the total number of neutrons produced from fast fission and the number produced by thermal fission and is known as the fast fission factor.

## 2.2 Fuel temperature increase

The increase in the fuel temperature in the reactor occurs practically instantaneous and is due to the energy released in the following: nuclear fission; which releases energy of about 200 MeV per event, scattering; capture of fission neutrons and radioactive decay of fission fragments. The energy carried by $\gamma$-rays is about 5 to 7 MeV from neutron capture and 10 MeV from fission. All these contributions can be divided into two categories, namely prompt and delayed released energy. Both categories are further subdivided into a part deposited in the fuel and a part deposited outside the fuel material, such as in the coolant, moderator or reflector.

The major part of the energy released from the fission process, about 83%, appears in the form of kinetic energy of the two fission fragments. The fission fragments are highly energetic and they lose their energy quickly through ionization within a small range of $< 1.0 \times 10^{-2}$ mm in the fuel. Thus, after a negligibly short time, the energy of the fission fragments is converted into temperature in a very small volume. Promptly deposited heat in the fuel kernel amounts to 90%, and 10% of the remaining heat production is delayed and/or is deposited outside of the fuel kernel. A smooth spatial distribution of heat produced from fission is obtained from the superposition of many fission tracks and by rapid heat transfer over a small volume compared with the typical fuel kernel diameter, where all of the energy of the fission fragments is deposited in the fuel. The effects of fuel temperature change in the reactor are discussed in the next section.

## 2.3 Effects of fuel temperature change on reactivity

Parameters that determine the reactivity of a reactor are thermal utilization, resonance escape probability, referring to the Doppler broadening effect, and diffusion length. Reactivity is the measure of the deviation of a nuclear reactor from criticality at any instant of time such that the positive and negative values correspond to supercritical and subcritical respectively. These parameters are a function of the temperature of the fuel, moderator, and coolant. An increase in the temperature of the reactor components (fuel, moderator and coolant) will lead to changes in reactivity. The temperature coefficient of reactivity, $\alpha_T$

[Lam66], is defined by the relation

$$\alpha_T = \frac{d\rho}{dT}, \tag{2.3}$$

where $\rho$ is the reactivity of the system and $T$ is the temperature of a specific component. So, if $T$ refers to the temperature of the fuel, $\alpha_T^F$ is called the fuel temperature coefficient or if $T$ refers to the temperature of the moderator, $\alpha_T^M$ is called the moderator temperature coefficient, and so forth. The reactivity of the system is given by $\rho(T) = 1 - k^{-1}(T)$, where $k$ is the multiplication factor of the reactor, so equation (2.3) is equivalent to

$$\alpha_T = \left(\frac{1}{k}\right)^2 \frac{dk}{dT}. \tag{2.4}$$

In most cases of interest (discussed in section 2.1), $k \approx 1$, which implies $k^2 \approx k$ and equation (2.4) may be written as

$$\alpha_T \cong \frac{1}{k}\frac{dk}{dT}. \tag{2.5}$$

The sign (either positive or negative) of $\alpha_T$ determines the behavior of reactivity after the change in temperature. If $\alpha_T$ is positive, and $\frac{dk}{dT}$ is also positive, then the reactivity in the reactor increases with increasing temperature. However, if $\alpha_T$ is negative, and $\frac{dk}{dT}$ is negative, then the reactivity decreases with increasing temperature. When the temperature of the reactor components increases, e.g. fuel and their temperature coefficient is positive, then $k$ value increases, which results in a power increase. This will lead to a further increase in temperature, which again increases $k$, and so on. The power of the reactor will continue to increase until the reactor is brought under control by external intervention, such as the control rods and cooling, or in the extreme scenario of core melting. A reactor with a positive temperature coefficient is thus inherently unstable with respect to changes in temperature. However, the reactor with a negative temperature coefficient does the opposite. An increase in temperature now leads to a decrease in $k$, which reduces the power level and returns the temperature to its original value.

Similarly, a decrease in temperature results in an increase in $k$, which increases the power and again returns the system to its initial temperature. Reactors having negative temperature coefficients are therefore stable with respect to temperature changes. The PBMR reactor behaves in a similar manner in response to an increase in reactivity. This is because the fuel temperature responds immediately to changes in power, whereas the temperature of the moderator and coolant must wait upon the transfer of heat from the fuel. For this reason, the fuel temperature coefficient is often called the prompt temperature coefficient. Suppose the fuel elements are uniformly distributed in a uniform neutron flux, then the temperature changes will be uniform throughout the system. From the above explanation, we learned that the parameters

which determine the reactivity in the reactor are functions of the temperature of the medium, $T_{\mathrm{m}}$, while others are functions of the effective neutron temperature, $T_{\mathrm{n}}$. For example, if the temperature of the medium, $T_{\mathrm{m}}$, increases, the medium expands, which results in the nuclei being further apart. Hence, the nuclear density $N$ decreases. When nuclear density decreases, then the macroscopic cross-section, $\bar{\Sigma}_a = N\bar{\sigma}_a$, also decreases. The microscopic cross-section $\bar{\sigma}_a$ is a function of $T_{\mathrm{n}}$, and is indirectly dependent upon $T_{\mathrm{m}}$. It is found that the $T_{\mathrm{n}}$ is directly proportional to $T_{\mathrm{m}}$ and can be written as

$$T_{\mathrm{n}} = aT_{\mathrm{m}}, \tag{2.6}$$

where $a$ is a parameter that depends upon the properties of the medium. The effective neutron temperature $T_n$ is generally found not to be the same as that of the medium [Gei65]. Both nuclear fission and neutron capture reactions can be used for determining the effective neutron temperature and the reaction rates are monitored by counting the resulting activities or nuclear transmutation. Theoretically, the effective neutron temperature could be determined from the simulated neutron energy spectrum within the core, and or at any location within the reactor, and this is explained in section 3.6. The simulation of the neutron energy spectrum in those places is performed in Chapter 3, however, we introduce the nuclear reactor of interest to this work.

## 2.4 The Pebble Bed Modular Reactor design

The PBMR is a Generation IV High Temperature graphite-moderated, helium Gas-cooled nuclear Reactor based on the original AVR reactor design (German: Arbeitsgemeinsschaft Versuchsreaktor) from the German Jülich Research Center [Kos03, Bau89, Nab84, Zie97]. The name Pebble Bed is derived from the geometry of the nuclear fuel used, namely spherical pebbles of a tennis ball size, stacked to make a bed of pebbles. Modular Reactor stands for one of the key features of this reactor, in that it can be built in modules and these modules can be combined according to the specific energy requirements of the user.

The reactor, shown in Fig. 2.1, has a vertical steel Reactor Pressure Vessel (RPV), which contains and supports a metallic core barrel. The core barrel supports the annular pebble fuel core and side reflectors. This annular fuel core, with a height of 11 m and a radius of 2.7 m, is surrounded by an outer graphite reflector of 90 cm width, and at the top and bottom by graphite structures which also function, as the neutron reflectors. Vertical holes in the side reflector are provided for the reactivity control elements. Two different reactivity control systems are provided, for normal active control and for shutting down the reactor.

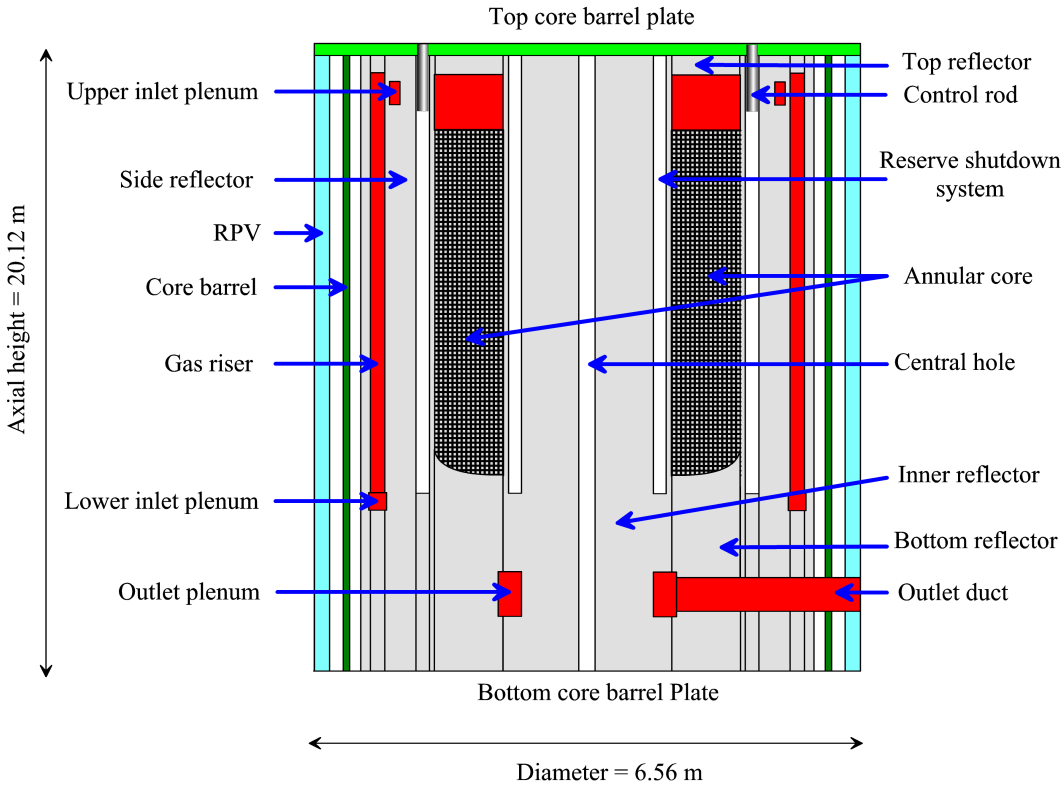


**Figure 2.1:** Dimensional size of the cross-sectional cut of PBMR reactor core [Vent05b]

## 2.5 The fuel design of the Pebble Bed Modular reactor

The PBMR fuel pebbles were developed at Necsa at Pelindaba. These fuel pebbles, with a diameter of 60 mm, consist of a 50 mm diameter fuel region, which contains about 15 600 TRISO coated particles mixed with graphite powder and phenolic resin to form a matrix. Each TRISO fuel particle of about 1 mm in diameter consists of 9.6 wt% enriched $UO_2$ surrounded by four coating layers, as shown in Fig. 2.2. The amount of enriched $UO_2$ in each pebble is about 9 g and the total uranium in one fuel load is 32.4 metric tons. The size and the physical characteristics are the same as the fuel which was developed for the German High Temperature Reactor programme [Pro06] or (HTR).

For the PBMR, the TRISO fuel particle first layer deposited on the kernels is porous carbon, followed by a thin but very dense coating of pyrolitic carbon, and a layer of silicon carbide for structural integrity which serves to retain the fission product inside the kernel. Finally, the last layer is made of pyrolitic carbon. The core of the reactor contains about 360 000 fuel pebbles. The PBMR reactor uses the continuous reloading scheme, where unloaded fuel spheres that have not reached the target burnup, are returned to the top of

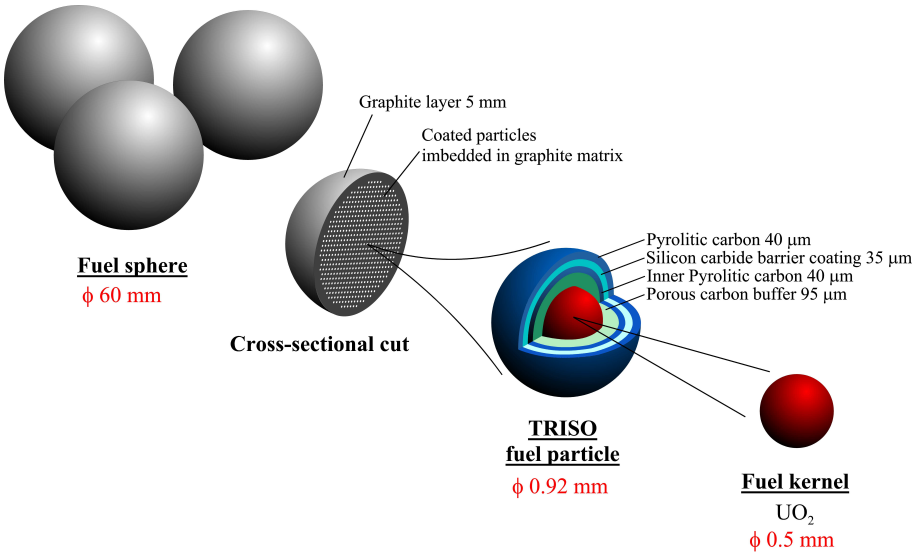


**Figure 2.2:** The design of the PBMR Fuel pebbles with coated particles embedded on the graphite matrix [Zib10].

the core. The temperature of the PBMR reactor during operation has been predicted using Computational Fluid Dynamics (CFD) [Vent05b], and the heat generated by the nuclear process is intended to be removed by helium gas which enters at the top of the reactor vessel at a temperature of 773 K and a pressure of 9 Mpa (70 bar) and exits the bottom of the vessel at a temperature of 1223 K [Ion04]. PBMR uses a direct cycle power conversion unit in which the heat is converted into electrical energy by means of a turbine-driven generator as shown in Fig. 2.3.

## 2.6 Safety features of Pebble Bed Modular Reactor design

The key safety features of the PBMR, in addition to the fission product retention capability of the fuel particle, is the small operational excess reactivity, a large negative temperature coefficient of reactivity, and the passive heat removal capability of the reactor design [Ion04].

Even in the event on the reactivity control systems not working properly, the combination of small excess reactivity and large negative temperature coefficient will still control the nuclear fission process with only a moderate temperature rise. In general, when the decay heat is not removed during shutdown, the fuel temperature will increase until its fission product retention capability is degraded. In the PBMR, the removal of decay heat is achieved by conduction, convection and radiation heat transfer from fuel through the reactor environment. The surface area is large compared to the volume of the core,

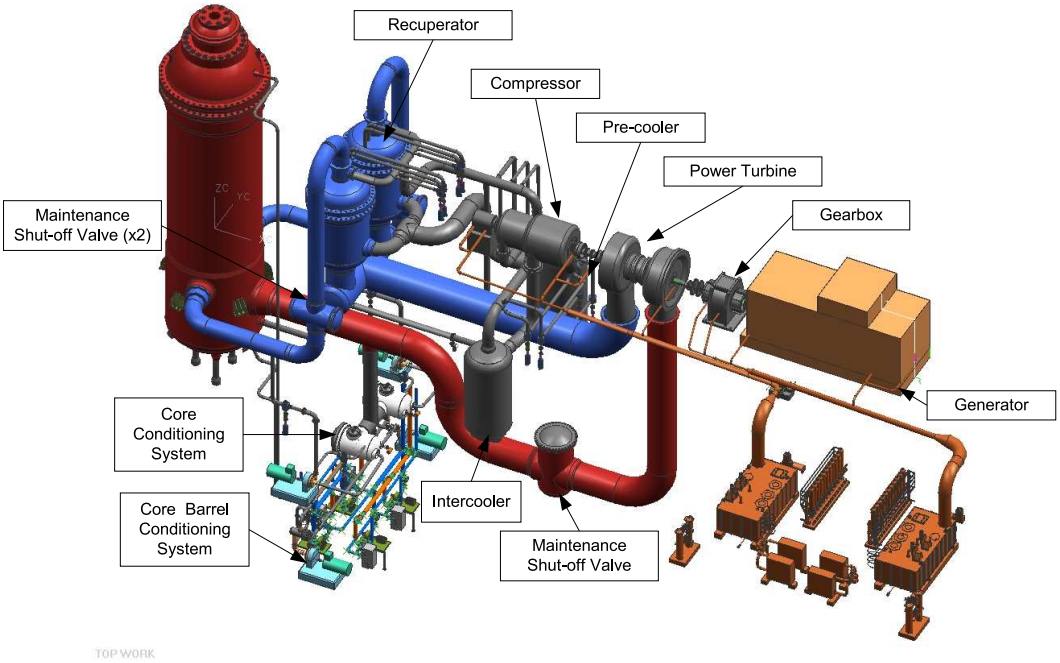


**Figure 2.3:** Schematic representation of the PBMR main power system [Vent05b].

which promotes the heat flow process and lowers the power density of the core. The high temperature resistance of the fuel ensures that the core never reaches a temperature at which significant degradation of the fuel can occur.

The large negative temperature coefficient of reactivity is caused by Doppler broadening of the resonance absorption cross-section as a result of a change in temperature of the fuel in the core. Since the Doppler broadening effect is dependent on the temperature of the fuel and affects the reactivity, the neutron energy spectrum is expected to change when the fuel temperature changes. In this work, the study of the effect of Doppler broadening is of high importance and simulations were performed using the MCNP code which is explained in detail in Chapter 3. The simulations were carried out in order to understand the Doppler broadening effect on the neutron energy spectrum as the temperature of the fuel increases, and to determine the possibility of monitoring the fuel temperature from this observation.

# Chapter 3

# Neutron transport in the nuclear reactor

Transport theory is used to describe the motion of particles, such as neutrons, protons, etc., in a nuclear reactor. The neutron transport equation can be considered to be an expression governing the neutron distribution in a reactor core and is of importance in the design of the reactor. However, the generality and inherent complexity of this equation, which involves both integration and a derivative function makes it difficult to solve. Typically, simplifying approximations are made to reduce its complexity. Hence, a concise introduction to transport theory is presented which serves to highlight the natural hierarchy of the approximations that are inherent in any reactor design model, and hence any corresponding computation.

## 3.1 Definition of terms in neutron transport theory

### 3.1.1 Neutron density

The neutron transport equation [Dud76] uses the field of probability density or distribution functions to describe the random motion of the neutron in nature. The neutron density $N(\vec{r},t)d^3r$ is defined as the expected number of neutrons in a volume element $d^3r$ at a point $\vec{r}$ at a time $t$ (see Fig. 3.1).

This neutron density, $N(\vec{r},t)$, determines the rate at which the neutron interactions are taking place at any point in the medium. Now suppose that all the neutrons in volume $V$ have the same speed $v$. The rate at which the neutron-induced nuclear reaction occurs can be expressed as the product of the neutron speed $v$ and the macroscopic cross-section $\Sigma$, $v\Sigma$ [cm·s$^{-1}$][cm$^{-1}$], i.e. the number of events per second. Hence, the definition of the reaction rate density $F(\vec{r},t)$ at any point in the system is

$$F(\vec{r},t) \equiv v\Sigma N(\vec{r},t), \tag{3.1}$$

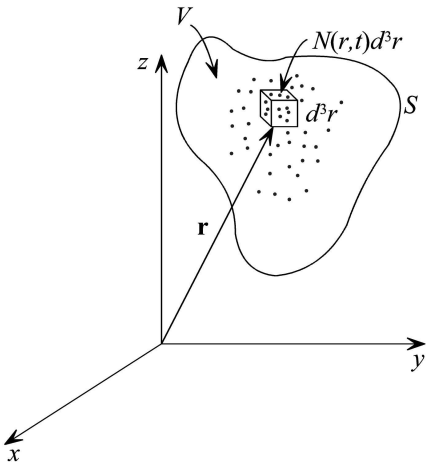


**Figure 3.1:** Neutron density $N(\vec{r},t)$ at position $\vec{r}$ at time $t$.

the rate at which interactions are occurring in volume element $d^3r$ about position $\vec{r}$ at time t. In the case where neutron density is different for various neutron energies $E$, the neutron density is defined as

$$N(\vec{r},E,t)d^3rdE,$$

and this is equivalent to the number of neutrons in volume element $d^3r$ about position $\vec{r}$, energy $E$ about $dE$, at time $t$. The concept of reaction rate density can also be generalized to include energy-dependent neutron density, hence

$$F(\vec{r},E,t) = v\Sigma(E)N(\vec{r},E,t). \tag{3.2}$$

### 3.1.2 Angular neutron density

The fundamental quantity of interest in modeling neutron transport is the angular neutron density $n(\vec{r},E,\hat{\Omega},t)$, where $\hat{\Omega} = \frac{\vec{v}}{|\vec{v}|}$ indicates the direction of motion of a neutron at a position $\vec{r}$ (see Fig. 3.2). This quantity represents the probability density of finding a neutron which has an energy $E$, at a position $\vec{r}$ moving in a direction $\hat{\Omega}$, at time $t$. The term "angular" refers to the neutron's directional dependence $\hat{\Omega}$. If the neutron distribution inside $V$ is spherically symmetric (i.e. it is isotropic), then the number of neutrons

$$N(\vec{r},E,t) = \int_{4\pi} n(\vec{r},E,\hat{\Omega},t)d\Omega. \tag{3.3}$$

Dividing equation (3.3) by the normalization factor $4\pi$ in the angular density, it becomes

$$n(\vec{r},E,\hat{\Omega},t) = \frac{1}{4\pi}N(\vec{r},E,t). \tag{3.4}$$

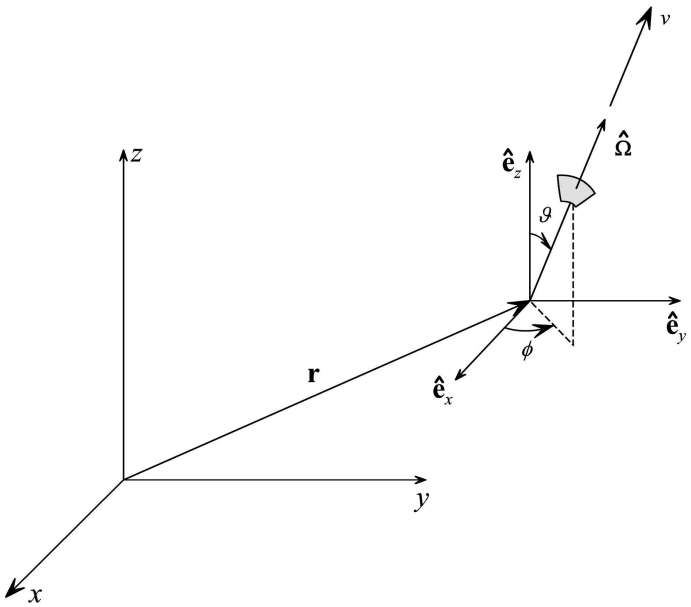


**Figure 3.2:** Variables representing the position and direction of neutrons.

More generally, $n(\vec{r}, E, \hat{\Omega}, t)$ will also have a directional dependence. The angular interaction rate can be defined as the product of neutron speed $v$, macroscopic cross-section $\Sigma(\vec{r}, E)$ and angular neutron density

$$F(\vec{r}, E, \hat{\Omega}, t) = v\Sigma(\vec{r}, E)n(\vec{r}, E, \hat{\Omega}, t). \tag{3.5}$$

### 3.1.3 Neutron flux

The product of velocity $\vec{v}$ and the particle density $N(\vec{r}, t)$ is called the neutron flux, $\phi(\vec{r}, t)$, as

$$\phi(\vec{r}, t) \equiv vN(\vec{r}, t) \quad [\mathrm{cm}^{-2} \cdot \mathrm{s}^{-1}]. \tag{3.6}$$

The integral of the angular flux over all directions, which is also equal to $vn(\vec{r}, E, t)$, is defined as the energy-dependent neutron flux, $\phi(\vec{r}, E, t)$, i.e.

$$\phi(\vec{r}, E, t) = \int_{4\pi} \phi(\vec{r}, E, \hat{\Omega}, t) d\Omega. \tag{3.7}$$

Thus, equation (3.7) is the neutron flux of energy $E$, at the position $\vec{r}$ and at time $t$ per unit energy.

### 3.1.4 Angular neutron flux

The neutron angular flux, denoted by $\phi(\vec{r}, E, \hat{\Omega}, t)$, is the total number of neutrons with energy $E$ passing at position $\vec{r}$ per second through an area

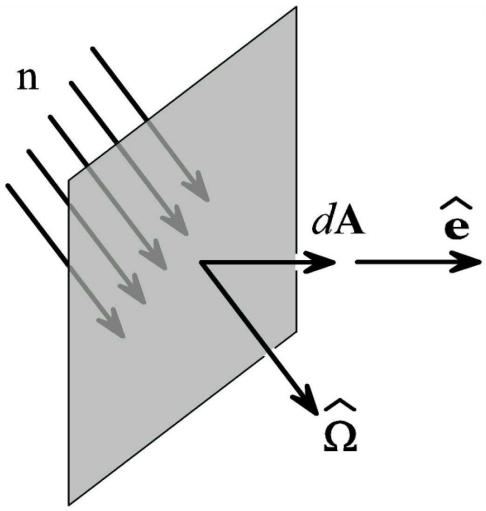


**Figure 3.3:** Neutron incident on a differential element of area $dA$.

perpendicular to $\hat{\Omega}$, around $\hat{\Omega}$ in the direction $d\hat{\Omega}$ at time $t$. The neutron angular flux equation is written as

$$\phi(\vec{r}, E, \hat{\Omega}, t) \equiv vn(\vec{r}, E, \hat{\Omega}, t). \tag{3.8}$$

Since the unit of neutron speed is cm·s$^{-1}$ and for neutron density is the n·cm$^{-3}$, therefore the unit of angular neutron flux is the n·cm$^{-2}$·s$^{-1}$.

### 3.1.5 Angular current density

In order to physically interpret the angular current density, a small area $dA$ at a position $\vec{r}$ is considered. Then $\vec{J}(\vec{r}, E, \hat{\Omega}, t)dAdEd\hat{\Omega}$ is defined as the expected number of neutrons passing through an area $dA$ per unit time $t$ with energy $E$ about $dE$, moving in direction $\hat{\Omega}$ in solid angle $d\hat{\Omega}$. The convention that $d\vec{A} = \vec{e_s}dA$, where $\vec{e_s}$ is the unit normal to the surface area element $dA$, is used.

The energy-dependent neutron current density $\vec{J}(\vec{r}, E, t)$, can be defined in terms of the angular current density, as follows:

$$\vec{J}(\vec{r}, E, t) \equiv \int_{4\pi} \vec{j}(\vec{r}, E, \hat{\Omega}, t)d\Omega, \tag{3.9}$$

and the current density, which is independent of energy, is equal to the integral of the neutron current with different energies, and is also equal to the multiple integral of neutron current at the position $\vec{r}$, at time $t$, with different energies $dE$ in all directions $d\hat{\Omega}$.

$$\vec{J}(\vec{r}, t) = \int_0^\infty \vec{J}(\vec{r}, E, t)dE = \int_0^\infty dE \int_{4\pi} \vec{j}(\vec{r}, E, \hat{\Omega}, t)d\Omega. \tag{3.10}$$

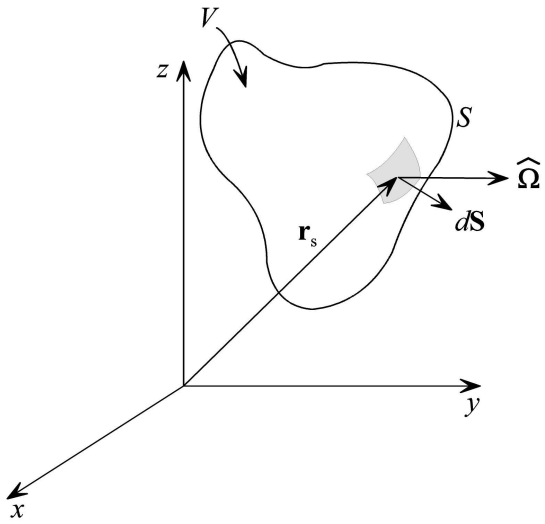


**Figure 3.4:** Arbitrary volume $V$ with surface area $S$.

The $\vec{J}(\vec{r},t)\cdot dA$ is a net rate at which neutrons pass through a surface oriented in a given direction. It is a useful quantity for describing neutron leakage from the reactor core.

## 3.2 Neutron transport equation

An arbitrary volume $V$ containing neutrons of specific energies is considered (see Fig. 3.4). With time, some of these neutrons are scattered or absorbed by nuclei, some may escape and others may enter the volume. Also, if neutron sources are present within the volume, additional neutrons may appear as they are emitted from the sources. In any event, neutrons within the volume should satisfy the condition of neutron conservation, namely, the time rate of change of the total number of neutrons in $V$ must be equal to the gain in neutrons in $V$ minus the loss of neutrons in $V$. If $n(\vec{r},E,\vec{\hat{\Omega}},t)$ is the neutron density at the point $\vec{r}$ with energy $E$ and $\hat{\Omega}$ space and time $t$, the total number of neutrons in $V$ is simply $\int_V n(\vec{r},E,\hat{\Omega},t)dVdEd\hat{\Omega}$. The neutron number conservation can then be written as

$$\frac{\partial}{\partial t}\int_0^\infty\int_{4\pi}\left(\int_V n(\vec{r},E,\hat{\Omega},t)dV\right)dEd\Omega=\frac{\partial}{\partial t}\int_V N(\vec{r},t)dV \qquad (3.11)$$

$$= \text{the rate of neutron gain in } V - \text{the rate of neutron loss from } V.$$

### 3.2.1 Neutron gain in volume $V$

The following neutron gain mechanisms are considered:

1. Any neutron source in a volume $V$ which could be as a result of nuclear fission.
   The production of neutrons can be represented by a source distribution function $s(\vec{r}, E, \hat{\Omega}, t)$, which is equal to the number of neutrons emitted in dV about $\vec{r}$, energy $E$ about $dE$, and $\hat{\Omega}$ about $d\hat{\Omega}$. The rate of production $R$ of neutrons in $V$ is the rate of change of the number of neutrons of all energies $E$ and in all directions $\Omega$ in volume $V$,

$$R = \frac{\partial}{\partial t} \int_0^\infty dE \int_{4\pi} d\Omega \left( \int_V s(\vec{r}, E, \hat{\Omega}, t) dV \right) dE d\Omega, \tag{3.12}$$

   where $s(\vec{r}, E, \hat{\Omega}, t)$ is called neutron source density.

2. Neutrons streaming into $V$ through surface $S$ as represented in Fig 3.1. The mathematical expression for this term is given together with the leakage term introduced in equation 3.18.

3. Neutron gain due to neutrons of different energy $E'$, direction $\hat{\Omega}'$ scattering into volume $V$ losing energy in the process from energy $E$ to $E'$ and changing direction from $d\hat{\Omega}$ to $d\hat{\Omega}'$.
   The mathematical expression for the gain mechanism due to neutron scattering from energy $E$ to $E'$ and direction $d\hat{\Omega}$ to $d\hat{\Omega}'$ is given in terms of the macroscopic double-differential scattering cross-section

$$\Sigma_{scat}(E, \hat{\Omega} \rightarrow E', \hat{\Omega}') = N(\vec{r}, E, t) \frac{\partial^2 \sigma}{\partial \Omega \partial E}, \tag{3.13}$$

   and then the rate at which neutrons scatter from $E$, $\hat{\Omega}$ to $E'$, $\hat{\Omega}'$ is

$$\left[ \int_V v \Sigma_{scat}(E, \hat{\Omega} \rightarrow E', \hat{\Omega}') n(\vec{r}, E, \hat{\Omega}, t) dV \right] dE' d\Omega'. \tag{3.14}$$

   The total rate at which the neutrons per unit volume are transfered is obtained by integrating the above equation over all initial neutron energies and directions, and summing over all reactions in the volume.

$$\int_0^\infty dE \int_{4\pi} d\Omega \left( \int_V dV v \Sigma_{scat}(\vec{r}, E, \hat{\Omega} \rightarrow E', \Omega') n(\vec{r}, E, \hat{\Omega}, t) dV \right) dE' d\Omega'. \tag{3.15}$$

   The above term characterizes neutron scattering from other energies and directions into $E'$, $\hat{\Omega}'$, therefore it is known as the in-scattering term.

### 3.2.2 Neutron loss mechanism

The following neutron loss mechanisms are considered:

1. Neutron leakage into and out of volume $V$ through the surface $S$.
   The leakage into $V$ through $S$ or from $V$ can be combined to calculate the net leakage through $S$. Using the definition of angular current density $J(\vec{r}, E, \hat{\Omega}, t)$, the rate at which neutrons of $E, \hat{\Omega}$ leak out of a differential surface area $d\vec{S}$ is

$$J(\vec{r}, E, \hat{\Omega}, t) \cdot d\vec{S} = v\hat{\Omega}n(\vec{r}, E, \hat{\Omega}, t) \cdot d\vec{S}. \tag{3.16}$$

   Hence the leakage contribution over the entire surface area S is

$$\int_S d\vec{S} \cdot v\hat{\Omega}n(\vec{r}, E, \hat{\Omega}, t).$$

   This term can be rewritten in terms of a volume integral by making use of the Gaussian theorem,

$$\int_S d\vec{S} \cdot \vec{A}(\vec{r}) = \int_V dV\vec{\nabla} \cdot \vec{A}(\vec{r}), \tag{3.17}$$

   to obtain

$$\begin{aligned}\int_S d\vec{S} \cdot v\hat{\Omega}n(\vec{r}, E, \hat{\Omega}, t)dEd\hat{\Omega} &= \int_V dV\vec{\nabla} \cdot V\hat{\Omega}n(\vec{r}, E, \hat{\Omega}, t)dEd\hat{\Omega} \\ &= \int_V dVv\hat{\Omega} \cdot \vec{\nabla}n(\vec{r}, E, \hat{\Omega}, t)dEd\hat{\Omega}. \end{aligned} \tag{3.18}$$

2. Neutron loss due to absorption in volume $V$.
   The neutron-nuclear interaction rate at a point $\vec{r}$ is

$$f_t(\vec{r}, E, \hat{\Omega}, t) = v\Sigma(\vec{r}, E)n(\vec{r}, E, \hat{\Omega}, t). \tag{3.19}$$

   Integrating the interaction rate given by equation (3.19) over $V$, the loss of neutrons due to collision is obtained as

$$\left[\int_V v\Sigma_t(\vec{r}, E)n(\vec{r}, E, \hat{\Omega}, t)dV\right] dEd\hat{\Omega}. \tag{3.20}$$

By combining all of the terms under the neutron gain and neutron loss mechanism, the rate of change in the number of neutrons in $V$ is given by

$$\begin{aligned}&\int_V d^3r \left[\frac{\partial n}{\partial t} + v\hat{\Omega} \cdot \vec{\nabla}n + v\Sigma_t(\vec{r}, E)n(\vec{r}, E, \hat{\Omega}, t)\right. \\ &\left. - \int_0^\infty dE \int_{4\pi} d\hat{\Omega}v'\Sigma_{scat}(\vec{r}, E, \hat{\Omega} \to E', \hat{\Omega}')n(\vec{r}, E', \hat{\Omega}', t) - s(\vec{r}, E, \hat{\Omega}, t)\right] dEd\hat{\Omega} = 0.\end{aligned} \tag{3.21}$$

The integral for $V$ will vanish when all its integrands are identical to zero [Dud76], that is

$$\int_{\text{any } V} f(\vec{r}) d^3r = 0. \tag{3.22}$$

Hence the neutron conservation equation is

$$\frac{\partial n}{\partial t} + v\hat{\Omega} \cdot \vec{\nabla} n + v\Sigma_t(\vec{r}, E, \hat{\Omega}, t) = s(\vec{r}, E, \hat{\Omega}, t) + \int_{4\pi} d\Omega \int_0^\infty dE \left( v\Sigma_{scat}(\vec{r}, E, \hat{\Omega} \rightarrow E', \hat{\Omega}') n(\vec{r}, E, \hat{\Omega}, t) \right). \tag{3.23}$$

Equation (3.23) is called the neutron transport equation for which the solution requires further simplification to enable an analytical solution represented for eventual numerical evaluation. The neutron transport equation 3.23 is numerically solved by either stochastic or other sophisticated deterministic methods. These methods solve the transport equation for the average particle behavior. The Monte Carlo simulations obtain answers by simulating individual particle events and record the tallies which provide information about their average behavior. This information can be used to interpret the average behavior of particles in the physical system. The deterministic methods provides a partially complete information about the flux throughout the phase space of the problem, whereas the Monte Carlo provides information about specific tallies with an associated error, which ensures that a confidence level is established in the obtained results. The errors depends on the the number of particles simulated. If more particles are simulated, the error associated with the tally becomes smaller.

The Monte Carlo method is applied to neutron transport to solve the complicated three-dimensional and time-dependent neutron transport problems. This method does not use phase space boxes, because there are no averaging approximations required in space, energy and time. This allows the detailed representations of all aspects of physical data in the neutron transport problem. In this project, a computational method based on a Monte Carlo particle tracking method is used to simulate neutron transport in the reactor core.

## 3.3 Monte Carlo method as applied to neutron transport

To investigate the effect of temperature change on the reactivity and the neutron energy distribution in the core and surrounding areas, a three-dimensional particle tracking code is required in order to simulate large numbers of events. A computer code distributed by RSICC (Radiation Safety Information Computational Center) of Los Alamos makes this possible. The two RSICC packages are Monte Carlo N Particle 5 (MCNP5) and Monte Carlo N-Particle X 2.6

(MCNPX 2.6). MCNPX is a general purpose Monte Carlo N particle radiation transport code designed to model the interaction of radiation with matter over a broad range of energies [MCN09]. The transportation of particles such as neutron, photon, electron, or coupled neutron/photon/electron particles can be simulated using the MCNP code. This code can also calculate eigenvalues for a critical system such as a nuclear reactor. Furthermore, it is also commonly used for radiation protection and dosimetry, radiation shielding, medical physics, nuclear reactor criticality calculations, detector design and analysis, and accelerator target design. The MCNP code is capable of treating an arbitrary 3D configuration, as well as using point-wise energy-dependent cross-sectional data that represents all possible nuclear reactions, that occurs in the reactor in the energy range $10^{-5}$ eV to 10 MeV. This makes the MCNP code a preferred choice over other neutron transport codes. The quantities calculated with MCNP are, for example the neutron flux, current, energy or charge deposited, heat reaction rates, response functions, radiographs, mesh tallies of neutrons causing fission, etc.

### 3.3.1 An overview of the MCNP input

As shown in Appendix A, a user creates an input file which is read into the MCNP code. This input file contains the descriptions of geometry, source particle and location, materials, selection of cross-section evaluations and tallies that the user wants to obtain. The geometry is defined in terms of cells, which represent the volume, and surfaces, which represent the boundaries. The user can request MCNP to count the number of particles that have entered the particular cell or crossed a particular surface. These are known as tallies and can be requested at any cell or surfaces except for those that have a particle importance of zero. The data table available to MCNP is listed in a directory file, XSDIR. Specific data tables can be selected through unique identifiers for each table, called ZAIDs (atomic number $Z$, mass number $A$, and library specifier ID). More than 836 neutron interaction tables are available for about 100 different isotopes and elements. MCNP utilizes the latest nuclear cross-section libraries and uses physics models for particle types and energies where tabular data are not available. Multiple tables for a single isotope are provided primarily because data have been processed from different evaluations and at different times, but also because of different temperature regimes and different processing tolerances. The MCNP code can be instructed in the input file to make various tallies related to particle flux and energy deposition. All tallies are normalized to be per starting particle, except in criticality calculation (KCODE), which are normalized to be per fission neutron generation. Fluxes will be averaged over surfaces, cells, cell segments, or sum of cells. Fluxes can also be tallied on a mesh and superimposed on the geometry defined in the input file.

The KCODE card is employed in the criticality calculations of the nuclear reactor. Once the geometry and the material specifications of the model is defined, the MCNP code still requires the information regarding the KCODE card in the input, in order to begin the criticality calculations. A typical KCODE card contains the following information:

- Nominal source size for each cycle.
- Initial guess for $k_{eff}$ (discussed in section 2.1).
- Number of cycles to skip before beginning tally accumulation (in case initial source guess is poor). After these cycles are discarded, it is assumed that the fission source distribution has converged to its stationary state (the fundamental mode) and tallies for reaction rates and a $k_{eff}$ value may be accumulated.
- Number of cycles to be done before the problem ends.

### 3.3.2 An overview of the MCNP output

The output file from MCNP contains tally information and a table with a standard summary of information to inform the user of how the simulation was processed. The information can give insights into the physics of neutron transport and the capability of the Monte Carlo simulations. The relative statistical errors corresponding to one standard deviation are printed with each tally. There is a detailed analysis after the tally report to help determine the confidence level in the results. When the program has completed the run, it prints a report on the calculated tally if it has passed ten statistics checks. Ten pass/no-pass checks are made for the user-selectable tally fluctuation chart (TFC) bin of each tally. Tally fluctuation charts are also automatically printed to show how a tally mean, error, variance of the variance, and slope of the largest history scores fluctuate as a function of the number of history runs.

## 3.4 Simulation of the generic HTGR core using MCNP code

In this work, the MCNP code was used to simulate a neutron energy spectrum that represents the neutron flux within the core. This was supposed to provide information on the expected neutron flux in the core and observe the change in the neutron energy distribution as the temperature of the fuel change. This is possible because the MCNP code has a cross-section library of materials at different energies and temperatures.

The information on how to create an MCNP input file for the generic HTGR core, provided in Appendix A, was obtained from the MCNP5 Criticality primer III document [Bre09]. This input sample was very useful in

obtaining more information on how to make a fuel lattice and fueling the core. Modifications to this input were performed to include a temperature (TMP) card and tallies. The fuel specifications were chosen to be different from the PBMR in order to observe the general behavior of the neutron energy spectrum change as the temperature of the fuel change in the generic HTGR core. As mentioned earlier, the PBMR project is been postponed, but the current project continue looking at the fact that there are other ongoing HTGR project in which the technique of neutron spectroscopy and, as a results, fuel temperature monitoring, could be effectively used.

### 3.4.1 Model assumptions

The assumptions made in the simulation of the generic HTGR core model with the MCNP code are listed below:

- The initial $k_{eff}$ for these calculations was set to one.
- The control rods were not part of the reactor in the MCNP model. This was done to observe the effect of Doppler broadening or self-control of the Generation-IV reactor design.
- Helium gas coolant was not part of the reactor MCNP model.
- The empty volumes of the reactor MCNP model were all void instead of air filling.
- A body centered cubic lattice distribution of the spheres and hexagonal packing of the fuel elements in the core is assumed over a few other possible distributions.
- The detectors are also assumed as empty inner volumes, this was to increase the statistical counting and to observe the raw neutron energy spectrum without the perturbation from the detector material.

In the input file, a thermal temperature TMP card was introduced to inform the MCNP code that the temperature of the reactor components was higher than room temperature and which cross-sectional library to use when transporting the particles. The TMP cards provide MCNP code with the time-dependent cell thermal temperatures that are necessary for the free-gas thermal treatment of low-energy neutron transport. Since the quantity that MCNP expects on the TMP input card is given in terms of thermal energy $E = kT$, all temperatures were also converted to energy in MeV (see Table 3.1). The thermal $S(\alpha, \beta)$ cross-sectional data at a temperature higher than 1200 K was not present in the MCNP 5 code used for this simulation hence, the simulations were done up to the highest temperature of 1200 K.

**Table 3.1:** The conversion table used for MCNP input. The temperatures are given in Kelvin, converted to energy, and the last column is the library extension identifier. The thermal S($\alpha, \beta$) cross-sectional data at a temperature higher than 1200 K was not present in the MCNP 5 code used for this simulation.

| Temperature (K) | Energy=kT (eV) | Cross-section libraries | Thermal S($\alpha, \beta$) libraries |
|---|---|---|---|
| 293 | $2.58 \times 10^{-2}$ | .70c | .10t |
| 600 | $5.17 \times 10^{-2}$ | .71c | .13t |
| 900 | $7.75 \times 10^{-2}$ | .72c | .15t* |
| 1200 | $1.03 \times 10^{-1}$ | .73c | .17t |

## 3.5 MCNP model simulation results

The analysis of the neutron energy spectrum from this simulation required an understanding of the theory that describes the neutron flux as a function of energy at different temperatures of the medium. In this section, the slow neutron energy spectrum generated in the medium is explained using the Maxwell-Boltzmann equation of an ideal gas.

### 3.5.1 Maxwell-Boltzmann spectrum

Neutron spectra generated in a volume without absorption, leakage and neutron source are described using the Maxwell-Boltzmann distribution theory. These spectra are characterized by the medium temperature $T_{\mathrm{m}}$, which implies that the neutrons will eventually reach thermal equilibrium with the medium nuclei. The neutron flux $\phi_M(E)$ as a function of neutron energy is given by the Maxwell-Boltzmann distribution [Lam66]

$$\phi_M(E,T) = \frac{2\pi n}{(\pi k_B T)^{3/2}} \left(\frac{2}{m}\right)^{1/2} E \exp\left(-E/k_B T\right), \tag{3.24}$$

where $n$ is the density of neutrons, $k_B$ is the Boltzmann constant, $m$ is the neutron mass in atomic mass units, and $T$ is the temperature of the medium. The energy at which $\phi_M(E,T)$ is maximum is denoted by $E_T$ and is obtained by equating the derivative of equation (3.24) to zero,

$$\frac{d\phi_M(E,T)}{dE} = \frac{2\pi n}{(\pi k_B T)^{3/2}} \left(\frac{2}{m}\right) \frac{d(E \exp\left(-E/k_B T\right))}{dE} = 0. \tag{3.25}$$

The solution of equation (3.25) is

$$E_T = k_B T. \tag{3.26}$$

The speed of the neutrons having an energy $E_T$ will be written as $v_T$, that is

$$\frac{1}{2} m v_T^2 = k_B T. \tag{3.27}$$

From equation (3.27), it is expected that the temperature of the medium would be equal to the neutron temperature if the spectrum is in thermal equilibrium. However, in a thermal nuclear reactor core the neutron energy distribution is never precisely in thermal equilibrium with the medium temperature. These effects all act to shift the neutron energy distribution away from thermal equilibrium.

### 3.5.2 The thermal flux

The thermal flux denoted by $\phi_T(\vec{r})$ is defined as the integral of the energy dependent flux $\phi(\vec{r}, E)$ over the thermal energies, that is

$$\phi_T(\vec{r}) = \int_0^\infty \phi(\vec{r}, E)dE. \tag{3.28}$$

In the absence of diffusion cooling, $\phi(\vec{r}, E)$ can be represented by equation (3.24), namely

$$\phi(\vec{r}, E) = \frac{2\pi n(\vec{r})}{(\pi k_B T_\mathrm{n})^{3/2}} \left(\frac{2}{m}\right)^{1/2} E \exp\left(-E/k_B T\right), \tag{3.29}$$

where $n(\vec{r})$ is the neutron density at $\vec{r}$ and $T_\mathrm{n}$ is the effective neutron temperature. Equation (3.29) can be substituted into (3.28) and the integration can be carried out from zero to infinity because the Maxwell-Boltzmann distribution dies off so rapidly beyond $E \approx 5k_B T_\mathrm{n}$. Thus,

$$\phi_T(\vec{r}) = \int_0^\infty \phi(\vec{r}, E)dE = \frac{2\pi n(\vec{r})}{(\pi k_B T_\mathrm{n})^{3/2}} \sqrt{\frac{2}{m}} \int_0^\infty E \exp^{(-E/k_B T)} \tag{3.30}$$

$$= \frac{2}{\sqrt{\pi}} n(\vec{r}) \left(\frac{2k_B T_\mathrm{n}}{m}\right)^{1/2}. \tag{3.31}$$

From equation (3.27),

$$v_T = \left(\frac{2k_B T}{m}\right)^{1/2}, \tag{3.32}$$

and substituting this into equation (3.31), one obtains

$$\phi_T(\vec{r}) = \frac{2}{\sqrt{\pi}} n(\vec{r}) v_T. \tag{3.33}$$

Since $v_T$ depends upon the effective neutron temperature $T_\mathrm{n}$, it follows that $\phi_T$ is also temperature dependent. If, for instance, the temperature is raised, the thermal flux increases, provided the neutron density is held constant.

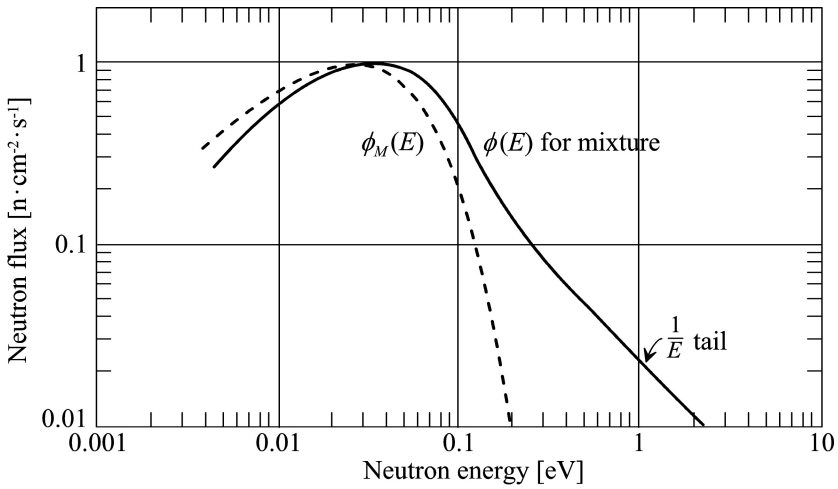


**Figure 3.5:** Simulated low-energy neutron flux $\phi(E)$ (solid line) with effective neutron temperature $T_n = 440$ K and the Maxwell-Boltzmann flux distribution $\phi_M(E)$ (dotted line) at 296 K, adapted from Ref. [Lam66].

### 3.5.3 Non-equilibrium slow neutron spectrum

The thermal flux discussed above will not be in equilibrium with the medium if there is neutron absorption, source, and leakage from the core during the slowing-down process. This flux $\phi(E)$, shown in Fig. 3.5, is acquired from the simulation of the neutron flux in a medium with absorber and water moderator at a temperature of 296 K [Lam66]. The plot of Maxwell-Boltzmann distribution $\phi_M(E)$ flux at the same temperature is also shown in the diagram. Both curves are normalized to maximum values of unity. It can be seen that the simulated flux, $\phi(E)$, is made up of two components.

For energies up to about 0.15 eV, $\phi(E)$ is similar to the shape of the Maxwell distribution, and for energies above 0.15 eV, $\phi(E)$ is proportional to $1/E$, owing to the low-energy flux in the moderating region. It can be seen that the simulated spectrum in Fig. 3.5 is shifted to larger values of neutron flux at higher energies than the Maxwell-Boltzmann distribution. This is due to the absorption at thermal energies that tends to remove lower energy neutrons because of the absorption cross-section, which is proportional to $1/v$. Another reason is due to the fact that fast neutrons slow-down into the thermal region from higher energies and the result is an increase in the average energy of the thermal neutrons. The neutron flux distribution in this case is said to be hardened. In a power reactor where about 90% of the uranium is $^{238}$U and 10% is $^{235}$U (see section 3.4), the absorption is so large that the thermal energy distribution is substantially different from a Maxwell-Boltzmann distribution.

The neutron flux $\phi(E)$ might not have exactly be a Maxwell-Boltzmann distribution, but it is convenient to assume that the slow neutron spectrum is still predominantly Maxwell-Boltzmann-like in shape. It was found [Lam66]

that the Maxwell-Boltzmann model at a temperature of 440 K provides a good fit to the slow neutron spectrum $\phi(E)$, and in this case 440 K was said to be the effective neutron temperature $T_{\mathrm{n}}$. Having concentrated absorbing material such as $^{238}$U as it was in this case, increases the effective neutron temperature $T_{\mathrm{n}}$. The condition of no absorption, leakage, and neutron source can not be fulfilled in a practical system, but the spectrum in the slow neutron energy region can still be described by a temperature adjusted Maxwell-Boltzmann distribution. Hence, the Maxwell-Boltzmann distribution will be used to fit and extract the effective neutron temperature from the MCNP-simulated neutron energy spectrum in the present work.

### 3.5.4 Neutron energy spectrum

The neutron flux $\phi(E)$ from the thermal reactor can be split into three energy groups, namely 1, 2, and 3, as shown in Fig. 3.6. These energy groups 1, 2, and 3 represent the slow-, intermediate- and fast neutron flux respectively. A standard formulation [Ges11] of the flux can be written as

$$\varphi(E,T,t) = \phi_1(t)f_1(E,T) + \phi_2(t)f_2(E) + \phi_3(t)f_3(E), \tag{3.34}$$

where 1, 2, and 3 refer to slow, intermediate, and fast neutrons respectively. The component levels $\phi_i$ can evolve with time $t$, whereas the spectrum function $f_i$ changes mainly with energy $E$ and temperature $T$. The spectrum is plotted as flux per unit lethargy, which is equal to the mid-energy of the bin $E$ times the differential flux as discussed in section 4.6.1. The lethargy plot maintains constant width energy bins by having the bin size changed logarithmically. This type of plot gives the best visual picture of relative neutron energies. Hence, it is preferred to plot the neutron spectra in flux per unit lethargy.

In the plot, Fig. 3.6, the highest part of the neutron energy spectrum at energies above 0.2 MeV is characteristic of a fission neutron spectrum (discussed in section 4.4.5). The intermediate part of the neutron energy spectrum, from 1 eV to 0.1 MeV, is from the slowing-down of the fast neutrons. The slow neutron flux, in the energy range below 0.3 eV, is a characteristic of a Maxwell-Boltzmann distribution, as discussed earlier in section 3.5.1. This spectrum shape is typical of all thermal reactors. The energy interval for the fast neutron flux, 0.2 MeV to 10 MeV, is wide enough to permit the assumption that all prompt neutrons from fission reactions are within this group. The intermediate energy neutrons are the result of the strong moderation due to neutrons scattering with graphite atoms leading to a $1/E$ slowing-down spectrum. In the slowing-down spectrum, the lethargy flux is decreasing for decreasing $E$, and has the dips caused by the resonance capture of $^{238}$U. The slowing-down process continues until the energy in the thermal motion of atoms in the moderator is equal to the neutron energy at which point a neutron can gain energy in a collision as well as lose it. This results in a distribution that has a shape

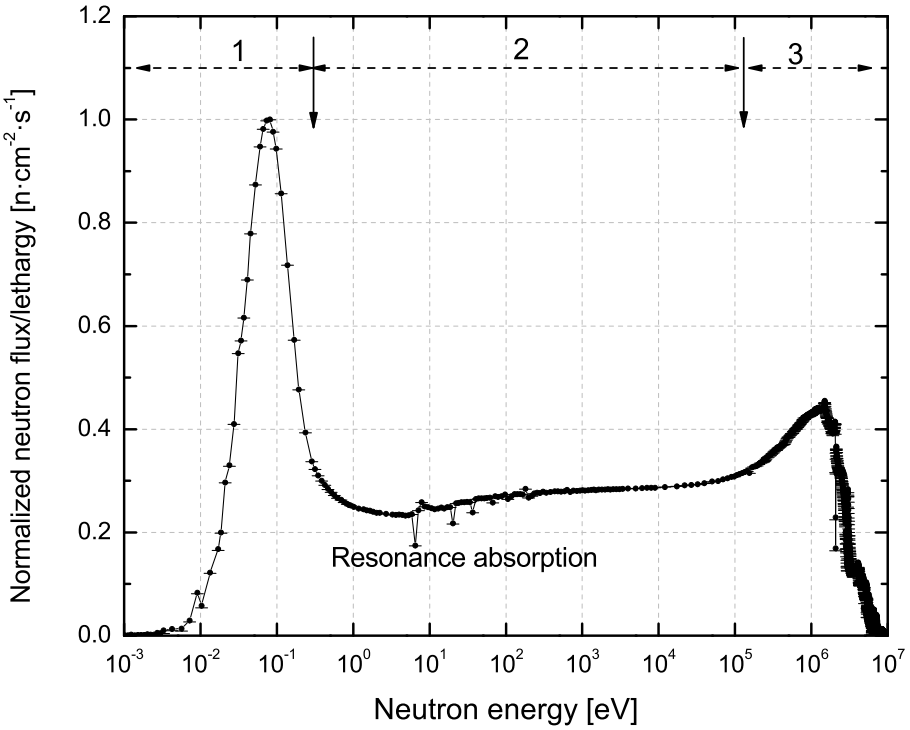


**Figure 3.6:** Normalized neutron energy spectrum within the core is split into three energy groups, namely 1, 2, and 3 which represent the slow-, intermediate- and fast neutron flux respectively.

similar to a Maxwell-Boltzmann distribution centered at the temperature of the moderator or reflector. At room temperature, the average neutron energy is 0.025 eV ($E = k_B T$); this energy is generally also used to define thermal neutron cross-sections and corresponds to the well-known thermal neutron velocity of 2200 m/s.

## 3.6 Neutron energy spectrum at different temperatures

As has been said earlier, in section 2.3, there are several parameters which determine the reactivity of a reactor, for example thermal utilization, resonance escape probability, diffusion length, etc. These parameters are functions of the temperature of the coolant, fuel, and moderator. Changes in the temperature of the reactor components (fuel, moderator and coolant) lead to changes in reactivity.

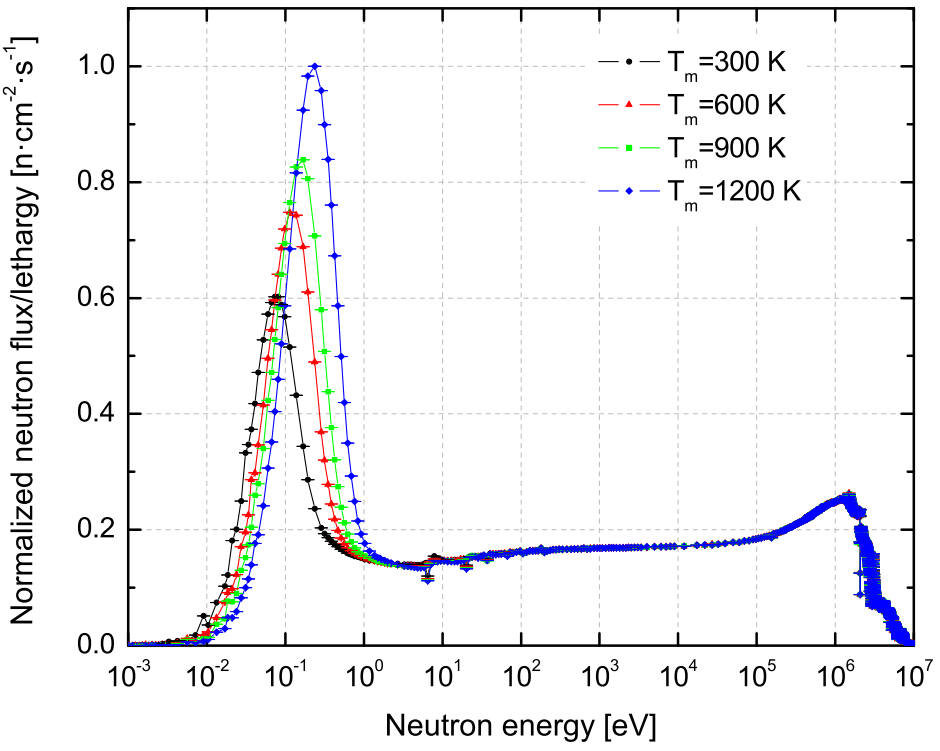


**Figure 3.7:** Normalized neutron energy spectra within the core at different temperatures.

In the MCNP simulation, the temperature of the fuel and moderator were increased to observe the effect on the neutron energy spectrum, which gives important information about the behaviour of reactivity. The neutron flux perturbation due to coolant was neglected in the simulation, since the coolant does not have a strong effect on reactivity compared with fuel and moderator temperature. The results are seen in the neutron energy spectrum shown in Fig. 3.7. The largest part of the fuel in the core is $^{238}$U, and the neutron capture cross-section of this isotope has several resonance. These resonances broaden as the temperature of the fuel increases. The neutron flux decreases significantly as they slow down passing through the resonance with a strong resonance at 6.67 eV as shown in Fig. 3.8. It can also be noticed that the dip in the flux becomes larger as the temperature increases. At higher temperatures the number of neutron captures in the intermediate energy region increases, and the slow neutron flux reduces as a result. Also, the absorption cross-section for most materials in the reactor behaves as $\sqrt{1/v}$ for lower neutron energies. Hence, the lower energy neutrons in the spectrum are depleted by

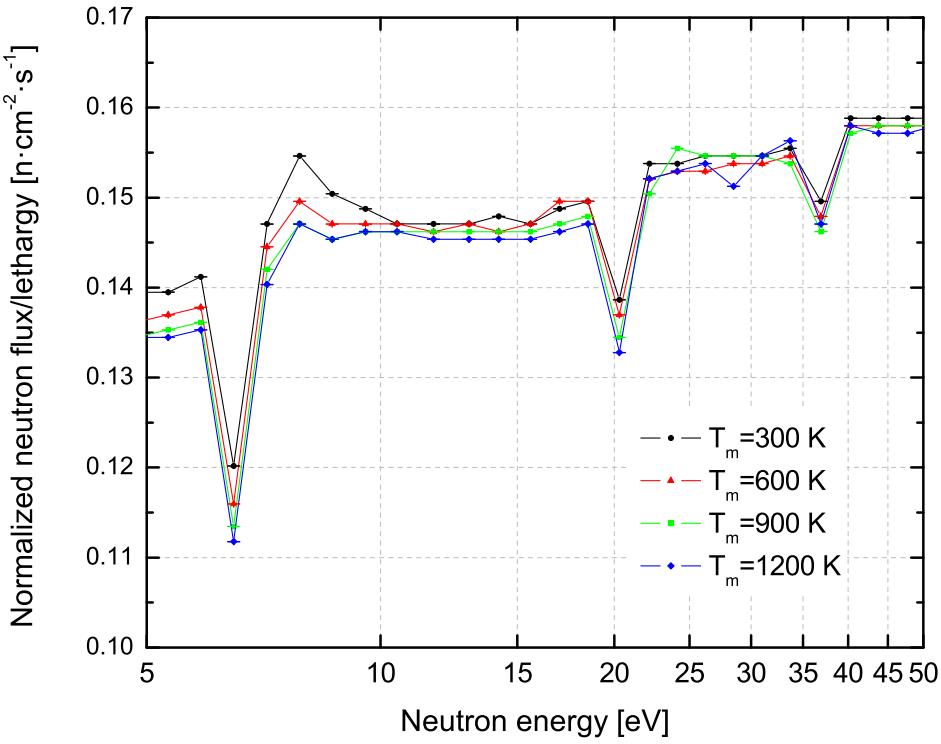


**Figure 3.8:** A closer view of the neutron flux dips near the strong absorption resonances between 5 and 50 eV.

absorption and shifted to larger value of neutron flux at higher energies. This spectrum is hardened, which refers to the 'hotter' high temperature neutrons. The rate of nuclear fission on $^{235}$U decreases with spectrum hardening, whereas it increases for $^{239}$Pu (populated through neutron capture in $^{238}$U) [Su70]. It is in the lower energy region of the neutron energy spectrum that an effect of fuel temperature change is strongly visible, the neutron spectrum shown in Fig. 3.7 is divided into two components, namely the slow neutron flux $E < 1.2$ eV and a fast neutron flux $E > 1.2$ eV to 10 MeV.

The slow neutron flux is expected not to be in equilibrium with the medium because of a $^{235}$U fission source, absorption of the intermediate neutrons by $^{238}$U and leakage of neutrons during the slowing-down process which changes as the fuel temperature changes. Thus, the slow neutron spectra deviates from the Maxwell-Boltzmann distribution of thermal equilibrium. However, as has been discussed earlier in section 3.5.3, the Maxwell-Boltzmann distribution function can still be used to determine the effective neutron temperature by fitting the slow neutron flux peak with the Maxwell-Boltzmann distribution.

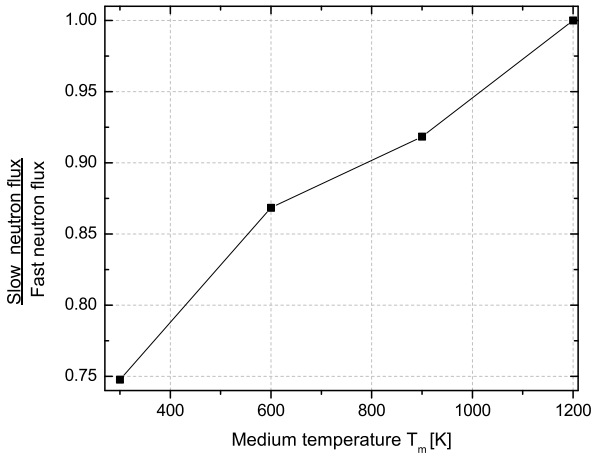


**Figure 3.9:** The ratio of slow to fast neutron flux a function of the temperature of the medium.

**Table 3.2:** The temperature distribution in the neutron energy spectra from the PBMR in Fig. 3.10.

| | Temperature [K] | | | |
|---|---|---|---|---|
| Line | Fuel kernel | Rest of the fuel | Reflector | RPV |
| Black | 1500 | 1500 | 1488 | 1400 |
| Red | 800 | 800 | 788 | 700 |
| Blue | 1500 | 800 | 788 | 700 |

In addition, it is observed that the counts in the slow neutron flux increase while those in the fast neutron flux remain relatively constant with an increase in temperature. The ratio of fast neutron flux to lower energy flux is plotted in Fig. 3.9. It can be noticed that the ratio of slow to fast neutron flux increases with an increase in temperature.

## 3.7 Benchmark of the generic HTGR MCNP model with the PBMR deterministic model

Simulations of the PBMR reactor operating at different temperatures had been performed earlier at the PBMR Company [Zam10], so it was important to verify whether the results from the present simulations are consistent with their results from the Generation-IV HTGR PBMR reactor. The benchmark spectrum was obtained from deterministic method criticality simulations as shown in Fig. 3.10. In general, the plot pattern looks somewhat similar

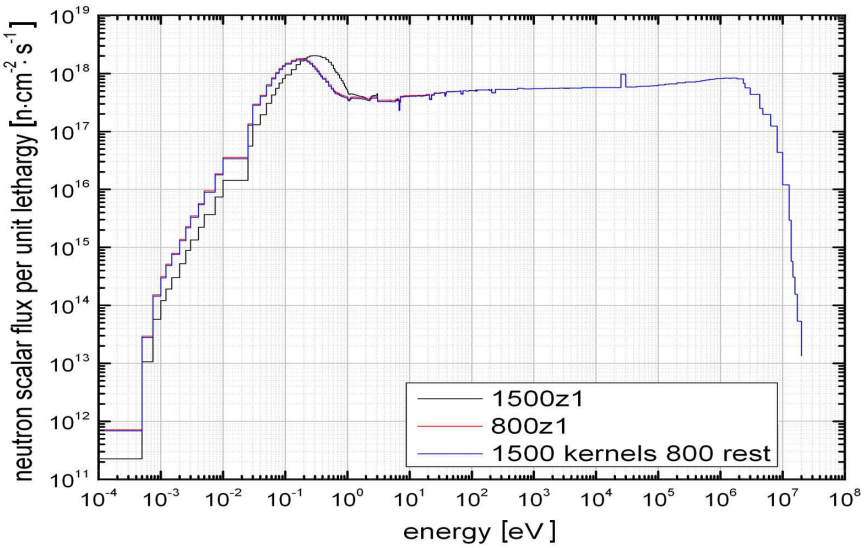


**Figure 3.10:** Neutron energy spectra within the core from PBMR simulated at the temperatures presented in Table 3.2, [Zam10].

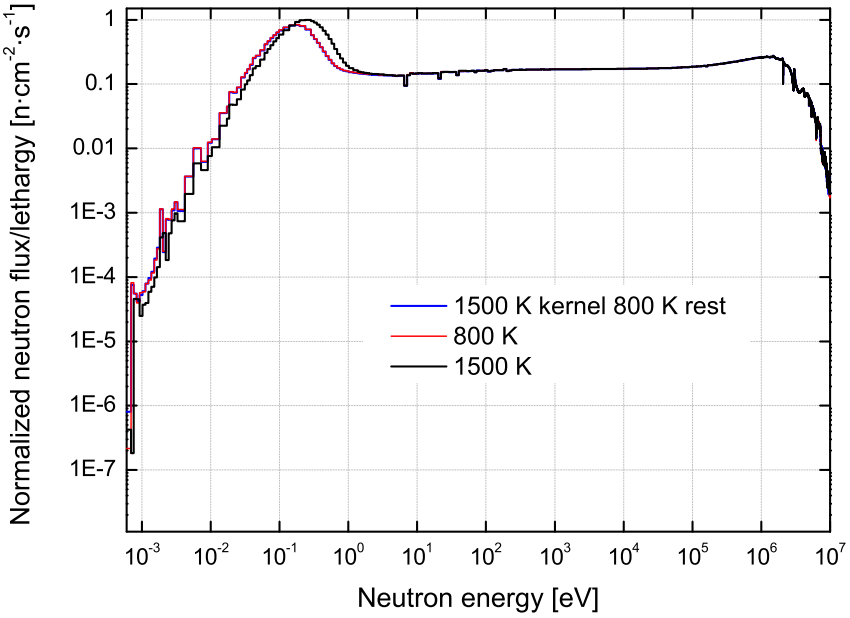


**Figure 3.11:** Normalized neutron energy spectra within the core at temperature of 1500 K for fuel and 800 K for the rest of the reactor components, 800 K for fuel and for the rest of reactor components, and 1500 K for fuel and for the rest of reactor components.

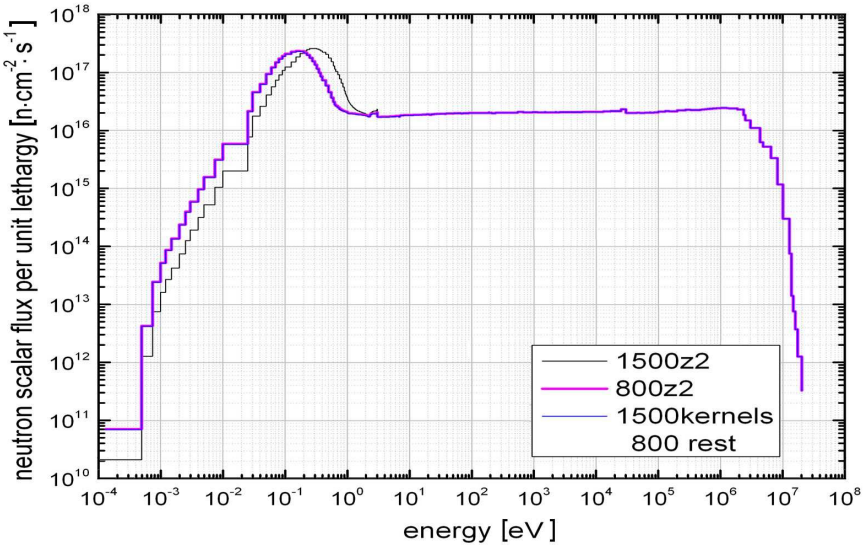


**Figure 3.12:** The neutron energy spectra at different temperatures within the outer graphite reflector of the PBMR reactor, [Zam10].

from low to high energy neutrons. In the low energy region, both spectra are hardened, i.e., shifted to larger value of neutron flux at higher energies as the temperature of the core increases. This is because of the factors that are discussed in section 2.3. The spectrum in Fig. 3.10 have more resonance absorption effects on the intermediate energy region as compared to that in spectrum in Fig. 3.11. These defects are due to some differences in cross-section libraries used in the two codes.

The neutron flux profile at different temperature at different places in the reactor was also obtained using the deterministic method. These were simulated to determine the effect of the outer graphite reflector and RPV to the neutron flux profile that leaks out of the core. As seen in Fig. 3.12, the neutron flux profile within the reflector has not changed much from the one within the core shown in Fig. 3.10, but the flux has reduced by two orders of magnitude. In contrast, neutron flux within the RPV, Fig. 3.13, have reduced and the profile have changed significantly from the one in the core. This is because fast neutrons are moderated and slow neutrons are absorbed as they attenuate the graphite, core barrel and RPV which contains the slow neutron absorbing material $^{10}$B.

## 3.8 Effective neutron temperature

As has been pointed out in section 3.5.4 that the neutron energy spectrum is the sum of the slow, intermediate and fast neutron spectrum. In this calculation, the slow neutron spectrum is of interest in determining the effective

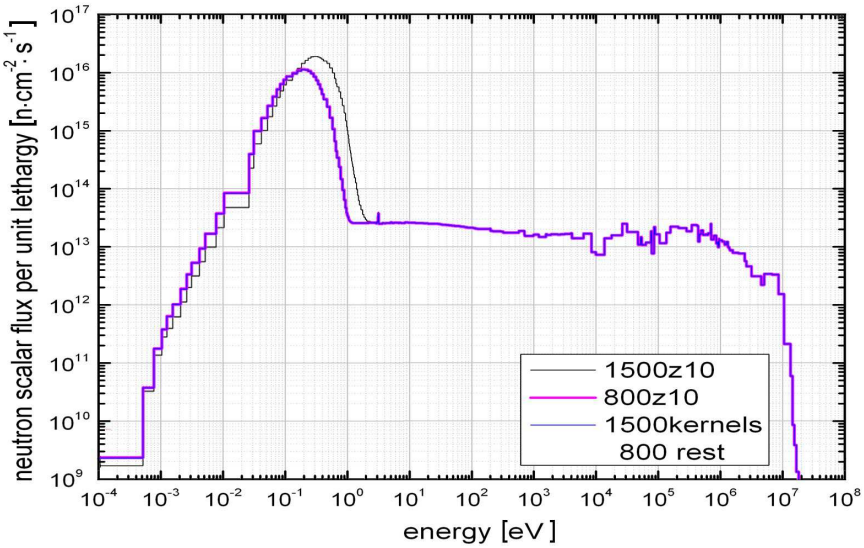


**Figure 3.13:** The neutron energy spectra at different temperatures within the reactor pressure vessel of the PBMR reactor, [Zam10].

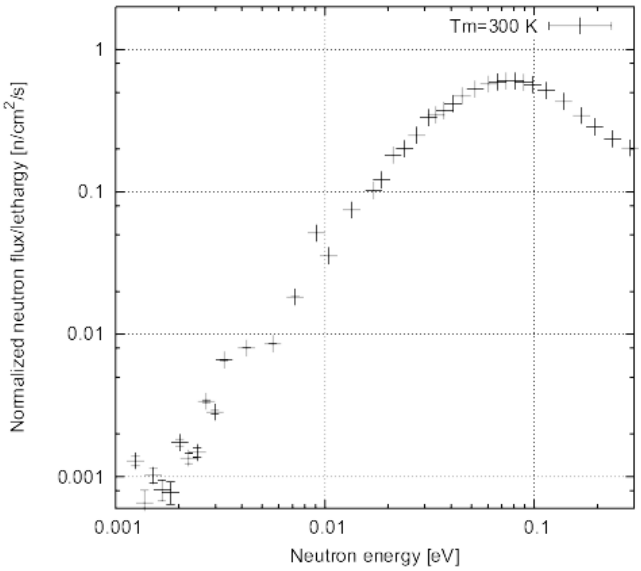


**Figure 3.14:** The resultant spectrum of lower neutron energies after subtraction of the intermediate and fast neutron spectra.

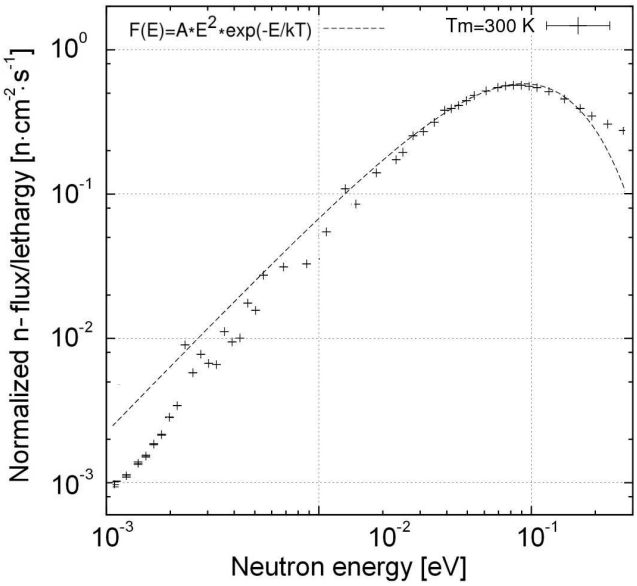


**Figure 3.15:** Maxwell distribution function shown in solid line does not fit the data at lower neutron energies well.

neutron temperature for each temperature of the medium. Therefore, an intermediate and fast neutron spectrum are subtracted from the neutron energy spectrum and the resulting spectrum is shown in Fig. 3.14. This slow neutron peak can now be fitted with a Maxwell-Boltzmann distribution equation (3.24);

$$\phi_M(E) = A \cdot E \exp\left(-E/k_B T\right). \tag{3.35}$$

Here, $A$ is a constant for normalization and $T$ is an energy parameter analogous to a moderator temperature in the reactor. Since the present slow neutron spectrum $\phi(E)$ is calculated per unit lethargy, the Maxwell-Boltzmann distribution $\phi_M(E)$ is multiplied with energy $E$ for normalization of the two spectra. Equation (3.35) becomes

$$E\phi_M(E) = A \cdot E^2 \exp\left(-E/k_B T\right). \tag{3.36}$$

Fig. 3.15 shows the fitting yields obtained with the function (3.36). It can be noticed that the function $E\phi_M(E)$ is not a good fit to the data at lower neutron energies $E < 2 \times 10^{-2}$ eV, and the fitting line is above the data. The Maxwell-Boltzmann distribution neglects some important physical effects when characterizing the slow neutron flux. These are the energy dependence of the absorption cross-section $\sigma_{abs}(E)$ for the material, neutrons entering into and leaking out of the core, and the source of neutrons through the fission process. In the reactor, the absorption cross-section for the fuel material is proportional to $1/v$ and the absorption at low energies tends to larger at the far

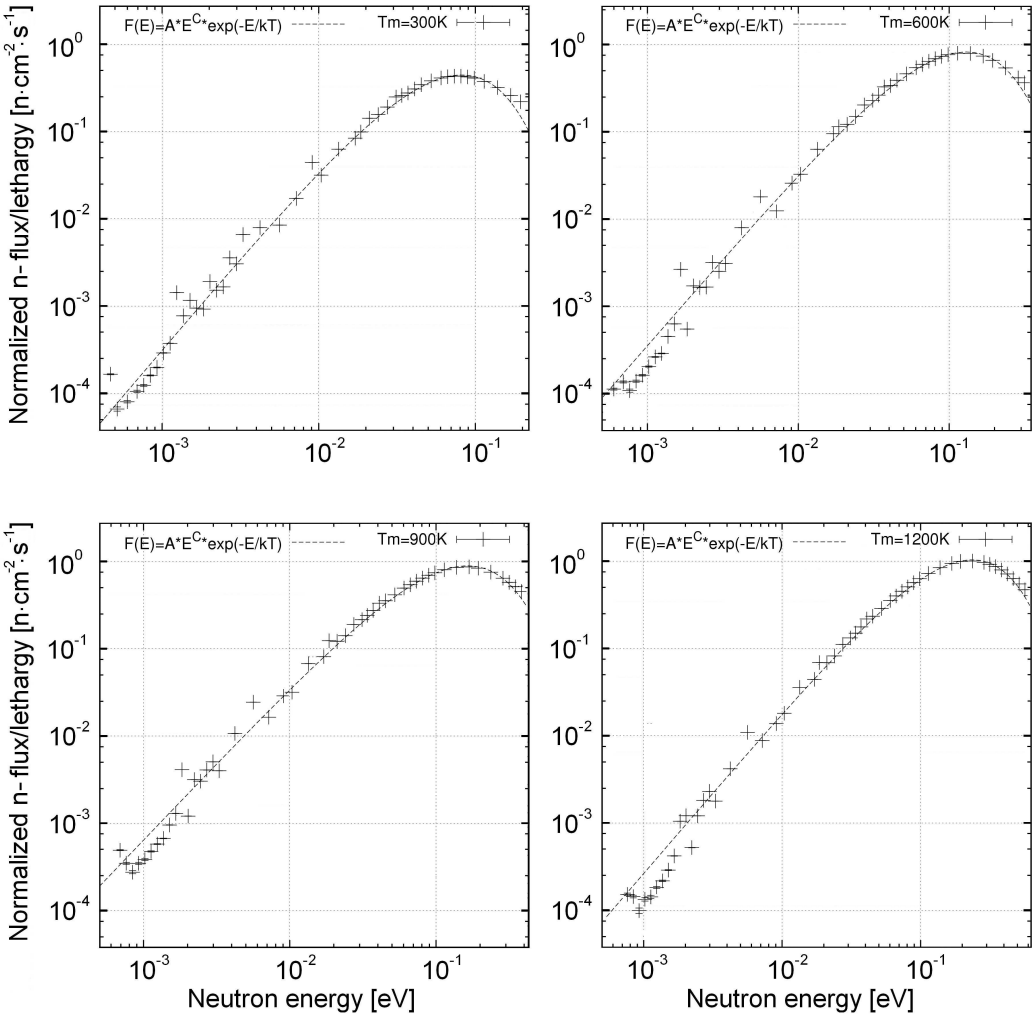


**Figure 3.16:** The slow neutron spectra of medium temperature $T_{\mathrm{m}} = 300$, 600, 900 and 1200 K are shown with a modified Maxwell-Boltzmann distribution function to fit the data.

**Table 3.3:** Fitting results for thermal flux spectra.

| $T_{\mathrm{m}}$ (K) | Parameter $C$ | $T_{\mathrm{n}}$ (K) | Parameter $A$ |
|---|---|---|---|
| 293 | $2.32 \pm 0.09$ | $401 \pm 5$ | $(3.00 \pm 0.09) \times 10^{21}$ |
| 600 | $2.19 \pm 0.06$ | $690 \pm 9$ | $(1.00 \pm 0.04) \times 10^{20}$ |
| 900 | $2.18 \pm 0.07$ | $875 \pm 6$ | $(9.0 \pm 0.1) \times 10^{19}$ |
| 1200 | $2.12 \pm 0.04$ | $1316 \pm 8$ | $(1.00 \pm 0.02) \times 10^{19}$ |

end of the low energy range. Also, the absorption resonance of $^{238}$U removes intermediate energy neutrons before being thermalized and become part of the slow neutron spectra. To compensate for the absorption effects, $\phi_M(E)$ is supposed to be multiplied by $E$, but if we considering that some fast neutrons escapes the absorption resonances as they slow down. Then, the new fitting function is defined as

$$\phi(E) = A \cdot E^C \exp\left(-E/k_B T\right). \tag{3.37}$$

The exponential parameter $C$ in equation (3.37) provides a good fit to the data when using the Gnuplot program [Gnu08]. Fig. 3.16 shows the optimum fitting of the slow neutron spectra and Table 3.3 shows the corresponding parameters obtained. The parameter $C$ decreases with an increase in temperature of the medium $T_{\mathrm{m}}$, which could be due to the effects explained earlier in this section. The results from the fit of the spectra shows that the effective neutron temperature is higher than the temperature of the medium as presented in the Table 3.3. In the fuel kernel where the fission products have deposited almost all of their energy, these temperatures $T_{\mathrm{n}}$ are even higher.

Developing a neutron detector that is sensitive to this neutron energy range will provide information about the change of temperature in the core. The discussion on in-core temperature monitoring is given in Chapter 7.

# Chapter 4

# Introduction to neutron physics

The successful development of a neutron detector is based on a good understanding of the physics involved in neutron detection. This includes determining the type of interaction that converts neutrons into charged particles and material sensitive to the neutron energy region of interest. Information about different types of neutron-producing reactions, neutron source intensity and their energy range are also of importance in the development of a neutron detector.

## 4.1 Neutron sources

Neutrons are neutral particles and are one of the constituents of the nucleus. The release of the neutrons requires a process that frees them from the strong nuclear forces that holds the nucleus together. Such processes are nuclear reactions, where two nuclei, neutron and a nucleus, charge particle and nucleus fuse to form a compound nucleus that de-excites by emitting neutrons, and spontaneous fission [Adl09] where a very unstable heavy nuclei undergoes spontaneous fission. In this section we describe the principal sources of neutrons.

### 4.1.1 Nuclear reactor neutron source

Nuclear reactors are the most abundant source of neutrons with a wide range of energies. The neutron energy distribution from the fission of $^{235}$U and the decay of fission products extends from a few keV to more than 10 MeV. Research reactors often have beam ports from which neutron beams emerge into experimental areas outside the main reactor shielding. These neutrons are usually degraded in energy, having passed through parts of the reactor core and coolant as well as the structural materials. A detailed discussion of the neutron production from the nuclear fission process is found in section 4.4.5.

### 4.1.2 Neutron generator source

The monoenergetic neutrons are produced through nuclear fusion reactions of two nuclei in the neutron generator device. This generator uses a compact linear accelerator to accelerate either deuterium (D), tritium (T), or a mixture of these two isotopes into a metal hydride target, which contains either D, T or a mixture to create a fusion reaction. In neutron generators, the two important fusion reactions are the D-T and D-D reactions. These reactions can occur with ions of a few hundreds keV in energy, and are exothermic.

The D-T reaction results in the formation of a $^{4}$He ion and a neutron with an average kinetic energy of approximately 14.1 MeV. The neutron sources employing this type of reaction are typically known as 14 MeV neutron generators, even though the neutron energy varies slightly, depending on the angle of emission. The neutron yield of current generators is up to $5 \times 10^{11}$ n·s$^{-1}$ and can potentially reach $10^{14}$ n·s$^{-1}$. The D-D reaction results in the formation of a $^{3}$He nucleus and the release of a neutron with a kinetic energy of approximately 2.45 MeV. The neutron yield can be up to $10^{12}$ n·s$^{-1}$. The D-T reaction provides a high yield of neutrons with low accelerated particle energy. Hence, the D-T reaction has become the most widely-used neutron-generating mechanism in field applications. The advantage of using a neutron generator source is that it can be switched off when not in use.

### 4.1.3 The $(\alpha, n)$ source

Neutrons are produced when an energetic $\alpha$ particle, emitted from various radionuclides such as $^{210}$Po, $^{226}$Ra, $^{239}$Pu or $^{241}$Am, interacts with light elements such as Be and B to induce ($\alpha$,n) reactions. An $\alpha$-source and light elements may be mixed together as powder and encapsulated to make a radioactive neutron source. In order to minimize the Coulomb repulsion between the $\alpha$ particle and the target nucleus, the light elements are used as converters. The neutron intensity from an $(\alpha, n)$ source dies off with the half-life of the $\alpha$-emitter [Tur95]. A continuous neutron energy spectrum up to a maximum is produced from this type of source. This is because the $\alpha$-particle slows down, through interaction with the source material, by different amounts of energy before striking a nucleus. The neutron and recoil nucleus share a total energy equal to the sum of the $Q$ value and kinetic energy that the $\alpha$ particle has as it strikes the nucleus. The ($\alpha$,n) neutron sources are listed in Table 4.1.

### 4.1.4 Photoneutron ($\gamma$,n) source

Neutrons are produced when energetic photons interact with nuclei through the ($\gamma$,n) reaction. The photons must possess sufficient energy to overcome the neutron binding energy in the nuclei and induce the reaction. The photoneutron production cross-section $\sigma_{(\gamma,n)}(E)$ for most nuclei has an energy threshold

**Table 4.1:** Some of the $\alpha$-particle neutron reactions.

| Source | Nuclear reaction | Average neutron Energy [MeV] | Half-life |
|---|---|---|---|
| $^{210}$PoBe | ($\alpha$,n) | 4.2 | 138 d |
| $^{210}$PoB | ($\alpha$,n) | 2.5 | 138 d |
| $^{226}$RaBe | ($\alpha$,n) | 3.9 | 1600 y |
| $^{226}$PoB | ($\alpha$,n) | 3.0 | 1600 y |
| $^{239}$PoBe | ($\alpha$,n) | 4.5 | 24100 y |

**Table 4.2:** The ($\gamma$,n) reaction for the neutron production.

| Nucleus | Threshold energy | reaction |
|---|---|---|
| $^{2}$H | 2.225 | $^{2}$H($\gamma$,n)$^{1}$H |
| $^{6}$Li | 3.698 | $^{6}$Li($\gamma$,n)$^{5}$Li |
| $^{9}$Be | 1.665 | $^{9}$Be($\gamma$,n)$\alpha\alpha$ |
| $^{13}$C | 4.946 | $^{13}$C($\gamma$,n)$^{12}$C |

of about 7 MeV, and increases by several orders of magnitude to a maximum of a few mb·nucleon$^{-1}$ at photon energies of about 20 MeV to 23 MeV for light nuclei (A $\leq$ 40) or 13 MeV to 18 MeV for medium and heavy nuclei [Joh11]. Only a few light nuclides have low thresholds (less than 7 MeV) for the ($\gamma$,n) photoneutron reactions. The threshold energy for some photoneutron source reactions are listed in Table 4.2. In a high energy electron accelerator, the bombardment of a target with energetic electrons produces intense Bremsstrahlung $\gamma$-rays with an energy distribution up to the incident electron energy [Liu01]. These photons are absorbed in the target nuclei, causing excitations that release energetic photoneutrons during the de-excitation process [Bha05]. The ($\gamma$,n) photoneutron production reaction mechanism can also be used to produce laboratory neutron sources by throughly mixing a beryllium compound with a radionuclide that emits high-energy ionizing photons such as americium (Am) and antimony (Sb). Alternatively, the encapsulated radionuclide can be surrounded by a beryllium-bearing shell. One of the most commonly used sources of photoneutrons is an antimony-beryllium (Sb-Be) mixture [Hum51], which has the advantage of being rejuvenated by exposing the source to reactor neutrons to transmute the stable $^{123}$Sb into radioactive $^{124}$Sb (60.2 days). Such sources typically emit about 30 neutrons per 10 Bq of $^{124}$Sb. Photoneutron sources emit reasonably mono-energetic neutrons.

### 4.1.5 Spontaneous fission neutron source

Neutrons are produced in the spontaneous fission of some heavy nuclei. These may be encapsulated and used as neutron sources in the laboratories. Examples of some important spontaneous fission sources are $^{254}$Cf, $^{252}$Cf, $^{244}$Cm,

$^{238}$Pu and $^{232}$U. Californium-252 is the most common and practical source because of its yield of $2.3 \times 10^{12}$ n·s$^{-1}$·g$^{-1}$ ($4.3 \times 10^{9}$ per curie). The neutrons are emitted with an energy distribution ranging from thermal up to several MeV, with an average of about 2.3 MeV. The half-life of $^{252}$Cf is 2.638 years, and transformation occurs by fission about 3% of the time and by $\alpha$-particle emission about 97% of the time. Of all the spontaneous neutron fission sources, $^{254}$Cf is a special case, as it decays almost completely by spontaneous fission with a 60-day half-life.

### 4.1.6 Accelerator-based neutron source

Particle accelerators such as the Van de Graaf or cyclotron are used to generate neutron beams by means of a number of nuclear reactions described in more detail in section 4.2.1. For example, an accelerated high energy proton from the cyclotron strikes a metal beryllium target and produces neutrons via the $^{9}$Be(p,n)$^{10}$B reaction. The energy of the accelerated particles or nuclei must be enough to overcome the Coulomb barrier between the projectile and the target nuclei in order for the reaction to occur. Neutrons released in this reaction have a distribution that is peaked in the direction of the proton beam and, depending on the number of protons in the incident beam, the cyclotron source can produce an intensely focused beam of neutrons. The energy distribution of the emitted neutrons depends on the target thickness and the reaction kinematics. A projectile of the same energy will loose much more energy in a thick target than in a thin target. The common neutron-yield targets are light mass nuclei such as $^{7}$Li and $^{9}$Be, typically in solid form.

## 4.2 Neutron interactions

The neutron interactions with matter are dominated and characterized by the strong nuclear force, which has an interaction range of the order of $\leq 10^{-14}$ m. This is because, neutrons are neutral and do not feel an electromagnetic force. The probability of the neutrons of a given energy interacting varies widely with the nature of the target. Neutron interactions with matter are subdivided into six groups: elastic scattering, inelastic scattering, radiative capture, charged particle emission, neutron emission and nuclear fission, as shown in Table 4.3. In most of these interactions, neutrons are incorporated into the nucleus and form an excited compound nucleus that has an atomic mass number increased by one in comparison to the target nucleus. In the formation of a compound nucleus, the kinetic energy of the incident neutron is all transfered to the target nucleus.

**Table 4.3:** Different types of neutron interactions.

| Elastic | Inelastic | Radiative capture | Charged particle emission | Neutron emission | Nuclear fission |
|---|---|---|---|---|---|
| (n,n) | (n,n′) | (n,$\gamma$) | (n,p)<br>(n,$\alpha$)<br>(n,d)<br>etc. | (n,2n)<br>(n,3n)<br>(n,4n)<br>etc. | (n,f) |

### 4.2.1 Nuclear reactions

A nuclear reaction is defined as the interaction between two nuclear particles, i.e. two nuclei or a nucleus and a nucleon, and the products are two or more nuclear particles or $\gamma$-rays. In a typical nuclear physics experiment, one of the particles will be the projectile and the other will be the target, and there are several possible reactions that can occur when the two interact. An example of a possible reaction when $^{235}$U is bombarded by low energy neutrons in the range of 0.025 eV is

$$ {}^{1}_{0}\mathrm{n} + {}^{235}_{92}\mathrm{U} \rightarrow {}^{236}_{92}\mathrm{U} + \gamma, \qquad \text{abbreviated as } {}^{235}_{92}\mathrm{U}(\mathrm{n},\gamma){}^{236}_{92}\mathrm{U}, \tag{4.1} $$

or when $^{16}$O is bombarded by energetic neutrons, one of the possible reactions is

$$ {}^{1}_{0}\mathrm{n} + {}^{16}_{8}\mathrm{O} \rightarrow {}^{16}_{8}\mathrm{N} + \mathrm{p}, \qquad \text{abbreviated as } {}^{16}_{8}\mathrm{O}(\mathrm{n},\mathrm{p}){}^{16}_{8}\mathrm{N}, \tag{4.2} $$

where the symbols n and p refer to the incident neutron and the emitted proton respectively. Nuclear reactions are governed by four fundamental laws; conservation of nucleons, charge, momentum, and energy. The principle of the conservation of energy can be used to predict whether a certain reaction is energetically possible. The total energy before a reaction is the sum of the energies of the projectile and target plus each of their rest-mass energies. In the same way, the energy after a reaction is the sum of the energies of the reaction products plus each of their rest-mass energies. By conservation of energy it then follows that

$$ E_A + E_B + [M_A + M_B]c^2 = E_C + E_D + [M_C + M_D]c^2, \tag{4.3} $$

where $E_A, E_B, E_C$ and $E_D$ are the kinetic energies of the particles, and $M_A$, $M_B$, $M_C$, and $M_D$ are the rest mass of the particles $A$, $B$, $C$, and $D$ respectively, and $c$ is the speed of light. Equation 4.3 can be rearranged in the form

$$ (E_A + E_B) - (E_C + E_D) = [-(M_A + M_B) + (M_C + M_D)]c^2. \tag{4.4} $$

The right-hand side of this equation is referred to as the reaction energy ($Q$-value). The sign of the $Q$-value defines the energy gained or lost due to the difference between the initial and final masses during the reaction. A reaction

where the $Q$-value is greater than zero ($Q > 0$) is called exothermic. In this reaction, the nuclear mass is converted into kinetic energy and there is a net increase in the kinetic energy of the particles. An endothermic reaction is when the $Q$-value is less than zero ($Q < 0$). In this reaction, kinetic energy of the projectile particle is converted into mass and there is a net decrease in the energies of the particles. There are a number of possible neutron-induced nuclear reactions, such as nuclear fission (n, fission), capture (n,$\gamma$), scattering (n,n$'$) and charge particle (n, $\alpha$) reactions. These are the reactions of most interest in the analysis of a nuclear fission reactor and the detection of neutrons.

The next section provides an overview of the different types of neutron-induced nuclear reactions. However, we first introduce the concept of a neutron-induced cross-section for the nuclear reactions in general.

## 4.3 Neutron cross-sections

The probability of a particular reaction between a neutron and a nucleus occurring is expressed in terms of cross-section. In the case of a neutron-induced nuclear reaction, the probability of a particular reaction taking place depends on the target nucleus and the incident neutron energy. Neutron interaction cross-sections vary as a function of the incident neutron energy and also as a function of the isotopes of the same element. The interaction cross-section can be expressed in two ways, microscopic $\sigma$ or macroscopic $\Sigma$ cross-section, and will be discussed in the next section.

### 4.3.1 Microscopic cross-sections

The microscopic cross-section defines the probability of interaction between a neutron and an individual nucleus. As shown in Fig., 4.1 a parallel monoenergetic neutron beam bombards a thin target of thickness $x$ and area $A$.

In this thin target, all target nuclei are exposed to the same beam intensity. The number of neutrons that collide with the target nuclei is proportional to the neutron beam intensity and the total number of nuclei in the target. In this geometry the intensity of the neutron beam is defined as equivalent to the neutron flux incident onto the target. Thus intensity of the incident neutron beam (in units of n·s$^{-1}$) is given by the neutron density $n$ multiplied by their average velocity $\bar{v}$,

$$I_0 = n\bar{v}. \tag{4.5}$$

The total number, $N_{\text{total}}$, of nuclei in the target of atomic density $N$ is defined as

$$N_{\text{total}} = NAx,$$

The number of collisions per second is

$$\sigma_t I_0 NAx, \tag{4.6}$$

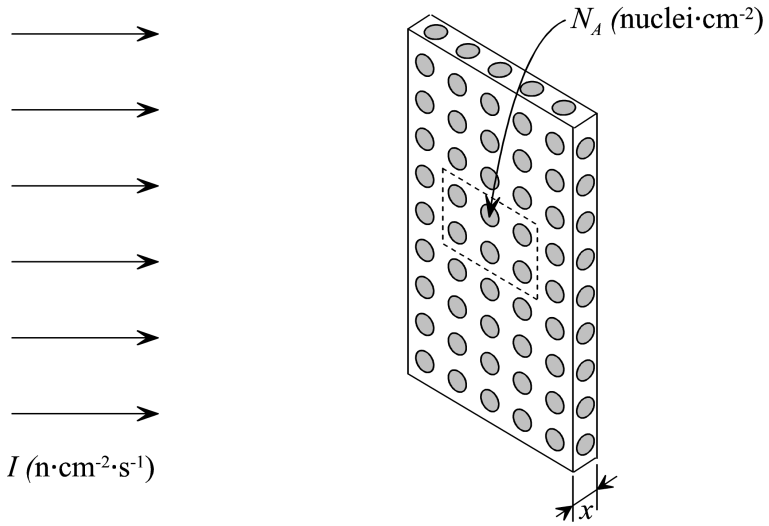


**Figure 4.1:** A monoenergetic neutron beam incident normally upon a thin target.

where $\sigma_t I_0$ represents the number of neutron collisions with a single target nucleus per unit time. Hence, $\sigma_t$ is the effective cross-sectional area presented by the nucleus to the beam of incident neutrons, and is measured in barn, hereinafter is represented by the symbol b, where b $= 10^{-24}$ cm$^2$.

### 4.3.2 Macroscopic cross-sections

The macroscopic cross-section defines the probability for a particular reaction with nuclei in bulk material such as a thick target. In a thicker target, the nuclei deeper within the target material tend to be hidden from the incident beam by the nuclei exposed to the incoming beam. The schematic diagram in Fig. 4.2 shows a neutron beam incident on a surface of a target of arbitrary thickness. The equation for the non-interacting beam intensity $I(x)$ at any point $x$ in the target is derived as follows. We consider a target with differential thickness between $x$ and $x + dx$. Since $dx$ is infinitesimally thin, the results from studies with thin targets may be used to calculate the rate at which neutrons undergo interactions in $dx$ per cm$^2$. The number of target nuclei per cm$^2$ in $dx$ is given by

$$dN_A = Ndx,$$

where N is the density of nuclei in the target. The total reaction rate per unit area in $dx$ then is

$$dR = \sigma_t I dN_A = \sigma_t I N dx. \tag{4.7}$$

Equating the reaction rate to the decrease in beam intensity between x and $x + dx$,

$$-dI(x) = -[I(x + dx) - I(x)] = \sigma_t I N dx. \tag{4.8}$$

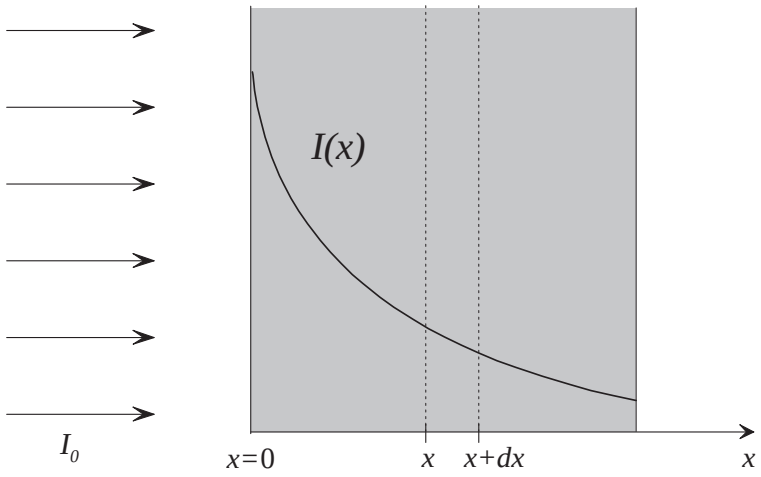


**Figure 4.2:** A monoenergetic beam attenuation through a thick target.

Dividing equation (4.8) by $dx$ results in a differential equation for the beam intensity $I(x)$ as given by,

$$\frac{dI}{dx} = -N\sigma_t I(x). \tag{4.9}$$

Equation (4.9) can be solved subject to an incident beam intensity of $I_0$ at $x = 0$ to obtain an exponential attenuation of the incident beam of the form

$$I(x) = I_0 \exp(-N\sigma_t x). \tag{4.10}$$

The product of the atomic number density $N$ and the microscopic cross-section $\sigma_t$ that appears in the exponential term is customarily denoted by a symbol,

$$\Sigma_t \equiv N\sigma_t$$

This symbol $\Sigma_t$ is referred to as the macroscopic cross-section characterizing the neutron interaction with bulk target material. The macroscopic cross-section $\Sigma_t$ can be interpreted as the probability per unit path length traversed by a neutron without any interaction. In this sense, $\exp(-\Sigma_t x)$ is the probability that a neutron travels a distance $dx$ without any interaction, and $\Sigma_t \exp(-\Sigma_t x)dx$ is the probability that a neutron has its first interaction in $dx$. With this interaction probability, one can calculate the average distance a neutron travels before interaction with a nucleus in the target

$$\bar{x} \equiv \int_0^\infty xp(x)dx = \Sigma_t \int_0^\infty x \exp(-\Sigma_t x)dx = \frac{1}{\Sigma_t}, \tag{4.11}$$

where $p(x)$ is the probability that a neutron has an interaction in $dx$. The symbol $\bar{x}$ represents the particles mean free path, since it essentially measures the average distance a neutron is likely to move freely before colliding with a nucleus.

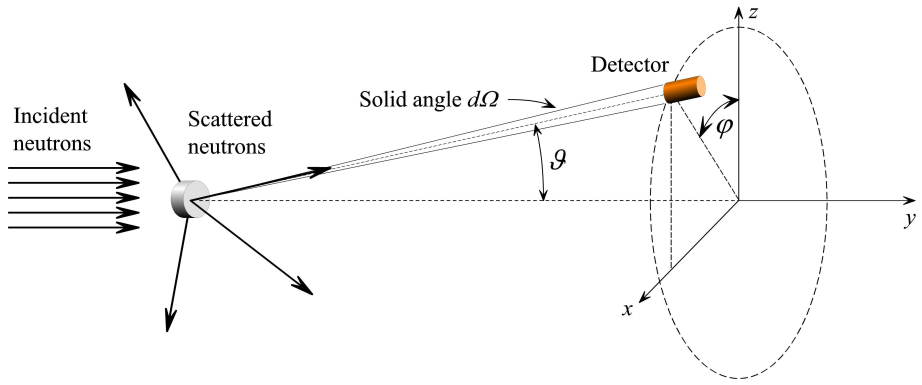


**Figure 4.3:** Angular scattering of the neutron into the detector system.

### 4.3.3 Angular distributions and differential cross-sections

If a neutron detector is placed at some distance behind the neutron-producing target, those neutrons that interact with the sensitive part of the detector will be counted. However, if the detector is moved off the axis of the incident beam, as shown in Fig. 4.3, only scattered neutrons will be observed. The number of neutrons scattered into the detector per unit time is a function of the angle $\theta$ of the detector about the direction of incident beam. If the aperture of the detector is doubled, roughly twice as many neutrons are able to enter per unit time. The scattered neutrons are also proportional to the intensity of the incident beam, atom density, area and thickness of the target and to the solid angle subtended by the detector. If the neutrons that arrive at the detector are as a result of elastic scattering, then the number of scattered neutrons entering the detector per unit time $dn(\theta)$ is written as

$$dn(\theta) = \sigma_s(\theta) I N A x d\Omega(\theta), \tag{4.12}$$

where $\sigma_s(\theta)$ is the microscopic angular scattering cross-section, $I$ is the intensity of the beam, $N$ is the density of the target atoms, $A$ is the area of the target, and $x$ and $d\Omega(\theta)$ are the thickness of the target and the solid angle subtended by the detector at the target, respectively. Since $dn(\theta)$ is the number of neutrons scattered per unit time from the beam into solid angle $d\Omega(\theta)$, it can be seen that the differential cross-section $\sigma_s$ is proportional to the probability that a neutron interacting in the target will be elastically scattered into the solid angle $d\Omega(\theta)$.

The probability that a neutron will be scattered through all angle is therefore equal to the integral of $\sigma_s(\theta)$ over the full solid angle. This, in turn, must be equal to the scattering cross-section $\sigma_s$, defined as

$$\sigma_s(\theta) = \int_{4\pi} \sigma_s(\theta) d\Omega(\theta), \tag{4.13}$$

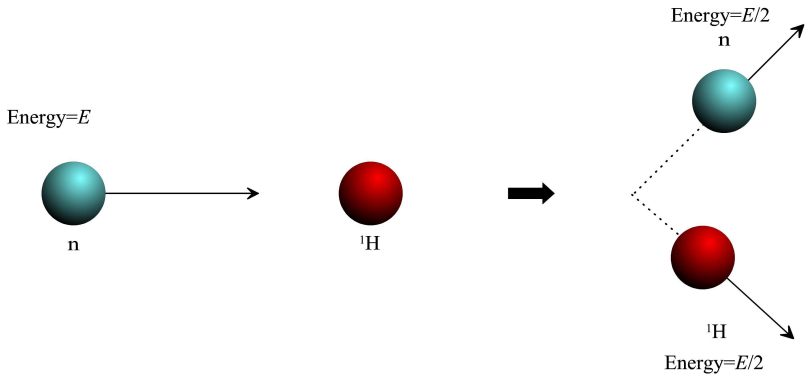


**Figure 4.4:** Schematic diagram of an elastic scattering interaction of a neutron with a hydrogen nucleus. The initial energy of the neutron is shared between the neutron and recoiling nuclei $E/2$.

where $4\pi$ indicates that the integration is to be carried out over the full solid angle. Since $\sigma_s(\theta)$ in this integral does not depend upon the angle $\varphi$, the differential solid angle can be written as $d\Omega = \sin\theta d\theta d\varphi = \int_0^{2\pi} d\varphi \sin\theta d\theta = 2\pi \sin\theta d\theta$, and equation (4.13) becomes

$$\sigma_s = 2\pi \int_{4\pi} \sigma(\theta) \sin\theta d\theta. \tag{4.14}$$

## 4.4 Scattering interaction reactions

When a neutron is scattered by a nucleus, its speed and direction change, but the mass number of the nucleus is conserved. The scattering events can be subdivided into elastic and inelastic scattering. Neutrons can interact with the nucleus through elastic scattering producing a recoiling nucleus while inelastic scattering produces an excited recoiling nucleus.

### 4.4.1 Elastic scattering $A$(n,n)$A$ reactions

In an elastic scattering reaction (Fig 4.4), a fraction of the kinetic energy of the incident neutron is transfered to the target nucleus which then moves at an increased speed. The momentum and kinetic energy of the neutron and the nucleus are conserved in the elastic scattering events.

$$M_n v_{ni} + M_t V_{ti} = M_n v_{nf} + M_t V_{tf},$$

and

$$\frac{1}{2} M_n v_{ni}^2 + \frac{1}{2} M_t V_{ti}^2 = \frac{1}{2} M_n v_{nf}^2 + \frac{1}{2} M_t V_{tf}^2,$$

where

- $M_n$ and $M_t$ are the mass of the neutron and target nucleus, respectively.
- $v_{ni}$ and $V_{ti}$ are the initial velocity of the neutron and target nucleus before the collision, respectively.
- $v_{nf}$ and $V_{tf}$ are the final velocity of the neutron and target nucleus after the collision, respectively.

Elastic scattering can occur in two ways, namely the potential and the resonance elastic scattering. In potential elastic scattering, the neutron and nucleus are visualized as billiard balls with impenetrable surfaces. This occurs when the kinetic energy of the incident neutrons is less than 1 MeV. The neutron is scattered by the short-range nuclear force at a distance close enough to the nucleus. In the resonance elastic scattering, the neutron is absorbed by the nucleus and forms an excited compound nucleus which is followed by the re-emission of the neutron in such a way that the total kinetic energy is conserved and the nucleus returns to its ground state. This process is dependent of the initial kinetic energy of the neutron. Elastic scattering is more important in slowing down fast neutrons, particularly in thermal neutron reactors. For a neutron of kinetic energy $E$ encountering a nucleus of atomic mass A, the average energy loss $\bar{E}$ is given by [Nucl11]

$$\bar{E} = 2E\frac{\mathrm{A}}{(\mathrm{A}+1)^2}. \tag{4.15}$$

This expression shows that, in order to reduce the speed of neutrons with a minimum number of elastic collisions, light elements should be used. By using a material with $A = 1$, the average energy loss has its largest value of $E/2$. This is because the mass of the neutron and the proton are practically identical. Hence, a neutron with 3 MeV of kinetic energy will on average lose 1.5 MeV with one elastic collision and 0.75 MeV after the second collision, and so on. To achieve the thermal neutron energy of 0.025 eV, a neutron will undergo an average of 75 elastic collisions.

### 4.4.2 Inelastic scattering $A$(n,n′)$A$ reactions

An inelastic scattering, A(n,n′)A, reaction occurs when the incident energy of the neutron is enough to place the target nucleus in one of its excited states. As a result, the inelastic cross-sections have the threshold energy. A general trend is that heavier nuclei have low excited energy levels while lighter mass nuclei have high excited energy levels and the excited states of the nuclei decrease with increasing mass number. The lighter nuclei have high nuclear excitation energies of a few MeV, while intermediate and heavy nuclei usually have the least excitation energy, in the range of 0.1 to 1 MeV. For these reasons, inelastic reactions occur only for relatively high neutron energies with low mass nuclei. An example of an energy level diagram for $^{12}$C is shown in Fig. 4.5.

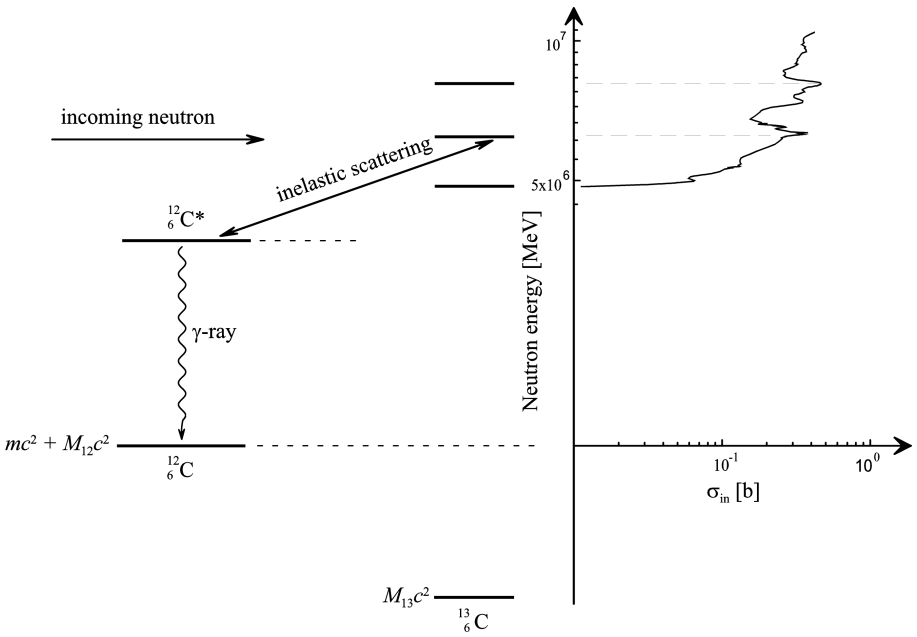


**Figure 4.5:** An energy level diagram of an inelastic neutron scattering reaction on $^{12}$C, data from [NNDC].

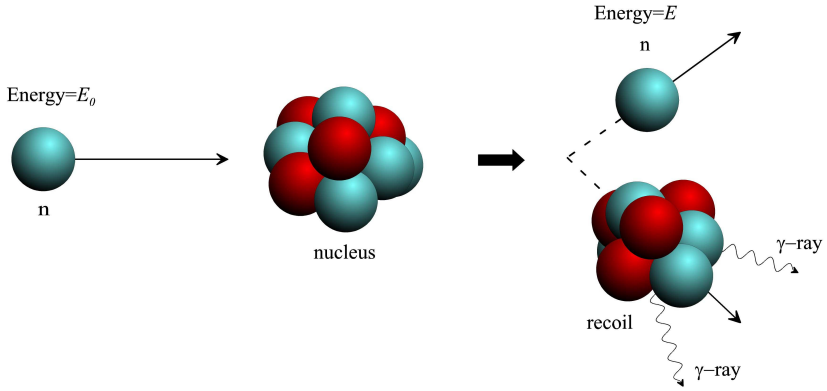


**Figure 4.6:** Schematic diagram of an inelastic neutron scattering interaction with a nucleus.

The inelastic scattering reaction proceeds as follows, as shown in Fig. 4.6, the neutron is firstly absorbed by the target nucleus to form a compound nucleus as an intermediate stage of the interaction process. The compound nucleus is formed in an excited state due to the energy brought by the incident neutron. The compound nucleus de-excites by emitting a neutron of lower kinetic energy, denoted by n′, $\gamma$-rays or breaking up into smaller fragments.

The inelastic scattering interaction plays an important role in slowing down high energy neutrons. If the kinetic energy of the incident neutron is high enough to excite several levels of the target nucleus, the energies of the emitted neutrons can be represented by a smooth function. Thus, $P(E \rightarrow E')dE$ is the probability that an inelastic neutron is emitted with an energy between $E'$ and $E' + dE'$ when the nucleus is struck by neutrons of energy $E$ and is defined as

$$P(E \rightarrow E')dE' = \frac{E'}{T^2} \exp(E/T^2)dE', \tag{4.16}$$

where temperature $T = 3.2\sqrt{E/A}$, and $A$ is the atomic mass number. Integrating equation (4.16) from 0 to infinity gives the average energy of an inelastic neutron as

$$\bar{E}' = \frac{1}{T^2} \int_0^\infty E' \exp(E/T^2)dE' = 2T. \tag{4.17}$$

Taking as an example, when 10 MeV neutrons bombard a $^{238}$U nucleus, the temperature $T = 3.2\sqrt{10/238} = 0.66$, hence the average energy $\bar{E}'$ of an inelastic neutron is 1.32 MeV, and the average energy loses $\bar{E} = 8.62$ MeV as a result of a single inelastic collision. Since neutrons are indistinguishable, it is not important to know whether it is an incident neutron that is emitted, as long as some neutrons are emitted from the interaction. Inelastic scattering interactions are effective at slowing down fast neutrons when compared to elastic scattering. For example, the same 10 MeV neutrons will lose $\bar{E} = \frac{E}{2}\left(1 - \left(\frac{A-1}{A+1}\right)^2\right) = 0.083$ MeV as a result of a single elastic collision with $^{238}$U.

### 4.4.3 Neutron capture A(n,$\gamma$)A reactions

The radiative capture (n, $\gamma$) reaction is one of the interactions that neutrons undergo with the matter. In this reaction, as shown in Fig. 4.7, the incident neutron is absorbed by the target nucleus of atomic mass $A$ to form an excited compound nucleus of atomic mass $A + 1$. In the formation of an excited compound nucleus, the incident neutron transfers all of its energy to the target nucleus. This excited compound nucleus subsequently decays by emitting $\gamma$-rays. The neutron capture cross-section is energy dependent and the absorption resonances appear at those energies at which the center-of-mass energy $E_{cm}$ plus the neutron binding energy $E_b$ match an energy level of the compound nucleus. An example of the absorption resonance situation for neutron

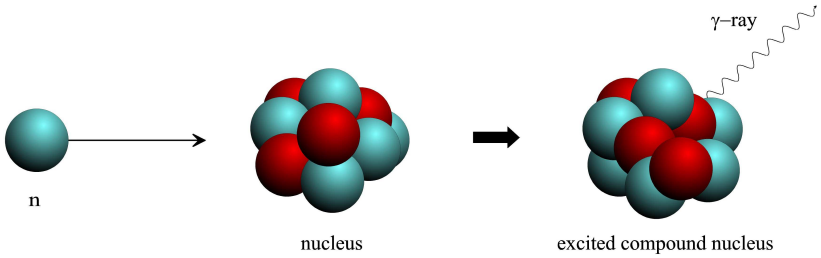


**Figure 4.7:** Schematic diagram of neutron capture interaction showing a compound nucleus loosing the excitation energy via $\gamma$-ray emission.

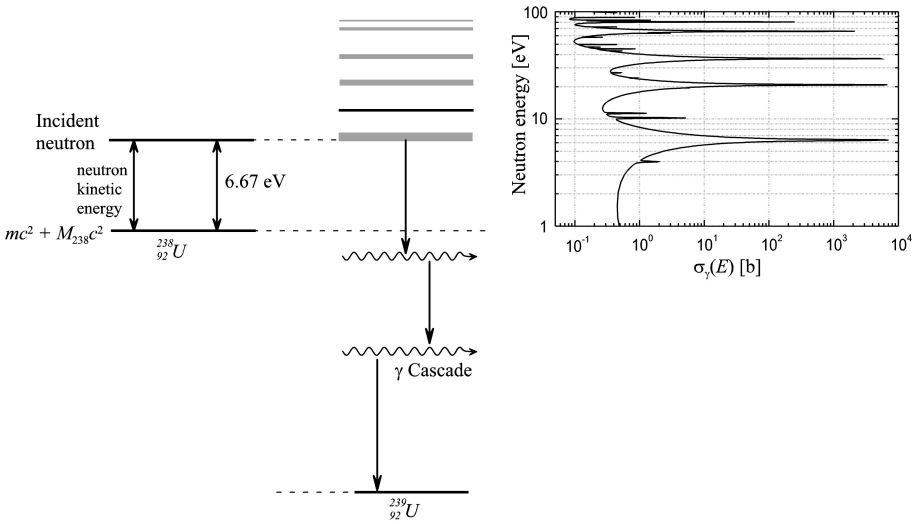


**Figure 4.8:** An energy level diagram of the capture resonance in $^{238}$U with the strong resonance at 6.67 eV, data from [NNDC].

capture in the $^{238}$U nucleus is shown in Fig. 4.8. Unlike the inelastic scattering interactions which have the energy threshold of several MeV on light nuclei, the neutron capture reaction require no specific energy level and the reaction can occur with neutrons of any energy. In general, the cross-section for these reactions are also large at low neutron energies and decreases rapidly as a function of neutron energy, shows the $1/v$ dependence. These reactions are almost always exothermic (positive $Q$-value) because the energy carried by the reaction products is larger than the sum of the energy of the incident neutron and the original nucleus.

For discrete energy levels, it is possible to describe the energy dependence of the capture cross-section by the *single-level resonance Breit-Wigner formula* [Dud76]:

$$\sigma_0(E_c) = \sigma_0 \frac{\Gamma_\gamma}{\Gamma} \left(\frac{E_0}{E_c}\right)^{1/2} \frac{1}{1+x^2}, \tag{4.18}$$

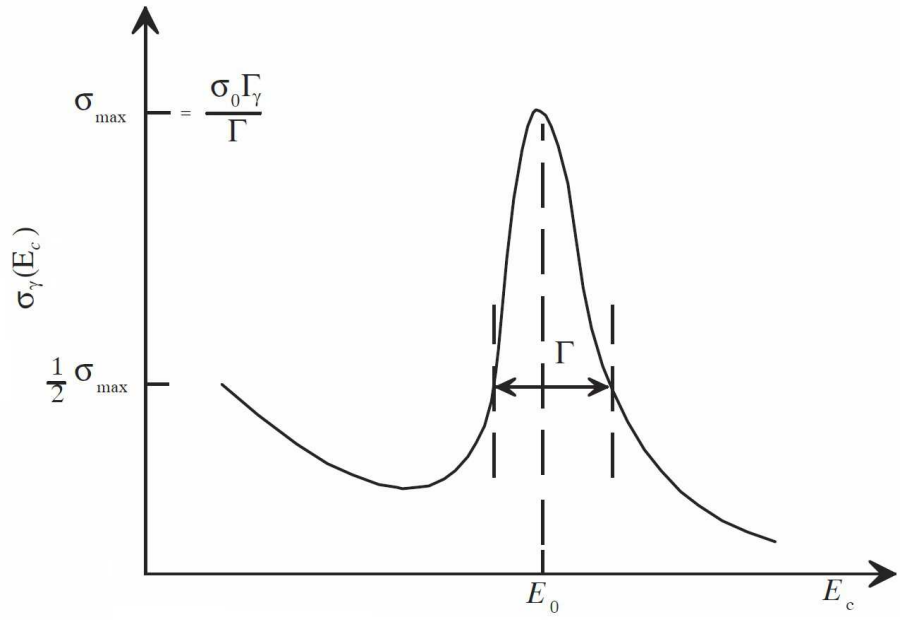


**Figure 4.9:** A single level capture resonance peak from $^{238}$U, data from [NNDC].

where the variable

$$x = \frac{2}{\Gamma}(E_c - E_0), \tag{4.19}$$

and

- $E_0$ is the resonance energy, i.e. the energy at which $E_c + E_b$ matches the energy level of the compound nucleus.
- As seen in Fig. 4.9, $\Gamma$ is the total level width of the resonance peak that essentially characterizes the width of the energy level and the full width at half-maximum (FWHM) of the resonance.
- $\Gamma_\gamma$ is the energy-independent partial level width for $\gamma$-ray emission.
- $\sigma_0$ is the cross-section at the resonance.

The cross-section $\sigma_t(E_0)$ at the resonance energy $E_0$ can be written in terms of the reduced neutron wavelength $\bar{\lambda}$ at $E_0$,

$$\sigma_0 = 4\pi\bar{\lambda}_0^2 g\frac{\Gamma_n}{\Gamma}, \tag{4.20}$$

where $\Gamma_n$ is the neutron level width that varies in energy as $\Gamma_n\ E^{1/2}$, and $g$ is the statistical spin factor defined in terms of the nuclear spin $I$ and total spin $J$,

$$g = \frac{(2J+1)}{2(2I+1)}. \tag{4.21}$$

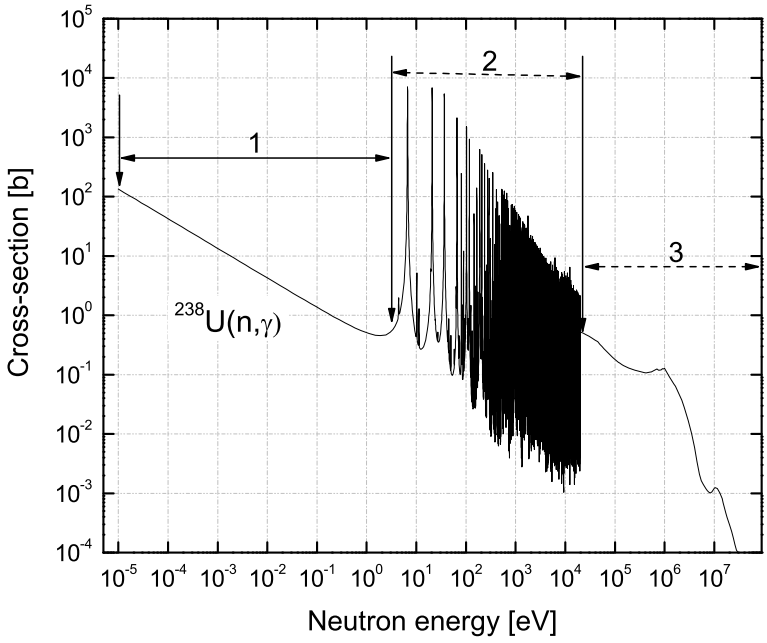


**Figure 4.10:** Capture cross-section of $^{238}$U as a function of incident energy $E$ at a temperature 0 K, data from [NNDC].

The Breit-Wigner resonance as a function of center-of-mass kinetic energy $E_c$ is shown schematically in Fig. 4.9. Resonance absorption occurs mostly in heavy nuclei, hence the center of mass $E_c \approx E$.

As shown in Fig. 4.10, the radiative capture cross-section is divided into the following three energy regions:

1. In the lower neutron energy $E << E_0$ region, in most nuclei, the radiative capture cross-section varies as $E^{-1/2}$, where $E$ is the energy of the incident neutron.

2. An energy region where $E = E_0$, below the region energy 1, is the energy range for resonance. The neutron capture cross-section in the resonance region is defined using the Breit-Wigner formula, (4.18). In Fig. 4.10, it can be seen that the absorption resonance peaks are so closely spaced that they cannot be resolved by experimental measurements.

3. Above the resonance $E >> E_0$ region ending around 1 keV in heavy nuclei and at higher energies in lighter nuclei, the neutron capture cross-section decrease fast and smoothly to very small values, less than 1 mb.

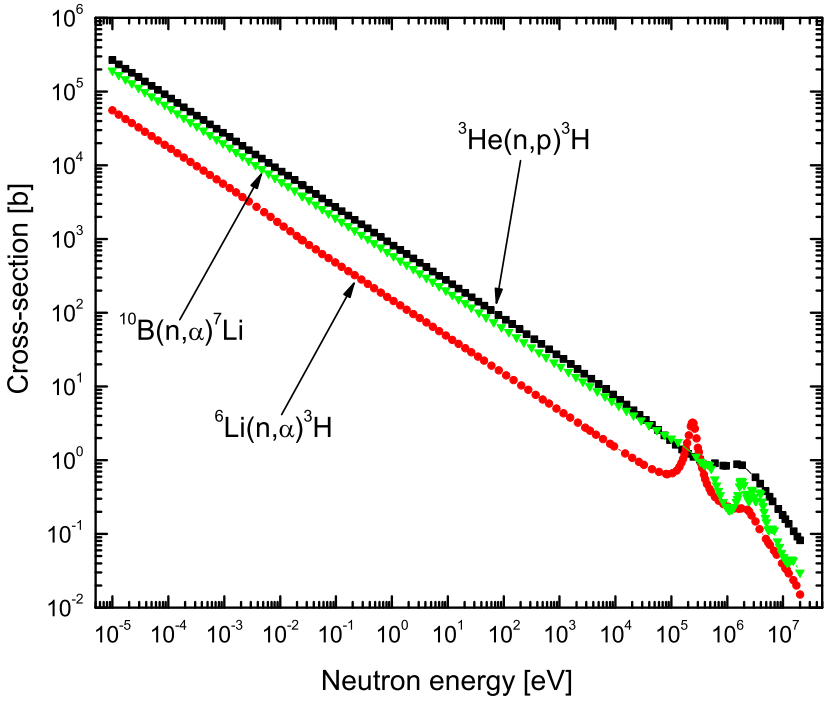


**Figure 4.11:** The cross-sectional plot for neutron-induced light element break-up reactions, data from [NNDC].

### 4.4.4 Charged particle ejection reactions

In charged particle ejection reactions, the incident neutron is absorbed by the target nucleus, forming an excited compound nucleus. This excitation energy is above the particle threshold, causing the compound nucleus to emit a proton or an $\alpha$-particle and a recoil nucleus, or undergo a break-up reaction. Thus, neutron-induced charged particle reactions are of importance in neutron detection since the neutral particle can produce more detectable radiations. Examples of a few important reactions in which the Q-value is positive are

1. $^{3}$He+n=$^{3}$H+p
2. $^{6}$Li+n=$^{3}$H+$\alpha$
3. $^{10}$B+n=$^{7}$Li*+$\alpha$, $^{7}$Li+$\alpha$

The cross-sectional plot for the reactions 1, 2 and 3 are shown in Fig. 4.11. The cross-section is very large at low neutron energies and as the neutron energy increases, the cross-section decreases rapidly following $1/v$ dependence. Hence, $^{3}$He, $^{6}$Li and $^{10}$B are widely used as neutron converters in slow neutron

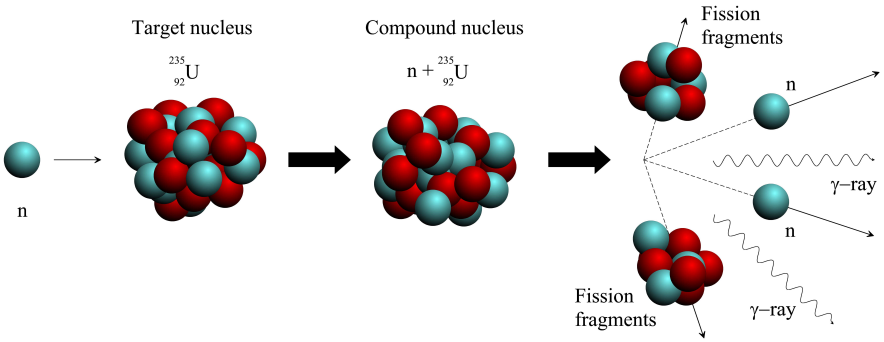


**Figure 4.12:** Schematic diagram of nuclear fission process where an unstable compound nucleus split into two fragments accompanied by neutrons and $\gamma$-rays.

detectors. The cross-section for neutron interactions with $^6$Li is shown in the second plot Fig. 4.11 and exhibits a resonance peak at energy 250 keV corresponding to the formation of the excited compound nucleus states in $^7$Li*. In this resonance peak, the cross-section is enhanced by one order of magnitude. The charged particles produced in this reaction are ejected in opposite directions with relatively high energies that can produce a considerable ionization along a short range. These reactions are the basic interactions upon which gas, plastic and glass scintillator neutron detectors are developed.

### 4.4.5 Nuclear fission reactions

In the nuclear fission reactions, neutrons of lower energy are essentially absorbed by heavy nuclei, which together form an excited compound nucleus. The probability for these reactions to occur is large with the neutrons of lower energy as seen in Fig. 4.13. As shown in a schematic diagram of the nuclear fission reaction in Fig. 4.12, the excited compound nucleus is unstable and breaks-up into two nuclei of intermediate mass called the fission fragments, accompanied by the release of two or three neutrons called the prompt neutrons. Nuclear fission of heavy elements is an exothermic reaction that releases large amounts of energy, both as $\gamma$-rays and as kinetic energy of the fission fragments. Energy of the order of 200 MeV, is released in each fission reaction. The fission fragments produced are both highly charged and energetic. They slow down via collisions with adjacent atoms, losing energy and charge (picking up electrons) in the process. This is in fact the principal mechanism by which the fission energy eventually appears as heat generated in the fuel material. Further, the fission fragments tend to have both excess energy and neutrons, so there is still some radioactive decay of these nuclei, which produce more neutrons. The energy released from this radioactive decay can amount to about 4-5% of the total energy released in the fission reaction, and is deposited as heat to the fuel. This decay heat appears corresponding to the half-lives of

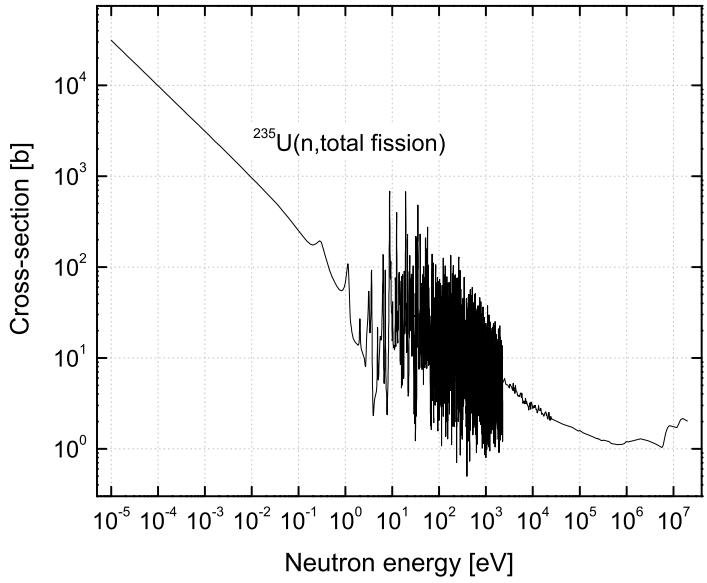


**Figure 4.13:** The cross-sectional plot of the nuclear fission $^{235}$U(n,f) reaction, data from [NNDC].

**Table 4.4:** The amount of energy released in the nuclear fission process.

| Fission reaction products | Energy (%) | Range | Time delay |
|---|---|---|---|
| KE of fission fragments | 80 | $< 0.01$ cm | prompt |
| Fast neutrons | 3 | 10 to 100 cm | prompt |
| Fission $\gamma$-rays | 4 | 100 cm | prompt |
| Fission product $\beta$-decay | 4 | $< 1$ cm | delayed |
| Neutrinos | 5 | non recoverable | delayed |
| Non fission reaction- due to neutron capture | 4 | 100 cm | delayed |

the various nuclei involved. The energy released in a nuclear fission reaction is distributed among a variety of reaction products. The reaction products are classified according to their energy as an approximate percentage of the fission energy, distance range and emission time (see Table 4.4).

#### 4.4.5.1 Nuclear fission prompt neutrons

The neutrons produced in nuclear fission reactions are used to propagate a fission chain reaction. Most of these fission neutrons appear within $10^{-14}$ s after the fission event, and about 1% appear later in time from the subsequent decay of the radioactive fission products. These are called prompt and delayed neu-

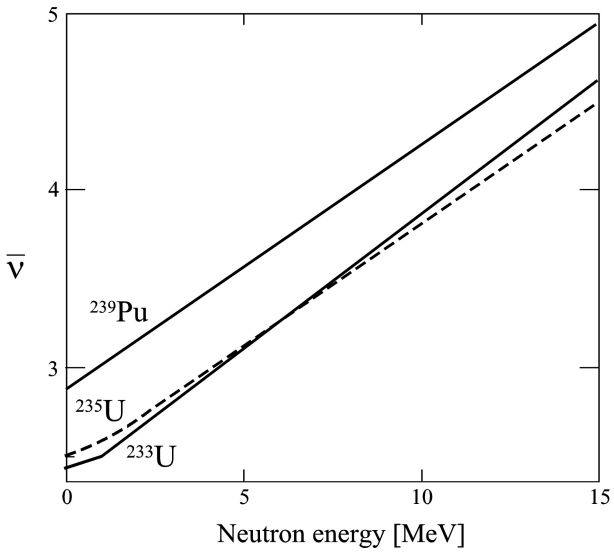


**Figure 4.14:** Average number of neutrons emitted per fission event as a function of energy, redrawn from [Dud76].

trons respectively. The total number of prompt and delayed neutrons released in a fission reaction varies, depending on the nucleus involved and the incident neutron energy. From these fission neutrons, the average number of neutrons released per fission event is considered, which is denoted by $\bar{\nu}$. Generally, it tends to increase with the increase in incident neutron energy. The average number of neutrons emitted per fission $\bar{\nu}(E)$ as a function of energy is plotted in Fig. 4.14 for $^{233}$U, $^{235}$U, and $^{239}$Pu. The neutrons produced in the fission reaction emerge with an energy distribution, with the average being about 2 MeV. As with other parameters, this distribution will depend on the isotope involved, and less on the incident neutron energy, and will differ for prompt and delayed neutrons. To characterize this variation in fission neutron energy, it is convenient to define the fission neutron energy spectrum $\chi(E)$ in terms of Maxwell-Boltzmann or Watt fission spectrum. The Maxwell-Boltzmann spectrum is defined as

$$\chi(E \to E') = \frac{2\pi}{(\pi k_B T)^{3/2}} \sqrt{E'} \exp(-E'/k_B T), \tag{4.22}$$

which is the number of neutrons emitted with an average energy $\bar{E} = \frac{3}{2} k_B T$ in the order of 2 MeV, as shown in Fig. 4.15, and the Watt fission spectrum [Wat52]

$$\chi(E \to E') = \sqrt{4/\pi a^3 b} \exp(-ab/4) \exp(-E'/a) \sinh(\sqrt{bE'}), \tag{4.23}$$

where $E$ and $E'$ are the energy of the neutron that induced the fission reaction, and energy of the emitted neutrons respectively. The parameters $a$ and $b$ are usually determined by fitting the Watt formula to the measured fission

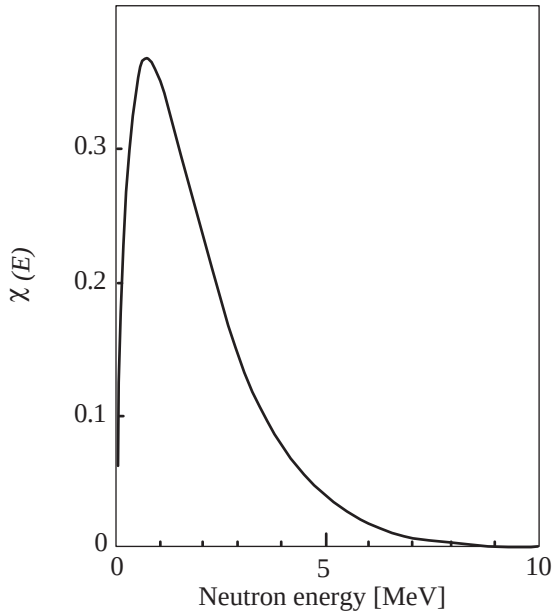


**Figure 4.15:** Fission neutron energy distributions for induced fission by thermal neutrons on uranium, redrawn from [Tat09].

spectrum data. An example of a normalized Watt fission spectrum for $^{235}$U is given as

$$\chi(E) = 0.453 \exp(-1.036E') \sinh(\sqrt{2.29E'}). \tag{4.24}$$

#### 4.4.5.2 Delayed fission neutrons

The delayed fission neutrons are important in the control of nuclear reactors. An example of a decay sequence that leads to delayed neutron emission is the $\beta$-decay of $^{87}$Br to $^{87}$Kr, followed by the subsequent decay of $^{87}$Kr* to $^{86}$Kr via neutron emission. The effective time delay of this process is controlled by the half-life of $^{87}$Kr*, which is 55 s. The fission fragments whose $\beta$-decay yields a daughter nucleus that subsequently decays via delayed neutron emission is referred to as a delayed neutron precursor. A large number of different delayed neutron precursor isotopes are produced in the fission chain reactions. These precursors are grouped into six classes, characterized by approximately their half-lives of 55, 22, 6, 2, 0.5 and 0.2 s [Dud76]. The energy spectrum for delayed fission neutrons is considerably lower than that of the prompt fission neutrons, and again depends on both the delayed neutron groups and the fissioning parent nuclei. The rough composite delayed neutron fission spectrum is shown in Fig. 4.16, along with typical measured spectra for the 55 s and 22 s groups of $^{235}$U.

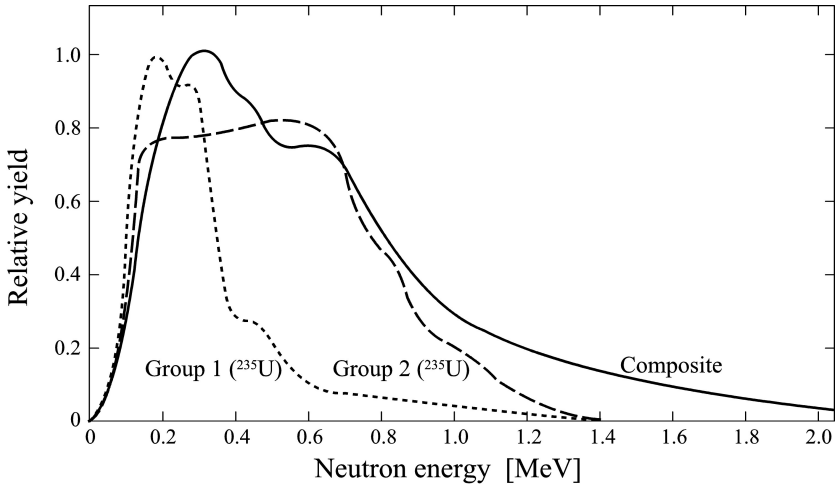


**Figure 4.16:** Delayed fission neutron groups, redrawn from [Dud76].

## 4.5 Neutron moderator materials

In nuclear reactors, the nuclear fission process and radioactive decays of the fission fragments emit fast neutrons, but for the next thermal fission reaction to occur, a neutron has to be in thermal energy $E_n = 0.025$ eV. Neutron moderators are employed to thermalize fast neutrons and increase the probability of interactions with a specific material. Moderating materials are selected according to their ability to slow down the neutrons to thermal energies in as few as possible collisions without absorption, which is known as the moderating power. The materials which have a relatively larger moderating power are preferred because less of that material is needed to achieve the same degree of moderation. The characteristics of this effective moderators are a high probability of an interaction and a high average energy loss in one scatter. The moderating power, $MP$, is defined as $\xi\Sigma_s$, where $\Sigma_s$ is the macroscopic scattering cross-section and $\xi$ is the average logarithmic energy decrement in a scatter $\ln(E_0) - \ln(E)$. When elastic collisions in an element with atomic weight $A$ dominate the scattering process, the decrement becomes

$$\xi = 1 - \frac{(\mathrm{A}-1)^2}{2\mathrm{A}} \ln \frac{\mathrm{A}+1}{\mathrm{A}-1}. \tag{4.25}$$

The moderator with large $MP$, and also, a large absorption cross-section might nevertheless be useless because it would effectively reduce the speed of the neutrons, but will also reduce the neutron flux. A more comprehensive measure of the moderating ability of a material is the moderating ratio $MR$:

$$MR = \xi \frac{\Sigma_s}{\Sigma_a}. \tag{4.26}$$

A good moderator will have a large moderating ratio, which means that it is a poor absorber. Since $\xi$ represents the average logarithmic energy loss per

**Table 4.5:** Slowing-down parameters of typical moderating materials [Nucl11].

| Moderator | A | $\xi$ | $\xi\Sigma_s$ | $\xi\frac{\Sigma_s}{\Sigma_a}$ | Number of collision, from $2 \times 10^6$ to 0.0253 eV |
|---|---|---|---|---|---|
| $H_2O$ | 18 | 0.107 | 1.42 | 62 | 19 |
| $D_2O$ | 20 | 0.096 | 0.18 | 4830 | 35 |
| He | 4 | 0.43 | $9 \times 10^{-6}$ | 51 | 42 |
| C | 12 | 0.16 | 0.08 | 216 | 114 |
| $CH_2$ | 14 | 0.14 | 3.26 | 122 | 132 |

collision, the total number of collisions required for a neutron to lose a given amount of energy is determined by the expression:

$$N = \frac{\ln E - \ln E_0}{\xi}. \tag{4.27}$$

Table 4.5 provides the moderating power $MP$, moderating ratio $MR$ and number of collisions required to reduce the energy of a neutron of 2 MeV down to thermal energy of 0.025 eV for some common moderator materials [Nucl11]. The solid materials given in Table 4.5 have a higher moderating ratio than ordinary water and can have manufacturing advantages, for example graphite and polyethylene are commonly selected as a moderator because of their high moderating power, relatively high moderating ratio and easy manufacturing.

## 4.6 Moderation of neutrons

The slowing-down density $q(\vec{r}, E)d^3r$ is the number of neutrons slowing-down past energy $E$ in $d^3r$ about $\vec{r}$. Since the differential scattering cross-section describes the probability that a neutron will scatter from an initial energy $E'$ to a final energy $E''$ in $dE''$, then the rate at which neutrons undergo interaction at energy $E'$ in $dE'$ slow down past the energy $E$ is given by [Dud76]

$$R(E' \to E'') = \left[\int_0^E \Sigma_s(E' \to E'')\phi(\vec{r}, E')dE''\right] dE'. \tag{4.28}$$

Thus the slowing-down density resulting from all initial energies $E' > E$ is given by

$$q(\vec{r}, E) = \int_E^\infty dE' \int_0^{E''} \Sigma_s(E' \to E'')\phi(\vec{r}, E')dE''. \tag{4.29}$$

In a non-absorbing, graphite moderator, the slowing down density becomes

$$q(E) = \int_0^E dE'' \left[ \int_E^\infty \frac{\Sigma_s(E')\phi(E')}{E'} dE' \right] \tag{4.30}$$

$$= \int_0^E dE'' \left[ \int_E^\infty \frac{(F_c(E') + S_0\delta(E' - E_0))}{E'} dE' \right] \tag{4.31}$$

$$= E \left[ \int_E^\infty \frac{F_c(E')}{E'} dE' + \frac{S_0}{E_0} \right] = EF_c(E) = S_0. \tag{4.32}$$

For this case, the slowing density is constant and equal to the source because there is no neutron absorption and leakage in and out of the core. All source neutrons must eventually slow down below energy $E$.

### 4.6.1 Neutron lethargy

The energy range covered by fission neutrons slowing down to slow neutron energies is extremely large, for example ranging from 10 MeV to $10^{-2}$ eV. On average, fission neutrons lose a fraction of their incident energy in the scattering interaction with the moderator nuclei to reach thermal equilibrium. The unit lethargy $u$ is used to assess the average logarithmic energy loss of these scattered neutrons and is defined as

$$u = \ln \frac{E_0}{E} = \ln(E_0) - ln(E), \tag{4.33}$$

where the energy $E_0$ is chosen to be the maximum neutron energy in the calculations. A neutron with energy $E_0$ has zero lethargy. As the neutron loses energy, i.e. its lethargy increases and it becomes more lethargic, $u$ is always positive, since no energy is greater than the maximum $E_0$. When performing nuclear reactor analysis, the neutron lethargy $u$ becomes a convenient variable and the neutron energy spectrum calculations are performed in terms of $u$ rather than $E$. Hence, the neutron energy spectra in this work are plotted in terms of lethargy. We compute the derivative of equation (4.33) to be

$$du = \left( \frac{E}{E_0} \right) \left( \frac{-E_0}{E^2} \right) dE = \frac{-dE}{E}. \tag{4.34}$$

The collision density can be expressed in terms of $u$ by noting that the collisions that occur in the lethargy interval $du$, namely $F(u)du$, are the same collisions that occur in the energy interval $dE$, specifically $F(E)dE$. That is

$$F(u)du = -F(E)dE, \tag{4.35}$$

where the negative sign is required because $E$ decreases as $u$ increases. The collision rate density $F(u)$ is constant in terms of the lethargy variable if

equation (4.35) is applied to an example of a neutron slowing down in a non-absorbing medium, then

$$F(u) = EF(E) = S_0. \tag{4.36}$$

This is because $F(u)$ is usually a much more slowly varying function of $u$ than $E$, and hence it is easier to approximate in the lethargy variable. The elastic scattering probability function $P(E' \to E)$ in lethargy is derived as

$$P(u' \to u)du = -P(E' \to E)dE. \tag{4.37}$$

Thus

$$P(u' \to u) = -\frac{dE}{du}P(E' \to E) = EP(E' \to E) \tag{4.38}$$

$$= \frac{1}{(1-\alpha)}\left(\frac{E}{E'}\right) = \frac{e^{u'-u}}{(1-\alpha)}. \tag{4.39}$$

Also

$$E < E' < E/\alpha \Rightarrow u - \ln(1/\alpha) < u' < u. \tag{4.40}$$

Hence

$$P(u'-u) = \begin{cases} \frac{e^{u'-u}}{(1-\alpha)} & u - \ln(1/\alpha) < u' < u, \\ 0 & \text{otherwise.} \end{cases} \tag{4.41}$$

Now, the slowing-down equation in a graphite medium, written in terms of the lethargy variable becomes

$$\Sigma_s(u)\phi(u) = \int_0^u e^{u'-u}\Sigma_s(u')\phi(u')du' + S(u). \tag{4.42}$$

From equation (4.29) and (4.41), it follows that the slowing-down density $q(u)$ in the lethargy variable is given by

$$q(u) = \int_0^u \Sigma_s(u')\phi(u')e^{u'-u}du'. \tag{4.43}$$

The derivative of the above equation with respect to $u$ will be given by

$$\frac{dq}{du} = -\int_0^u \Sigma_s(u')\phi(u')e^{u'-u}du' + \Sigma_s(u)\phi(u). \tag{4.44}$$

Hence, we can re-identify $q(u)$ from equation (4.43), and substitute into equation (4.44) to obtain

$$\frac{dq}{du} + q(u) = \Sigma_s(u)\phi(u). \tag{4.45}$$

The average lethargy gain $\xi$ of a neutron in a collision with a nucleus of arbitrary mass number is computed as

$$\xi = \frac{1}{E_i(1-\alpha)}\int_{\alpha E_i}^{E_i} \ln\left(\frac{E_0}{E_f}\right) - \ln\left(\frac{E_0}{E_i}\right) dE_f. \tag{4.46}$$

The integral can be evaluated by making the substitution $x = E'/E$, thus

$$\xi = \frac{1}{1-\alpha}\int_1^\alpha \ln x dx \tag{4.47}$$

$$= 1 + \frac{\alpha}{1-\alpha}\ln\alpha \tag{4.48}$$

$$\xi = 1 - \frac{(A-1)^2}{2A}\ln\left(\frac{A+1}{A-1}\right) \tag{4.49}$$

Except for small values of $A$, the logarithm in equation (4.49) can be expanded in series, which is closely approximated by the simple formula,

$$\xi = \frac{2}{A+2/3}. \tag{4.50}$$

The values of $\xi$ are displayed in Table 4.5.

## 4.7 Moderation of neutrons in the presence of absorbing isotope

In the previous section, the slowing down of a neutron was as a result of scattering interactions with the moderator material such as graphite and the actual absorption cross-section was ignored, since it is negligible. This section describes the slowing down of a neutron in the presence of a strongly absorbing isotope such as $^{238}$U mixed with graphite. For simplicity, it is assumed that $^{238}$U does not slow down neutrons, but only absorbs them, thus the inelastic scattering is also ignored. The slowing down equation with a monoenergetic source at energy $E_0$ is defined as

$$[\Sigma_a(E) + \Sigma_s(E)]\,\phi(E) = \int_E^{E_0} \Sigma_s(E')\phi(E')\frac{dE'}{E'} + S_0\delta(E - E_0), \tag{4.51}$$

where $S_0$ is the neutron source, $\Sigma_a(E)$ and $\Sigma_s(E)$ are the macroscopic cross-section for absorption in the heavy nuclei and scattering in graphite respectively. The total collision density $F(E) = \Sigma_t(E)\phi(E)$ is defined as the sum of a interacted and un-interacted contribution. The interacted collision density contribution $F_c(E)$ is defined as

$$F_c(E) = \int_E^{E_0} \frac{\Sigma_s(E')F_c(E')}{\Sigma_t(E')}\frac{dE'}{E'} + \frac{\Sigma_s(E_0)}{\Sigma_t(E_0)}\frac{S_0}{E_0}. \tag{4.52}$$

The effective source term $S_0$ in this equation corresponds to the neutrons from the source that has interacted with the moderator material, and is divided by

$E_0$ to account for neutron absorption at the energy $E_0$. When differentiating equation (4.52) with respect to E, we obtain

$$\frac{dF_c}{dE} = -\left[\frac{\Sigma_s(E)}{E\Sigma_t(E)}\right] F_c(E). \tag{4.53}$$

This ordinary differential equation (4.53) can be integrated using the initial condition, $E = E_0$, implied by equation (4.52), to find

$$F_c(E) = \frac{\Sigma_s(E_0)}{\Sigma_t(E_0)}\frac{S_0}{E_0}\exp\left(-\int_E^{E_0}\frac{\Sigma_a(E')}{\Sigma_t(E')}\frac{dE'}{E'}\right). \tag{4.54}$$

If $\Sigma_a \equiv 0$, then $F_c(E) = S_0/E$. Hence, we can compute the slowing-down density to obtain

$$q(E) = EF_c(E) = \frac{\Sigma_s(E_0)}{\Sigma_t(E_0)}S_0\exp\left(-\int_E^{E_0}\frac{\Sigma_a(E')}{\Sigma_t(E')}\frac{dE'}{E'}\right). \tag{4.55}$$

If $S_0$ is the rate at which the source emits neutrons with energy $E_0$, and $q(E)$ is the rate at which neutrons slow down past $E$, then $\frac{q(E)}{S_0}$ is the probability that a neutron is not absorbed while slowing down from $E_0$ to $E$. Since the most absorption in the slowing-down energy range is due to the resonance absorption cross-section, the resonance escape probability $p$ as a function of energy $E$ in graphite is just

$$p(E) = \frac{q(E)}{S_0} = \exp\left(-\int_E^{E_0}\frac{\Sigma_a(E')}{\Sigma_t(E')}\frac{dE'}{E'}\right). \tag{4.56}$$

In the next section, the absorption of the slowing-down neutron near-resonance energy range is discussed.

## 4.8 Neutron absorption resonance

As the neutrons slow down in the moderator from fission energies in a nuclear reactor, they encounter a large absorption probability in the numerous sharp capture resonances shown in Fig. 4.10 that characterizes heavy nuclei. This neutron absorption resonance is of importance in a nuclear reactor because it affects the reactor multiplication, and reactor control characteristics. As seen in the neutron capture cross-section plot of $^{238}$U, there is absorption in the well-resolved low-energy resonance and also in the unresolved high-energy resonance. Of most significance, in the thermal reactor, is the absorption in the well-resolved low-energy resonance. Above several keV in fertile material, and as low as 50 eV in fissile isotopes, the capture resonance peaks are so closely spaced that they can no longer be resolved individually.

There is a decrease in the neutron flux at the energies in the neighborhood of strong resonance as is shown, in Fig 3.7, section 3.6. The amount of such

absorption depends sensitively on the fuel temperature through the Doppler broadening mechanism of importance. We will consider neutrons slowing down in an infinite homogeneous mixture of heavy nuclei characterized by absorption with scattering resonances and a moderator material having a constant scattering cross-section with negligible absorption cross-section. Specifically, we will study the case of neutrons slowing down in the vicinity of a well-isolated resonance.

### 4.8.1 Resonance absorption in heavy nuclei

Neutrons are slowed down by the moderator due to a scattering interaction with the light nuclei, e.g. carbon, and absorbed by the heavier nuclei, e.g. $^{238}$U. The scattering interactions by the heavier nuclei and absorption by the moderator are ignored [Dud76], because they are relatively small and negligible. The neutron slowing-down equation (4.51) is solved for this case to find the flux $\phi(E)$,

$$\phi(E) = \frac{q(E_0)}{E\Sigma_t(E)} p(E), \tag{4.57}$$

where $q(E)$ is the slowing-down density at energy $E$, given by

$$q(E) = \frac{\Sigma_s(E_0)}{\Sigma_t(E_0)} S_0, \tag{4.58}$$

and $p(E)$ is the resonance escape probability for a single resonance to energy $E_0$ given by

$$p(E) = \exp\left( - \int_E^{E_0} dE' \frac{\Sigma_A(E')}{E'\Sigma_t(E')} \right). \tag{4.59}$$

The factor $\frac{q(E)}{E\Sigma_t(E)}$ is called the loss-free spectrum. Since the scattering due to the moderator is much greater than that due to heavier nuclei $N_m\sigma_s^m >> N_A\sigma_s^A$ and the absorption due to the heavier nuclei is much greater than that due to the moderator $\sigma_\gamma^m << \sigma_\gamma^A$, the resonance escape probability for this particular resonance is written as

$$p = \exp\left( - \int_E^{E_0} \frac{dE'}{E'} \frac{N_A\sigma_\gamma^A(E')}{N_m\sigma_s^m + N_A\sigma_\gamma^A(E')} \right). \tag{4.60}$$

The integral is to be performed over energies in the neighborhood of the resonance. Recalling the Bethe-Placzek cross-section [Bet36],

$$\sigma_\gamma^A = \sigma_0 \frac{\Gamma_\gamma}{\Gamma} \psi(\zeta, x), \zeta = \Gamma \left( \frac{A}{4E_0kT} \right)^{1/2}, x = 2\left( \frac{E - E_0}{\Gamma} \right). \tag{4.61}$$

There are two cases of resonance absorption to consider, namely infinite dilution and the finite dilution approximation:

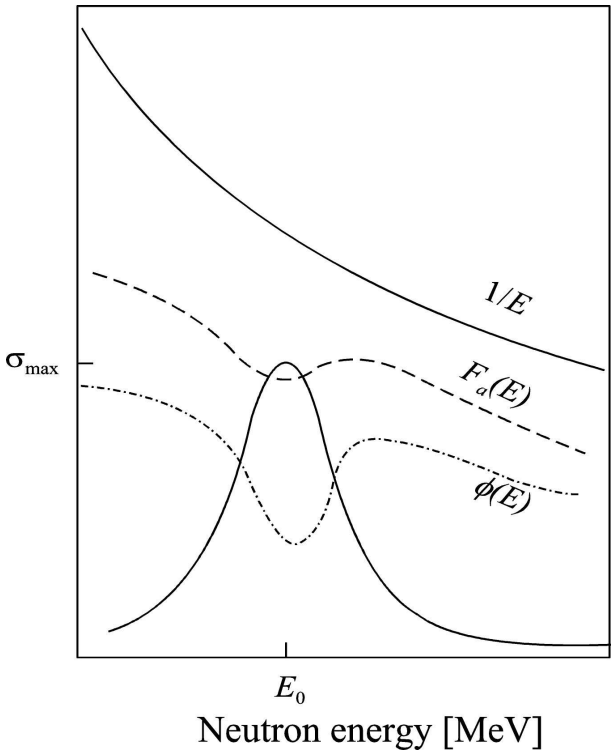


**Figure 4.17:** The slope $1/E$ is as a results of fast neutrons slowing down past through resonance, where a small portion of the neutron flux is absorbed during the collision as shown by $F_a(E)$ plot and a decrease of neutron flux $\phi(E)$ near the strong absorption resonance, redrawn from [Dud76].

- The infinite dilution approximation is when the absorber concentration is so diluted that the neutron capture resonances do not perturb the slowing down neutron flux. Using this approximation in equation (4.60), the resonance escape probability becomes

$$p \to \left[ -\frac{N_A}{N_m \sigma_s^m} \int_{E_0} \frac{dE'}{E'} \sigma_\gamma^A(E') \right] \equiv p^\infty. \tag{4.62}$$

The major contribution to the integral comes from those energies close to resonance, $E' \approx E_0$. This implies that $1/E' \approx 1/E_0$, hence

$$\int_{E_0} \frac{dE'}{E'} \sigma_r^A(E') \cong 1/E_0 \int_{E_0} dE' \sigma_r^A(E') \cong \frac{\sigma_0 \Gamma_r}{2E_0} \int_{-\infty}^{\infty} \psi(\zeta, x) dx. \tag{4.63}$$

The probability of the neutrons escaping the resonance increases with increasing moderator density. This is because neutrons slow down through the resonance more rapidly. This is understood by recalling the asymptotic collision density behavior $F(E) = 1/E$. Hence, lower-energy neutrons will go through more collisions with absorber nuclei and have a high probability of being absorbed. However, neutrons are absorbed

more effectively when the energy $E_0$ of the capture resonances is lower. For this reason, the most important resonance absorption in the thermal reactor occurs in the lower lying resonances $E_0 = 6.67$ eV in $^{238}$U. The resonance cross-section $\sigma_r^A(E,T)$ is temperature dependent through the Doppler broadening mechanism. In the finite dilution case, the absorber concentration is too low to decrease the neutron flux. Hence, there is no self-shielding.

- The finite dilution approximation is when the absorber concentration is so strong that the neutron capture at the resonances decreases the slowing down neutron flux. This occurs in the nuclear reactor where a larger part of the fuel is $^{238}$U. If we substitute equation (4.61) for $\sigma_r^A(E)$ into equation (4.60) and extend the limits of integration, then the general results for the resonance escape probability will be

$$p = \exp\left(-\frac{\Gamma}{E_0} J(\zeta,\beta)\right), \tag{4.64}$$

where

$$J(\zeta,\beta) \equiv \int_0^\infty \frac{\psi(\zeta,x)}{\beta+\psi(\zeta,x)} dx, \tag{4.65}$$

and

$$\beta \equiv N_m \sigma_s^m \Gamma / N_A \sigma_0. \tag{4.66}$$

The finite dilution resonance integral is temperature dependent. An increase in temperature causes the resonance peak of $^{238}$U to broaden, which increases the energy range over which the neutron absorption occurs. Although the resonance peak lower down slightly, the absorption at the peak still dominates and this enhances the absorption with increasing temperature. As shown in Fig. 4.17, the slowing down neutron flux $\phi(E)$ is decreased for those energies in the neighborhood of the resonance.

## 4.9 Theory on Doppler broadening of the resonance peak

The rise in the fuel temperature, discussed in section 2.2 and 2.3, has effects on the thermal motion of the nuclei. The thermal motion of the nuclei increases as the temperature of the reactor components increase, and this motion have to be considered in the nuclear reactor analysis because it has an effect on the reactivity of the reactor. This is due to the fact that the cross-section for neutron interactions for most material in the reactor depends on the center-of mass energy between the neutron and the nuclei. Here are the two cases where the motion of the nuclei has to be taken into account:

1. When the thermal energy of the nuclei is comparable to the neutron energy with $E < 1$ eV, that is $V \cong V_{th} = (k_B T/m)^{1/2}$ or $E = k_B T$.

2. When the neutron speed is much larger than that of the nuclei.

Case 2 arises when considering the process by which the neutron capture cross-section exhibits sharp resonances. Since the width of the resonances may be narrow, much less than 1 eV in most cases, even the smallest thermal motion of the nucleus can extensively affect the energy dependence of the neutron cross-section in the vicinity of the resonance.

An average interaction rate between a neutron and a nucleus moving at a velocity $\vec{v}$ and $\vec{V}$, respectively, is defined by the expression

$$\vec{R} = |\vec{v} - \vec{V}|\sigma(|\vec{v} - \vec{V}|)N, \tag{4.67}$$

where $N$ is the atomic number density of these nuclei, $|\vec{v} - \vec{V}|$ is the relative speed between the neutron and a nucleus, and $\sigma$ is the microscopic interaction cross-section. Since the velocity $\vec{V}$ of the moving nuclei is not exactly a well defined value, the distribution of nuclear velocities is given by the expression $\eta(\vec{V})d^3\vec{V}$, which is the number of target atoms per cm$^3$ with velocities $\vec{V}$ in d$\vec{V}$ about $\vec{V}$. Then, the probability of a neutron interacting per second with a nucleus of any velocity is obtained by averaging equation (4.67) over $\eta(\vec{V})$,

$$vN\bar{\sigma}(v) \equiv \int |\vec{v} - \vec{V}|\sigma(|\vec{v} - \vec{V}|)\eta(\vec{V})d^3\vec{V}. \tag{4.68}$$

The above expression (4.68) can basically be used to define an average cross-section $\bar{\sigma}(v)$ depending on the neutron speed $v$. The average cross-section characterizing neutrons moving with speed $v$ through a sample of nuclei with velocity distribution $\eta(\vec{V})$ is

$$\bar{\sigma}(v) = \frac{1}{vN} \int |\vec{v} - \vec{V}|\sigma(|\vec{v} - \vec{V}|)\eta(\vec{V})d^3\vec{V}. \tag{4.69}$$

Since the distribution function depends on the temperature characterizing the material, the thermal averaged cross-section will similarly depend on temperature. For most nuclei the cross-section for slow neutron absorption behaves essentially as $1/v$ below the resonance energy region. If nuclear motion is to be included, such behavior would be expressed as

$$\sigma(|\vec{v} - \vec{V}|) = \frac{\gamma}{|\vec{v} - \vec{V}|}. \tag{4.70}$$

If equation (4.70) is substituted into equation (4.69), then the nuclear velocity distribution function is normalized such that

$$\int \eta(\vec{V}, T)d^3\vec{V} = N. \tag{4.71}$$

The average cross-section as a function of neutron speed $v$ and temperature $T$ will then be

$$\bar{\sigma}(v,T) = \frac{\gamma}{v}. \tag{4.72}$$

When the cross-section $\sigma(|\vec{v} - \vec{V}|)$, given in equation (4.70), is a slowly varying function of relative speed and the nuclear velocity distribution is sharply peaked around $\vec{V} = \vec{V}_{th}$, equation (4.69) can be approximated by neglecting $\vec{V}$ in the integrand for neutron speeds, which higher than the nuclei speed $v >> V_{th}$. In this case, the average cross-section becomes temperature independent and is defines as

$$\bar{\sigma}(v,T) \cong \sigma(v). \tag{4.73}$$

This behavior appears frequently on the scattering cross-section for many reactor materials. For the small neutron speed $v << V_{th}$, we examine the behavior of the averaged cross-section. Then $|\vec{v} - \vec{V}|$ can be replaced by the speed $V$ in the integrand in equation (4.69)

$$\bar{\sigma}(v,T) \to \frac{1}{vN} \int V\sigma(V)\eta(\vec{V},T)d^3V \quad \text{as} \quad v \to 0. \tag{4.74}$$

The integral is now a constant, independent of the neutron speed $v$, and the behavior of $\bar{\sigma}(v,T)$ as $v$ becomes very small is

$$\bar{\sigma}(v,T) \approx C/v \quad \text{as} \quad v \to 0. \tag{4.75}$$

The effective cross-section for a neutron with velocity $\vec{v}$ is defined as the cross-section that gives the same reaction rate for stationary nuclei as the actual cross-section for moving nuclei,

$$\bar{\sigma}(v,T) = \frac{1}{v} \int |v - V|\sigma(|v - V|)P(\vec{V},T)d^3V, \tag{4.76}$$

where $P(\vec{V},T)$ is the nuclear velocity distribution at a temperature $T$. For many cases of interest this velocity distribution can be taken as a Maxwell-Boltzmann distribution characterizing an ideal gas in thermal equilibrium with the medium at a temperature T, as

$$P(\vec{V},T) = \left(\frac{m}{2\pi k_B T}\right)^{3/2} \exp\left(-mV^2/2k_B T\right), \tag{4.77}$$

where $m$ is the atomic mass number and $k_B$ is the Boltzmann's constant. As said earlier that the interaction cross-section depends on the relative speed between the neutron and the target nucleus. The difference in the relative speed causes a shift in the resonance peak. To take this effect into account, a single-level Breit-Wigner formula is substituted into an expression for the

thermally averaged cross-section in equation (4.69) or (4.76) with few approximations, the Bethe-Placzek cross-section is obtained for the neighborhood of the resonance with

$$\zeta \equiv \Gamma/\Gamma_D, \tag{4.78}$$

where

$$\Gamma = \gamma(E_0) \quad \text{is the total width at the resonance energy,} \tag{4.79}$$

$$\Gamma_D \equiv \left(\frac{4mE_0k_BT}{M}\right)^{1/2} \tag{4.80}$$

is called the Doppler width of the resonance, $m$ and $M$ is the neutron energy and capture nuclei mass respectively. The Bethe-Placzek cross-section is defined as [Bet36]

$$\sigma = \sigma_0 N \psi(\zeta, x) \tag{4.81}$$

where

$$x = 2\frac{E_0 - E}{\Gamma}, \tag{4.82}$$

$$\psi(\zeta, x) = \frac{\zeta}{\sqrt{\pi}} \int_{-\infty}^{\infty} \frac{\exp\left(-\zeta^2(x-y)^2\right)}{1+y^2} dy. \tag{4.83}$$

This Bethe-Placzek cross-section is of importance in the analysis of Doppler broadening of the resonance peak. The area under the Bethe-Placzek cross-section is almost independent of the temperature. As the temperature $T$ increases, the resonance cross-section becomes broader and the peak becomes lower. The minima between resonances become flatter. At extremely high temperatures, the entire resonance structure disappears and the cross-section approaches a simple $1/v$ shape, it is inversely proportional to the speed on the neutron. The cross-section reduces rapidly as the neutron energy increases. Doppler-broadening of neutron cross-section resonances has a very important effect on resonance self-shielding in neutron transport calculations discussed in previous Chapter 3. From equation (4.81), the dependence of thermally averaged capture cross-sections on energy for several different temperatures $T$ is given in Fig. 4.18.

### 4.9.1 Doppler broadening in the nuclear reactor fuel

In a nuclear reactor, the broadening of capture resonance peaks shown in Fig. 4.18 is directly associated with the temperature of the fuel. As said earlier, the probability of a neutron being captured by $^{238}$U depends on the relative speed between the neutron and the target nucleus, but mostly on the exact value of the neutron kinetic energy. Since the increase in the temperature of nuclear fuel causes the thermal motion of $^{238}$U nucleus in the fuel to increases, the relative speed between the neutron and $^{238}$U nucleus causes the shape of the

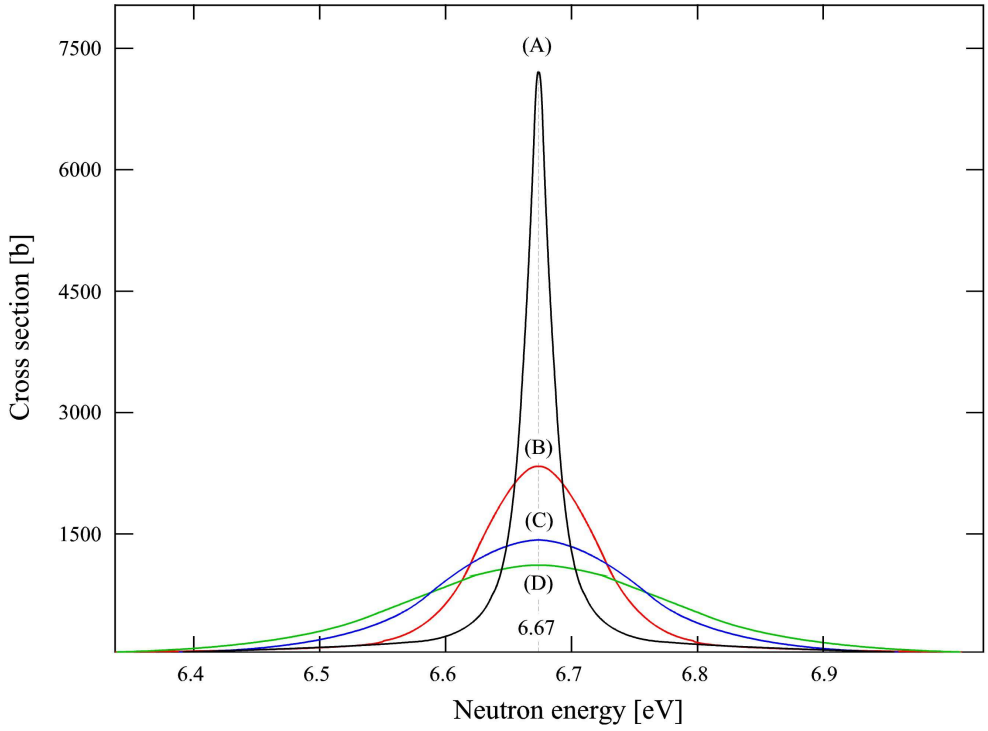


**Figure 4.18:** The nuclear capture resonance of $^{238}$U at a strong resonance of 6.67 eV, labeled A, B, C, D for different temperatures $T = 0, 300, 600, 1800$ K, respectively, redrawn from [Reu08].

resonance peak to change. This change in the resonance peak is explained with the schematic diagram shown in Fig. 4.19. Consider a nucleus at rest, as shown Fig. 4.19(a), a neutron that has kinetic energy $E_{\mathrm{n}}$ corresponding to the peak of the resonance $E_{\mathrm{res}}$ will have a high probability of being absorbed, whereas the one that has a lower or higher kinetic energy will have less probability of being absorbed. If the temperature in the fuel increases, the $^{238}$U nucleus starts to vibrate back and forth. A neutron whose energy falls outside the energy of the resonance may encounter a $^{238}$U nucleus that is moving at that instant in such a way that the kinetic energy of the neutron relative to the nucleus coincides with the peak. The schematic diagram in Fig. 4.19(b) shows a neutron whose kinetic energy is above the resonance energy of the resonance, but encounters a nucleus moving in the same direction at a speed that makes the neutron's speed of approach the same as it was in (a). In the view of the nucleus, this neutron appears to be within the resonance peak. A similar case happens to a neutron whose kinetic energy is less than the energy at the resonance, but encounters a hot $^{238}$U nucleus moving towards it at exactly the right speed, see Fig 4.19(c).

The overall effect of fuel temperature rise is that the resonance peak appears broadened as shown in Fig. 4.18. Although the height of the peak reduces

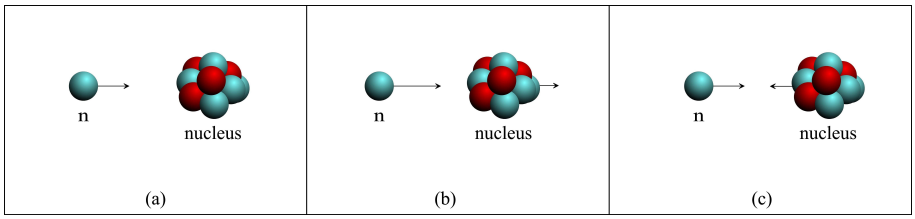


**Figure 4.19:** A schematic representation of the Doppler broadening mechanism, where $E_{\mathrm{n}}$ and $E_{\mathrm{res}}$ represents the kinetic energy of the neutron and energy at the resonance peak respectively. Here (a) is the nucleus at rest, (b) the nucleus moving away from the neutron, (c) the nucleus moving toward the neutron.

as the temperature of the fuel increases, the neutron capture cross-section is still as large that any incoming neutron with an energy in the range of the resonance will be captured. The mean free path of the neutrons in the fuel becomes very short, 0.025 mm. This is how the $^{238}$ nuclei deplete intermediate energy neutron flux before they are thermalized to cause another nuclear fission and as a result change in the reactivity.

Uranium-238, which forms the large part of the fuel in the reactor, reduces the number of thermal neutrons available to propagate the fission chain reaction and consequently the reactivity is reduced. Doppler broadening therefore creates a negative feedback loop, as was discussed in section 2.3. The PBMR reactor is designed so that the Doppler broadening effect is stronger, and at a specific temperature the reactor controls itself without the need to insert the control rods. This is the main passive safety feature of the PBMR, and it makes the design unique, compared with all other conventional water cooled reactors that require active safety control.

# Chapter 5

# Neutron detectors

## 5.1 Neutron detection methods

In general, the detection of neutrons is more challenging than other radiation because of their neutrality, and their extremely short range interaction with the nuclei. There are two basic types of neutron-interactions used in the detection of neutrons namely, neutron scattering and neutron-induced nuclear reactions. The kinetic energy of the incoming neutrons to be detected determines the type of interaction to be used in the detection. The slow neutrons are detected through neutron-induced nuclear reaction while fast neutrons are detected through scattering interaction. In the scattering interaction, a fraction of the kinetic energy of the neutrons is transferred to a nucleus and when enough energy is transferred, the resulting recoiling nucleus, usually hydrogen, ionizes the detection medium surrounding the point of interaction. In neutron-induced nuclear reactions, a neutron is absorbed by the target nucleus and reaction products are emitted. The reaction products, such as protons, $\alpha$-particles, $\gamma$-rays and fission fragments, can transfer their energy to the atoms of the detection medium. The neutron detectors that make use of the neutron induced nuclear reactions to detect fast neutrons are usually surrounded by moderating material to reduce the kinetic energy of the incident neutron first and hence increase the probability for the reactions. The neutron detectors employing neutron induced nuclear reaction or scattering interaction can use solid, liquid or gas-filled detection media. This chapter describes gas-filled proportional counters (in section 5.2) and scintillator detectors (in section 5.3) that can be used as either slow or fast neutron detectors, employing different types of interaction mechanisms, and detection media.

Most of the detection systems that employ the nuclear reaction mechanism cannot provide specific energy information of the neutron that induced the reaction, whereas, the hydrogen recoil-type detectors mostly measure only the first interaction event. Since only a fraction of neutron energy is deposited in the detector, the energy information obtained is whether a slow or fast neutron

induced the interaction. When moderators are employed, the information of the initial neutron energy before moderation is lost, so what the detector record is the reaction energy. Thus, in general, neutron detectors provide information on the energy range and the number of neutrons that induced the reactions. Information regarding the energy range of the neutrons detected can usually be inferred from the reaction rate, knowing the cross-section profile of the neutron conversion material in the detector and the neutron flux profile.

### 5.1.1 Neutron-induced nuclear reactions for slow neutron detectors

There are several factors to be considered when searching for the reaction that might be used for neutron detection, such as the neutron interaction cross-section, isotopic abundance, discrimination over $\gamma$-ray events and the $Q$-value of the reaction. The cross-section must be as large as possible so that an efficient detector with small dimensions can be built. This is of importance for detectors in which the neutron converter material is a gas. The target nuclide should either be of high isotopic abundance in the natural element or alternatively, a source of artificial enriched material should be available for detector fabrication. In many practical applications, neutrons are accompanied by an intense field of $\gamma$-rays, so the neutron reaction chosen should have the ability to discriminate against these $\gamma$-rays in the detection process. The $Q$-value that influences the amount of energy released from the reaction after the neutron capture is also of importance when choosing the reaction. The higher the $Q$-value, the greater the energy given to the reaction products, and the easier the task of discriminating against the $\gamma$-ray events using amplitude discrimination. The most common neutron conversion reaction used to detect neutrons results in a charged particle, as shown below:

$$\text{neutron} + \text{target nucleus} \rightarrow \begin{cases} \text{recoil nucleus} \\ \text{proton} \\ \alpha - \text{particle} \\ \text{fission fragments} \end{cases}$$

The neutron-induced nuclear reactions are exothermic such that the kinetic energy of the reaction products determined by the $Q$-value of the reaction does not reflect the energy of the incident neutron. The distance traveled by the emitted reaction products is of great importance in the detector design. The detector must be designed with an active volume that is large enough to fully stop the particles. If the detection medium is a solid, the range of any of the reaction products shown above does not exceed a few tenths of a millimeter. However, if the detection medium is a gas, the range of the reaction products (typically several centimeters) can be significant when compared with the dimensions of the detector. In this case, some reaction products may not

deposit all their energy inside the detector volume. If the detector volume is large enough such that these losses can be neglected, the response function will be very simple, consisting only of a single full-energy peak and the ability to discriminate against low-amplitude events such as $\gamma$-ray-induced events would be maximized. If, in contrast, a significant number of reaction products do not deposit their full energy, a low-energy tail is added to the pulse height distribution and, as a result, the efficiency of the detector is compromised.

#### 5.1.1.1 The $^{10}$B(n,$\alpha$) reaction

Boron-10 is an isotope that is widely used for the detection of lower-energy neutrons, because of the high cross-section for the (n,$\alpha$) reactions. As shown in Fig. 4.11, the cross-section for this reaction is 3840 b at thermal-neutron energy ($E_{\mathrm{n}} = 0.025$ eV), but it drops rapidly with increasing neutron energy (i.e. the cross-section is proportional to $1/v$, where $v$ is the neutron speed). The following two neutron reactions take place:

$$\mathrm{n} + {}^{10}\mathrm{B} \rightarrow \begin{cases} {}^{7}\mathrm{Li} + \alpha & Q\text{-value} = 2.792 \text{ MeV} \quad \text{(ground state)} \\ {}^{7}\mathrm{Li}^{*} + \alpha & Q\text{-value} = 2.310 \text{ MeV} \quad \text{(excited state)} \end{cases}$$

From this reaction, $^{7}$Li may be left either in the ground state or first excited state, denoted by *. When the thermal neutrons ($E_{\mathrm{n}} = 0.025$ eV) are used to induce the reaction, about 94% of all reactions lead to the excited state and only 6% directly to the ground state. In all the cases, the $Q$-value of the reaction is very large (2.310 and 2.792 MeV) compared with the energy of the incident neutron. The kinetic energy of the incident neutron is converted into a much larger reaction energy, and it is not possible to extract any information about its original value. Since the linear momentum of an incoming thermal neutron is very small, the reaction products also shows a net momentum of essentially zero. Hence, the reaction products are emitted in exactly opposite directions, with energy equal to the $Q$-value being shared between them. An $\alpha$-particle will take 1.47 MeV and a $^{7}$Li nucleus will take 0.84 MeV of energy. The advantages of using this reaction in neutron detection is that the cross-section for the (n,$\alpha$) reaction is large and because boron, highly enriched in $^{10}$B concentration, is readily available. In nature, boron material has about 19.9% of $^{10}$B and the rest is $^{11}$B.

#### 5.1.1.2 The $^{6}$Li(n,$\alpha$)$^{3}$H reaction

The next widely used reaction for slow-neutron detection is the $^{6}$Li(n,$\alpha$)$^{3}$H reaction. As shown in Fig 4.11, the cross-section for this reaction, which is about 940 b at thermal-neutron energy ($E_{\mathrm{n}} = 0.025$ eV), drops rapidly with increasing neutron energy. The cross-section is also proportional to $1/v$.

The $^{6}$Li(n,$\alpha$)$^{3}$H reaction releases a large amount of energy, $Q-$value = 4.78 MeV, via the interaction

$$\mathrm{n} + {}^{6}\mathrm{Li} \rightarrow \alpha + {}^{3}\mathrm{H} \quad Q\text{-value} = 4.78 \text{ MeV}.$$

The reaction energy shared by the reaction products is as follows:

$$E_{\mathrm{H}} = 2.73 \text{ MeV} \quad E_{\alpha} = 2.05 \text{ MeV}.$$

The isotope $^{6}$Li, which constitutes 7.40% of natural lithium, has a large capture cross-section that remains below that for the $^{10}$B reaction until the resonance region at an energy of 250 keV. The high $Q$-value from this reaction makes up for the lower cross-section.

#### 5.1.1.3 The $^{3}$He(n,p)$^{3}$H reaction

The gas $^{3}$He is also used in the detection of neutrons through the reaction

$${}^{3}\mathrm{He} + \mathrm{n} \rightarrow {}^{3}\mathrm{H} + \mathrm{p} \qquad Q\text{-value} = 0.765 \text{ MeV}.$$

The thermal neutron cross-section for this reaction is 5330 b, higher than that for the boron and lithium reactions. This cross-section is also proportional to $1/v$ (see Fig. 4.11). For reactions induced by thermal neutrons, the $Q$-value of 0.765 MeV leads to oppositely directed reaction products with energies

$$E_{\mathrm{p}} = 0.574 \text{ MeV} \quad \text{and} \quad E_{^{3}\mathrm{H}} = 0.191 \text{ MeV}.$$

Although $^{3}$He is still commercially available, its relatively high cost is often prohibitive for some applications. Further more it is not going to be available commercially in the future due to nuclear proliferation safeguard issue.

#### 5.1.1.4 Neutron-induced fission reactions

The fission cross-sections of $^{233}$U, $^{235}$U and $^{239}$Pu are relatively large at lower neutron energies (see Fig. 4.13), and hence these materials are used as the basis of slow-neutron detection. The fission reaction has an extremely large $Q$-value which is approximately 200 MeV compared with previously discussed reactions. Consequently, detectors based on fission reactions can often give output pulses larger than those induced from competing reactions or incident $\gamma$-rays, and very clear discrimination can be accomplished. Any neutron detector that incorporates fissile nuclides will show a spontaneous output signal due to $\alpha$-decay. This is because almost all fissile nuclides are naturally $\alpha$-particle emitters. These events can usually be discriminated against easily on a pulse amplitude basis given that the energy (typically $E_{\alpha} < 10$ MeV) of the $\alpha$ decays is always smaller than the energy given off in a fission reaction.

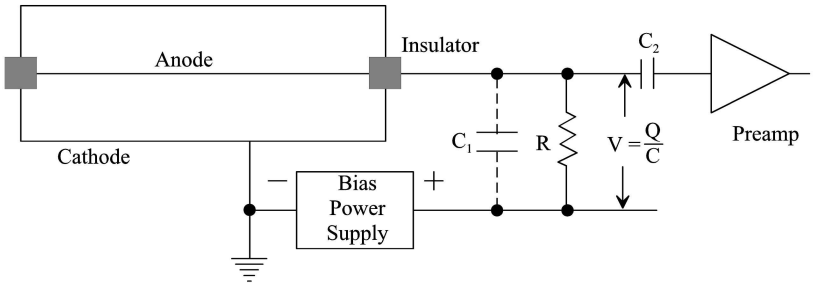


**Figure 5.1:** Gas-filled neutron detector setup, redrawn from [Cra].

## 5.2 Gas-filled detectors for neutron detection

The neutron interactions discussed in section 4.2 are essential for the detection of slow or fast neutrons in the gas filled detector. The slow or fast neutrons can be detected via neutron-induced nuclear reactions or neutron scattering interactions respectively. Irrespective of the neutron conversion material, either $^{3}$He or $^{10}$B, the setup of the gas detector is the same. Since the magnitude of the induced signal from different reactions might be different, the high voltage or amplifier gain settings can be adjusted to compensate for this change. A schematic diagram of a typical gas filled detector for neutron detection is shown in Fig 5.1.

Gas-filled detectors are built from a stainless steel or aluminum cylinder, with walls of about 0.5 mm thick. The cylinders have an electrical connector at one end or, occasionally, at both ends for position-sensitive measurements. The difference in these materials is the neutron transmission or structural strength. The aluminum walls will have less of an influence to neutron flux, with a neutron absorption of about 0.5%, compared with steel walls with an absorption of about 3%. However, the advantage of using steel tubes is that they require less careful handling during assembly, and impurities in the material can be kept lower. The interior walls of the gas filled detectors are coated with activated charcoal to absorb the electronegative gases that build up during neutron irradiation [Eva76].

As described earlier, the detection of neutrons requires the transfer of some or all of their kinetic energy to the charged particle reaction products. These charged particles will collide with the gas atoms knocking off few electrons and create ions until their energy is exhausted, about 30 eV is required to create an ion pair. From this required energy, the maximum number of ions that can be produced is $E/30$ eV, where $E$ represents the kinetic energy of the charged particle in eV. Once the positive voltage is applied to the anode wire of a gas filled detector, as shown in Fig. 5.1, the electrons and positively charged ions move towards the anode and cathode respectively. The amount of

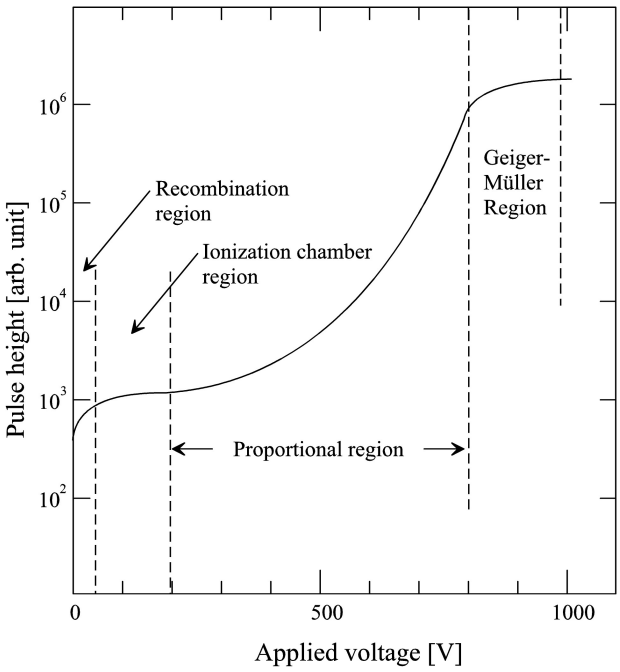


**Figure 5.2:** The ionization, proportional and Geiger-Müller region of operation of gas filled detectors, redrawn from [Kno00].

applied voltage, fill gas and the geometry of the tube determines the electrical output signal from the gas filled detector. From these parameters, the gas filled detector can operate either in the *ionization*, *proportional*, or *Geiger-Müller* region, as illustrated in Fig. 5.2. The applied voltage allows the device to work continuously by sweeping up electrons and preventing the build-up of events. A full peak is reached when enough voltage is applied and even a small further increase in voltage yields no more electrons. Detectors operating in the ionization region are called ionization chambers and their output signals are proportional to the energy deposited in the gas by the charged particles, and it does not dependent on the applied voltage.

In the region beyond the ionization regime is the proportional counter region. In this region, the strength of the electric field is large enough such that the primary electrons can gain enough energy to ionize the other gas molecules and create secondary ionizations. However, if the strength of the electric field is increased further, the secondary electrons can also ionize other gas molecules and create more ions. As long as the electric field strength increases, the production of the ion pairs from the primary event will also increase. This cumulative amplification process is known as avalanche ionization. When a total of "N" ion pairs result from a single primary event, it implies that the process has a gas amplification factor of N. This quantity will be unity if no secondary ions are formed in the ionization chamber, and as high as $10^3$ to $10^6$ in a well designed proportional counter. In the proportional region, the current

of the electrons collected is linearly proportional to the energy deposited in the gas by the charged particles. For the amplification process to occur, an electron must gain enough energy in one or more mean-free paths. The mean-free path of an electron is the average distance traveled between collisions, and it depends on the filling gas pressure of the proportional counter. In a proportional counter, the electron's drift velocity is larger than that of the positive ions. The time it takes for the electrons with larger drift velocity to be collected in the anode is very short, about $10^{-8}$ s. The anode wire is near to where the avalanche is formed, hence the very short time for collection. The positive ions are slower and collected over a much longer time interval on the cathode. The pulses observed have two rise times, the fast electron and slow motion of the ions produce an initial fast and slower rise-time respectively. The amplitude of the pulse is dependent on the drifting velocity of the positive ions from the anode to cathode gap, and the highest amplitude is reached only when the positive ions are fully collected. This collection process may take 200 $\mu$s for a typical proportional counter. However, there is time dispersion in the drift time which depends on tube voltage and diameter as has been reported by [Atw74].

Saturation effects at the anode wire might appear when the applied voltage is increased further, and the proportionality between the energy of the primary charge deposited and the output signal can be gradually lost. When the primary electrons reach the region of high electric field near the anode wire, the avalanche process starts and quickly increases to a maximum value because the secondary electrons create additional avalanches axially along the wire. In this region the avalanche extends to the full length of the anode wire and the secondary electron multiplication process stops only when the electrostatic field is sufficiently distorted to prevent the further acceleration of secondary electrons. For low energy ionizing primary events, it is possible to reach an amplification factor of about $10^{10}$. Gas filled detectors operated in this region are known as the Geiger-Müller counters. The Geiger counter cannot be used in high-count-rate applications since they saturate at relatively low event rates. However, they can still be used as low-level survey meters for field inspection. Gas-filled detectors typically employ $BF_3$, $^3$He, $^4$He, or $CH_4$ as primary constituent, at pressures between 101.3 kPa and 2.03 MPa, depending on the application. Other, heavier atomic mass gases are often added to enhance the performance of the detector. For example, the range of the reaction products can be reduced by adding argon gas. This increases the energy deposition within the gas and, as a result, the output pulse-height resolution can be improved. The other advantage of adding a heavier gas is that the charge collection time can be significantly reduced. However, the negative effect is that the $\gamma$-ray sensitivity is increased as the cross-section evolves with the atomic number $Z^4$ [Rei79].

### 5.2.1 Detection mode of operation

Gas-filled detectors, ionization and proportional counters, can be operated in either pulse or current mode. These modes of operation also applies to the scintillator detectors, which is discussed in the review later in this chapter. In pulse mode, each neutron interaction must be separated by sufficient time so that it may be resolved as an individual pulse. This mode is therefore limited to lower rates of neutron flux measurements, but offers the benefits of $\gamma$-ray discrimination through simple amplitude selection of the output pulse. The pulse mode operation of most detectors is conventionally limited to rates below about $10^5$ $s^{-1}$, although the improvements in chamber design can raise the limit to as high as $10^7$ $s^{-1}$ [Ell93, Ell73]. At very high neutron flux levels, pulse mode operation is no longer possible because the time between adjacent events becomes too short to carry out an adequate analysis, or the current pulse from successive events may overlap in time. In this event, gas-filled detectors are often operated in current mode. With proper ion chambers, the range of operation can be extended to the maximum flux level of interest in the reactor before serious non-linear effects due to ion electron recombination set in. The lower limits of current mode operation are usually determined by leakage current that arises in the detector insulation and cable dielectric material. The inherent $\gamma$-ray discrimination between pulses, whether large or small, is compromised by operating the chamber in current mode. The review of the gas-filled detectors that employ those nuclear reactions discussed in section 5.1.1, is performed in the next sections.

### 5.2.2 Boron trifluoride proportional counters

The boron trifluoride ($BF_3$) gas detector is commonly used for slow neutron detection where $BF_3$ serves both as the neutron converter material as well as a proportional gas. This detector is preferred widely because of its superior properties as a proportional gas, as well as its high concentration of highly enriched $^{10}B$. This makes the efficiency of the detector at least five times greater than if the gas contains naturally occurring boron. The operating gas pressure of a $BF_3$ proportional counter is limited to a pressure of about 0.5 to 1.0 atm, because the efficiency decreases when operated at higher pressures.

Because the momentum of the incoming neutron is small, the two reaction products, $^7Li$ and an $\alpha$-particle, are oppositely directed when emitted and slow down in the gas, causing ionization. Therefore, a somewhat idealized pulse-height response of a detector would appear, as shown in Fig. 5.3. For a large $BF_3$ tube, nearly all the reactions occur sufficiently far from the walls of the detector and the reaction products deposit their full energy in the proportional gas. In that event, all the energy of the reaction is deposited in the detector, and the only variation is a result of the branching of the reaction between the excited and the ground state of the $^7Li$ product nucleus. The stronger peak

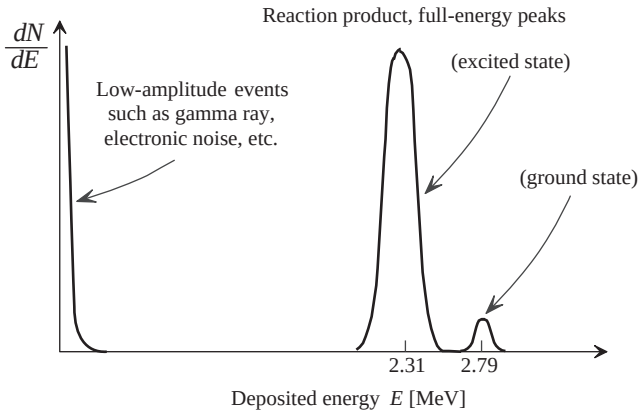


**Figure 5.3:** Low amplitude events expected pulse height spectra from a large diameter $BF_3$ tubes where all reaction products deposit their energy in the gas, redrawn from [Kno00].

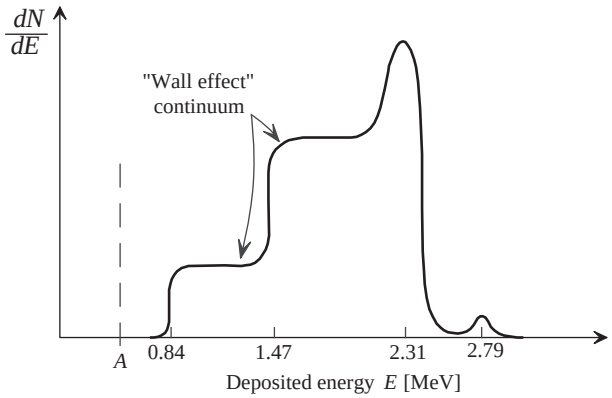


**Figure 5.4:** In small diameter $BF_3$ tubes, as presented in this diagram, the wall-effect continuum appears when one of the reaction products hits the wall, redrawn from [Kno00].

corresponds to the $Q$-value of 2.310 MeV for the excited state of $^7$Li, which is about 94% of the events, and the weaker peak corresponds to the $Q$-value of 2.792 MeV for the ground state of $^7$Li, which is about 6%. Once the size of the tube is no longer large compared to the range of the $^7$Li and $\alpha$-particles produced in the reaction, some events no longer deposit the full reaction energy in the gas. If either $^7$Li or $\alpha$-particles hit the chamber wall, a smaller pulse is produced and a collection of these smaller pulses is known as the *wall effect*. The wall effect will be significant in tubes with a small diameter, because the range of $\alpha$-particles produced in the reaction is already of the order of 1 cm for a typical $BF_3$ gas pressure. In Fig. 5.4, the differential pulse height spectrum from the tube in which the wall effect appears is shown, and is explained as follows: if the $\alpha$-particle strikes a wall, then, as a result, $^7$Li is directed away

from the wall and may deposit its full energy within the gas. In contrast, if the $^{7}$Li nucleus hits a wall, the entire energy of the $\alpha$ particle is fully absorbed in the gas. Hence, there should be wall losses for only one reaction product at a time.

A $BF_3$ tube is an example of a detector where the differential pulse height spectrum does not provide information about the energy of the incident neutron, but is rather a function of the size and geometry of the detector itself. In many applications, a pulse height spectrum is not required, but the stable operation point is considered. This is achieved by setting a discriminator level at the point labeled A in Fig. 5.4.

#### 5.2.2.1 Boron trifluoride neutron detection efficiency

The detection efficiency, $\epsilon$, of $BF_3$ detectors can be expressed as [Hui04]

$$\epsilon(E) = 1 - \exp\left(-\Sigma_a(E) \times L\right), \tag{5.1}$$

where $\Sigma_a$ is the macroscopic neutron absorption cross-section of $^{10}$B at an energy $E$, and the active length of the tube is represented by $L$. As the cross-section drops off rapidly with energy, this equation shows that the detector efficiency decreases rapidly with increasing neutron energy, making the detector mainly a slow neutron detector. Most practical $BF_3$ counters have a length of 0.3 m, filled with pure $BF_3$ gas to a pressure of 80 kPa. The fill gas is enriched to about 96% in $^{10}$B. The efficiency of the detector varies with the energy of the incident neutron travelling parallel to its axis, e.g. $|\epsilon| = 92\%$ at a neutron energy of 0.025 eV, 12% at 10 eV and 4% at 100 eV. Equation (5.1) slightly overestimates the neutron-counting efficiency, because there are regions near the end of the tube in which the charge collection is inefficient, resulting in a reduced neutron response. Boron trifluoride proportional counter gas is sometimes manufactered using a mixture of $BF_3$ with Argon gas to improve the pulse height spectrum where peaks are cleary visible but the detection efficiency decreases.

#### 5.2.2.2 The design of a boron trifluoride tube

The neutron detection efficiency can be increased and the wall effect can be suppressed by increasing the size of the tube. In addition, if the pressure of the $BF_3$ fill gas is increased, the efficiency can also be improved. A successful construction and operation of $BF_3$ tubes with a diameter of up to 15 cm and a length of 180 cm has been reported by Fowler [Fow63] with the filling gas pressure from about 13 to 80 kPa. However, the resolution is optimum at pressures between 27 to 40 kPa. When the pressure is increased further, the full energy peaks broaden considerably due to recombination and negative ion formation. In practice, the poorer resolution of the peaks does not affect the

counting of neutron-induced events, and tubes with higher pressure gas are quite acceptable.

In a $BF_3$ tube, the outer diameter cathode, are commonly manufactured using aluminum or stainless steel cylinders, and the central small diameter is an anode wire. The diameter of the anode determines the operating voltage; the larger the diameter and or the higher the fill gas pressure, the higher the voltage. For example, with an anode diameter of 0.1 mm or less, operating voltages tend to be about 2000 to 3000 V and the typical gas multiplication factors are of the order of 100 to 500.

$BF_3$ counters of a typical size are normally limited to an operating temperature of about 100°C, but specially designed tubes can extend the operating range to as high as 150°C. These limitations are due to the insulating material used in fixed connectors. Sakai *et al.* [Sak83] reported that the pulse height decreases and the peak width broadens as the temperature increases. These changes are related to the possible out-gassing of impurities from the counter walls or other components. Counters can be operated continuously at 100°C without an appreciable change in characteristics and it is a conservative maximum temperature rating for these tubes for continuous operation.

Because of the relatively high operating voltage, spurious pulses of about the same size as the signal pulse can sometimes arise from the fluctuations in leakage currents through the insulators. This occurs especially under conditions of high humidity. Spurious pulses may also arise if the $BF_3$ counters are subjected to vibrations and shocks.

#### 5.2.2.3 Boron trifluoride response to $\gamma$-radiation

In many applications of the $BF_3$ detector, the ability to discriminate against $\gamma$-ray events is considered important. Gamma-rays interact primarily with the counter walls and create secondary electrons that may produce ionization in the gas. Since the stopping power for electrons in gases is quite low, an electron created from $\gamma$-ray events will deposit a small fraction of its initial energy within the gas before reaching the wall of the counter. Hence, the $\gamma$-rays will produce low-amplitude pulses that will lie in the tail of the low-energy part of the spectrum in Fig. 5.4. Pulse height discrimination can be used to eliminate these $\gamma$-ray events without compromising the neutron detection efficiency.

If the $\gamma$-ray flux is sufficiently high, however, several complications can reduce the effectiveness of this pulse height discrimination. At high $\gamma$-ray fluxes, pulse pile-up may produce a peak amplitude that is considerably larger than any individual pulse. Short time constants are desirable to reduce the $\gamma$-ray pile-up but may lead to a reduction in the neutron-induced amplitude due to incomplete charge integration [Bro74]. In addition, if the $\gamma$-ray flux is quite high, $\gamma$-rays can themselves interact with the gas, breaking its chemical bonding and deteriorating the performance of the $BF_3$ detector as a proportional counter. In extreme cases, the radiation-induced chemical changes can result

in permanent damage to the tube. There is successful discrimination of $\gamma$-ray events at exposure rates of about 1.431 Sievert per hour using a conventional $BF_3$ tube [Ver74]. Boron trifluoride tubes that employs activated charcoal inside the tube to act as an absorbing agent for contaminants has been developed and improve the operating characteristics [Sto66].

### 5.2.3 Boron-lined proportional counters

The interior walls of the boron-lined proportional counters are coated with enriched $^{10}B$ in a solid form. This configuration has the advantage that a more suitable proportional gas can be used in order to reduce the chemical degradation problem as experienced by $BF_3$ gas when exposed to high $\gamma$-ray fluxes. Since the maximum range, for $\alpha$-particles from the boron reaction is of the order of 1 mg·cm$^{-2}$, increasing the thickness of the coating can improve the efficiency of the counter. However, creating a thicker coating will simply result in a layer that is too far from the filling gas to permit any reaction products to reach the gas, and the efficiency will drop slightly due to the added attenuation of the incident neutrons.

In the boron-lined counters, the nuclear reaction occurs in the wall, and the reaction products are oppositely directed. This implies that only one reaction product can be expected per interaction. Since the range of the $\alpha$ particle is about 1 mg·cm$^{-2}$ in boron, the coating must be thin and the detection efficiency (of order of 10%) is lower than for $BF_3$ gas-filled counters. Since the nuclear reaction occurs at the wall and the reaction product fly to the fill gas, so the fill gas can be optimized for time-of-flight measurements. The argon gas at a pressure of 0.25 atm with a small admixture of $CO_2$, is mostly used in the boron-lined proportional counters. These counters operate in the proportional region at a voltage of 600 to 850 V.

The detection efficiency of the $^{10}B$-lined counter depends on the kinetic energy of the neutrons, slow and fast neutrons are detected with moderate and low efficiency respectively. The $^{10}B$-lined counter has a lower $\gamma$-ray sensitivity relative to the $BF_3$ gas filled counters. This is because of the lower fill gas pressure, and lower operating voltage, which reduce the size of the $\gamma$-ray pulse relative to the neutron pulse. It can be very useful for applications where neutrons are detected in the presence of high $\gamma$-ray fluxes of about 10 Sv·h$^{-1}$. In this case, the loss of neutron detection efficiency is about 50%, resulting from a high discriminator setting required to reject the pile-up from $\gamma$-rays.

### 5.2.4 The $^3$He proportional counter

The $^3$He(n,p)$^3$H reaction makes an attractive alternative for the slow neutron detection to the $^{10}$B(n,$\alpha$) reaction because of higher absorption cross-section. Helium-3 gas of sufficient purity is used as a neutron-conversion target and proportional gas in the $^3$He proportional counter. The general properties of

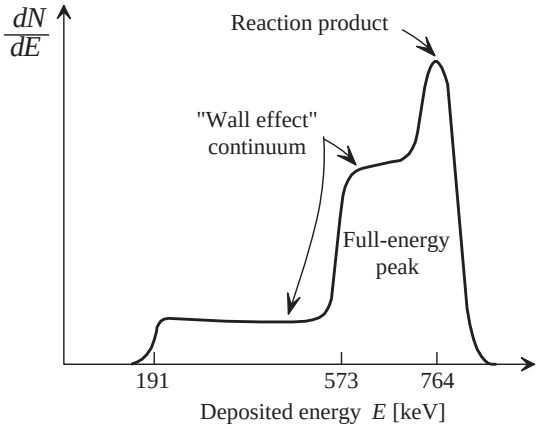


**Figure 5.5:** The wall-effect continuum in $^3$He proportional counter where one of the reaction products hit the wall of the tube, redrawn from [Kno00].

$^3$He proportional tubes are reviewed in Ref. [Mil62]. In a large detector, the expected energy deposition from the reaction product is 0.764 MeV. Because $^3$He gas has a lower atomic number, the range of the reaction products in the gas is not always small compared with the dimension of the proportional tube. The wall effect discussed earlier in $BF_3$ can also be significant in the $^3$He proportional counter. This effect causes the continuum in the pulse height spectrum. However, it is expected that increasing the dimensions of the counter tubes will reduce the effect because most of the neutron interactions will occur within the gas.

Helium-3 proportional counters can be operated at a high pressure, from 200 kPa up to 2 MPa, due to the higher saturation (condensation) pressure of the gas. This provides a higher detection efficiency and also makes its easier to minimize the wall effect. A heavier gas, such as krypton, is usually added to shorten the range of charged particles and to stop them from reaching the wall [Sha69]. A pulse height spectrum for $^3$He tube is schematically shown in Fig. 5.5. The step structure to the left of the peak is similar to that shown in Fig 5.4 for $BF_3$ tubes, except that the discontinuities will occur at energies corresponding to that of the proton (0.573 MeV) and the triton (0.191 MeV). A single full energy peak is expected for neutron energies that are small compared to 0.764 MeV.

The purity of the fill gas is critical, as the leakage of air into the proportional counter tube over a long period of time will cause failure which also happens with all other proportional counters. Another factor that can cause failure is the buildup of electronegative poison in the gas. A layer of activated charcoal within the tube has been shown to be effective in removing these poisons and can extend the useful lifetime of a $^3$He detector [Eva76]. The acceptable operating temperature for a $^3$He tubes has been reviewed in Ref. [Sak80] and [Gle88] and is shown to be as high as 250°C.

Gamma-rays, as in the case of $BF_3$ detectors, produce a detectable signal by releasing electrons via interactions within the metallic walls of the tube. However, in the case of the $^3$He proportional counters, the signals produced by electrons arising from the $\gamma$-ray interactions are more difficult to discriminate against using their amplitude, due to the lower $Q$-value = 0.764 MeV of the $^3$He(n,p) reaction. An increased energy deposition by electrons as they traverse the gas, which in turn increases the amplitude of the signal associated with the $\gamma$-rays, is another problem, because the detector operates at higher gas pressure. Hence, $^3$He proportional counters are more sensitive to $\gamma$-rays than $BF_3$ counters. Being a monatomic gas, helium does not decompose under intense $\gamma$-ray exposure and such detectors can sustain very high $\gamma$ fields.

### 5.2.5 The fission chamber neutron detector

Fission chambers are another type of gas-filled detectors that operate in the ionization region described earlier in this chapter. These devices are available in smaller sizes, i.e. lengths of about 40 to 300 mm and diameters of about 6.0 to 50 mm. A very thin layer (0.02 to 2 mg·cm$^{-2}$ surface thickness) of fissionable material is electroplated, evaporated or painted on to the inner walls and directly exposed to the detector gas. This fissionable material is usually highly enriched in $^{235}$U. Since the nuclear fission of $^{235}$U releases a large amount of energy 200 MeV, a low background events can be easily be decerned in the fission chambers and neutron counting can practically be carried out at very low counting rates. In the fission chambers, the fissile material is not part of the proportional counter gas, because of its adverse chemical and physical properties. The fissile deposition thickness and the geometry of where the fission fragments are collected determine the pulse height spectrum to be expected from the fission chambers. The double-humped fission fragments energy spectrum shown in Fig. 5.6(a) appears for deposition that is very thin compared with the fragment ranges. This is observed, with light and heavy fragment distributions peaking at about 100 and 70 MeV respectively. Increasing the deposition thickness reduces the average range of the fission fragments and distorts the shape of the measured distribution. The expected change in the spectrum shape as the thickness of the deposition of $UO_2$ increases is shown in Fig. 5.6(b). The energy-loss effects limit the practical deposit thickness to about 2-3 mg·cm$^{-2}$ of highly enriched $^{235}$U [Kah65] and the corresponding detection efficiency in $2\pi$ counting geometry is about 0.5% at thermal energy, dropping to about 0.1% at 0.5 eV. Typical fission chambers employ a single layer, and are thus limited to an equivalent neutron detection efficiency. However, more advanced fission chambers with a higher detection efficiency are designed by providing multiple layers of fissile deposits and detecting fragments in each segment of the chamber between the layers [Val85, Dou05, Gio96].

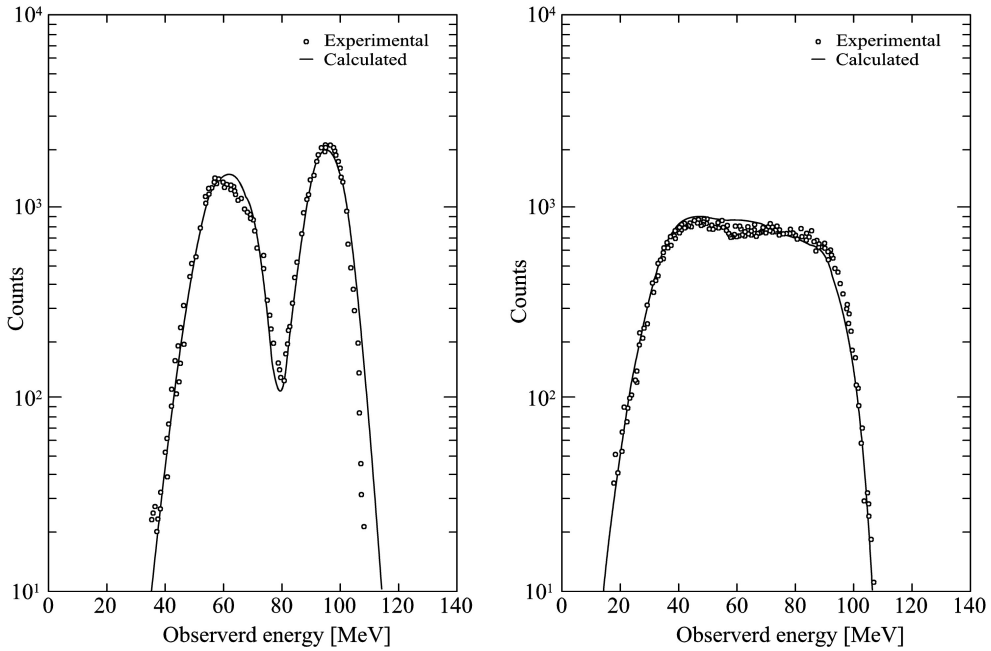


**Figure 5.6:** The fission fragments energy spectra from $UO_2$ deposits of two different thicknesses: (a) deposit thickness = $2.86 \times 10^{-2}$ mg·cm$^{-2}$, (b) deposit thickness = 1.30 mg·cm$^{-2}$, [Kah65].

These neutron detectors are made with dual fission chambers that have extremely thin backing material underneath a thin fissile deposit to allow both fission fragments to escape into opposite halves of a dual fission chamber. As a result, the simultaneous detection of both fission fragments from the same event can be achieved. Since the fissile materials contain $\alpha$-emitting isotopes, the background caused by $\alpha$-particles will appear at low energies. These $\alpha$-particles are emitted with energies of about 5 MeV, whereas the energy from the fission fragment is an order of magnitude higher. Thus, to eliminate the $\alpha$-particle background, the threshold setting of the electronics must be set higher than the $\alpha$-induced signal. However, some of the low-energy pulses from the fission fragments will be lost. There is more $\alpha$-particle activity in plutonium than in uranium, hence the threshold must be set higher for the plutonium-lined fission chambers . Fission chambers have the lowest sensitivity to $\gamma$-radiation $10^6$ R·h$^{-1}$ than any other neutron detector, which is due to the fact that fission fragments deposit a large amount of energy in the detection medium compared to $\gamma$-ray events. Fission chambers are used in nuclear reactors to perform direct unshielded neutron measurements of spent fuel. Fission chambers have inherently low detection efficiency, however the large fission cross-section and number of neutrons available for counting balances the effect. The sensitivity of a fission chamber is defined as

$$S = (\pi dLt)N\sigma_f \left(1 - \frac{t}{2R_f}\right), \tag{5.2}$$

where $d$ is the diameter of the cylindrical fission chamber, $L$ is its length, $N$ is the nuclear density of the fission material, $t$ is the thickness of the fission material coating, $\sigma_f$ is the microscopic fission cross-section and $R_f$ is the range of the fission fragments in the coating. For a typical chamber, enriched to 93% of $^{235}$U with $d = 25$ mm, $L = 20$ cm and coated with 1 $\mu$m $UO_2$ with $N = 2.33 \times 10^{23}$ atoms·cm$^{-3}$, $R_f = 15$ $\mu$m, $\sigma_f = 536$ b for neutrons of energy $E = 0.025$ eV, the thermal neutron sensitivity is equal to 0.18 cps/n·cm$^{-2}$·s$^{-1}$ (cps = counts per second). The sensitivity can be changed by changing the coating of the fission material or the nuclear density.

## 5.3 Scintillation detectors for neutron detection

In general, scintillator detectors have a high density detection medium which offers a higher neutron detection efficiency than gas filled detectors. This detection medium can be in the form of solid (plastic or glass) or liquid material and their atoms are easily excited during the interaction with secondary charged particles. The excited atoms emit visible light when they de-excite to their ground state. Materials such as crystals of lithium iodide and certain plastics are commonly used as scintillators. These materials are attached to one end of a photomultiplier tube, and the photons emitted by the scintillator are converted into an electric signal which is sent to an electronic counter. Scintillator detectors are ideal for current mode type applications where the neutron flux is too high to resolve individual pulses.

Plastic or liquid scintillators that use proton-recoil interaction are mostly used for fast neutron detection because they are quick to respond during irradiation and affordable. Plastic scintillator detectors are mostly used for coincidence counting measurents because the discrimination between the real and the accidental events can be easily achieved. For fast neutron detection applications, the coincidence resolving time is usually in the range of tens of nanoseconds from the sample to the detectors, while for a system that moderates the fast neutrons before detection, the resolving times of a coincidence counting system is in the range of tens of microseconds, which is the time required for thermalization. The organic scintillators have high $\gamma$-ray sensitivity, which is a disadvantage when they are employed for neutron counting in a high radiation field. Detection probabilities for neutrons and $\gamma$-rays are comparable, and the resulting pulse-height spectra from monoenergetic radiation of both types are broad and overlapping. The pulse resolution is not sufficient to discriminate between neutron and the $\gamma$-ray signals.

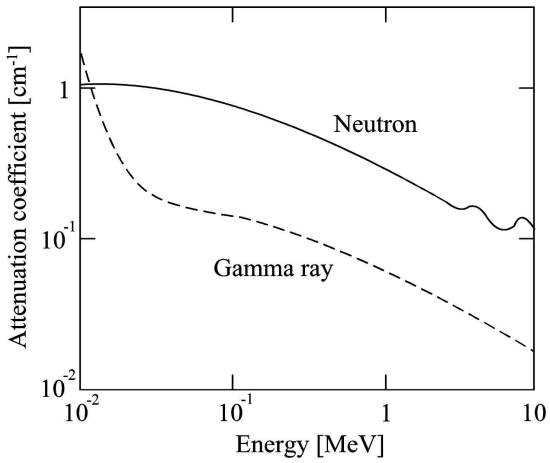


**Figure 5.7:** The neutron and $\gamma$-ray attenuation coefficient as a function of incident energy in an NE213 scintillator, redrawn from [Cra70].

### 5.3.1 Fast neutron measurements with scintillator detector

Fast neutrons interact in a scintillator detector through scattering with hydrogen or carbon nuclei, but the most useful scintillator light comes from recoiling hydrogen nuclei. This occurs because the neutron mass is similar to the proton mass, thus a neutron transfers all of its kinetic energy in head-on elastic scattering interactions to a recoiling proton in the forward direction. The scintillation light is collected and converted to an electronic pulse whose magnitude is proportional to the kinetic energy of the recoiling hydrogen in a photomultiplier tube, which is optically coupled to the scintillator. A good scintillating material should have the characteristics such as a relatively high efficiency for converting recoiling nuclei energy to fluorescent radiation, high transparency to its own radiation, and good matching of the fluorescent light spectrum to the photomultiplier tube response. Several scintillators are commercially available for fast neutron measurements, such as NE102 and NE213, which adequately satisfy these criteria. Although the mechanism by which the kinetic energy of the incident fast neutrons is transfered to protons in an organic scintillator is similar to that in a hydrogen recoil proportional counter, the overall detection process is different. The difference is in the physical properties of organic scintillators and gases. This is because the density of the organic scintillator is of the order of unity whereas that of the proportional counter is of the order of $10^{-3}$ g·cm$^{-3}$. This implies that the probability of interaction for both neutrons and $\gamma$-rays will be substantially higher in the scintillator than in the gas filled proportional counter.

As shown in Fig. 5.7, the interaction probability in NE213 scintillator depends on the energy of the neutron and $\gamma$-ray. It can be seen that the in-

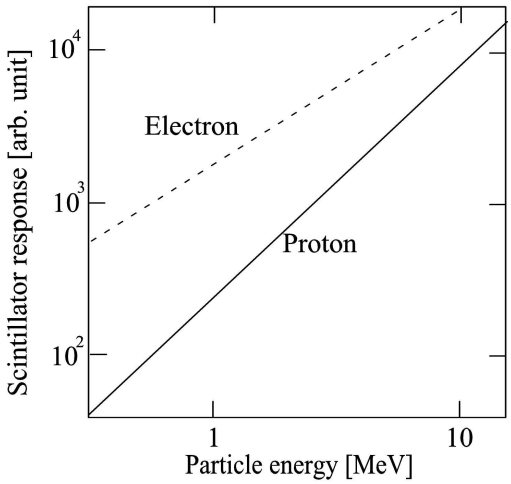


**Figure 5.8:** Scintillation light yield as a function of particle energy for electrons and protons in an NE 102, redrawn from [Kno00, Cra70].

teraction probability for neutrons in this scintillator is higher when compared to that of $\gamma$-rays of the same energy. Since the particles travel longer in a less dense material, such as gas, the ranges of the recoiling protons and electrons from photon interactions will be substantially shorter in the scintillator than in the gas filled detector. The events occurring near the boundaries of the detectors, are of less important in the scintillator detector than in gas-filled detectors where the wall-effect appears in the pulse shape spectrum. High-energy electrons from the photon interaction can stop inside the detector volume and this can have an effect in the pulse shape spectrum. In addition, recoiling electrons and protons of the same initial energy can produce different amounts of light in a scintillator, which is caused by the different ionization densities along the slowing-down paths. As shown in Fig. 5.8, the light output for protons is always less than that for electrons of the same energy. In some cases, the scintillation efficiency may be independent of energy, leading to a dependence of the light yield on initial energy.

#### 5.3.1.1 Pulse-shape discrimination in liquid scintillator

In a liquid scintillator, the process of transforming the kinetic energy of the recoiling particles into visible light is complex. This is because the decay times of the major components of the scintillator light, called the prompt fluorescence, is of the order of a few nanoseconds. It also represents most of the observed scintillation light and in principle, liquid scintillators can operate at very high counting rates. However, a longer lived component of the scintillator light, which has a decay time of several hundred nanoseconds is also observed in many cases, corresponding to delayed fluorescence. As a result, the total light output can often be represented by the sum of two exponential decays, referred

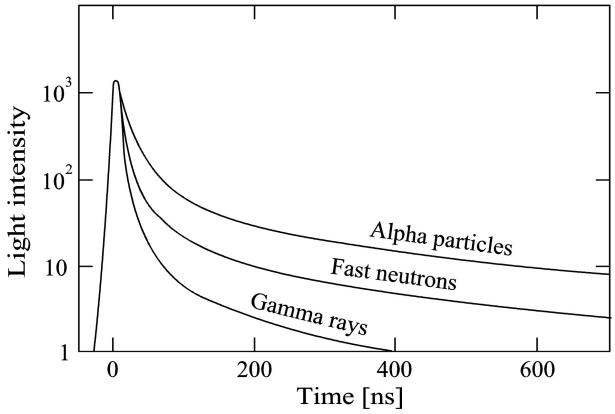


**Figure 5.9:** The time dependence of scintillator pulse in stilbene when excited by different incident particles types, redrawn from [Bol61].

to as the fast and slow component of the scintillation. Depending on the type of particle, either electron or proton, that has induced the radiation, the fraction of the total light observed in the slower component will vary. Heavier particles, such as protons, have a higher specific ionization and produce more delayed fluorescence light. In Fig. 5.9, the time dependence of the organic crystal scintillator pulse when excited by radiation of different types is shown. This time dependence makes it possible to identify particles by looking at the rate of energy loss, $dE/dx$ but producing the same amount of light in the scintillator.

### 5.3.2 Slow neutron measurements with a scintillator detector

Slow neutrons can be measured with a scintillator detector containing $^6$Li material. This detector is commonly used because of the large $Q$-value for the $^6$Li(n,$\alpha$)$^3$H reaction, which offers some advantages when it comes to the discrimination against $\gamma$-ray background and other low-amplitude events. For slow neutron interactions, this reaction also proceeds exclusively to the ground state of the product nucleus, and the energy is always shared between the $\alpha$ and tritium particles.

Lithium-containing scintillators are manufactured in the form of crystalline lithium iodide, LiI. The crystals are generally large compared to the ranges of either of the neutron-induced reaction products. Therefore, the pulse height response will be free of wall effects and the spectrum will show a single peak for slow neutron interactions. The range of secondary electrons produced by $\gamma$-rays will not be large compared with typical crystal dimensions. The scintillation efficiency for lithium iodide is nearly the same for both electrons and heavy charged particles. For example, a 4.1 MeV electron will yield about the same light as the 4.78 MeV reaction products. Therefore, a single $\gamma$-ray interaction

in LiI is capable of producing a maximum pulse height approximately proportional to the energy of the $\gamma$-ray, whereas each neutron interaction produces a pulse equivalent to 4.1 MeV on the same scale. The $\gamma$-ray discrimination characteristics are lower than those of typical gas-filled neutron detectors, in which a $\gamma$-ray can only deposit a small fraction of its energy. The $^6$LiI scintillator is very hygroscopic and has to be used in an hermetically sealed assembly [Syn04] to avoid exposure to water vapor. If a small amount (less than 0.1%) of europium is added as an activator to LiI, light output of about 40% of the equivalent NaI(Tl) yield can be achieved [Syn04]. The scintillation decay time is approximately 0.3 $\mu$s [Nic55]. The intrinsic efficiency of the $^6$Li(Eu) crystal for neutron capture can be expressed by the formula

$$\epsilon = 1 - \exp(-n\sigma x), \tag{5.3}$$

where $n$ is the number of $^6$Li atoms per unit volume, $\sigma$ is the neutron capture cross-section, and $x$ is the thickness of the detector. The high density nature of the Li scintillator makes it possible to design small sized detectors with efficiencies of 25 to 100% for thermal neutrons. For example, a 10 mm thick crystal prepared from highly enriched $^6$LiI remains nearly 100% efficient for neutrons with energies from thermal to 0.5 eV [Ale03]. A $^6$LiF/ZnS:Ag scintillator with a thickness of 0.42 mm has also achieved a 100% effiency for thermal neutrons [Bae02]. Because of their small thickness, $\gamma$-ray discrimination is very effective, since a large fraction of the $\gamma$-rays and secondary electrons created by $\gamma$-ray interactions will escape without depositing their full energy. The ratio of the light yield in thermal neutron detection to that in $\gamma$-ray detection decreases with temperature [Yuk11] for lithium glass scintillators. This decrease in the relative light yield of neutron detection may be caused by a reduction in the numbers of the excited electrons which contributes to the scintillation luminescence. Other modern lithium-loaded glass scintillators are made from various mixtures of $LiO_2$, $Al_2O_3$, $Ce_2O_3$ and $SiO_2$ [Bro86].

## 5.4 Neutron detector for reactor measurements

A large amount of the nuclear energy generated in thermal reactors is through the nuclear fission process induced by slow neutrons. Hence, to monitor the reactor, a neutron detection system that measures the thermal neutron flux must be part of reactor control safety systems. In principle, some of the detector types detailed earlier in this chapter can be adapted for the purpose of reactor measurements. However, the extreme conditions (high radiation, temperature and pressure) associated with a reactor at full operation often lead to substantial changes in the detector design. The slow neutron detector design specifically for reactor environment applications has gradually evolved to adapt to reactor conditions.

In principle, the reactor instruments can be divided into two categories: *in-core* and *out-core* systems. In-core detectors are small devices located within the narrow coolant channels or central reflector in the reactor core to provide detailed information about the neutron spectrum within the core. These sensors can be either fixed in one location or brought inside by a movable drive. Out-core detectors are larger in size compared to in-core detectors and are placed either inside or outside the reactor pressure vessels. In this reactor area, the environmental conditions are much less severe compared to those inside the core. These out-core detectors respond to properties of the neutron flux integrated over the entire core.

The majority of neutron detection systems for reactor applications are of the gas-filled type because of their inherent $\gamma$-ray discrimination, wide dynamic range, long-term stability and resistance to radiation damage. Detectors based on scintillation process are less suitable because of the enhanced $\gamma$-ray sensitivity of a solid or liquid scintillators. Semiconductors are very sensitive to radiation damage and are never used in reactor environments.

## 5.5 In-core neutron detectors

Neutron detectors that can provide information about the neutron flux profile within the core are of importance in ensuring the safe operation of the reactor. Much emphasis is placed on compactness and miniaturization of the detectors because of the small space about 7 cm in which it must be located in the core. These detectors are either fitted to a motorized drive to enable them to travel through the reactor or fixed to the center core. Some may provide a continuous readout, whereas others provide a readout only at periodic intervals. Typical operating conditions depend on the type of reactor, whether it is a conventional water or high temperature gas-cooled reactor. This has been described earlier in Chapter 2, section 2.4.

### 5.5.1 Review studies of in-core neutron detectors

Neutron detectors that have the ability to perform real-time measurements within the core where the operating conditions are characterized by intense radiation fields and high temperature are required to monitor and ensure safe operation of the reactor. A few neutron detectors that have some of these characteristics were developed recently. The following review provides background information regarding the development of high flux neutron detectors, their strength and limitations with respect to in-core reactor measurements.

#### 5.5.1.1 Micro-Pocket Fission Detector

A Micro-Pocket Fission Detector (MPFD) is a gas-filled neutron detector developed to monitor the power level, slow and fast neutron flux profile in real-

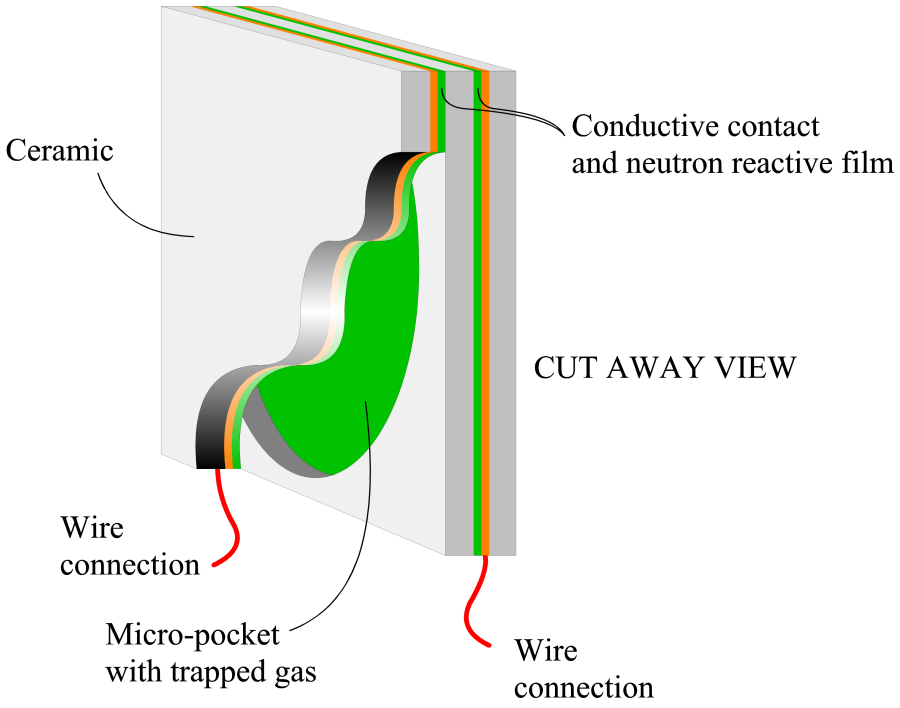


**Figure 5.10:** A schematic diagram of the micro-pocket fission detector (MPFD), redrawn from [Dou05].

time within a nuclear reactor [Dou05]. As seen in Fig. 5.10, the detector is made from the ceramic aluminum oxide or oxidized silicon materials with a diameter of 4 mm and height of 2 mm and, a gas pocket with diameter of 3 mm and height of 1 mm. The opposite sides of each gas pocket are coated with a conductive layer followed by a neutron reactive film for converting neutrons to charged particles. The design makes use of a neutron reactive material such as $^{235}$U, $^{232}$Th, $^{10}$B or some material containing $^{6}$Li, confined within a gas pocket filled with methane based P-10 gas. The fission products from neutron induced events enter the gas pocket and ionize the gas molecules to form electron ion pairs which produce a current that is recognized and measured by sensitive external electronics.

The device is operated in the same way as the other gas filled detector described earlier, but here the voltage is applied across the gas chamber. Because the stopping power of electrons in a gas is substantially lower than the stopping power of fission fragments, the charge-induced signals are significantly larger for fission fragments than for recoil electrons in the MPFD. Special insulation material is used to seal the connecting wires from the device to the power supply and for taking information to the computer and also to ensure that no gas

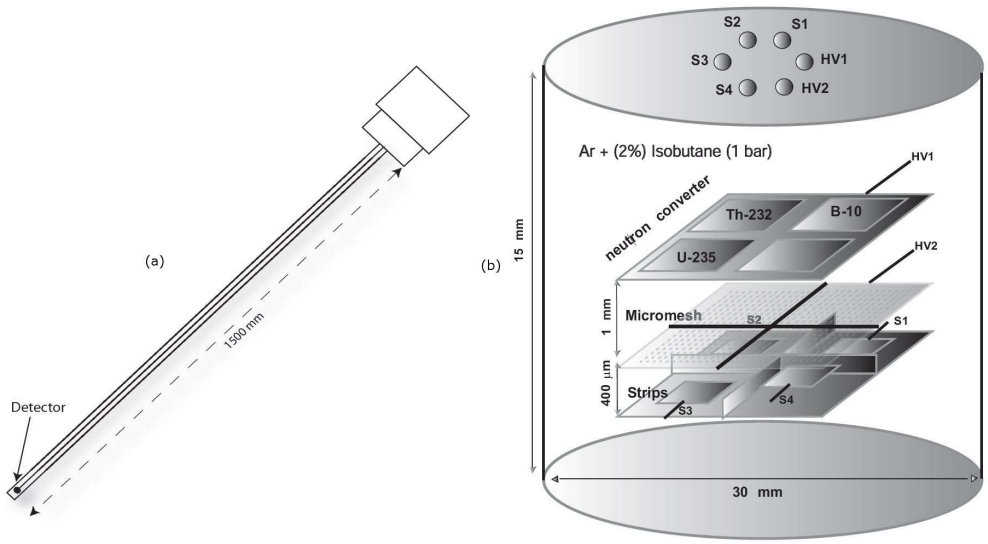


**Figure 5.11:** The schematic representation of the PICCOLO neutron detector which is based on the MICROMEGAS structure [Gio96].

leaks out. A high-temperature cement is required to seal the ceramic pieces.

The MPFD has a small size that enables them to be placed throughout the core for three dimensional mapping of the neutron flux profile in real-time. The MPFD has been tested in a thermal neutron beam port tangential to the Kansas State University (K-State) TRIGA (Training, Research, Isotopes, General Atomics) Mark-II research reactor and in the center of the core. When the device is placed within the center of the core, cables connecting the device to the preamplifier are extended from the reactor core up to above the water line. An aluminum tubes needed to be inserted to seal the cables from water leaks and to keep the electronics away from high radiation. Measurements of 15-min duration were performed with the reactor power incrementally changing in power from 1 mW up to 225 kW, and the thermal neutron flux at the detector location ranging from $10^3$ to over $10^{12}$ n·cm$^{-2}$·s$^{-1}$. Since the range of the thermal neutron flux in this reactor are low energy for the detector electronics to resolve individual pulses, the MPFD was operated in pulse mode for the entire test. The MPFD was found to be radiation hard and potentially capable of operating in a neutron fluence exceeding $10^{19}$ n·cm$^{-2}$ without noticeable degradation.

#### 5.5.1.2 PICCOLO in-core neutron detector

The PICCOLO in-core neutron detector is based on the MICRO MEsh GAseous Structure (MICROMEGAS) technology [Fan04]. As shown in Fig. 5.11 (a), the detector is placed in a 1500 mm long cylindrical chamber made of stainless steel with a 35 mm external diameter and 30 mm internal diameter. The

detector is held at the end of the chamber by a stainless steel rod. Inside the micromegas detection module are four micromegas detectors of 5 $mm^2$ with a common 30 $\mu$m thick stainless steel micromesh of 500 LPI (see Fig 5.11(b)). Six wires from the detector to the top of the chamber connect the four cathode pads, the micromesh and the drift electrode. The drift electrode is put on a ceramic piece with four holes, of which one is empty and three hold different neutron conversion materials. The three neutron conversion materials used in this device are $^{10}$B (50 $\mu g \cdot cm^{-2}$), $^{232}$Th (140 $\mu g \cdot cm^{-2}$) and $^{235}$U (50 $\mu g \cdot cm^{-2}$). The drift gap is 1 mm in the case of the 3 neutron converter materials whereas it is 3 mm for the empty one. The 160 $\mu$m amplification gap is fixed mechanically by a stainless steel piece with four holes.

Micromegas is composed of two stages separated by a micromesh: a drift or ionization space with a low electric field ($\approx$ 1 $kV \cdot cm^{-1}$), and an amplification space with a high electric field ($\approx$ 10 $kV \cdot cm^{-1}$) [Gio96]. Electrons produced from the ionization of the gas, drift toward the micromesh under the action of the low electric field. The detector can use both pulse mode when the counting rate is low, or current mode when the counting rate become too high for pulse mode.

The long cylindrical chamber can be placed inside an empty rod of a TRIGA (Training, Research, Isotopes, General Atomics)-type reactor for in-core measurements. The Piccolo detector has been tested inside the 1 MW TRIGA nuclear reactor of the ENEA center in Casaccia (Italy) sealed in for a duration of two weeks [Gio96]. The chamber was hermetically sealed at the top with watertight connections for the signals, the high voltages and the gas. The measurements were performed with the reactor operating at a power ranging from 10 W to 400 kW at two different positions (in the center and on the periphery) inside the reactor. At a reactor power of 100 kW, the $\gamma$-ray flux in the center of the core was about $10^9$ $\gamma \cdot cm^{-2} \cdot s^{-1}$ and the detector was operated in both pulse and current mode.

# Chapter 6

# Development of a high flux neutron detection system

From the review of the detectors described in section 5.5.1, one can conclude that the MPFD and MICROMEGAS neutron detectors are less suitable for use as in-core neutron detectors in the HTGR for a number of reasons. The power leads and signal cables from the device to the electronics require special insulation in order to survive the extremely harsh environment of the HTGR. The harsh conditions are the high temperature of 950°C, the pressure of 9 MPa, and the radiation flux of about $10^{14}$ n·cm$^{-2}$·s$^{-1}$, and the comparable flux of $\gamma$-rays. These detectors could, however, be placed outside, where the temperature and radiation levels are lower compared to inside the core. For the purpose of monitoring a reactor core like that of the HTGR, a special design of detector that does not require cables running from the reactor to the electronics could be a solution. Hence, this project investigates the feasibility of developing such a detector system. This is a high flux neutron detection system that incorporates a mass analyzer to quantify certain reaction products from neutron-induced break-up reactions for slow and fast neutron flux measurements.

## 6.1 Description of the high flux neutron detection system

The newly developed high flux neutron detection system, shown in Fig. 6.1, consists of:

- A reaction chamber which is the stainless steel container, either for $^{6}$Li or $^{12}$C neutron converting materials,
- An evacuation stainless steel pipe where a gas flows through from reaction chamber to the mass analyzer,

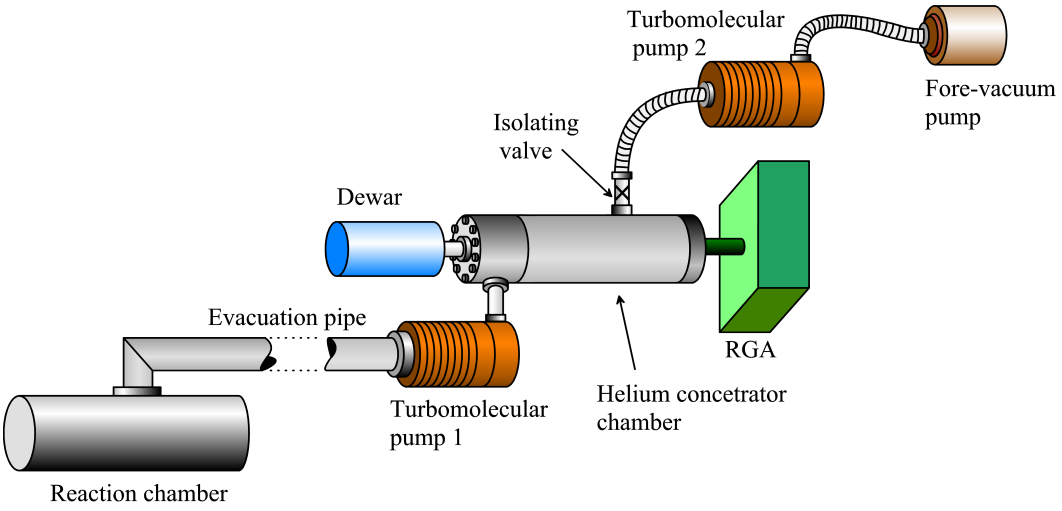


**Figure 6.1:** A schematic diagram of the high flux neutron detection system setup.

- The vacuum pumps which evacuate the gas molecules from the vacuum chamber and maintain a low pressure of residual gas,
- The cryogenic traps which remove the gas impurities in the vacuum system and,
- The Residual Gas Analyzer (RGA) which analyzes the gas in the vacuum system.

This system is capable of measuring a high flux of slow and fast energy neutrons, by filling the reaction chamber with a neutron conversion material sensitive to either slow or fast neutrons, separately. For both energy ranges, the mechanism of converting neutrons into charged particles is similar. Neutrons induce break-up reactions in the reaction chamber, where $^4$He nuclei ($\alpha$-particles) are emitted as decay products. The $\alpha$-particles, in turn, will capture electrons to form $^4$He atoms, which diffuse and move out in the form of a gas to be later quantified by an RGA and hence, the information about the neutron flux can be derived.

Irrespective of the neutron energy range, either slow or fast neutrons, that needs to be measured, the experimental setup down-stream of the reaction chamber is the same. The $^4$He atoms created in the reaction chamber will diffuse and move out with the help of a pressure gradient provided by a turbomolecular pump in combination with a dry backing scroll pump through a 4 m long and 0.07 m diameter evacuation pipe. The two pumps first evacuate the reaction chamber and the evacuation pipe in order to have a minimum background of other gases that are not of interest. A cryogenic trap filled with a molecular sieve essentially freezes out the water vapour and adsorbs gas impurities present in the vacuum system. The mass spectrometer (RGA) is employed to measure the gases flowing out of the reaction chamber into the

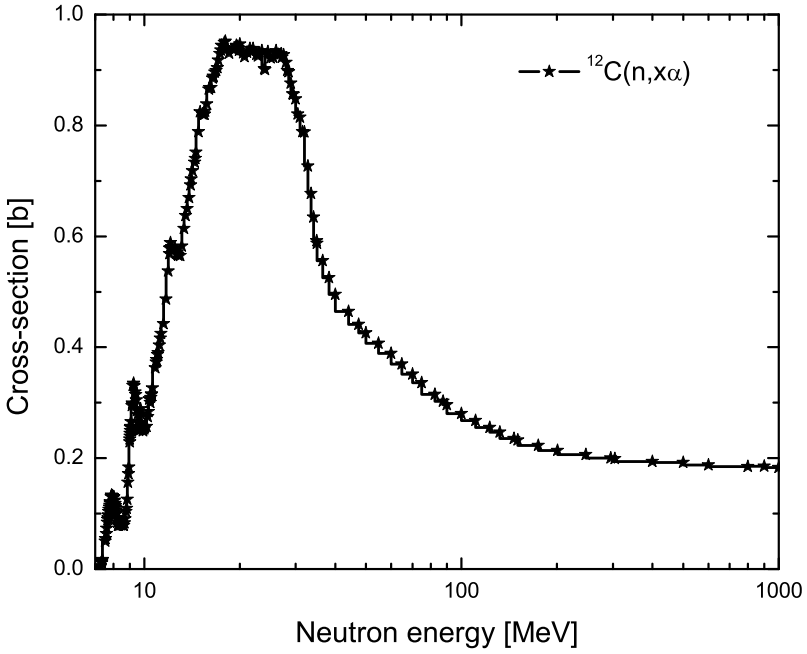


**Figure 6.2:** The total cross-section data for $\alpha$-production with neutrons on $^{12}$C material, [NNDC].

vacuum, and is placed after the cryogenic trap. The position of the mass spectrometer close to the cryogenic trap is preferred because of reduced impurities in the $^{4}$He gas to be quantified

### 6.1.1 Fast neutron detection

Fast neutrons with an energy of 7 MeV and higher are measured in the high flux neutron detection system through $^{12}$C(n,n′$\alpha$)$^{9}$Be and $^{12}$C(n,n′)3$\alpha$ reactions. In the total cross-section data of the $^{12}$C(n,n′$\alpha$) reaction shown in Fig. 6.2, it can be seen that the threshold energy for $\alpha$ production in $^{12}$C is 7 MeV. This implies that neutrons with energies equal to or greater than the threshold energy will potentially produce one or more $\alpha$-particles in the reaction chamber.

The reaction chamber shown in Fig. 6.3 is a leak-tight stainless steel container, 60 cm long and 10 cm in diameter, filled with 1 kg of graphite for the conversion of neutrons into $\alpha$-particles. This graphite, 96.5% carbon, is in the form of a fine powder, with 5 $\mu$m grain size, and a bulk density of 0.2 g·cm$^{-3}$. It was supplied by Graphit Kropf*ü*hl AG [Gra10]. There are several factors that have influenced the dimensions of this reaction chamber and the quantity of the graphite powder. With the density at 0.2 g·cm$^{-3}$, it was calculated and

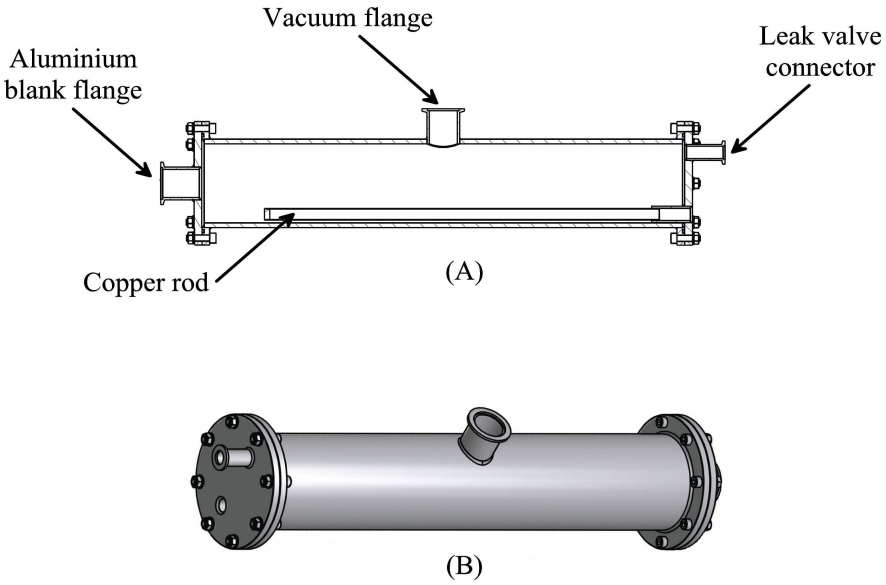


**Figure 6.3:** The carbon reaction chamber consisting of a $600 \times \varnothing 100$ mm stainless steel container filled with 1 kg of graphite powder.

verified that the average mean-free path of the fast neutrons in this powder is about 50 cm, the $^{12}$C(n,n′$\alpha$) reaction cross-section is relatively small (less than 1 b), intensity of the secondary neutron beam available at the iThemba LABS facility is about $10^{10}$ n·s$^{-1}$. As a result, the reaction chamber was placed in such a way that the 60 cm length was along the neutron beam axis. This increases the probability of fast neutron interactions as they traverse through the powder, which in turn maximizes the $^4$He atoms production.

## 6.2 Characteristics of the high flux neutron detection system

The detection systems for monitoring the neutron flux in a reactor core where there is a high flux of fast neutrons and $\gamma$-rays, as well as high temperature and pressure, should be stable in situ for a long period of time. The detector should also have high sensitivity to the neutron energy range, either slow or fast neutrons, be insensitive to $\gamma$-rays and perform real-time measurements. These are some of the characteristics required for a high flux neutron detector and what follows is a short discussion of these characteristics.

### 6.2.1 Neutron detector stability

The high flux neutron detector is designed specifically for a reactor environment like that of the PBMR. For this reason, the reaction chamber to be

exposed to high radiation is built from radiation-hard material, such as nuclear grade stainless steel. The advantage of using stainless steel is that of low activation with a high neutron flux but a low perturbation to the intensity of the neutron flux. Stainless steel material is also rigid, with a low deterioration rate in high-radiation environments. It can also be used as a vacuum chamber, because it has very little out-gassing under a high-vacuum system. This design makes the detector suitable for long exposure time in the high neutron flux environment.

### 6.2.2 Neutron flux detection modes

The high neutron flux detection system is adapted to measure high intensity neutron beam, $10^{12}$n·s$^{-1}$, in current modes whereas the accumulation mode is employed to measure the lower intensity neutron beam between $10^{10}$n·s$^{-1}$ and $10^{12}$n·s$^{-1}$. The weak signal from the low neutron flux is strengthened by accumulating the $^{4}$He gas produced while irradiating the reaction chamber. In the schematic diagram shown in Fig. 6.1, the isolating valve, denoted by a symbol x, is fitted in the detection setup in order to allow the accumulation mode. This is done by closing an isolating valve and allowing the partial pressure of $^{4}$He gas to build-up inside the helium concentrator chamber. The current mode is the direct through-flow neutron flux measurement method. This is done by measuring the $^{4}$He gas produced with the isolating valve open and the turbomolecular pump at the exhaust of the concentrator allowing continuous streaming through the evacuated system.

### 6.2.3 Sensitivity to neutron energy range

The future intention is to incorporate the slow and fast neutron detectors into HTGR reactors to indirectly monitor the temperature by measuring and characterizing the neutron flux profile within the core. As shown in Fig. 3.6, the neutron energy spectrum can be divided into three components. Fig. 3.7 shows that the slow neutron component flux varies relative to the fast neutron component flux as a function of the temperature. This means that the high flux neutron detection system has to be sensitive to slow and fast neutron energy ranges to efficiently monitor the in-core flux. Hence, the method of using multiple detectors with different energy detection efficiencies is employed. Neutron converter materials, $^{6}$Li and $^{12}$C, are used in the lower and higher energy ranges respectively. Measuring the absolute neutron flux in the slow and fast regions and deducing the ratio can inform on the average temperature of the fuel particles.

### 6.2.4 Insensitivity to $\gamma$-radiation

Unlike the gas-filled and scintillator detectors, mentioned in Chapter 5, which use the neutron detection technique of ionizing the detection medium and excitation of molecules that emit visible photons while de-exiting, the high flux neutron detection system measures the reaction products in the form of a gas with a mass analyzer.

The high flux neutron detection system is expected to be insensitive to $\gamma$-rays as the photodissociation of $^{6}$Li and $^{12}$C nuclei has a much lower cross-section compared to neutron-induced break-up reactions. The products that are in the form of a $^{4}$He gas are uniquely quantified using an RGA.

As shown in Fig. 4.11, the cross-section of the neutron-induced break-up $^{6}$Li(n,$\alpha$)$^{3}$H reaction is 1000 b at an incident neutron energy of $2.5 \times 10^{-2}$ eV and drops to 0.085 b at an energy of 5 MeV, whereas the photodissociation cross-section of the $^{6}$Li($\gamma$,np)$^{4}$He reaction, as shown in Fig. 6.4, with an energy threshold of about 5 MeV, corresponding to the cross-section of 0.3 mb [Ber65]. Thus, the neutron-induced reaction in the slow energy range on $^{6}$Li dominates the $\gamma$-induced reaction. This makes the slow neutron detection system to be about seven orders of magnitude less sensitive to $\gamma$-rays with energy greater than 5 MeV than for neutrons and absolutely insensitive to $\gamma$-rays with energy less than 5 MeV.

The total $\alpha$ production neutron cross-section on $^{12}$C is shown in Fig. 6.2 with an energy threshold energy of 7.5 MeV. The $^{12}$C($\gamma$,3$\alpha$) reaction cross-section has been measured by Garnier *et al.* [Gar60]. They found that $\sigma = 0.044 \pm 0.011$ mb at 14 MeV and increases to $0.19 \pm 0.021$ mb at 17.6 MeV. The $^{12}$C(n,x$\alpha$) reaction cross-section within the fast neutron energy range is about four orders of magnitude higher than the cross-section of $^{12}$C photodissociation. The energy threshold for $\gamma$-ray is very high $E_\gamma > 7$ MeV, and the flux of such $\gamma$-rays is expected to be very low compared to the fast neutron flux.

The high neutron conversion cross-section and the detection technique of the reaction products makes the high flux neutron detection system to be insensitive to $\gamma$-rays.

### 6.2.5 Real-time data reading system

A real-time response of the neutron detector is required to monitor the change of the reactivity in the reactor core, since this change can occur over relatively short periods of time. A high flux neutron detection system must be able to respond rapidly to a change in neutron flux incident on the reaction chamber. The quantity of the reaction products will be used to determine the reaction rate and to deduce the neutron flux. The high flux neutron detector is developed to offer an immediate reading of the neutron flux and can be used as a real-time monitoring device of the slow and fast neutrons in the core.

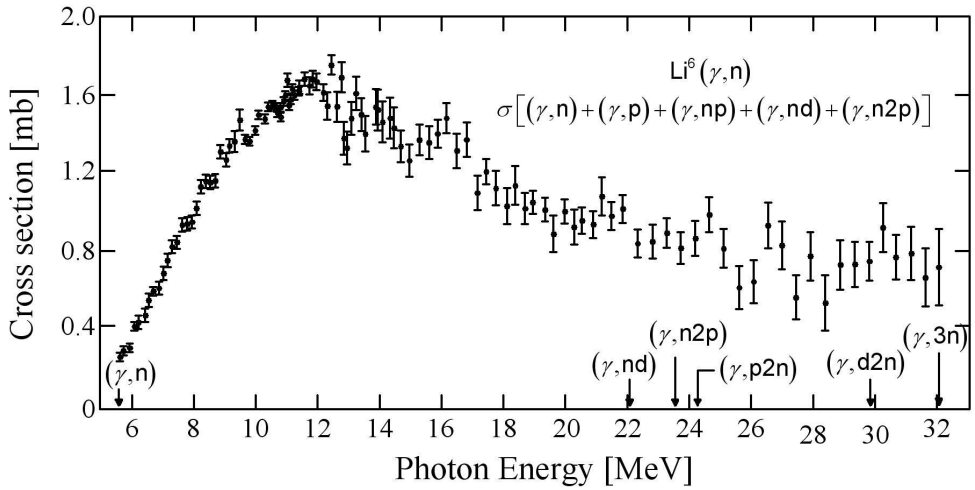


**Figure 6.4:** The photodissociation cross-sectional data of $^{6}$Li($\gamma$,np)$^{4}$He reaction, as a function of photon energy, [Ber65].

### 6.2.6 Radiation damage to the detector

It is well known that the electronic components are very sensitive to neutron radiation and cannot work for long periods in a high-radiation environment. To overcome this problem, the reaction products are transported from the reaction chamber to an RGA through an evacuation pipe. The length of the pipe from the reaction chamber to the electronics can be adjusted. The electronic components can be placed at a large distance from the neutron source and consequently can also be shielded easily. As long as the reaction chamber containing $^{6}$Li and $^{12}$C materials keep its integrity, there is no defined lifetime of the detector in a reactor environment, or practical limit in terms of the flux and can be many orders of magnitude greater than $10^{14}$ n·cm$^{-2}$·s$^{-1}$.

## 6.3 Components of the high flux neutron detection system

In the high flux neutron detection system, the reaction products are allowed to diffuse out of the conversion material and are measured with an RGA. The measurements are expected to be performed under high vacuum, which minimizes the ion-molecule reactions, scattering and neutralizing the ions of interest. With the reduced background, the products from neutron-induced reactions are measured efficiently. This is achieved by using vacuum pumps and cryogenic traps to create vacuum space, and an RGA to measure the the partial pressure of the reaction products and of the residual gas.

### 6.3.1 Vacuum pumps

For the test measurements, the partial pressure of $^4$He is expected to be within the detection limit of an RGA. Therefore, it is necessary to remove other gas molecules from the vacuum chamber and to maintain the pressure of the residual gas as low as possible. Achieving and maintaining the low pressure will depend upon the matching of the gas loads and the pumping speed of the vacuum pump used. The pumping speed is of importance because it determines the quality of the high vacuum. High pumping speed is required to obtain lower pressures. The positive-displacement fore-vacuum and a high vacuum turbomolecular pump were used for evacuating and creating a high vacuum space (reaction chamber and the pipe) respectively. Using these two pumps for evacuating the 20 L system for several days, a total pressure of about $1.0 \times 10^{-5}$ mbar was achieved. The pressure was measured with the vacuum meters installed at the opposite side of the pipe. The mass spectrum of the partial pressure of the residual gas was measured.

#### 6.3.1.1 Positive-displacement fore-vacuum pump

The positive-displacement fore-vacuum pumps have the highest performance for removing gas molecules from the leak-tight vacuum system at atmospheric pressure. However, the speed declines sharply as the pump begins to achieve its lowest attainable pressure of $10^{-2}$ mbar. Such pressure is required by the turbomolecular pump which operates at much lower differential pressures. In this work, an oil-free positive-displacement pump was used to fore-vacuum the system. The vacuum is then created by reducing the volume of the trapped environment and compressing the gases to an exhaust. The positive-displacement pumps are more efficient in evacuating or compressing molecules, irrespective of their mass, than what turbomolecular pumps are.

The dry pump is preferred over the oil pump because it eliminates the possibility of backstreaming pump oil into the vacuum chamber. This pump oil can dissociate into molecules and atoms of lighter masses, such as hydrogen and carbon, causing a background increase in the lighter mass region of the spectrum.

#### 6.3.1.2 High vacuum turbomolecular pump

The creation of high vacuum with a turbomolecular pump begins at a reduced pressure of about 1 mbar and, if operated at a pressure higher that this value, the blades of the pump might be damaged as the torque applied on the high speed motor would be too high. A turbomolecular pump is a type of momentum-transfer vacuum pump. In a turbomolecular pump, gas molecules are accelerated from the chamber to the exhaust by high-speed rotating blades. As shown in Fig. 6.5, the turbomolecular pumps consist of two types of blades, namely rotating and fixed disks, called rotors and stators, respectively. The

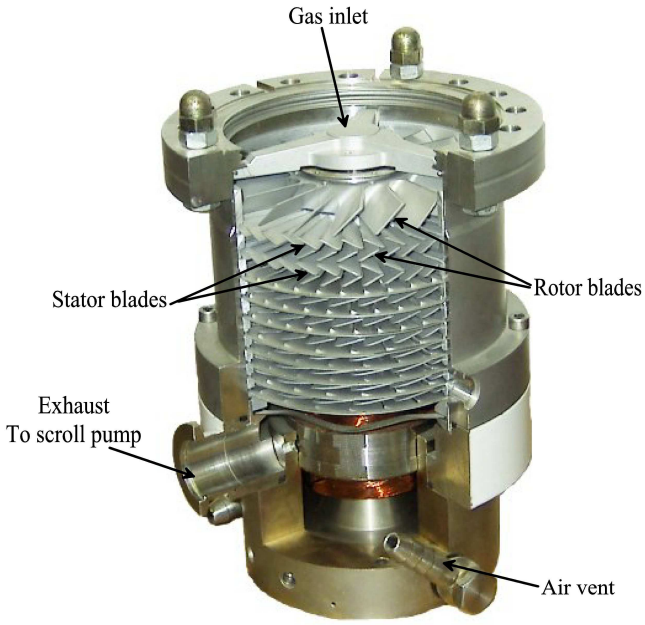


**Figure 6.5:** The cross-sectional cut of the Pfeiffer turbomolecular pump, showing the different types of blades, adapted from [Wiki11].

rapidly rotating rotor blades (9 000-90 000 rpm) hit gas molecules from the inlet of the pump and accelerate them towards the exhaust in order to draw the molecules towards the backing pump and create a vacuum space.

The physics of elastic collisions can be used to model the operation of the turbomolecular pumping. The gas molecules gain the momentum when they collide with the fast-moving blades of the turbomolecular pump, and leave through the exhaust at a high speed. If the velocity of the blade is $\vec{V}_b$ and that of the molecule is $\vec{V}_m$, then the final velocity of the molecules after the collision will be $\vec{V}_m + 2\vec{V}_b$, considering that the molecule velocity is normal to the blade and initially towards it. The rate of pumping for a particular gas is directly related to the fractional increase in its momentum as a result of colliding with the blade. Hence, the pumping rate is proportional to $2\vec{V}_b/\vec{V}_m$. If $\vec{V}_m > \vec{V}_b$, then the pumping efficiency will fall off rapidly. The average kinetic energy of the gas molecules $\bar{E}_{\text{kin}}$, is determined by

$$\bar{E}_{\text{kin}} = \frac{3}{2}kT = \frac{1}{2}m\vec{V}^2_{\text{rms}}, \tag{6.1}$$

where $k$ is the Boltzmann constant, $T$ is the temperature, $m$ is the mass of the molecule and $\vec{V}_m$ is the velocity of the molecule. Since $\vec{V}_{\text{rms}} = \sqrt{\frac{2\bar{E}_k}{m}}$, lighter molecules will have a higher $\vec{V}_{\text{rms}}$ and, as a result, the pumping efficiency of the turbomolecular pump drops off rapidly. For example, the TPH-170 turbomolecular high vacuum pump [Pfe10] used in this work has a pumping speed of 170 L/s for $N_2$, 130 L/s for $^4$He and 110 L/s for $H_2$. The compression

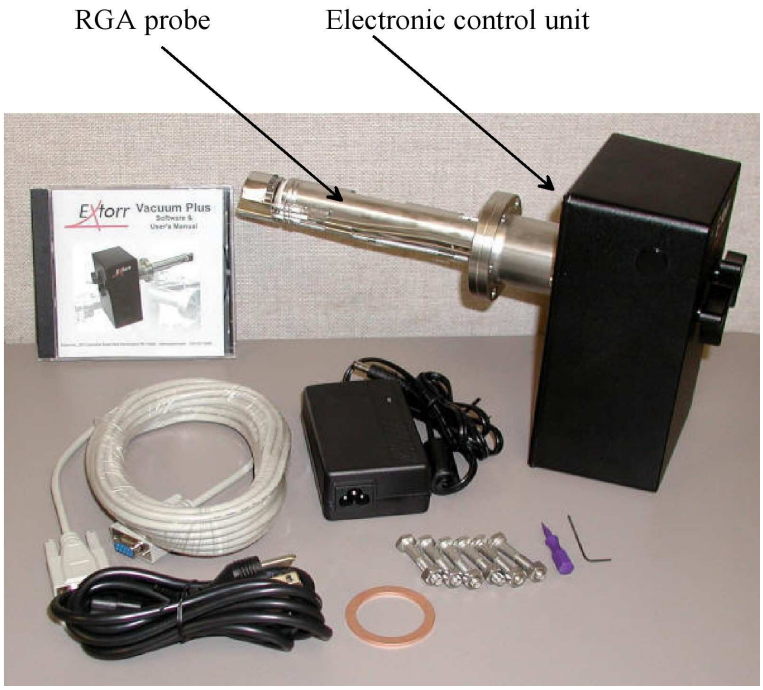


**Figure 6.6:** The complete Extorr package of the RGA used in the present work, [Ext11].

ratio of different species of gas with this kind of pump will also depend on the mass of the molecules. This refers to a measure of the differential pressure between the outlet and inlet sides of the pump. This turbomolecular pump has a compression ratio of $8 \times 10^8$ for $N_2$, $2 \times 10^4$ for $^4$He and $1.1 \times 10^3$ for $H_2$. The differences in compression ratio for the various gases is understood, qualitatively, by comparing the most probable velocity for He (1300 m/s) and $N_2$ (500 m/s) at $T = 300$ K with the tangential velocity of a 15 cm diameter turbo rotor rotating at 43 000 rpm. To improve the pumping of these lighter molecules a cryogenic trap, which is more efficient, was employed.

### 6.3.2 Residual gas analyzer

The Extorr RGA components used in the present work are shown in Fig. 6.6. The RGA is a mass spectrometer that analyzes the gas species in a vacuum by measuring the current of ions in a mass range from 1 to 200 amu. As seen in the image of the Extorr package, the RGA system includes the analyzer probe, which is fitted inside the vacuum chamber, the electronics, which operates the analyzer, and software working in conjunction with an external computer to control the electronics and display output data in the form of a mass spectrum. The analyzer probe consists of three parts: an ion source or ionizer, a quadrupole mass analyzer, and an ion detector. Looking at the schematic diagram shown in Fig. 6.7, the RGA operates as follows:

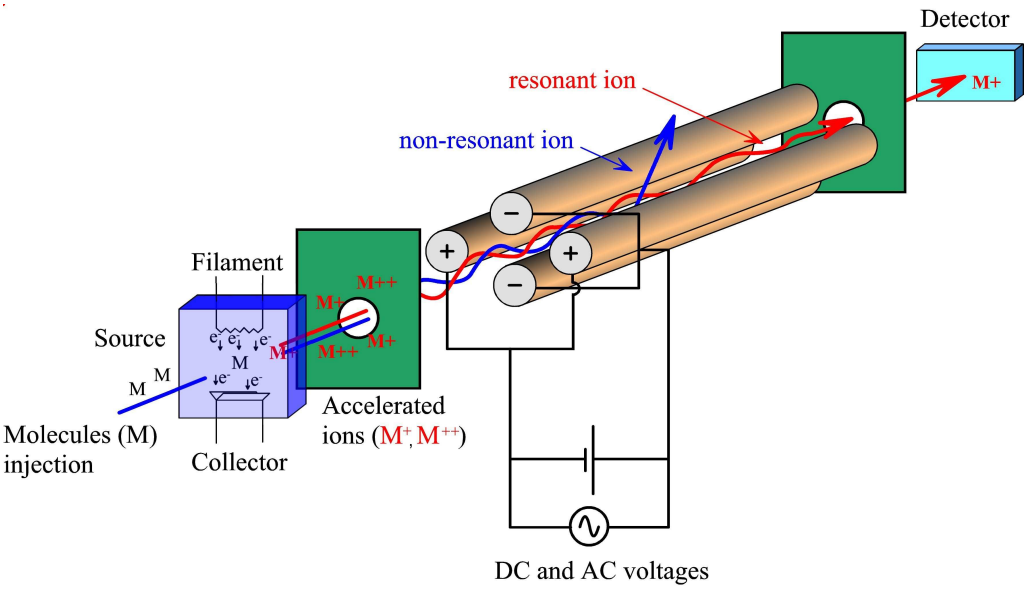


**Figure 6.7:** Schematic diagram for the configuration of the quadrupole mass analyzer with four rods.

the residual gas (atoms and/or molecules) is turned into ions by an ionizer through electron impact ionization, that is, energetic electrons are emitted by an ionizer and collide with the gas molecules, knocking out one or more electrons to produce positively charged, either $M^+$ or $M^{++}$ ions. The removal of the electrons depends on the electron energy but strongly on the molecular structure. The singly ionized charge state dominates the double ionized state. The resulting ions are then accelerated into the mass analyzer by an adjustable electric field. The Radio Frequency (RF) quadrupole mass analyzer separates the ions according to their mass-to-charge $m/z$ ratio.

The quadrupole mass analyzer shown in Fig. 6.7 has four cylindrical rods that are operated by a combination of Direct Current (DC) and Alternating current (AC) voltages of varying frequency to filter the ions. Only ions that possess the right mass-to-charge ratio can reach the ion detector for a given applied frequency. The ion detector is a Faraday cup and is used for measuring ion current with low sensitivity, while for higher sensitivity measurements, a secondary electron multiplier is used.

The output of an RGA displays a graph of an analog mass spectrum that shows the relative intensities of the various species present in the gas. This graph has the mass-to-charge ratio on the x-axis and the relative intensity on the y-axis, which is a reflection of the partial pressure of different gas species within the vacuum system. The peaks exhibited within the mass spectrum need to be interpreted properly, since, in certain cases, two different molecules can exhibit the same mass-to-charge ratio. The mass resolution of the RGA is sufficient to resolve atomic mass units, but not enough to measure the mass

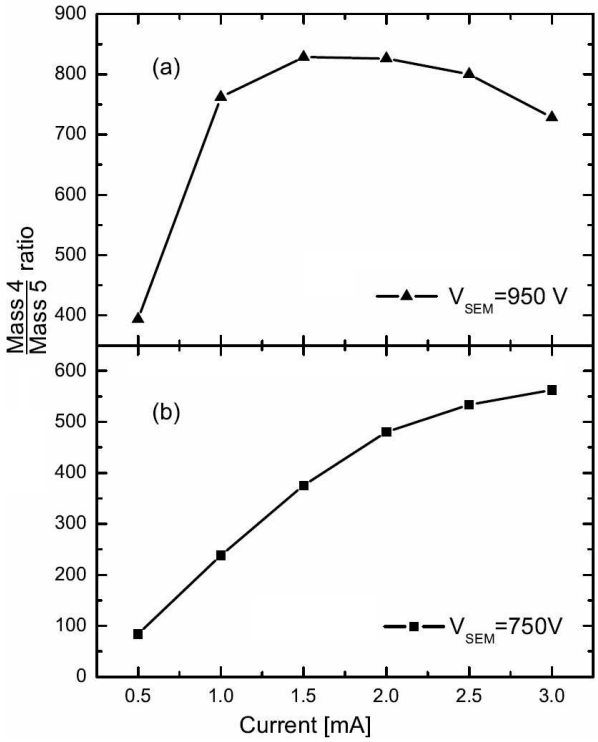


**Figure 6.8:** The optimization of RGA sensitivity to $^4$He obtained by calculating the ratio of $^4$He to H$^4$He at different electron beam current and with multiplier voltages $V_{SEM}$ set to 750 and 950 V.

excess between two different molecules with identical m/z ratio. For example, deuterium molecules, $D_2$, with a mass of 4.0278 amu, and $^4$He, with an atomic weight of 4.0026 amu, have a mass difference of $\Delta(D_2 - ^4\text{He})/^4\text{He} = 0.6\%$. Hence, deuterium will result in the same peak as $^4$He atoms. The knowledge of how two different molecules with the same mass would dissociate into smaller fragments of different mass-to-charge ratios allows for the absolute identification of the gas. The user can also select to view a trend line of a single ion, which shows the partial pressure as a function of time in seconds.

#### 6.3.2.1 The residual gas analyzer detection limit

There are two types of ion detectors within the RGA: the Faraday cup (FC) and the Secondary Electron Multiplier (SEM). If only the Faraday cup detector is used, then the partial pressure measurements can be performed from $10^{-4}$ to $10^{-11}$ mbar. It follows that the signal at the Faraday cup will be limited by the background at lower pressures. This means that, at pressures below the $10^{-11}$ mbar range, the signal-to-noise ratio from the Faraday cup exceeds acceptable levels and prevents reasonable acquisition due to the excessive filtering required to differentiate the signal from the noise. To solve this problem and increase the detection limit of the RGA, an SEM is switched on.

The SEM device is coated with a material that can produce a large yield of secondary electrons when knocked by the energetic ions from the mass filter. About two to three electrons are produced from an impact of a single primary electron. For this device to work, a large negative potential is applied to attract the positive ions as they come out of the mass analyzer causing them to hit the coating at the top of the SEM. This increases the electron signal, which is then detected by a Faraday cup and fed to the current amplifier. Depending on the applied voltage the current gain can be up to $\approx 10^3$ so that the detection limit of the analyzer is increased.

In this experiment, all measurements were performed with the SEM enabled so that the signals were amplified by a factor of 1000, leading to detection limits of $10^{-14}$ mbar. The measured current of ions at the detector cup is amplified and scaled, typically to be displayed as a partial pressure signal by the instrument software.

Since $^4$He will be the reaction product that will be measured with the RGA for the detection of neutrons in this work, it was important to determine the operating parameters for efficient measurements of this gas. This was carried out by performing a series of measurements where the parameters such as the electron beam current and multiplier voltages ($V_{SEM}$) were varied, but the electron energy was kept constant. The electron energy that controls the sensitivity of the RGA to specific atoms or molecules was kept constant at 80 eV, because it is was tested and found to be the optimal ionization energy for $^4$He atoms, which agrees to the measurements performed by Montague *et al.* [Mon84]. At this energy, the ionization cross-section is about 33.8 Mb. As shown in Fig. 6.8(a), the parameters at which the ratio of $^4$He to H$^4$He is at a maximum are when the current I = 1.5 mA, with $V_{SEM}$ = 950 V and electron energy = 80 eV. At these parameters, the RGA sensitivity was optimal for $^4$He measurements and they were therefore employed for the experiment with the fast neutron beam.

## 6.4 Determination of total and partial pressure

The total pressure of the residual gas is measured using a built-in Penning, or ionization gauge, and a Piranni gauge of the RGA. The ion gauge converts the ion current from the residual gas to pressure and also protects the heating filament from being oxidized by switching it off when the pressure in the vacuum system is above a threshold of $10^{-4}$ mbar. The vacuum measurements which have been performed using the Pirani gauge are based on the thermal conductivity of the gas. The vacuum gauges operate at different pressure levels; the Pirani gauge operates at atmospheric pressure, while the ion gauge measures the total pressure at a nominal $10^{-2}$ mbar up to its x-ray limit of $2.66 \times 10^{-9}$ mbar, and the quadrupole mass analyzer measures the partial pressure at a nominal $10^{-4}$ mbar to well below $10^{-11}$ mbar. The total pressure read by the

ionization gauge is the sum of all the partial pressures of the gases within the vacuum system. This partial pressure is determined by the expression [Ext11]

$$P = \frac{I}{e \cdot k}, \tag{6.2}$$

where $I$ is the molecular ion current, $e$ is the electron current to the ionizer, $k$ depends on the molecular composition of the gas and its units are the inverse of the pressure. The partial pressure measurements are the most challenging compared with other vacuum measurements. This is because they depend on various parameters, such as the ionization cross-section, the cracking pattern of each molecule, the inherent discrimination of the ions according to their mass-to-charge, and the secondary electron yields for different ions. The system needs to be calibrated to take most of these factors into account when performing measurements with the RGA.

The present measurements of $^4$He partial pressure are not on an absolute scale because absolute calibrations were not performed. The calibration was only relative and was obtained by using the calibrated helium leak, which has a known leak rate to obtain the $^4$He atoms that could have been produced during the reaction. The partial pressures contain some unknown scaling factor, and therefore are measured in arbitrary units.

## 6.5 Helium-4 diffusion test

In order to determine the quantity of $^4$He atoms produced during the experiment, a standard helium leak with a known leak rate was connected to the vacuum system. The calibration measurements were performed in both current and accumulation modes, with the reaction chamber empty and filled with graphite respectively. The calibrated helium leak was connected to the vacuum system through a helium leak valve in the reaction chamber. This calibrated helium leak has a leak rate of $1.4 \times 10^{-8}$ atm·cm$^3$·s$^{-1}$, equivalent to $3.773 \times 10^{11}$ atoms·s$^{-1}$.

The measurements of $^4$He in an empty reaction chamber were performed to observe the diffusion speed of $^4$He from the reaction chamber side to the RGA. The setup is shown in Fig. 6.9, where it can be seen that the turbomolecular pump (Leybold 361 turbo vac) was installed directly onto the evacuation pipe, backed by the fore-vacuum pipe. The helium partial pressure from the calibrated helium leak was measured to be $3.99 \times 10^{-8}$ arb. unit in current mode. The other measurements were performed with the reaction chamber filled with 1 kg of graphite powder to test the diffusion of $^4$He through the graphite powder. The detector setup is shown in Fig. 6.15, and Fig. 6.26 shows the plot obtained.

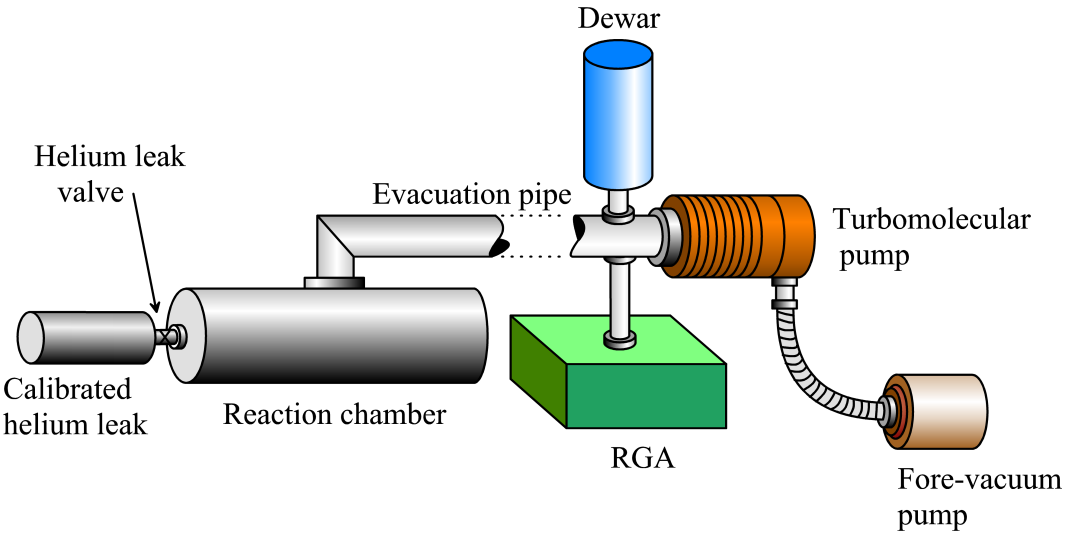


**Figure 6.9:** Schematic diagram of the experimental setup with a turbomolecular and a fore-vacuum pump, and a calibrated helium leak connected to the reaction chamber.

## 6.6 The cryogenic trap

The cryogenic trap contains a porous material called a molecular sieve, which, when cooled, selectively adsorbs gases and water vapour from the vacuum system. There are several standard sieve pore sizes available commercially, such as 3Å, 4Å, 5Å and 10Å (1 Ångström $= 1\times10^{-10}$ m). In the present design, a cryogenic trap with a 5Å molecular sieve cooled by liquid nitrogen ($LN_2$) was used. The pore size determines the adsorption efficiency of molecules of various sizes. Those molecules with a critical diameter of less than the sieve's pore size of 0.5 nm will be adsorbed, while large molecules will be excluded.

This cryogenic trap operates as an adsorption pump, which creates vacuum by reducing the amount of gas molecules within the chamber. This is achieved by cooling the frame (box or cylinder) that contains the molecular sieve pellets to the temperature of $LN_2$ (77 K), by conducting the heat from the trap towards a Dewar through a cold finger. The heat is then removed by the evaporation of $LN_2$. Water vapour freezes at the trap, and gases either condensate or adsorbed on the molecular sieve. Table 6.1 shows the critical diameter of some species present in the vacuum system that are expected to be adsorbed by the molecular sieve after cooling in the trap.

### 6.6.1 The design of the cryogenic trap

The frame of the cryogenic trap was built with copper material and lined with a fine stainless steel mesh. Copper material is used for its excellent heat conduction properties, and the mesh has pores, which allow gas molecules to

**Table 6.1:** Critical diameters of common molecules present in the vacuum system.

| Gas species | Critical diameter Å |
|---|---|
| Hydrogen | 2.4 |
| Helium | 2.0 |
| Oxygen | 2.8 |
| Carbon monoxide | 2.8 |
| Carbon dioxide | 2.8 |
| Argon | 3.8 |
| Nitrogen | 3.0 |
| Water | 3.2 |

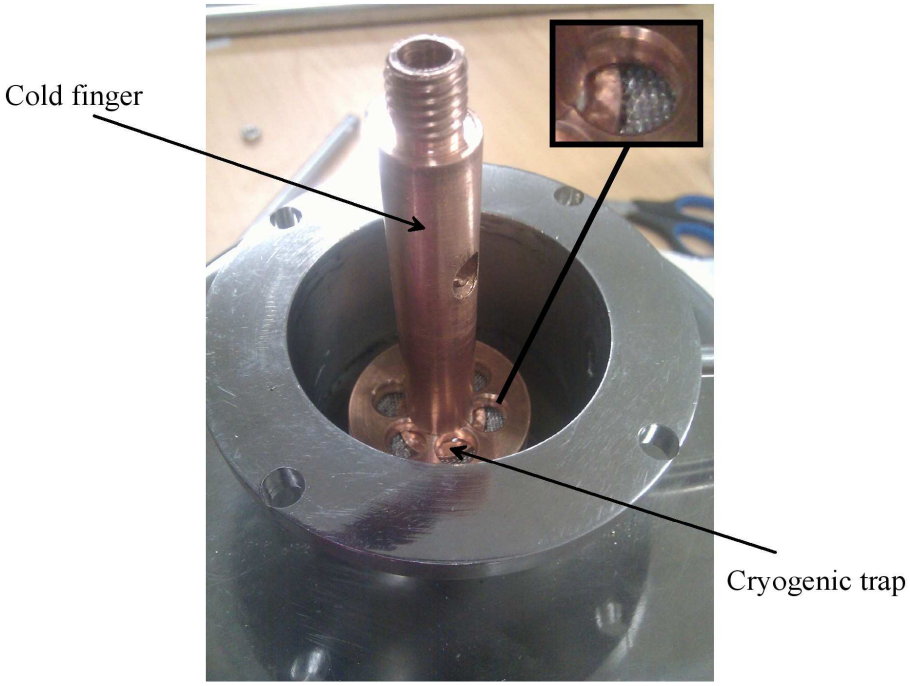


**Figure 6.10:** A cryogenic trap made of copper plate with holes, lined by a fine stainless steel mesh and attached to the cold finger.

enter the trap. Two traps were constructed and were placed at different places inside the vacuum system, attached to the Dewar, filled with $LN_2$, through a 20 mm copper rod also called a cold finger. One of the traps, which hold about 300 g of pellets, was placed inside the evacuation pipe, and the second trap, which holds about 100 g of pellets, was placed inside the helium concentrator chamber (discussed in section 6.8). Fig. 6.10 shows one of the cryogenic traps, with the copper disc, mesh and cold finger attached to a Dewar at the bottom.

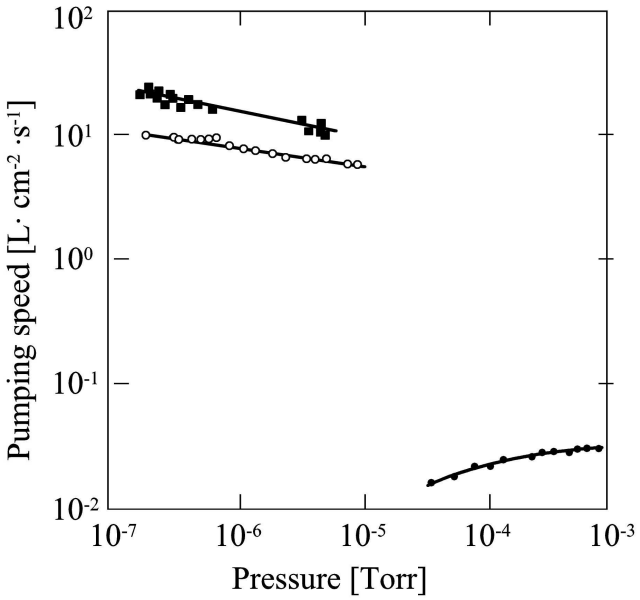


**Figure 6.11:** The pumping efficiency of a 5Å molecular sieve for $^4$He is very low compared to $H_2$ at 20.4 K; the solid squares are $H_2$ at 20.4 K, the open circles are $^4$He at 4.2 K, and the solid dots are $^4$He at 20.4 K, data from [Bew76].

### 6.6.2 The adsorption efficiency of the molecular sieve

The adsorption efficiency defines the capacity of the molecular sieves to remove different species of gas in the vacuum system. This has been found to be dependent on the molecular sieve surface temperature [Bew76]. For example, the adsorption speed of $H_2$ on a 5Å molecular sieve is found to be about 7 L·cm$^{-2}$·s$^{-1}$ at a temperature of 20.4 K, while for $^4$He it is a very low 0.1 L·cm$^{-2}$·s$^{-1}$ at the same temperature (see Fig. 6.11). Helium-4 is adsorbed much faster when the sieve is cooled to an even lower temperature of 4.2 K. Also seen in Fig. 6.11, is the pumping speed, which varies slowly with pressure. These measurements were done at a low pressure range of $10^{-8}$ to $10^{-4}$ mbar, about the same level as in the present experiment. This observation gives us insight into what to expect from the present measurements with the cryogenic trap filled with the same size of molecular sieve. However, the present cryogenic traps and molecular sieve were chilled to 77 K, about 56.6 K higher than needed for the adsorption of $H_2$, and 72.8 K higher than for the adsorption of $^4$He. At 77 K, the $^4$He is expected to flow through the sieve while, $H_2$ is adsorbed efficiently. Similar measurements have been performed by Bekris *et al.* [Bek03]. In the present measurements, a total pressure of the gases in the 20 L vacuum system dropped by two orders of magnitude, from $10^{-4}$ to $10^{-6}$ in less than 30 min after chilling with $LN_2$. This was an effective method of reducing the total pressure of the residual gas, especially the heavy molecules, when used in combination with turbomolecular and backing pumps. The pumping speed

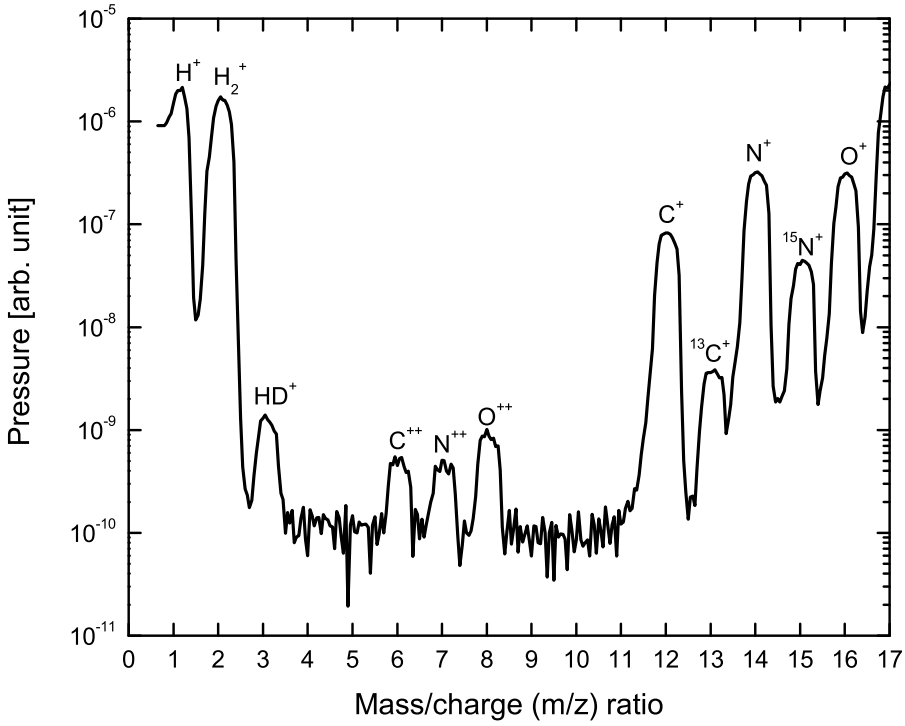


**Figure 6.12:** Pressure of the gas species in the vacuum as a function of mass-to-charge ratio (from m/z = 1 to 17) and $^4$He partial pressure is at a background level of $10^{-10}$ arb. unit.

of the cryogenic trap, however, reduced when the surface of the sieve pallets were saturated. This occurred after long pumping periods or when exposed to a high pressure. Hence, the molecular sieve requires rigorous regeneration between measurements.

## 6.7 Analysis of the residual gas in the vacuum system

The graph shown in Fig. 6.12 presents the pressures as a function of mass-to-charge ratio (m/z) of various gas species in the vacuum system. The scan is of a vacuum system at a total pressure of about $8 \times 10^{-6}$ arb. unit after pumping with the cryogenic trap.

The log-scale plot presents a closer view of the lighter mass gases, from m/z = 1 to 17. This is to allows a better view of m/z = 4, which is of interest in this work. This is at a background level of $10^{-10}$ arb. unit, which implies that

there is no contamination of $^4He^+$ that could interfere with the measurements. Other peaks shown in the spectrum are from the following species: The atomic hydrogen ion $H^+$ peak is at m/z = 1 and the hydrogen isotope $^2H^+$ is at m/z = 2. The peak at m/z = 3 could be due to isotopic hydrogen HD. The doubly ionized atoms of carbon, nitrogen and oxygen appear at m/z = 6, 7 and 8 respectively. The possibility of $H^+$ ions colliding with $^4He^+$ ions to form $^4He^+H^+$ ions is quite low, hence m/z = 5 is at the level of the background. This $^4He^+$ ionic formation was previously observed by Anort *et al.*, 1939 [Arn39]. The singly ionized atomic ions $C^+$, $N^+$ and $O^+$ produce peaks at m/z = 12, 14 and 16 respectively.

## 6.8 Accumulation mode $^4$He compression

Unlike in a nuclear reactor, where the neutron flux is of the order of $10^{14}$ n·cm$^{-2}$·s$^{-1}$, the accelerator-based neutron source at iThemba LABS delivers a beam of about four orders of magnitude less. The test of the high flux neutron detection system was to be performed in the laboratory with a neutron beam of about $10^{10}$ n·s$^{-1}$. With this beam it was anticipated that the $^4$He atoms produced from neutron-induced break-up reactions would be near the detection limit of the RGA, hence the need of developing a system that can compress the residual gas into a small chamber emerged. In this way the concentration of $^4$He within the residual gas could be increased.

The residual gas is compressed into a small stainless steel chamber called a helium concentrator to increase the concentration of $^4$He atoms. As shown in Fig. 6.13, this chamber hosts the RGA probe and the cryogenic trap. The gas enters through the inlet indicated in Fig. 6.13 and finds an opening on the copper rod, which guides the flow to the concentrator through the cryogenic trap 2. This allows for the impurities flowing with $^4$He to be trapped by the molecular sieve, and for the residual gas, containing $^4$He atoms, to be concentrated, and its partial pressure to be measured with the RGA. The volume where the gas enters is confined between Kapton foils to avoid the gas flowing to the Dewar and to the concentrator without going through the opening provided on the copper rod. The cryogenic trap 1 is placed inside the neck of the Dewar to trap impurities that manage to leak through the Kapton windows and to maintain high vacuum within the insulation of the container. The gas is evacuated through the outlet flange on the helium concentrator chamber. The purpose of placing the cryogenic trap inside the helium concentrator chamber and before the RGA probe was to trap impurities before they are ionized and characterized by the RGA. The cryogenic trap also ensures a minimum pressure of $10^{-5}$ arb. unit when the isolating valve is closed. The complete design of the helium concentrator is shown in Fig. 6.14, where the bottom part is the Dewar, which removes thermal energy from the cryogenic trap through the cold finger shown in Fig. 6.10, and the top part is the helium concentrator

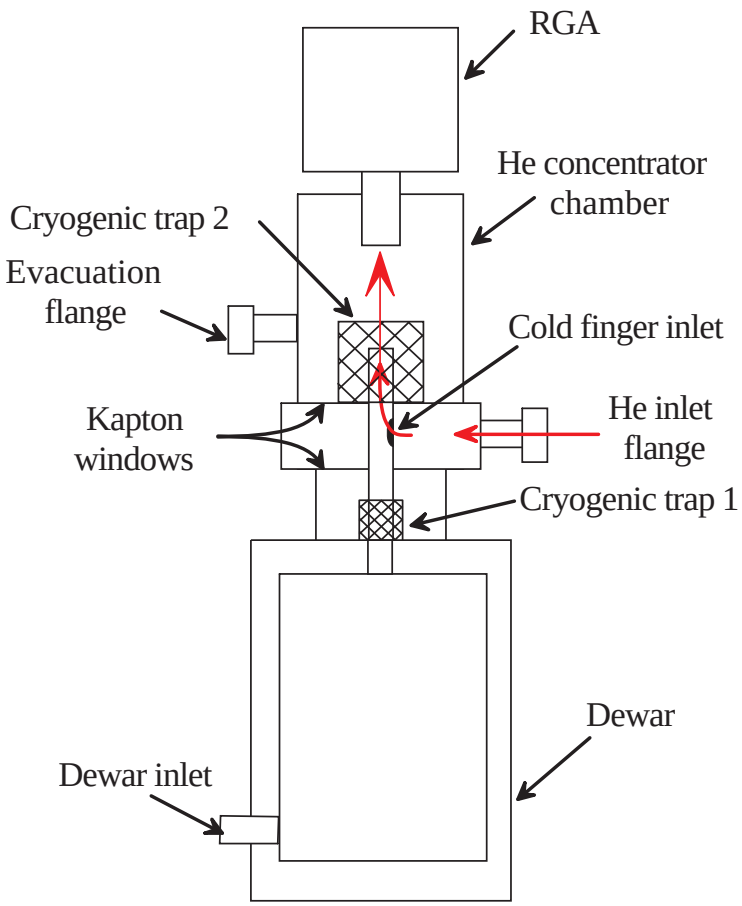


**Figure 6.13:** Schematic diagram of the helium concentrator chamber with a gas flow diagram. Molecules flow in via the inlet flange, find the opening at the copper finger and flow through to the cryogenic trap. Impurities are adsorbed and the residual containing $^4$He atoms is characterized.

chamber.

### 6.8.1 Techniques employed to compress $^4$He

The compression of a low partial pressure of $^4$He was tested with a positive displacement pump that can compress the gas into the helium concentrator chamber to obtain a strong signal in accumulation mode. However, no positive displacement pump was found on the market that is designed to operate with such a low differential pressure. Several experimental setups of compressing the $^4$He from the calibrated helium leak, which has a leak rate of $1.4 \times 10^{-8}$ atm·cm$^3$·s$^{-1}$, into a helium concentrator chamber, were tested.

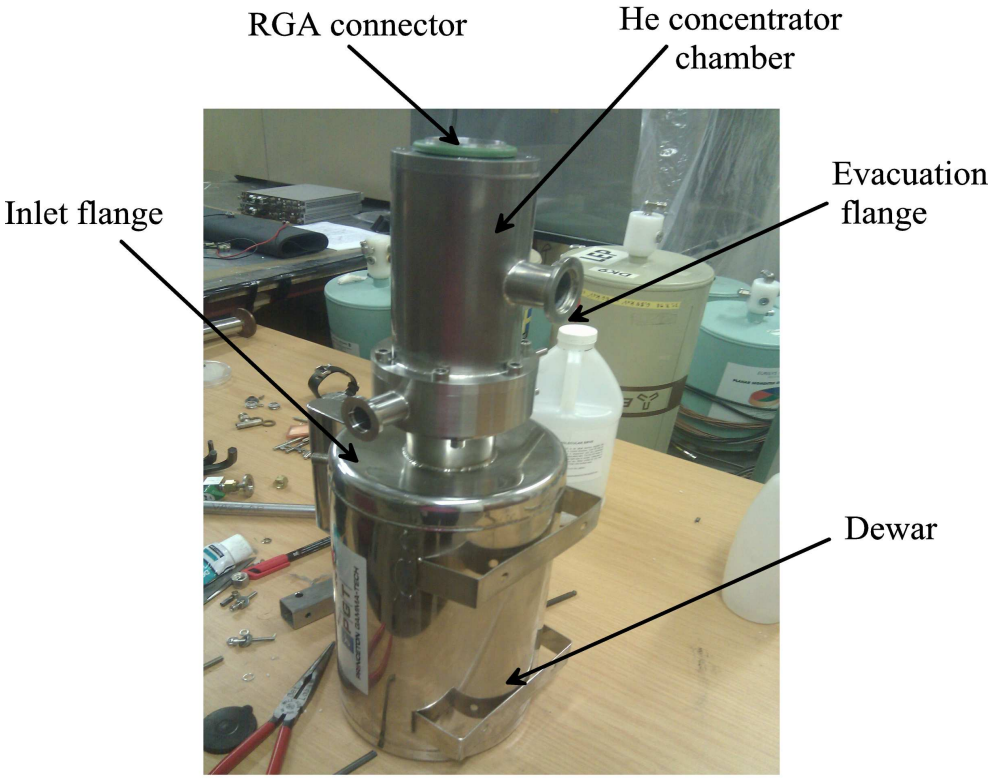


**Figure 6.14:** An image of the helium concentrator attached to the Dewar that contain $LN_2$.

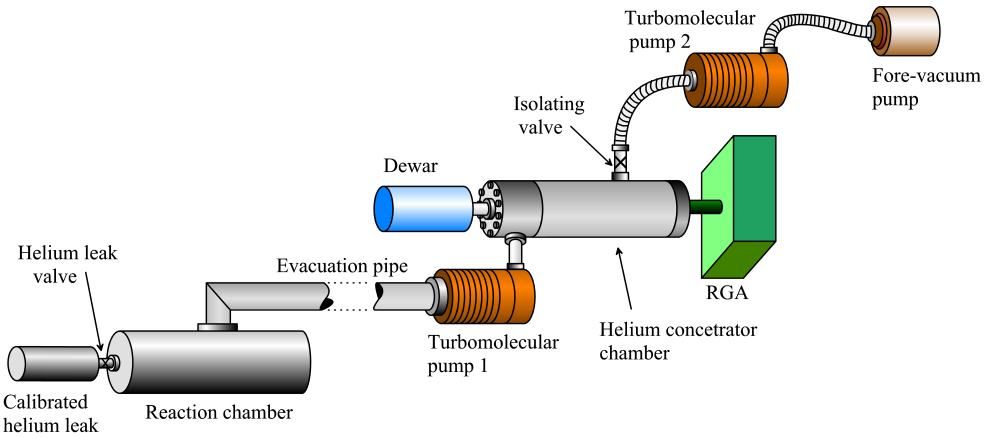


**Figure 6.15:** Schematic diagram of the setup with turbomolecular pump 1 compressing the $^4$He from the calibrated helium leak into the helium concentrator chamber, which is evacuated by turbomolecular pump 2, backed by a fore-vacuum pump.

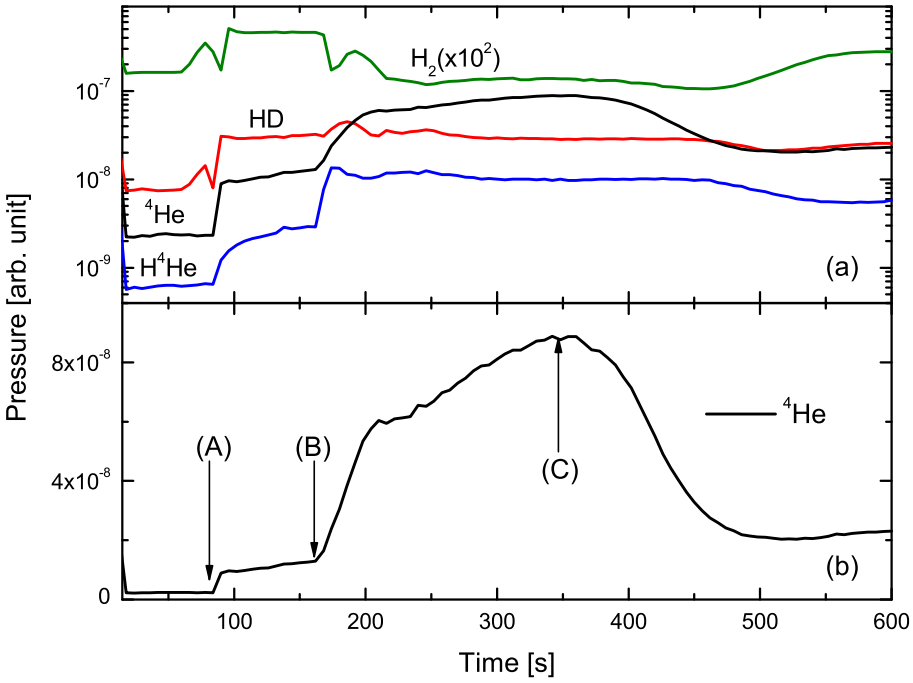


**Figure 6.16:** Gas compression with turbomolecular pump, (a) shows the behavior of different gases as the pump is switched on and off, and (b) shows the different slopes of $^4$He partial pressure: from point (A) to (B) the turbomolecular pump was switched off and (B) to (C) the turbomolecular pump was on.

#### 6.8.1.1 Compression of $^4$He with one turbomolecular pump

An experimental setup of $^4$He compression with one turbomolecular pump is shown in Fig. 6.15. In this setup, a Pfeiffer TPU 170 L/s turbomolecular pump 1 was connected directly to the evacuation pipe and the exhaust was connected to the helium concentrator chamber, which is evacuated by the Pfeiffer TPU 170 L/s turbomolecular pump 2 backed by a fore-vacuum pump. Helium-4 gas was introduced into the system through a calibrated helium leak attached to the reaction chamber by the helium leak valve. In this measurements, the helium leak valve was open at all times and the isolating valve was open for evacuation and closed to stop evacuation of helium during accumulation. The results from these measurements are shown in Fig. 6.16(a) and (b), where (b) is the mass trend of $^4He^+$ ions only in linear scale, whereas (a) shows the mass trend of $H_2^+$, $H^+D^+$, $^4He^+$, and $^4He^+H^+$ ions. The behavior of plot (b) is interpreted as follows: the turbomolecular pump 1 was off with the isolating valve open up till time A, from time A to B, the isolating valve was closed

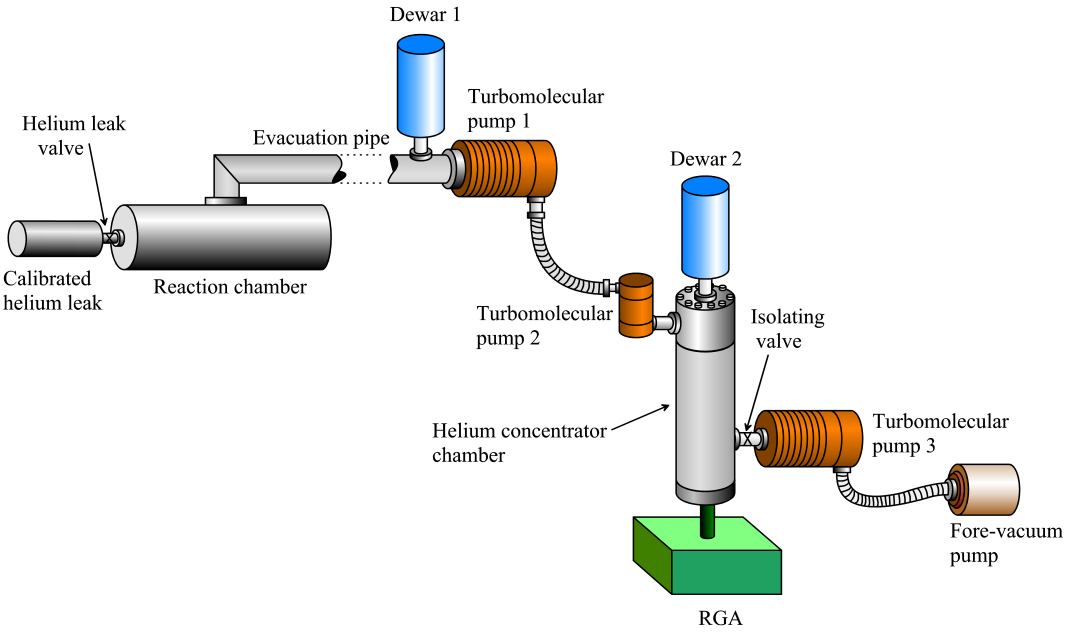


**Figure 6.17:** Schematic diagram showing the experimental setup with two of three turbomolecular pumps connected in series before the helium concentrator chamber. The third turbomolecular pump is used for evacuating the chamber backed by the fore-vacuum pump.

but the turbomolecular pump 1 remained off, hence the $^4$He partial pressure remained almost flat. From point (B), the isolating valve was closed and turbomolecular pump 1 was on, compressing the gas to the helium concentrator chamber. From these results, it can be seen that an increase of $^4$He partial pressure in the helium concentrator chamber depends on the pumping speed of the turbomolecular pump. When the turbomolecular pump was switched off, the partial pressure increases slowly, and when the turbomolecular pump was switched on from time B, the partial pressure increased with a steeper slope. At the time 200 s the maximum pumping speed of the turbomolecular to $^4$He was reached and the partial pressure increased according to the accumulation ratio of the calibrated helium leak. The $^4$He partial pressure decreased sharply to the lower level as the turbomolecular pump was switched off at time C. A compression factor 6 was achieved with this setup.

#### 6.8.1.2 Compression of $^4$He with two turbomolecular pumps

The schematic diagram of experimental setup of two turbomolecular pumps employed to compress $^4$He into a helium concentrator chamber is shown in Fig. 6.17. These are turbomolecular pumps of different sizes connected in series to increase the compression factor. The bigger Leybold turbovac 361 L/s turbomolecular pump 1 was installed directly on the evacuation pipe, and the exhaust was connected to the inlet of a high speed Leybold turbovac 50 L/s

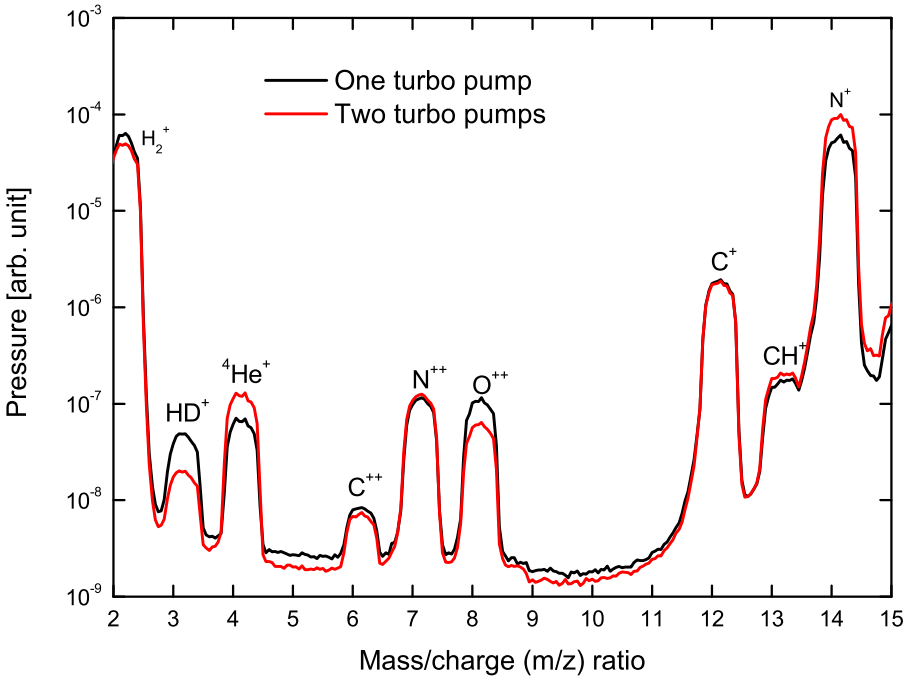


**Figure 6.18:** Gas pressure as a function of m/z compressed into the helium concentrator chamber with one of the two (solid line), and a combination of the two turbomolecular pumps (dashed line). The identification of the peaks is shown by the symbols of the atoms or molecules individually.

turbomolecular pump 2. The exhaust of turbomolecular pump 2 was connected to the inlet of helium concentrator chamber. This chamber was evacuated through the isolating valve by the Pfeiffer TPU 170 L/s turbomolecular pump 3, backed by a fore-vacuum pump. The reason for two turbomulecular pumps connected in series before the chamber, was to test two stage $^4$He compression efficiency.

The measurements were performed in two cases: (1) with one of the two turbomolecular pumps off, and (2) with both turbomolecular pumps on. The results are presented in Fig. 6.18. It can be seen that when both turbomolecular pumps were compressing the gas, the compression of $^4$He was a factor two larger than that when compressing with one pump. Some of the other gas molecules shown in the spectra did not benefit from the compression of gas. This is because the molecular sieve adsorbs them efficiently. Fig. 6.19 shows the partial pressure behavior of $O_2$, and $^4$He. From time 10 to 30 s, the isolating valve is open and the pressure of $^4$He is low at $2 \times 10^{-8}$ arb. unit. At time 30 s, the helium leak valve was open to allow helium to flow into

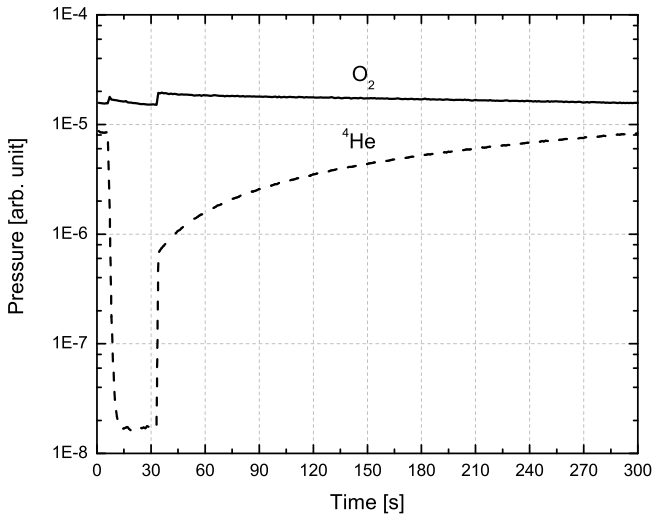


**Figure 6.19:** Gas pressure as a function of time compressed with two turbomolecular pumps. The partial pressure of $^4$He drops down when the turbomolecular pumps 1 and 2 were switched off between 10 and 30 s, and it increases as they were switched on at time 30 s.

the vacuum system, but the isolating valve was closed for accumulation mode and as a results, the partial pressure of $^4$He raised to reach saturation level at $1 \times 10^{-5}$ arb. unit in the helium concentrator chamber. It can be noticed that a compression effect of $O_2$ was not adsorbed because these molecules are adsorbed within the molecular sieve, and the partial pressure remained constant. The limiting factor was the heat from the RGA filament, which caused the out-gassing of the cryogenic trap inside the concentrator and increased the total pressure of the gas in the vacuum system, so the longer the time spent in accumulation mode, the greater the increase in total pressure. This defect was addressed with a modification of the cryogenic trap by reducing its size.

#### 6.8.1.3 Compression of $^4$He with Roots belted pump

A positive-displacement compressor similar to the Roots Blower [Rit68] was also employed during the compression test of $^4$He into the helium concentrator chamber. A small and compact positive-displacement compressor, of which the schematic diagram is shown in Fig. 6.20, was designed and constructed especially for this research. The compressor consists of two aluminum rotors rotating in opposite directions, with a cylindrical transparent rubber belt as shown in Fig. 6.22 (top-left picture insert). The relative position of the rotors is maintained by a pair of phasing gears, see Fig. 6.22 (top-left picture insert). The body of the positive-displacement pump was made of a PVC material,

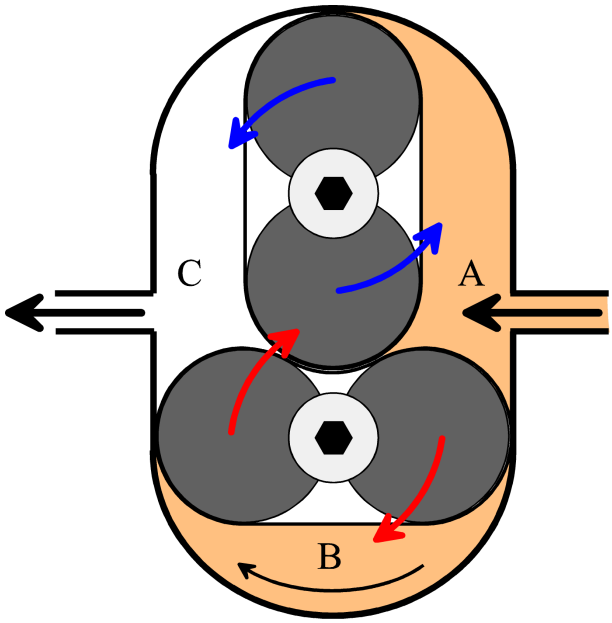


**Figure 6.20:** The schematic diagram of a two-lobe positive-displacement gas compressor. The gas enters in region (A), is pushed to region (B) and exits through region (C).

and the bottom and top lids out of aluminum plate as shown in Fig. 6.22 (top-right picture insert).

It operates by compressing the gas with two pairs of lobes. The gas enters through the inlet in region (A), is trapped in the pockets between the lobes and the body of the pump (B), and is compressed into the exhaust (C). The lobes remain in contact with the wall of the pump to prevent the gas from leaking backwards to the inlet.

The schematic diagram of the experimental setup is shown in Fig. 6.21. In the diagram, it can be seen that the calibrated helium leak was connected to the system through a helium leak valve and the positive-displacement compressor was compressing the gas to the helium concentrator chamber. The helium concentrator chamber was evacuated by means of the Pfeiffer TPU 170 L/s turbomolecular pump backed with a fore-vacuum pump. The measurements were performed as follows: the positive-displacement compressor was compressing the residual gas to the helium concentrator chamber (direction A to C, in the schematic diagram in Fig. 6.20), and from the helium concentrator chamber to the evacuation pipe, (direction C to A). During the forward compression, the backward leak was not expected. However, $^4$He was found to back-stream through the narrow gaps between the belts and the body of the pump and possibly in between the belts and the closing (bottom and top) cover of the compressor. The partial pressure of $^4$He increases during forward compression, into the helium concentrator chamber, and drops as the compression stops. As seen in Fig. 6.23, a compression factor of about 1.5 was

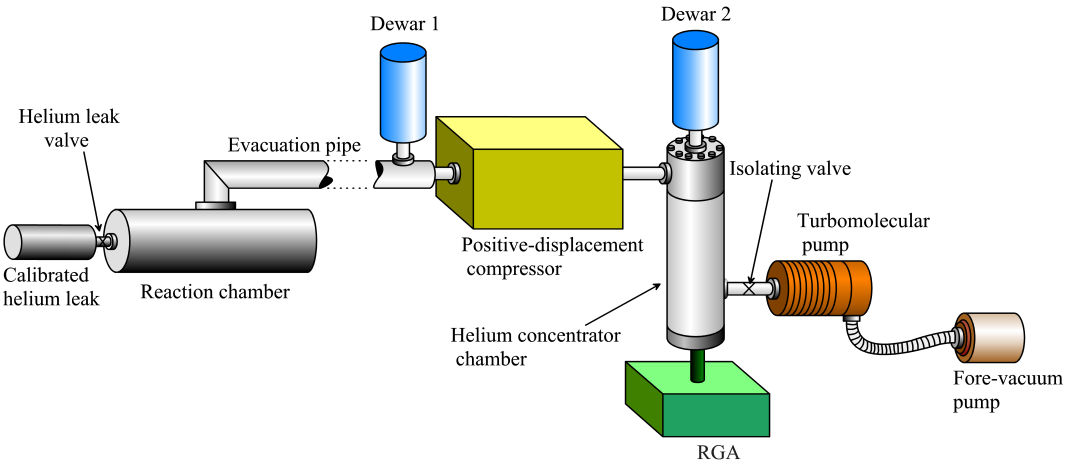


**Figure 6.21:** Schematic diagram of the experimental setup with a positive-displacement compressor compressing the gas into the helium concentrator chamber, and a turbomolecular pump evacuating the chamber with the fore-vacuum pump.

achieved. The partial pressure of $^4$He was supposed to remain constant with termination of the compression. However, it was found to decay as a results of $^4$He leakage. Fig. 6.24. This plot also presents the results of the reverse compression. The $^4$He partial pressure sharply decreases as the rotors rotate backward taking the residual gas from the helium concentrator chamber to the evacuation pipe with a decompression factor of 1.6.

Out of these three tests, it was decided to employ an experimental setup with one turbomolecular pump compressing the residual $^4$He because of the following reasons: the volume of the vacuum system is smaller compared to the other two experimental setups, the compression factor was better, and unlike the experimental setup with a positive-displacement compressor, the $^4$He partial pressure was preserved in the helium concentrator chamber during accumulation mode.

### 6.8.2 Observed $^4$He background in accumulation mode

Helium gas was introduced into the vacuum system from the calibrated helium leak through the isolating leak valve, as discussed in section 6.8.1. However, residual helium gas was observed with the RGA after the calibrated helium leak was removed, and this was not anticipated. This $^4$He background appears when running in accumulation mode. The turbomolecular pump compresses the gas into the helium concentrator chamber when the isolating valve is closed. The partial pressure of $^4$He increases by factor 5 on the mass trend spectrum. There are several potential places where the helium gas could have been trapped and stored in the vacuum system, namely, the Dewar, the cryogenic trap and/or contamination from the natural occurrence of helium in air.

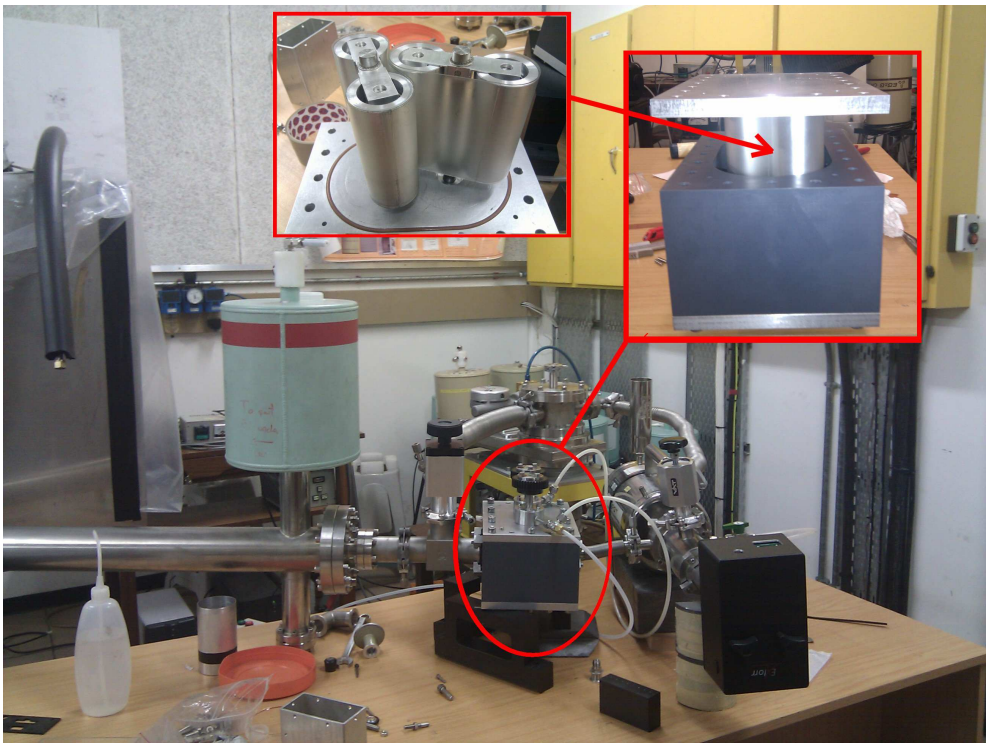

**Figure 6.22:** An image of the experimental setup with the positive-displacement compressor shown in the red circle. The top right insert picture shows the compressor box opened, and at the top left insert shows the cylinders with transparent rubber belt.

The Dewars, made of multi-layered insulation, could be trapping $^4$He when it enters between the thin interstices. The spectra that show the gases present in the vacuum system when the Dewar 2 valve is open, and the combination of Dewar 1 and 2 are presented in Fig. 6.25(a) and (b), respectively. These two Dewars can be seen in the setup shown in Fig. 6.21. In spectra (a) and (b), the partial pressure of $^4$He was also found to increase when compared with H$^4$He. When the valves that isolate the Dewar 1 and 2 are open (b), there is a larger increase of $^4$He partial pressure compared to when only one Dewar 2(a) is used. This could imply that some $^4$He gas was trapped in the multi-layered insulation of the Dewars.

The $^4$He background could also have a contribution from deuterium molecular hydrogen. This is a naturally-occurring isotope of hydrogen and about 0.02% of hydrogen in nature is deuterium. Apart from natural occurrence in air, molecular deuterium could be coming from the wall of the stainless steel evacuation pipe or concentrator from the outgassing under high vacuum [Jia10] and from water ($D_2O$ component).

The molecular sieve inside the cryogenic trap could also be trapping some $^4$He when it is chilled to a temperature of 77 K with liquid nitrogen. The tests were performed in both current and accumulation modes using the calibrated

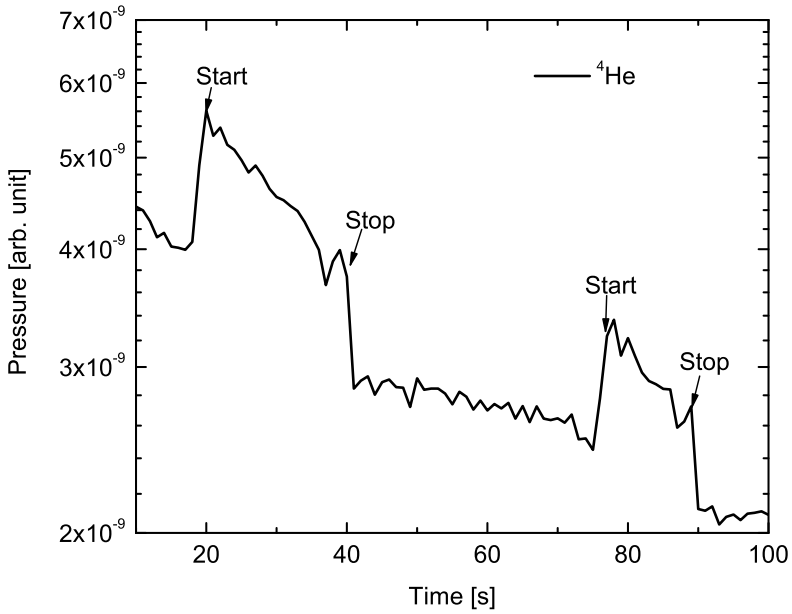


**Figure 6.23:** The effect of forward compression can be seen by a rise of $^4$He partial pressure as the positive-displacement compressor starts to compress $^4$He into the helium concentrator chamber.

helium leak. The results are shown in Fig. 6.26. At the end of region (1) the isolating leak valve was open for a short period of time and the partial pressure increases sharply. The isolating valve 2 was open in region (2) to evacuate all gases, hence the partial pressure of $^4$HeH, $^4$He and $^3$H dropped, except for $^2$H, which dropped but increased again. When the gas is compressed, it is found that the partial pressure increases, but reaches saturation levels in region (3). The partial pressure was expected to increase linearly, but a saturation effect indicates that $^4$He is trapped somehow in the closed system.

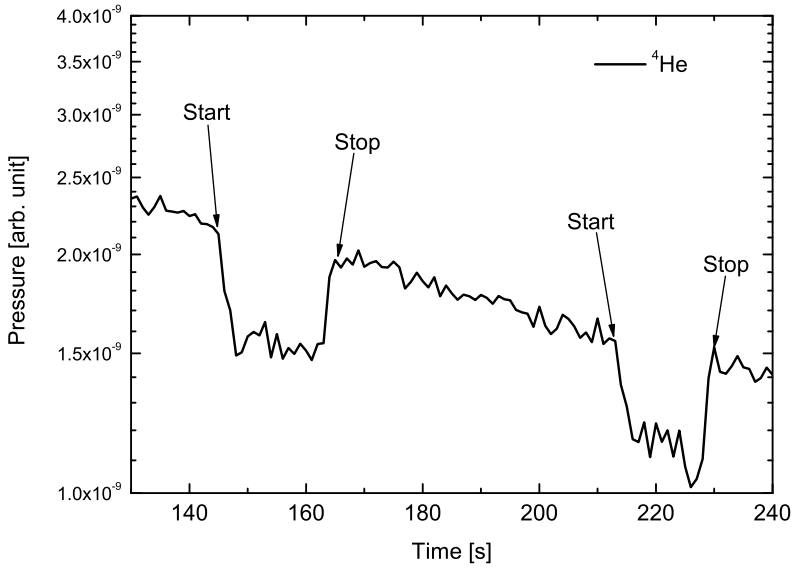


**Figure 6.24:** The effect of reverse compression can be seen by a drop of $^4$He partial pressure as the positive-displacement compressor starts to compress $^4$He towards the evacuation pipe.

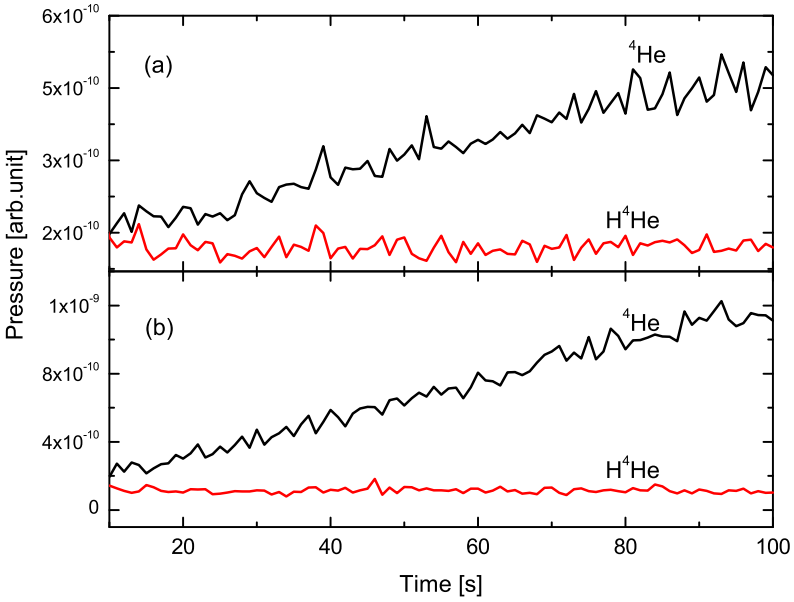


**Figure 6.25:** An increase in partial pressure of $^4$He was observed from (a) Dewar 2 and (b) both Dewar 1 and 2 (see Fig. 6.21).

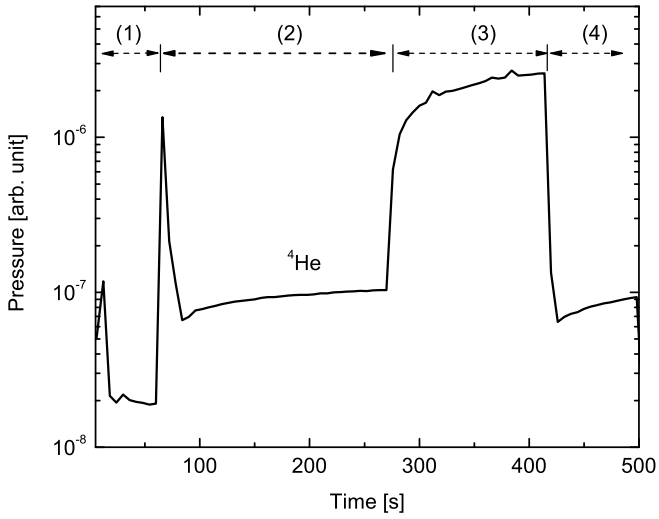


**Figure 6.26:** Measurements of $^4$He with calibrated helium leak, helium leak valve is in region (1) closed and open in (2), accumulation mode in (3), evacuation of the helium concentrator chamber in region (4).

# Chapter 7

# Experimental measurements

The test to show the proof of principle for the high flux neutron detection system was performed with high energy protons and neutrons in two separate experimental measurements at the iThemba Laboratory for Accelerator Based Science (iTL) at Faure, South Africa. This is a national facility that produces particle beams by means of accelerator for basic nuclear and material research and medical therapy purposes. As shown in Fig. 7.1, the facility consists of the Electron Cyclotron Resonance (ECR) source, Solid Pole Cyclotron (SPC) 1 and 2, and Separated Sector Cyclotron (SSC), which can accelerate protons up to 200 MeV onto a fixed target for the production of secondary beams such as neutrons. The particle beam can be delivered to the experimental (A, D, F and K-lines), radiotherapy and radioisotope vaults. In the present work, the proton beam was delivered to the D-line (neutron) experimental vault for proton beam measurements, and also to the neutron therapy vault, where the test of fast the neutron detection was performed.

The measurements with proton beams were performed first because of the availability of high-intensity proton beam compared to the lower intensity secondary neutron beam. This means that there are more protons per second bombarding the reaction chamber, hence a large production of helium atoms. Also, the proton inelastic scattering cross-section with $^{12}$C atoms is similar to that of neutrons, with a threshold energy of about 8 MeV for both.

## 7.1 High energy proton beam measurements

The experiment with the high energy proton beam was performed in the D-line neutron experimental vault. As shown in Fig. 7.2, the D-line consists of a target chamber, a beam deflection magnet, a beam dump equipped with beam centering and current-integration equipment, a shielding wall and collimation channels for the low neutron flux measurements. After the target chamber, there is a bending magnet that is designed to bend up to 200 MeV protons and other charged particles into the beam stop at 15° with respect to the incident

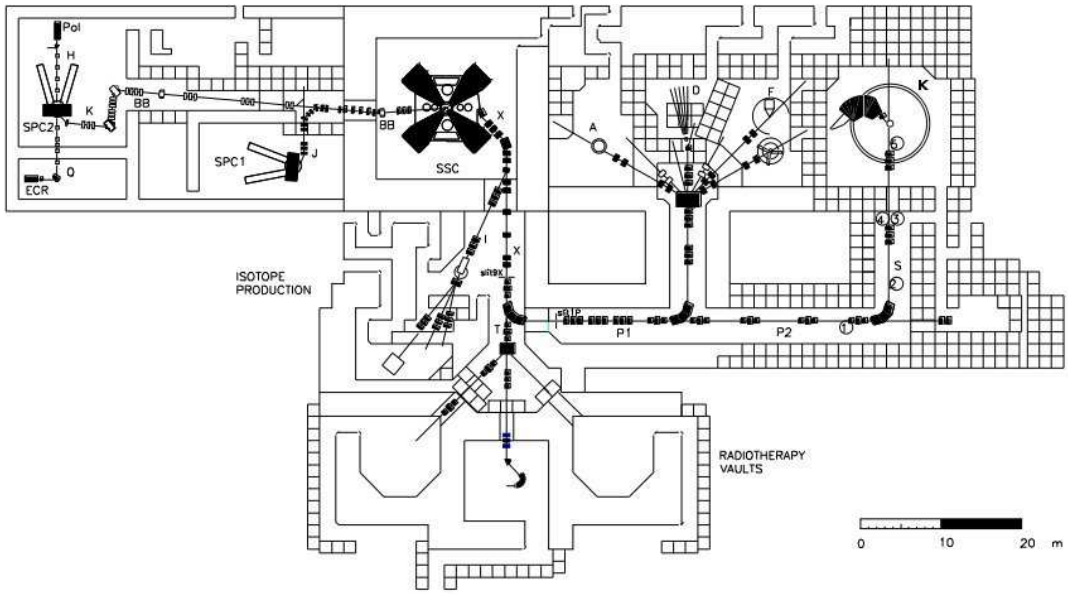


**Figure 7.1:** The schematic diagram of the iThemba LABS cyclotron facility, which consists of the ECR source, SPC 1 and 2, and the SSC, which can accelerate protons up to 200 MeV to the experimental (A, D, F and K-line), radiotherapy and isotope production vaults.

beam direction. The beam stop is fitted with a Faraday cup, which is used to collect the charge for beam current measurements.

### 7.1.1 Experimental procedure

The layout of a high flux neutron detection system inside the D-line experimental vault is shown in Fig. 7.2. The aim of this experiment was to produce a large number of helium atoms from the 1 kg graphite and determine the capability of the system in measuring high-incident flux. Also to obtain important information regarding the diffusion speed of $^{4}$He atoms from the break-up reaction through graphite powder with a 5 $\mu$m grain size. Hence, the use of high flux 66 MeV proton beams to induce the break-up reactions in $^{12}$C.

The experimental setup is depicted in the schematic shown in Fig. 7.2. The proton beam was focused onto the reaction chamber filled with graphite material placed at $\theta = 0^{\circ}$ along the beam axis, (4), where the $^{12}$C(p,p'$\alpha$)$^{9}$Be and $^{12}$C(p,p'3$\alpha$) reactions occurred. On the schematic diagram, the RGA is placed at the opposite side of the pipe surrounded by a cryogenic trap. This position is preferred because the impurities flowing with $^{4}$He are trapped by the cryogenic trap and the pressure of the residual gas is measured with the RGA. The combination of turbomolecular pump (7) and backing pump (8) were employed to evacuate the gas from the vacuum system. As seen in the

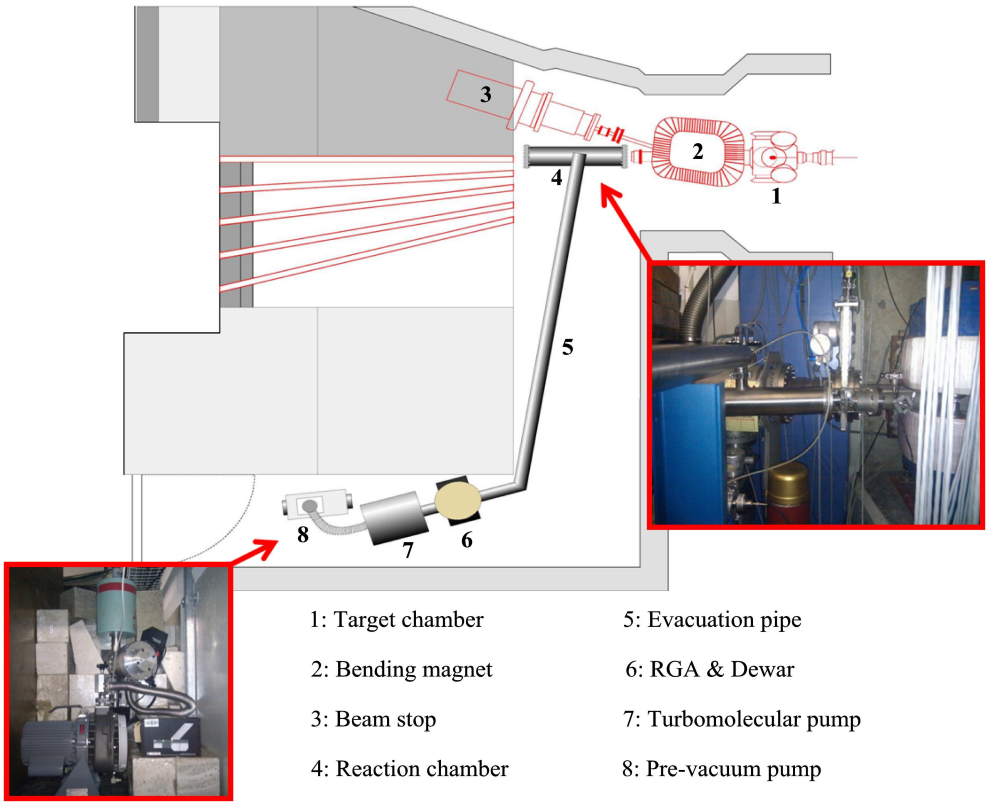


**Figure 7.2:** Schematic diagram of the high flux neutron detection system setup at iThemba LABS D-line experimental vault.

diagram, the evacuation pipe was bent around the chicane and borated wax bricks were placed to protect the RGA from the direct irradiation, and hence reduce the radiation dose.

### 7.1.2 Reaction rate of $^{12}$C with high energy protons

Calculations to determine the production of $\alpha$-particles with a 66 MeV proton beam of varying intensity were performed using the cross-section library [NDS11] and the energy loss profile from the SRIM code developed by Ziegler *et al.* [Zie08]. The graphite was discretized into discs of 1 cm thickness in order to obtain an estimate of the reaction rate induced by high energy protons as they interact with the carbon atoms in the graphite. The SRIM code was used to calculate the energy loss of 66 MeV protons per cm of graphite in order to determine the actual stopping range in graphite powder with a density of 0.2 g·cm$^3$. For each thickness, the average energy of the transmitted protons and the corresponding cross-section value (taken from Fig. 7.3) were used to calculate the reaction rate within the sample. The protons were found to stop at an average distance of 18 cm inside the graphite powder. The reaction rate

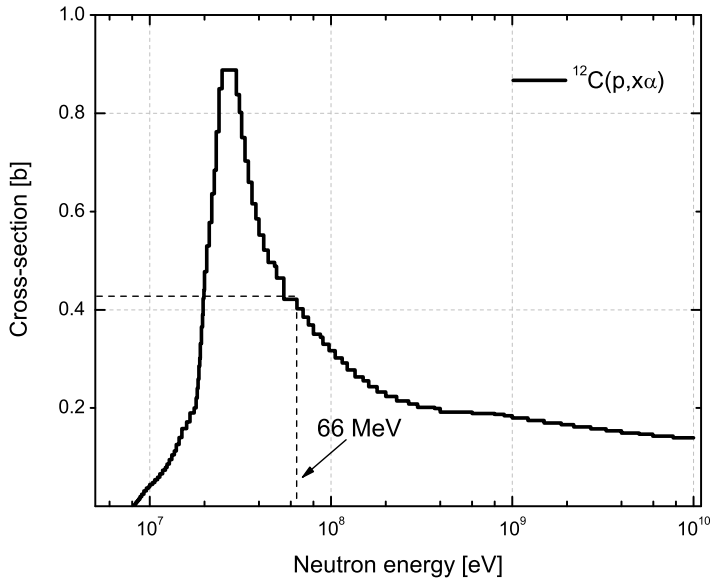


**Figure 7.3:** Total cross-section for $^{12}$C(n,xα) reaction with the average cross-section for the 66 MeV proton beam shown in dotted line, data from [NDS11]

is calculated using the general expression

$$R_{\text{rate}}(E) = \int_{7}^{66} \sigma_{\text{inel}}(E) \times I_{\text{proton}}(E) \times N_{\text{t}} dE, \tag{7.1}$$

where $R_{\text{rate}}(E)$, the number of $\alpha$-particles produced per second, is the integral of the product of the number of graphite atoms per cm$^2$ $N_{\text{t}}$, the reaction cross-section $\sigma$ and the proton beam current over all energies $I_{\text{proton}}(E)$. The limits of integration are set to 7 MeV which is the energy threshold for the $\alpha$ production break-up reaction and 66 MeV was the maximum energy of the proton beam. The general expression of the reaction rate is a crude approximation, as the flux of particles is considered constant from incident energy to below the threshold energy. In the experiment, some protons were lost as they underwent scattering or reactions with materials before they reached the distance of 18 cm into the graphite. The results of these calculations are shown in Table 7.1, and the quantity of $^4$He atoms produced is about $6 \times 10^8$ $^4$He/nA.

### 7.1.3 Results of the measurements for high energy proton beam

The sensitivity of the high flux neutron detection system was determined by varying proton beam intensities incident on the reaction chamber. The beam

**Table 7.1:** The expected reaction rates for the production of $^4$He atoms.

| Proton beam current (nA) | Number of protons/s | Reaction rate ($^4$He/s) |
|---|---|---|
| 50 | $3.1 \times 10^{11}$ | $2.9 \times 10^{10}$ |
| 75 | $4.7 \times 10^{11}$ | $4.4 \times 10^{10}$ |
| 100 | $6.2 \times 10^{11}$ | $5.9 \times 10^{10}$ |
| 150 | $9.4 \times 10^{11}$ | $8.8 \times 10^{10}$ |

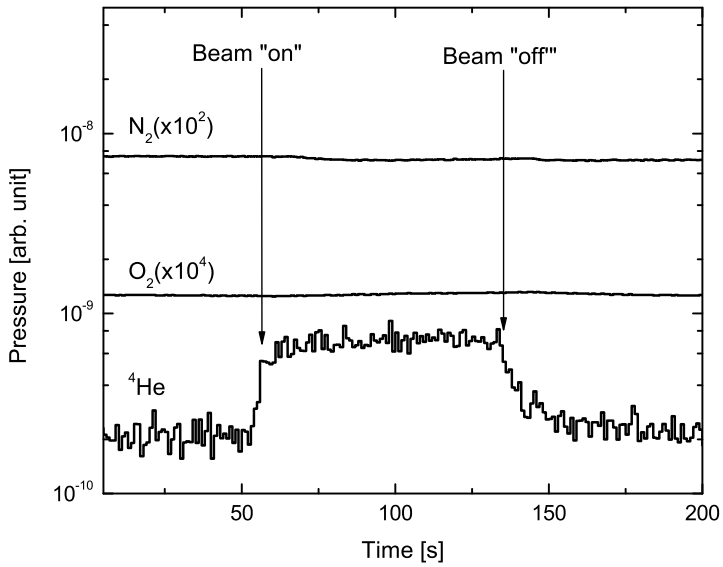


**Figure 7.4:** The partial pressure of $^4$He increases to about $6 \times 10^{10}$ arb. unit while $O_2$ and $N_2$ remain constant when a 50 nA proton beam intensity incident on the reaction chamber filled with graphite.

current was increased in four steps, from 50 to 150 nA and at each step, the beam current was stabilized and the response of the detection system was observed through the relative increase of $^4$He partial pressure in the vacuum system. The partial pressures for different gases, measured for the minimum 50 nA and the maximum 150 nA proton beam intensity, are shown in Fig. 7.4 and 7.5 respectively. In Fig. 7.4, it can be seen that the response of the detector is practically immediate, with a rise time of approximately 3 s for $^4$He, while the partial pressures of other gases remain constant. Once the beam is switched off, the partial pressure of $^4$He drops exponentially. This non-immediate response is caused by $^4$He atoms trapped by the molecular sieve, as well as possibly the slow diffusion through the graphite particles. A similar response is also seen in Fig. 7.5. However, now the partial pressure of $N_2$ increases slightly during the beam-on period, while $O_2$ decreases. This increase is thought to be due to the

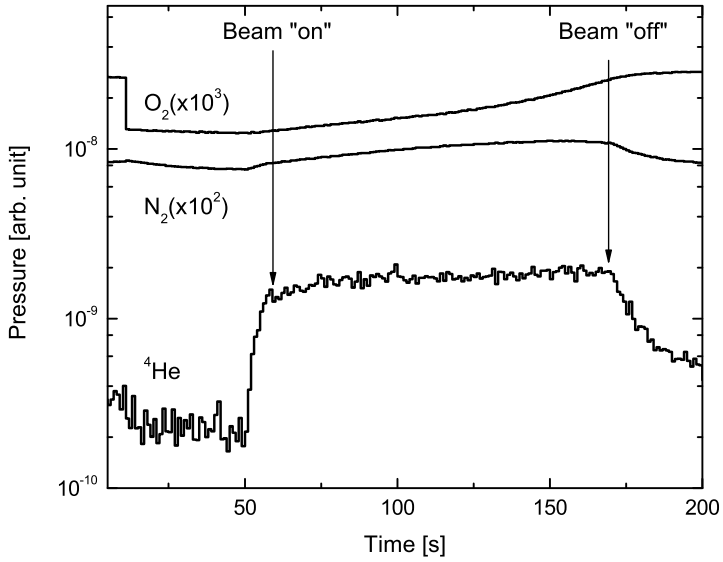


**Figure 7.5:** The partial pressure of $^4$He increased to $1.1 \times 10^{-9}$ arb. unit when the proton beam intensity was increased to 150 nA. The background level after the beam-off period has increased due to $^4$He trapped within the graphite grains and slowly diffusing out to the RGA.

out-gassing of graphite as the partial pressure is increasing gradually, which is believed to be related to the energy of about 6.6 J·s$^{-1}$ deposited by the protons in the form of heat in the graphite. The high flux neutron detection system is sensitive to an increase in the intensity of the incident proton beam. The partial pressures of $^4$He for all the various proton beam intensities are presented in Fig. 7.6. From the plot it can be seen that the production of $^4$He atoms is proportional to the incident proton beam current. However, the background level after the beam-off period increases with an increase in beam intensity due to the slow diffusion of $^4$He through the graphite particles

From helium diffusion test with the helium calibrated leak, we deduced the number of $^4$He atoms that could have been produced in the reaction chamber with the proton beam, as shown in Table 7.2, column 3. In this calculation, the response of the detector is found to be linear but the deduced number of $^4$He atoms produced per second is almost one order of magnitude lower than the expected values shown in Table 7.1. Fig 7.7 shows the expected yield and the measured yield plotted in one axis. The loss of $^4$He could be due to the molecular sieve trapping $^4$He and the slow diffusion through the graphite particles. But, the protons also lose energy as they attenuate through the 5 mm thick plate of the graphite container and the graphite powder. Once the energy of the protons falls below the threshold energy of 8 MeV, they will

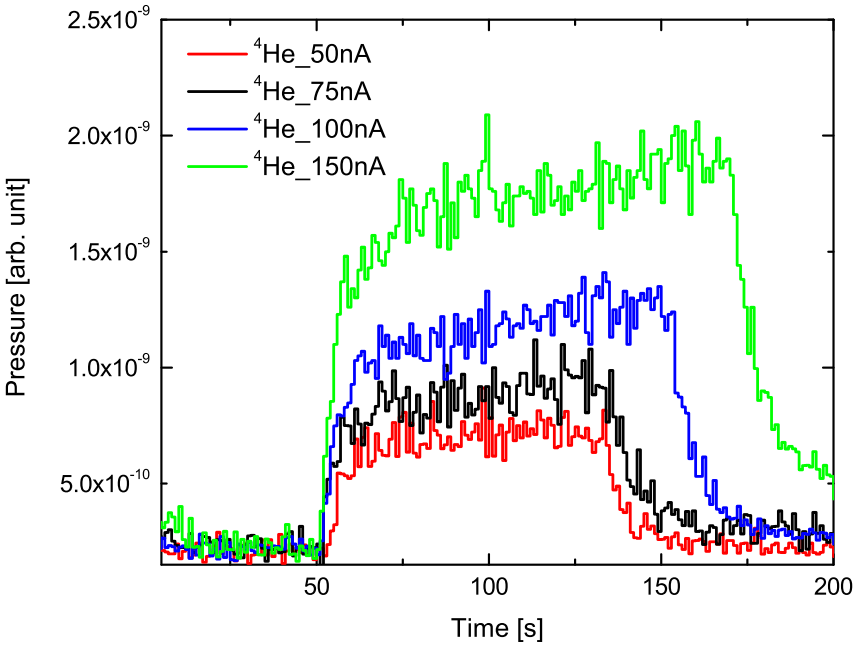


**Figure 7.6:** The different levels of $^4$He partial pressure that were observed when the beam intensity was increased from 50 nA to 150 nA. The trapping of $^4$He atoms in the graphite causes the exponential decay trend when the beam was switched off.

**Table 7.2:** The average pressure of $^4$He increased directly proportionally to the proton beam intensity.

| Beam current (nA) | $^4$He partial pressure [arb. unit] | Reaction rate ($^4$He/s) |
|---|---|---|
| 50 | $6.9 \times 10^{-10} \pm 8 \times 10^{-11}$ | $1.6 \times 10^9$ |
| 75 | $8.7 \times 10^{-10} \pm 9 \times 10^{-11}$ | $3.2 \times 10^9$ |
| 100 | $1.2 \times 10^{-9} \pm 1 \times 10^{-10}$ | $4.3 \times 10^9$ |
| 150 | $1.7 \times 10^{-9} \pm 2 \times 10^{-10}$ | $6.4 \times 10^9$ |

not produce $\alpha$-particles in their interactions with $^{12}$C atoms. This reduces the number of protons that will reach a distance of 18 cm into the graphite powder (as assumed in the calculation) as well as the production of $\alpha$-particles. Another factor could be that the cross-sectional data used in the model are possibly not accurate.

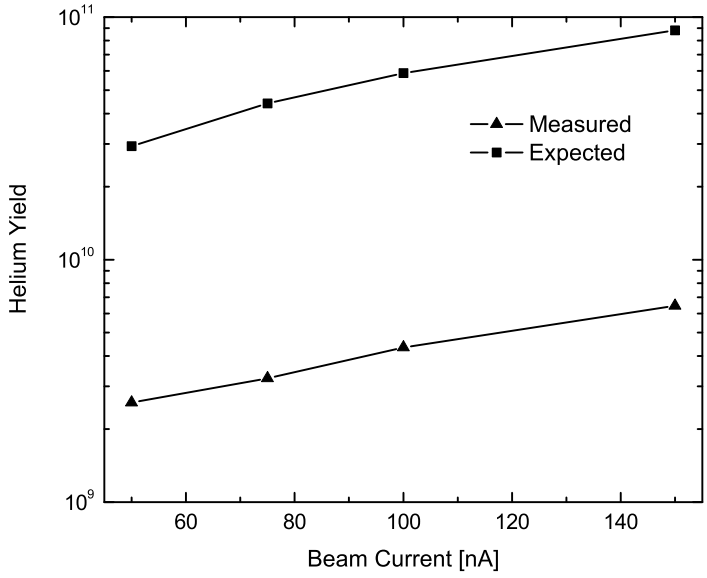


**Figure 7.7:** The expected and measured yields of $^4$He atoms.

## 7.2 Fast neutron beam measurements

The fast neutron measurements were performed at the iThemba LABS neutron therapy vault [Jon88]. This neutron therapy vault consists of an isocentric gantry that can rotate through an angle of $\theta = \pm 185°$. An isocentric gantry refers to the design technique where all beams used from various angles, have a common focus point. The gantry consists of a beam collimator, which has a continuously variable aperture, providing rectangular field sizes from $5 \times 5$ cm$^2$ to $30 \times 30$ cm$^2$. The collimator consists of five layers of four interlocking blocks of iron and borated polyethylene, geared to provide a tapered aperture. The neutron-producing target is at a distance of 150 cm from the collimator. Neutrons are produced by bombarding a 19.6 mm thick copper-backed Be target with a 66 MeV proton beam of intensity 32 $\mu$A which represents $2 \times 10^{14}$ protons per second. This Be target is water cooled to avoid melting of the material as approximately $2.2 \times 10^3$ J/s of energy is deposited by the proton beam. The energy loss of the protons on the Be target is 40 MeV [Jon92] and the neutron yield is about $2.6 \times 10^{12}$ n/s, with an average energy of 33 MeV.

### 7.2.1 Experimental procedure

The graphite reaction chamber, with a radius of 5 cm and a length of 60 cm was placed at a distance of 150 cm from the Be target exposed to the beam

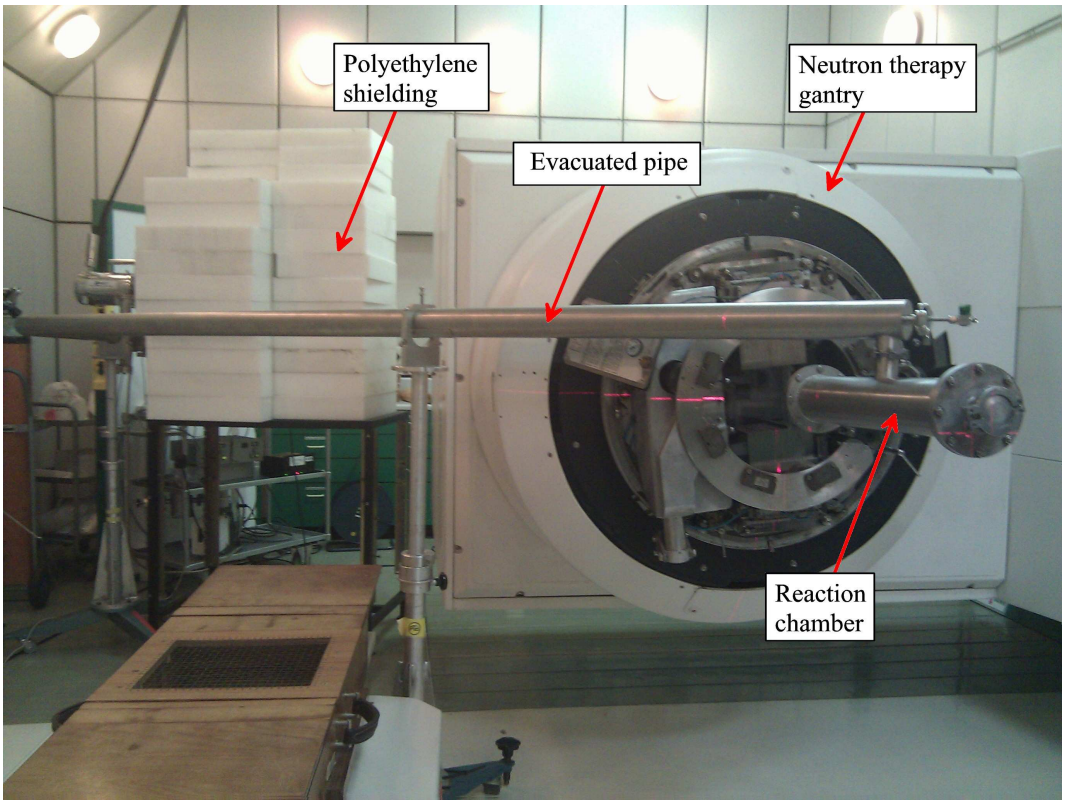


**Figure 7.8:** The neutron detector setup placed in front of the neutron therapy gantry at iThemba LABS.

and at $\theta = 0°$ along the neutron beam axis, as shown in Fig. 7.8. The gantry rotation angle was set to 270° to provide a horizontal beam, and the beam collimator was opened to an aperture of $30 \times 30$ cm$^2$. The neutron yield over the front surface of the reaction chamber was about $1.1 \times 10^{10}$ n/s [Jon88]. The vacuum pumps, together with the RGA, were on the left side of the gantry, shielded with polyethylene blocks to avoid the fast neutrons causing single event upsets or damaging the electronics.

### 7.2.2 Results of the measurements for fast neutron beam

As shown in the neutron spectrum in Fig. 7.9, the secondary neutrons had enough energy to induce the break-up of $^{12}$C into $^{4}$He nuclei, and the expected number of $^{4}$He atoms produced was about $4 \times 10^9$ $^{4}$He atoms/s. Helium-4 atoms produced in the $^{12}$C(n,n′$\alpha$)$^{8}$Be and $^{12}$C(n,n′)3$\alpha$ reactions were measured in both current and accumulation mode. Shown in Fig. 7.10 is the mass trend spectrum of gas species present in the vacuum system and produced during the beam-on period in current mode. Each data point is obtained for a time integration of 6 s to obtain better statistics. A closer view of the $^{4}$He plot

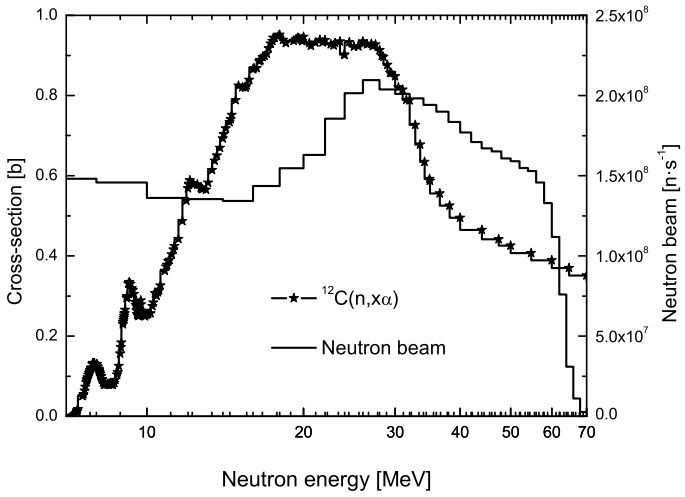


**Figure 7.9:** The region of overlap between the total $^{12}$C(n,x$\alpha$) reaction cross-section for the fast neutron detector and neutron beam provided by iThemba LABS neutron therapy, data from [NNDC, Jon92].

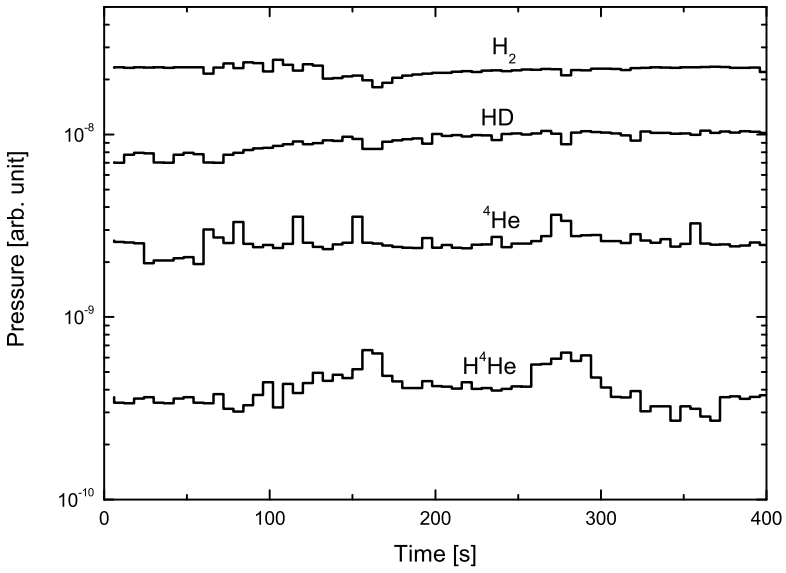


**Figure 7.10:** The measured pressure of some of the gas species in the vacuum system.

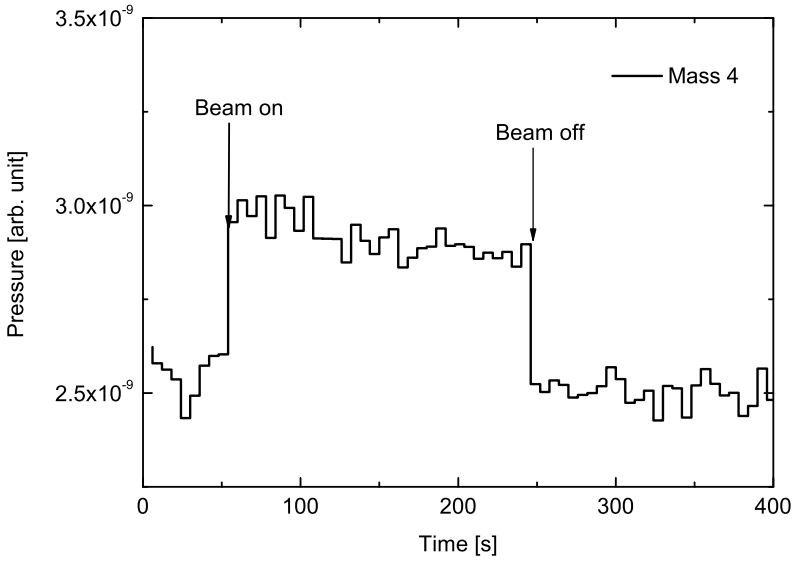


**Figure 7.11:** The partial pressure of $^4$He increases during a beam-on period.

(C), shown in Fig. 7.10, which is of interest to these measurements, is shown in Fig. 7.11. A prompt increase in $^4$He partial pressure can be seen from time 49 s, when the beam was switched on, to 243 s when it was switched off. The average increase in the partial pressure of $^4$He was $2.900 \pm 0.071 \times 10^{-9}$ arb. unit. The number of $^4$He atoms created during the beam-on period was $1.1 \times 10^8$ $^4$He/s, which is ten times less than with the proton beam.

During the accumulation mode, as seen in Fig. 7.12, the partial pressure of $^4$He increased almost linearly, whereas the partial pressure of HD decreased slightly. A data analysis of the $^4$He plot was performed with the help of the Diffrac-plus software package from Bruker Axs for diffraction data analysis [Bru11]. The background was subtracted using the Bezier function to fit data of arbitrary curvature. Fig. 7.13 shows the spectrum after the background was subtracted. This represents the $^4$He atoms produced during the beam-on period in the accumulation mode. Through the differentiation and smoothing of this data, a significant increase in the $^4$He partial pressure from time 270 to 378 s is shown in Fig. 7.14. An average increase in partial pressure of $(5.80 \pm 0.44) \times 10^{-10}$ arb. unit from time 276 to 373 s represents a production of about $2.6 \times 10^9$ $^4$He/s. The objectives of the accumulation mode was to enhance the $^4$He partial pressure when the production is low as a result of a low neutron flux incident on the reaction chamber. Looking at the results from these two modes, it can be noticed that the partial pressure of $^4$He measured in accumulation mode is significantly higher when compared with the current mode for the same neutron flux.

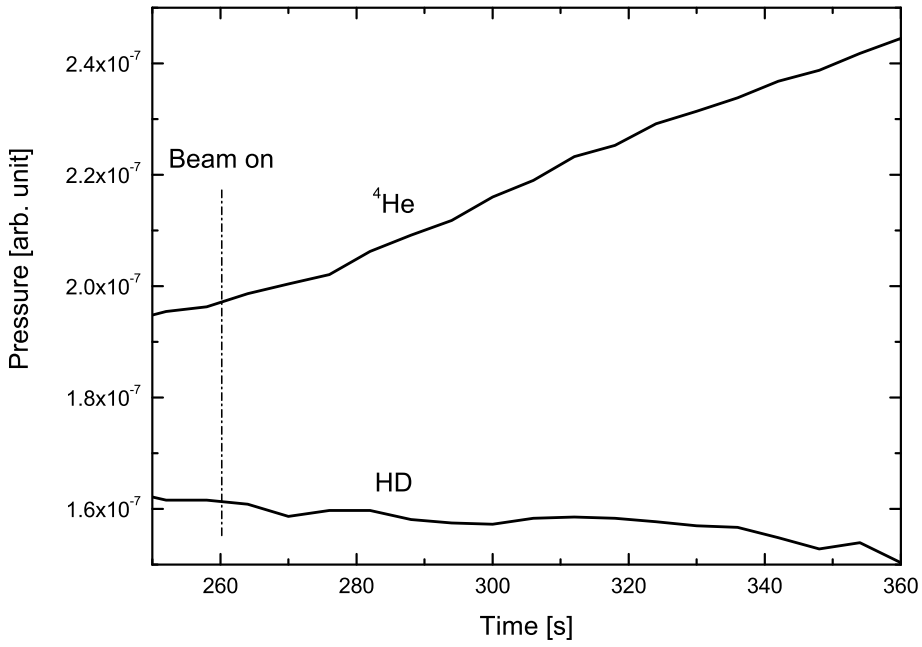


**Figure 7.12:** An example of the increase in $^4$He partial pressure during accumulation mode while HD is decreasing.

## 7.3 The slow neutron detection system

The $^6$Li conversion material is sensitive to slow neutrons and is placed inside the reaction chamber in a high flux neutron detection system for the slow neutron measurements. The slow neutrons are measured through the $^6$Li(n,$\alpha$)$^3$H reaction. As discussed earlier in Chapter 5, section 5.1.1.2, $^6$Li is widely used for slow neutron detection because of the large absorption cross-section. The reaction chamber shown in Fig 7.15 is a leak-tight stainless steel container, 4 cm long and 6 cm in diameter. This chamber could contain neutron-reactive material such as liquid $^6$Li, LiF or $^{10}$B material for the conversion of slow neutrons into $^4$He atoms. The dish shown in Fig 7.15(2) is made of aluminum and is designed to hold 10 g of liquid lithium. The enriched lithium material with 95% $^6$Li was supplied by Cambridge Isotopes [Cam10] in the form of a solid 10 g chunk. It was expected that the diffusion of $^4$He in this solid chunk would be slow, hence the design of the reaction chamber includes a copper heating rod to melt the lithium under vacuum. Due to thermal isolation and the presence of a vacuum heat loss from the dish to the environment is limited. Indirect heating via the copper rod is thus sufficient to melt the lithium. In this design, the open top flange will connect to the evacuation pipe to allow

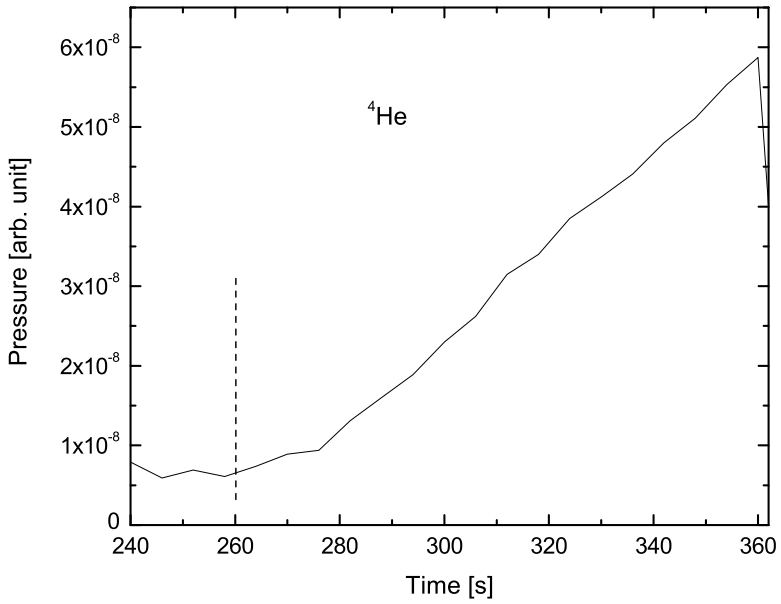


**Figure 7.13:** Background corrected spectrum of $^4$He acquired in accumulation mode when the beam was switched on.

the reaction products to flow to the RGA during operation.

The slow neutron measurements require a neutron flux energy distribution that overlaps with the cross-section profile of $^6$Li to achieve high sensitivity. The neutron beam should be at least $10^{10}$ n·s$^{-1}$ to obtain an equivalent $^4$He signal comparable to the previous test experiment results. The fast neutron beam from iThemba LABS would require a moderator to slow down the neutrons to have a profile that overlaps with the cross-section profile of $^6$Li. However, some neutrons are absorbed or scattered and, as a result, the neutron intensity is reduced during neutron moderation. The $^4$He atoms created from the resulting small beam intensity will be below the detection limit of the RGA. Necsa hosts a research reactor with beam ports that run from the core to the experimental room. This reactor produces a low energy neutron flux of about $10^{10}$n·cm$^{-2}$·s$^{-1}$. This could be an ideal place to perform the test measurements of a high flux neutron detection system with slow neutron flux.

Since the experimental setup of the high flux neutron detection system remains the same irrespective of the neutron conversion material used to detect slow or fast neutrons, the response of the system is expected to be the same provided there is a sufficient flux of thermal neutrons incident on the reaction chamber. The expected reaction rate from the slow neutron detection is calculated using the slow neutron flux profile obtained from the MCNP

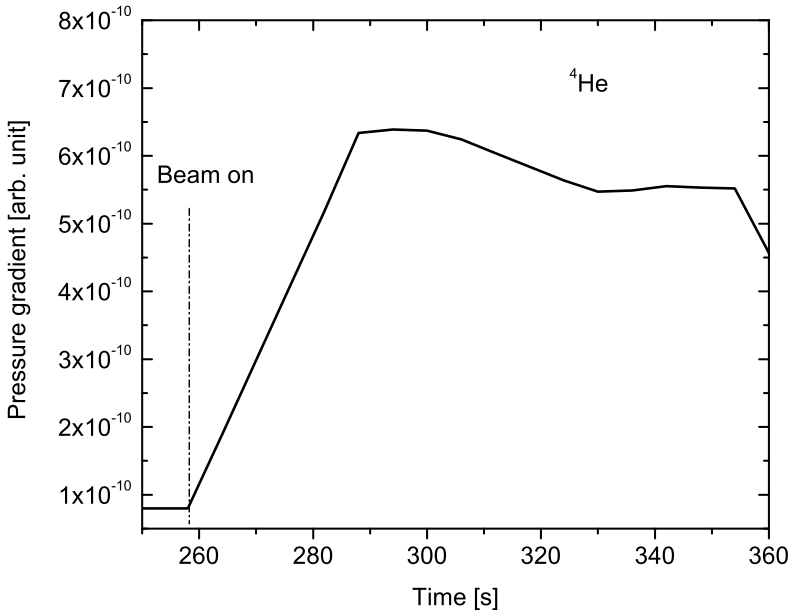


**Figure 7.14:** Through differentiation of the background subtracted data and smoothing, an increase in the $^4$He partial pressure during the beam on period in the accumulation mode of operation is clearly revealed.

simulation, discussed earlier in the Chapter 3.3, and the cross-section profile of $^6$Li material, which is intended to be used for slow neutron conversion. The neutron-induced break-up reaction rate of slow neutron flux with the $^6$Li cross-section have been performed and the results are presented in the next section.

### 7.3.1 Techniques of monitoring in-core temperature

The peak of the slow neutron flux (see section 3.6) was found to shift to higher energies as the temperature of the fuel increased. The temperature effect can be obtained by measuring the slow and fast neutron flux using a high flux neutron detection system. The neutron conversion material sensitive to slow and fast neutrons are placed in different reaction chambers. The neutron-induced break-up reaction rate in the slow neutron detector will change because of the distribution shift of lower energy neutrons to high energies. Fig. 7.16 shows the region of overlap between the $^6$Li(n,$\alpha$)$^3$H reaction cross-section in the detector, and the slow neutron flux profile. The quantity of $^6$Li material is 10 g, which represents about $1.0 \times 10^{24}$ target atoms. The $^6$Li(n,$\alpha$)$^3$H reaction

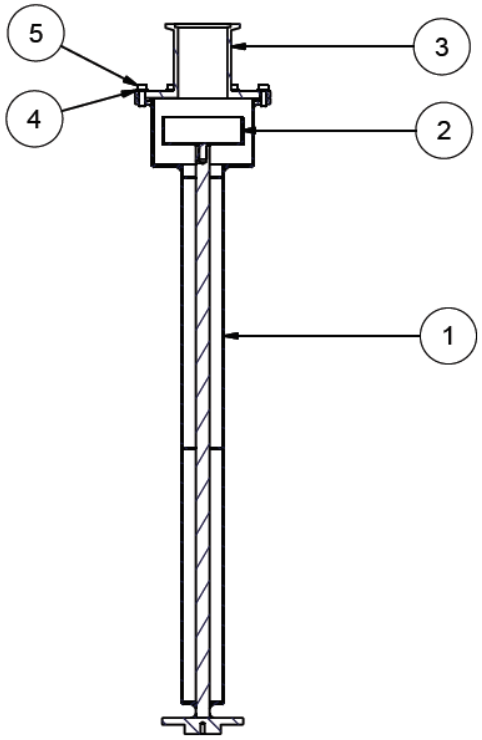


**Figure 7.15:** A schematic diagram of the lithium reaction chamber, label (1) long heating pipe, (2) lithium holder container, (3) vacuum flange. The heating is done from outside in order to avoid overheating the wires.

rate $R$ in the detector is calculated using the expression

$$R(t) = N_i(t)\phi_1(t) \times \int_0^\infty f_1(E,T)\sigma(E)dE, \tag{7.2}$$

where $N_i(t)$ is the number of remaining $^6$Li atoms as a function of time, $\phi_1(t)$ is the component level for slow neutrons, and $f_1(E,T)$ is the slow neutron spectrum function which varies with energy $E$ and temperature $T$, and $\sigma(E)$ is the microscopic cross-section. Table 7.3 presents the calculated reaction rate results, which show that the reaction rate is decreasing with an increase in temperature of the fuel. This is due to the fact that, as the lower energy neutron flux shifts to higher energies, the $^6$Li cross-section is decreasing with a $1/v$ slope, where $v$ is the neutron velocity. At the higher temperatures, for example 1200 K, the peak of the slow neutron flux becomes narrower, and this reduces the region of overlap between the cross-section and the slow neutron flux, which results in less production of $^4$He nuclei. $\beta$ The observation of this change of reaction rate with the high flux neutron detection system can be related to the change of temperature of the fuel. However, in order to obtain the total neutron flux in the core, the reaction rate has to be corrected by multiplying with a factor that compensates for the decrease of the cross-

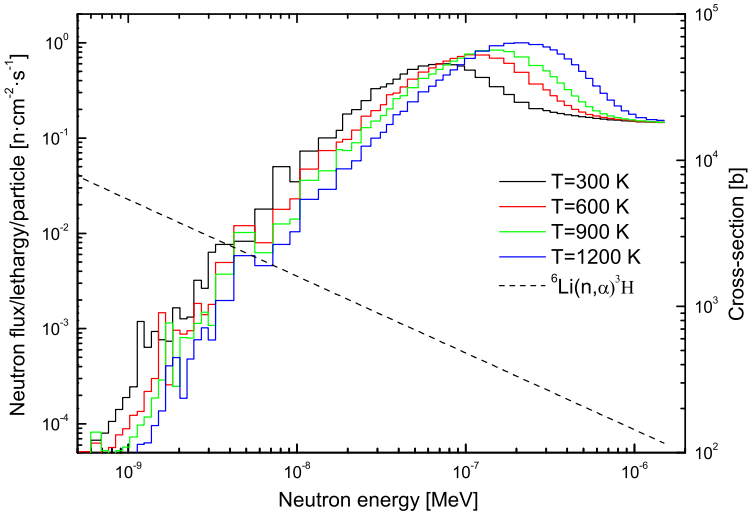


**Figure 7.16:** Convolution of slow neutron flux (solid-line) with $^{6}$Li(n, $\alpha$)$^{3}$H cross-sectional data (dash-line). The area of overlap between the flux and the cross-section can be seen, and the cross-section reduces sharply following the $1/v$ law, data from [NNDC].

**Table 7.3:** Reaction rates in the slow neutron flux energy region.

| Medium temperature (K) | Slow neutron flux (n·cm$^{-2}$·s$^{-1}$) | Reaction rate ($^{4}$He/s) |
|---|---|---|
| 300 | $2.29 \times 10^{5}$ | $1.38 \times 10^{8}$ |
| 600 | $2.54 \times 10^{5}$ | $1.32 \times 10^{8}$ |
| 900 | $2.71 \times 10^{5}$ | $1.27 \times 10^{8}$ |
| 1200 | $3.12 \times 10^{5}$ | $1.23 \times 10^{8}$ |

section. It would be ideal to use a cross-section that deviates from the $1/v$ trend in slow energy range such as $^{176}$Lu [Gei65].

# Chapter 8

# Summary

The neutron energy spectra of the PBMR reactor operating at temperatures presented in Table 3.2 were simulated using the deterministic neutron transport method by Zamonsky *et al.* [Zam10]. The peaks of the low energy neutron spectra, $E_{\mathrm{n}} < 1.2$ eV, with a shape similar to a Maxwell-Boltzmann distribution, were found to shift to higher energies and increase in flux (Fig 3.7), while the fast neutrons, $E_{\mathrm{n}} > 1.2$ eV, represented by Watt spectra remained relatively constant. The present simulations performed with the stochastic neutron transport method also gave similar results. This confirmed the general behavior of spectrum hardening in the HTGR type reactor as the fuel temperature increases. The difference between the energy spectra is in the intermediate energy region due to the difference in the cross-sectional data on the two neutron transport codes used. In this energy region, as seen in Fig. 3.7, the Doppler effect was found to be increasing as the temperature of the fuel increased. This effect enhances the neutron capture at the epithermal energy region causing a decrease in the flux before being thermalized, hence reducing the rate of the $^{235}$U fission chain reaction. The fitting of the slow neutron spectra at different temperatures and the determination of the effective neutron temperature $T_{\mathrm{n}}$ was performed with a modified Maxwell-Boltzmann distribution

$$\phi(E) = \frac{2\pi n(\vec{r})}{(\pi k T_{\mathrm{n}})^{3/2}} \left(\frac{2}{m}\right)^{1/2} E^{C} \exp(-E/kT), \tag{8.1}$$

where the parameterization of the exponent $C$ accounts for the $1/v$ dependence of the radiative neutron capture, leakage into and out of the core, and a neutron source. Geiger *et al.* [Gei65] also pointed out that when a system with neutrons emitted from a source, absorbed within the medium or leaking out of the system, the low energy neutron spectrum deviates from Maxwell-Boltzmann distribution and that the $T_{\mathrm{n}}$ is found to be above the medium temperatures $T_{\mathrm{m}}$. As seen in Table 3.3, the results of the fit shows that $T_{\mathrm{n}}$ is found to be above the $T_{\mathrm{m}}$. An increase of $T_{\mathrm{n}}$ above the $T_{\mathrm{m}}$ is caused by the incomplete thermal equilibrium and is proportional to the ratio of intermediate to slow neutron flux density. This is consistent with the results from the experiment

performed by Lui *et al.* [Liu01] and Su *et al.* [Su70]. Since the neutron energy spectrum was divided into two energy regions, slow and fast neutron spectra, the ratio of fast to slow neutrons was found to be rapidly decreasing with an increase in temperature.

The difference in the neutron flux profile, shown in Fig. 3.12 and 3.13, from within the core to the RPV provided the insights to where the high flux neutron detection system must be placed in the PBMR reactor or any other HTGR reactor in order to obtain the accurate measurements of slow and fast neutron flux in the core. If the system is placed outside the RPV, the slow neutron fluxes that will be measured are not directly from the core; fast neutrons are moderated by the graphite and other materials and enter the energy region of the slow neutron flux. The slow neutrons were depleted as they leak outside the core, hence the total flux within the RPV is less than in the core. The temperature of the core will be underestimated if determined from the neutron flux in the RPV. Hence, it is recommended that the detector system be integrated into the design of the reactor and placed in the core and not outside.

A high neutron flux detection system was developed and the principle of detection was confirmed. It was proven that a highly sensitive RGA which quantifies the residual gas under high vacuum can be implemented in the measurements of neutron fluxes. The high vacuum was achieved by the combination of turbomolecular, fore-vacuum pumps and cryogenic traps. The cryogenic traps were designed to essentially filter the residual gas by freezing and adsorption of the impurities in the system before characterization with the RGA. The cryogenic trap contained 5 Å molecular sieve pellets which operate effectively when chilled to liguid nitrogen temperature (77 K). Several reports are published [Bek03, Bew76] regarding the use of this type of sieve in removing efficiently other molecules such as hydrogen from the helium flow at a low temperature around 20 K.

The uncalibrated scale or the use of arbitrary units did not affect the $^{4}$He measurements. What was important was to observe the relative increase in the partial pressure in order to deduce the quantity of $^{4}$He atoms produced from the in-beam reactions with the high energy protons and fast neutrons.

High energy proton and fast neutron beam measurements were performed at the iThemba LABS facility in the D-line experimental and neutron therapy vaults respectively. The increase of the partial pressure of $^{4}$He was observed and compared to the expected quantity of $^{4}$He atoms created from neutron and proton induced reactions. These 66 MeV proton beam measurements were performed at different beam intensities from 50 nA to 150 nA. The response of the high flux neutron detection system during irradiation in the form of a sharp increase of $^{4}$He atoms resulting from the break-up of $^{12}$C nuclei. We found that as the beam intensity increased the $^{4}$He partial pressure increased linearly. That is, the response of the detector is directly proportional to the intensity of the incident beam. The measurements were performed in real-

time with a rise time of a few seconds after the start of the irradiation. During the beam-on period, at 50 nA the partial pressure of $^4$He remained relatively stable, but for larger intensities of 75 to 150 nA, the $^4$He partial pressure increased steadily. This increase is believed to reduce exponentially and reach equilibrium when the rate of $^4$He gas released through diffusion of the $^4$He trapped within the graphite particles and effusion through the cryogenic traps equals to the number of $^4$He nuclei produced per second. This is a defect in the present setup and should be addressed by increasing the temperature of the graphite material for faster diffusion/effusion $^4$He whilst maintaining trapping of unwanted gas species.

Fast neutron measurements with neutron beam of $10^{10}$ n/s were performed. The partial pressure of $^4$He was observed in both current and accumulation modes. The response of the high flux neutron detection system with such neutron beam intensity was comparable to the 66 MeV proton beam measurements. There was a sharp increase at the start of the irradiation and sharp decrease as the irradiation stopped. The loss of $^4$He partial partial pressure in the vacuum system was observed by comparing the experimental values with the expected values and attributed to the trapping of the gas in the molecular sieve. There was also an inevitable $^4$He background in the vacuum system suspected to originate from $^4$He atoms trapped within the cryogenic trap and the walls of the vacuum system effusing slowly with time. The trapping within the cryogenic trap is probably not due to adsorption as previous studies showed that this gas requires much lower temperature as low as 4.2 K to be efficiently adsorbed as compared to $H_2$ molecules. Trapping and subsequent effusion must therefore be due to a more physical confinement mechanism. Such background was observed with partial pressures in current mode at the limit of the sensitivity of the RGA stipulated in the user's manual [Ext11] to be in the order of $10^{-14}$ mbar. It was best seen in accumulation mode where the Helium partial pressure increases while the other gas species are trapped within the molecular sieve and the total pressure remains fairly constant.

The deconvolution calculations of the distorted Maxwell-Boltzmann distribution (slow neutron flux profile) with the $^6$Li cross-section profile, in Fig. 7.16, have been performed. The results presented in Table 7.3 shows that the $^6$Li(n,$\alpha$)$^3$He reaction rate decreases as the spectrum shifts to higher neutron energies, which is as a result of the $1/v$ slope of the cross-section. Within a reactor environment, the decrease of the reaction rate of slow neutrons with $^6$Li material could be caused by the decrease in the region of overlap between the neutron flux profile and the reaction cross-section as the temperature increases. Therefore the temperature of the moderating material must be known to correct for this effect and deduce correctly the slow neutron flux. Thus, with the slow neutron detection system, the neutron temperature change can be monitored if the temperature of the moderator is known.

A neutron detection system that uses a unique technique of measuring the reaction products from neutron-induced events was developed. It is designed

to be insensitive to $\gamma$-rays, and is able to perform real time and energy sensitive measurements of high fluxes of neutrons in a nuclear reactor environment. The inherent robustness of the sensitive part of the detector material can withstand the extremely harsh conditions associated with the nuclear reactors and last for period of times comparable to the life-time of the reactor. The results from fast neutron measurements performed at iThemba LABS facility demonstrated the proof of principle. The insensitivity of the neutron detector is mostly due to a much lower cross-section of photodissociation of $^{6}$Li and $^{12}$C nuclei as compared to neutron induced break-up reactions. The other components which were developed to improve the test measurements managed to produce positive results even though they require some future improvements for the optimal neutron flux measurements. These are the cryogenic trap, which reduced the total pressure in the vacuum system by two orders of magnitude within a short time, and the accumulation mode, which increases the concentration of helium in a small chamber.

Future work; it is planned to carry out a lower energy neutron flux measurement at Necsa to confirm the capability of the high flux neutron detection system in measuring fluxes of low energy neutrons.

Finally, we can conclude that the high flux neutron detection system can be used in the future to monitor the neutron flux in various energy regions in the HTGR reactor. This can be performed by measuring the slow and fast neutron flux with the $^{6}$Li and $^{12}$C placed in the reaction chamber separately, and observe the expected decrease in ratio of fast neutron to slow neutrons as the temperature of the fuel increases. The dimensional size of the high flux neutron detection system can be adjusted to fit into the space available in the core.

# Appendix A

The geometry and fuel specifications of the generic HTGR reactor input file to the MCNP code. This is one of the input files that simulates the reactor at different temperatures, to observe the change in the neutron energy distribution as the fuel temperature change.

```
c Cell Cards
c
 101 2 7.086e-2 -101      u=50 imp:n=1 tmp=1.03e-7 \$ uranium oxycarbide region
 102 1 5.0147e-2 101 -102 u=50 imp:n=1 tmp=1.03e-7 \$ porous carbon buffer
 103 3 9.5279e-2 102 -103 u=50 imp:n=1 tmp=1.03e-7 \$ inner pyrolytic carbon
 104 4 9.6136e-2 103 -104 u=50 imp:n=1 tmp=1.03e-7 \$ silicon carbide region
 105 5 9.5279e-2 104 -105 u=50 imp:n=1 tmp=1.03e-7 \$ outer pyrolytic carbon
 106 6 -1.7      105      u=50 imp:n=1 tmp=1.03e-7 \$ graphite matrix
c
 200 6 -1.7 -200 lat=1 u=40 imp:n=1 tmp=1.03e-7 fill= -7:7 -7:7 0:0
      40 40 40 40 40 40 40 40 40 40 40 40 40 40 40
       40 40 40 40 40 40 40 50 40 40 40 40 40 40 40
        40 40 40 40 50 50 50 50 50 50 50 40 40 40 40
         40 40 40 50 50 50 50 50 50 50 50 50 40 40 40
          40 40 50 50 50 50 50 50 50 50 50 50 50 40 40
           40 40 50 50 50 50 50 50 50 50 50 50 50 40 40
            40 40 50 50 50 50 50 50 50 50 50 50 50 40 40
             40 50 50 50 50 50 50 50 50 50 50 50 50 50 40
              40 40 50 50 50 50 50 50 50 50 50 50 50 40 40
               40 40 50 50 50 50 50 50 50 50 50 50 50 40 40
                40 40 50 50 50 50 50 50 50 50 50 50 50 40 40
                 40 40 40 50 50 50 50 50 50 50 50 50 40 40 40
                  40 40 40 40 50 50 50 50 50 50 50 40 40 40 40
                   40 40 40 40 40 40 40 50 40 40 40 40 40 40 40
                    40 40 40 40 40 40 40 40 40 40 40 40 40 40 40
 201 0 -201 lat=1 fill=40 imp:n=1 u=41 tmp=1.03e-7 fit 15 \$ cubic region
c
 300 0 -300 fill=41 u=5 imp:n=1 tmp=1.03e-7 \$ fuel compact region
c
 301 0 300 -301 u=5 imp:n=1 tmp=1.03e-7 \$  void outside fuel pin
```

```
 302 7 8.725580e-2 301 u=5 imp:n=1 tmp=1.03e-7 \$ grphite wall
c
400 0 -400 u=6 imp:n=1 tmp=9.2e-8 \$ larger coolant hole
401 7 8.725580e-2 400 u=6 imp:n=1 tmp=1.03e-7 \$ graphite wall
c
500 7 8.725580e-2 -501 502 -503 504 -505 506 tmp=1.03e-7 lat=2 u=4 imp:n=1
       fill=-11:11 -11:11 0:0
        4 4 4 4 4 4 4 4 4 4 4 4 4 4 4 4 4 4 4 4 4 4 4
        4 4 4 4 4 4 4 4 4 4 4 5 5 6 5 5 6 5 5 6 5 5 4
        4 4 4 4 4 4 4 4 4 4 5 6 5 5 6 5 5 6 5 5 6 5 4
        4 4 4 4 4 4 4 4 4 6 5 5 6 5 5 6 5 5 6 5 5 6 4
        4 4 4 4 4 4 4 4 5 5 6 5 5 6 5 5 6 5 5 6 5 5 4
        4 4 4 4 4 4 4 5 6 5 5 6 5 5 6 5 5 6 5 5 6 5 4
        4 4 4 4 4 4 6 5 5 6 5 5 6 5 5 6 5 5 6 5 5 6 4
        4 4 4 4 4 5 5 6 5 5 6 5 5 6 5 5 6 5 5 6 5 5 4
        4 4 4 4 5 6 5 5 6 5 5 6 5 5 6 5 5 6 5 5 6 5 4
        4 4 4 6 5 5 6 5 5 6 5 5 6 5 5 6 5 5 6 5 5 6 4
        4 4 5 5 6 5 5 6 5 5 6 5 5 6 5 5 6 5 5 6 5 5 4
        4 5 6 5 5 6 5 5 6 5 5 6 5 5 6 5 5 6 5 5 6 5 4
        4 5 5 6 5 5 6 5 5 6 5 5 6 5 5 6 5 5 6 5 5 4 4
        4 6 5 5 6 5 5 6 5 5 6 5 5 6 5 5 6 5 5 6 4 4 4
        4 5 6 5 5 6 5 5 6 5 5 6 5 5 6 5 5 6 5 4 4 4 4
        4 5 5 6 5 5 6 5 5 6 5 5 6 5 5 6 5 5 4 4 4 4 4
        4 6 5 5 6 5 5 6 5 5 6 5 5 6 5 5 6 4 4 4 4 4 4
        4 5 6 5 5 6 5 5 6 5 5 6 5 5 6 5 4 4 4 4 4 4 4
        4 5 5 6 5 5 6 5 5 6 5 5 6 5 5 4 4 4 4 4 4 4 4
        4 6 5 5 6 5 5 6 5 5 6 5 5 6 4 4 4 4 4 4 4 4 4
        4 5 6 5 5 6 5 5 6 5 5 6 5 4 4 4 4 4 4 4 4 4 4
        4 5 5 6 5 5 6 5 5 6 5 5 4 4 4 4 4 4 4 4 4 4 4
        4 4 4 4 4 4 4 4 4 4 4 4 4 4 4 4 4 4 4 4 4 4 4
c
 601 0 -601 *fill=4 (0 0 0 30 120 90 60 30 90 90 90 0) u=3 tmp=1.0e-7 imp:n=1
 602 8 8.725580e-2 -602 u=3 imp:n=1 tmp=1.024e-7 \$ top reflector column
 603 8 8.725580e-2 -603 u=3 imp:n=1 tmp=1.024e-7 \$ bottom reflector
 604 0 601 #602 #603    u=3 imp:n=1 tmp=1.024e-7 \$ void outside column
c
 700 9 8.725580e-2 -700 u=2 imp:n=1 tmp=1.024e-7 \$ replaceable reflector
 701 0 700 u=2 imp:n=1 tmp=1.024e-7 \$ void outside the
c
 800 0 -800 u=2 lat=2 imp:n=1 tmp=1.024e-7 fill=3 fill=-11:11 -11:11 0:0
     2 2 2 2 2 2 2 2 2 2 2 2 2 2 2 2 2 2 2 2 2 2 2
     2 2 2 2 2 2 2 2 2 2 2 2 2 2 2 2 2 2 2 2 2 2 2
     2 2 2 2 2 2 2 2 2 2 2 2 2 2 2 2 2 2 2 2 2 2 2
     2 2 2 2 2 2 2 2 2 2 2 2 2 2 2 2 2 2 2 2 2 2 2
```

```
     2 2 2 2 2 2 2 2 2 2 2 3 3 3 3 3 3 2 2 2 2 2
     2 2 2 2 2 2 2 2 2 2 3 3 3 3 3 3 3 3 2 2 2 2
     2 2 2 2 2 2 2 2 2 3 3 3 3 3 3 3 3 3 2 2 2 2
     2 2 2 2 2 2 2 2 3 3 3 2 2 2 2 3 3 3 2 2 2 2
     2 2 2 2 2 2 2 3 3 3 2 2 2 2 2 2 3 3 3 2 2 2 2
     2 2 2 2 2 2 3 3 3 2 2 2 2 2 2 2 3 3 3 2 2 2 2
     2 2 2 2 2 3 3 3 2 2 2 2 2 2 2 2 3 3 3 2 2 2 2
     2 2 2 2 2 3 3 2 2 2 2 2 2 2 2 2 3 3 2 2 2 2 2
     2 2 2 2 3 3 3 2 2 2 2 2 2 2 2 3 3 3 2 2 2 2 2
     2 2 2 2 3 3 3 2 2 2 2 2 2 2 3 3 3 2 2 2 2 2 2
     2 2 2 2 3 3 3 2 2 2 2 2 2 3 3 3 2 2 2 2 2 2 2
     2 2 2 2 3 3 3 2 2 2 2 2 3 3 3 2 2 2 2 2 2 2 2
     2 2 2 2 3 3 3 3 3 3 3 3 3 2 2 2 2 2 2 2 2 2 2
     2 2 2 2 3 3 3 3 3 3 3 3 2 2 2 2 2 2 2 2 2 2 2
     2 2 2 2 2 3 3 3 3 3 3 2 2 2 2 2 2 2 2 2 2 2 2
     2 2 2 2 2 2 2 2 2 2 2 2 2 2 2 2 2 2 2 2 2 2 2
     2 2 2 2 2 2 2 2 2 2 2 2 2 2 2 2 2 2 2 2 2 2 2
     2 2 2 2 2 2 2 2 2 2 2 2 2 2 2 2 2 2 2 2 2 2 2
     2 2 2 2 2 2 2 2 2 2 2 2 2 2 2 2 2 2 2 2 2 2 2
c
 900 0 -900 fill=2 imp:n=1 tmp=9.482e-8 \$ reactor core
 901 10 -7.6  900  -901  tmp=9.482e-8    imp:n=1 \$ outside the core
 902 11 -7.8  901  -902  tmp=9.482e-8   imp:n=1
 903  0    902  -903   tmp=9.482e-8     imp:n=1
 904  0    903               imp:n=0
c

c Surface Cards
c
 101 so 0.0175 \$ uranium oxycarbide surface
 102 so 0.0275 \$ porous carbon buffer surface
 103 so 0.0315 \$ inner pyrolytic carbon surface
 104 so 0.0350 \$ silicon carbide surface
 105 so 0.0390 \$ outer pyrolytic carbon
c
 200 rpp -0.04755 0.04755 -0.04755 0.04755 -0.04755 0.04755
 201 rpp -0.71325 0.71325 -0.71325 0.71325 -0.04755 0.04755
c
 300 cz 0.6225 \$ fuel compact cylinder surface
 301 cz 0.635 \$ gap surface outside the fuel compacts
c
 400 cz 0.432 \$ largercylinder coolant hole surf
c
 501 px 0.9398
```

```
 502 px -0.9398
 503 p 1 1.7320508076 0 1.8796
 504 p 1 1.7320508076 0 -1.8796
 505 p -1 1.7320508076 0 1.8796
 506 p -1 1.7320508076 0 -1.8796
c
 601 hex 0 0 79.3 0 0 793 17.9985 0 0 \$ hexagonal fuel surf
 602 hex 0 0 872.3 0 0 79.3 17.9985 0 0 \$ top refector
 603 hex 0 0 0 0 0 79.3 17.9985 0 0 \$ bottom refector
c
 700 hex 0 0 0 0 0 951.6 18.9985 0 0 \$ central and side refl
 800 hex 0 0 0 0 0 951.6 18.05 0 0 \$ Lattice cell
 900 rcc 0 0 0 0 0 951.6 441.63 \$ outer barrel of core
 901 rcc 0 0 0 0 0 955.0 451.63
 902 rcc 0 0 0 0 0 955.0 470.63
 903 so 1500
c

c
c Run a neutron problem
c
mode n p
phys:n
c Material cards
m1 6000.73c 1
mt1 grph.17t
c
m2 92235.73c 1.06e-3 92238.73c 1.004e-2 8016.73c 2.30e-2
mt2 u/o2.17t o2/u.17t
c
m3 6000.73c 1
mt3 grph.17t
c
m4 6000.73c 0.048068 14028.73c 8.53e-3 14029.73c 4.23e-4 14030.73c 2.68e-4
mt4 grph.17t
c
m5 6000.73c 1
mt5 grph.17t
c
m6 6000.73c 1
mt6 grph.17t
c
m7 6000.73c 8.7255e-02 5010.73c 7.22e-07
mt7 grph.17t
```

```
c
m8 6000.73c 8.7255e-02 5010.73c 7.22e-07 \$ grpht,top \& bottom refl
mt8 grph.17t
c
m9 6000.73c 8.7255e-02 5010.73c 7.22e-07 \$ grpht,replaceable refl
mt9 grph.17t
c
m10   6000.73c  -4.300e-04     \$ C-nat
      7014.73c  -6.723e-04     \$ N-14
      7015.73c  -2.673e-06     \$ N-15
      8016.73c  -5.385e-04     \$ O-16
      14028.73c  -2.900e-03    \$ Si-nat
      15031.73c  -2.200e-04    \$ P-31
      16032.73c  -1.900e-04    \$ S-nat
      22046.73c  -2.000e-04    \$ Ti-nat
      23000.73c  -9.100e-04    \$ V-nat
      24050.73c  -7.734e-03    \$ Cr-50
      24052.73c  -1.550e-01    \$ Cr-52
      24053.73c  -1.792e-02    \$ Cr-53
      24054.73c  -4.545e-03    \$ Cr-54
      25055.73c  -1.490e-02    \$ Mn-55
      26054.73c  -3.837e-02    \$ Fe-54
      26056.73c  -6.186e-01    \$ Fe-56
      26057.73c  -1.441e-02    \$ Fe-57
      26058.73c  -1.952e-03    \$ Fe-58
      27059.73c  -1.800e-03    \$ Co-59
      28058.73c  -6.281e-02    \$ Ni-58
      28060.73c  -2.486e-02    \$ Ni-60
      28061.73c  -1.093e-03    \$ Ni-61
      28062.73c  -3.530e-03    \$ Ni-62
      28064.73c  -9.236e-04    \$ Ni-64
      29063.73c  -3.082e-03    \$ Cu-63
      29065.73c  -1.417e-03    \$ Cu-65
      33075.73c  -7.000e-05    \$ As-nat
      42092.73c  -2.020e-02    \$ Mo-nat
      73181.73c  -4.991e-04    \$ Ta-181
      82206.73c  -1.916e-05    \$ Pb-206
      82207.73c  -1.766e-05    \$ Pb-207
      82208.73c  -4.207e-05    \$ Pb-208
c
m11  6000.73c -2.300e-03      \$ c-nat
     25055.73c -1.570e-02     \$ mn-55
     14028.73c -2.700e-03     \$ si-nat
     24050.73c -3.757e-05     \$ cr-50
```

```
     24052.73c -7.533e-04     \$ cr-52
     24053.73c -8.706e-05     \$ cr-53
     24054.73c -2.208e-05     \$ cr-54
     28058.73c -4.718e-03     \$ ni-58
     28060.73c -1.866e-03     \$ ni-60
     28061.73c -8.211e-05     \$ ni-61
     28062.73c -2.652e-04     \$ ni-62
     28064.73c -6.937e-05     \$ ni-64
     27059.73c -2.000e-04     \$ co-59
     15031.73c -1.800e-04     \$ p-31
     16032.73c -1.500e-04     \$ s-nat
     13027.73c -3.700e-04     \$ al-27
     26054.73c -5.485e-02     \$ fe-54
     26056.73c -8.842e-01     \$ fe-56
     26057.73c -2.060e-02     \$ fe-57
     26058.73c -2.791e-03     \$ fe-58
     29063.73c -8.905e-04     \$ cu-63
     29065.73c -4.095e-04     \$ cu-65
     8016.73c -1.157e-04      \$ o-16
     73181.73c -5.000e-04     \$ ta-181
     7014.73c -1.444e-04      \$ n-14
     7015.73c -5.742e-07      \$ mo-nat
     33075.73c -1.300e-04     \$ as-nat
     23000.73c -1.000e-04     \$ v-nat
     5010.73c -2.212e-06      \$ b-10
     5011.73c -9.788e-06      \$ b-11
c KCODE description
c
kcode 50000 1.0 200 500
ksrc  180.5 2 120 0 202.5 436.15 -202.5 0 515.45
c Tallies description
c
fc4 fuel kernels
f4:n  101
e4    1.1024e-11 1198i 10
c
fc14 fuel pin
f14:n  201
e14  1.1024e-11 1198i 10
c
fc24 reactor core
f24:n  900
e24  1.1024e-11 1198i 10
c
```

```
fc44 Neutron flux within the flector
f44:n  700
e44  1.1024e-11 1198i 10
c
fc54 Outside core barrel
f54:n  901
e54  1.1024e-11 1198i 10
c
fc64 outside RPV
f64:n  902
e64  1.1024e-11 1198i 10
fc74 void outsie the reactor building
f74:n  903
e74  1.1024e-11  1198i 10
c nps 100
c
c ctme   60
c prdmp   2j 1 1 1
c For debugging purposes
print
```

# References

[Adl09] Adloff J.P., One hundred years after the discovery of radioactivity, Oldenbourg Wissenschaftsverlag, Pg. 123, (2009).

[Agr88] Agrawal P. C. and Ramsey B. D., Nucl. Instr. and Meth. A, Vol. 273, Issue 1, Pg. 331, (1988).

[Ale03] Alevra A. V. and Thomas D. J., Rad. Prot. Dosim., Vol. 107, No. 1-3, Pg. 37, (2003).

[Arn39] Arnot F. L. and Marjorie B. M'Ewen, Proceedings of the Royal Society of London, Series A, Maths. and Phys. Sci. Vol 171, No. 944, Pg. 106 (1939).

[Atw74] Atwell T. L. and Menlove H. O., Measurements of the time resolution of several $^4$He and $CH_4$ proportional counters in Nuclear safeguards research program status report, September-December 1973, Los Alamos Scientific Laboratory report LA-5557-PR (February 1974).

[AVR90] AVR-experimental high-temperature reactor-21 years of successful operation for a future energy technology. VDI-Verlag Düsseldorf (1990).

[Bau10] Baumann T., Neutron Detection & Spectroscopy, National Superconducting Cyclotron Laboratory, Michigan state university, (2010).

[Bau89] Bäumer R., THTR 300 Erfahrungen mit einer fortschrittlichen Technologie, Atomwirtschaft Mai, (1989).

[Bae02] Baechler S., Kardjilovc N., Dierickd M., Joliee J., Kühneb G., Lehmannb E., and Maternae T., Nucl. Instr. and Meth. A, Vol. 491, Issue 3, Pg. 481, (2002).

[Bec07] Beckwith T. G., Marangoni D. R., and Lienhard H. J. Mechanical Measurements, 6th Edition, Pearson Prentice Hall, (2007).

[Bek03] Bekris N., Caldwell-Nichols C., and Hutter E., Fusion Engineering and Design, Vol. 69, Pg. 21-25, (2003).

[Ber05] Bergenwall B. E., Atac A., and Kulander S., Nucl. Phys. A, Vol. 747, Pg. 152, (2005).

[Ber65] Berman B. L., Bramblett J., Cadwell J. T., Harvey R. R., and Fultz S. C., Phys. Rev. Lett., Vol. 15, Pg. 727, (1965).

[Bet36] Bethe H. A. and Placzek G., Phys. Rev., Vol. 51, Pg. 450, (1936).

[Bew76] Bewilogua L., Binneberg A., and Jackel M., Cryogenics, Pg. 238, (1976).

[Bol70] Boland J. F., Nuclear Reactor Instrumentation (in-core), An AEC monograph, Argonne national laboratory, Gordon and Breach Science publisher, Inc. New York, (1970).

[Bol61] Bollinger L. M. and Thomas G. E., Rev. Sci. Instr., Vol. 32, Pg. 1044, (1961).

[Bol62] Bollinger L. M., Thomas G. E., and Ginther R. J., Nucl. Instr. and Meth., Vol. 17, Issue 1, Pg. 97-116, September (1962).

[Bra60] Bramblett R. L., Ewing R. I., and Bonner T. W., Nucl. Instr. and Meth., Vol. 9, Issue 1, Pg. 1, (1960).

[Bre36] Breit G. and Wigner E., Phys. Rev., Vol. 49, Pg. 519, (1936).

[Bre09] Brewer R., MCNP5 criticallity primer, 3rd edition, *online: http://mcnp-green.lanl.gov/publication/pdf/CriticalityPrimerIII-LA-UR-09-00380.pdf* (2009).

[Bri64] Brinkley T. A., Robson B. A., and Titterton E. W., Proc. Phys. Soc., Vol. 84, (1964).

[Bri82] Brixy H., Hecker R., Oehmen J., Barbonus P., and Hans R., International Atomic Energy Agency IAEA-TC-389/6-7, Pg. 1, (1982).

[Bro59] Brooks F. D., Nucl. Instr. and Meth., Vol 4, Pg. 151, (1959).

[Bro86] Bross A. D., Nucl. Instr. Meth. A, Vol. 247, Issue 2, Pg. 319, (1986).

[Bro74] Brown D. P., IEEE Trans. Nucl. Sci. NS-21 (1), Pg. 763, (1974).

[Bru11] Bruker AXS, X-ray Diffraction-XRD Phase analysis, *www.bruker-axs.com*

[Cam10] Cambridge Isotope Laboratories, Inc. (CIL), *http://www.isotope.com/cil/index.cfm*, United State of America, (2010).

[Cra] Crane T. W. and Baker M. P., Neutron Detectors, Chapter 13, Pg. 379-406, *www.fas.org/sgp/othergov/doe/lanl/lib-www/la-pubs/00326408.pdf.*

[Cra70] Craun R. L. and Smith D. L., Nucl. Instr. Meth., Vol. 80, Pg. 239, (1970).

[Dek94] De Kruijf W. J. M., Reactor Physics Analysis of the Pin Cell Doppler Broadening Effect in a Thermal Nuclear Reactor, PhD thesis, Delft University of Technology, Netherlands, (1994).

[Dev09] De Villiers G. J., In-core Temperature Measurements for the PBMR Using Fiber Bragg Gratings, MSC thesis, University of Stellenbosch, Department of Engineering, South Africa, (2009).

[Deu60] Deutsch R. W., Reactor of Science and Technology (J.N.E. Parts A/B), 1961, Vol. 14, Pg. 168, (1960).

[Dud76] Duderstadt J. J. and Hamilton, L. J., Nuclear Reactor Analysis, John Wiley & Sons, Inc., New York (1976).

[Eis09] Eisen Y. and Shor A., IEEE Trans. Nucl. Sci., Vol. 56, Issue 4, (2009).

[Ell73] Ellis W. H., Cooper J. L., and Sanders G. H., IEEE Trans. Nucl. Sci. NS-20(1), Pg. 639, (1973).

[Ell93] Ellis W. H., Ferrari A. M., Choi W. Y., and He Q., IEEE Trans. Nucl. Sci. NS-40(4), Pg. 826, (1993).

[Eva76] Evans A. E., Menlove H. O., Walton R.B., and Smith D. B., Nucl. Instr. Meth A., Vol. 133, Pg. 577, (1976).

[Ext11] Extorr Inc., Extorr RGA User Manual, 307 Columbia Road, New Kensington, PA 15068, www.extorr.com.

[Fan04] Fanourakis G. K., Geralis T., Kousouris K., Zachariadou K., Giomataris I., Giokaris N., Loudos G., Lebessi M., and Stiliaris E., Nucl. Instr. and Meth. A, Vol. 527, Pg. 62, (2004).

[Fow63] Fowler I. L., Rev. Sci. Instr., Vol. 34, Pg. 731, (1963)

[Fran82] Franklin R. and Rodriguez C., Approach to the HTGR Core Outlet Temperature Measurements in the United States, General Atomic Company, USA, (1982).

[Gar60] Garnier M., Gauvin H., and Sabaoun W., J. Phys., Vol. 21, Pg. 893, (1960).

[Gei65] Geiger K. W. and Van Der Zwan L., Metrologia, Vol. 2, Issue 1, Pg. 1, (1965).

[Ges11] Geslot B., Vermeeren l., Filliatre P., Legrand Lopez A., Barbot L., Jammes C., Bréaud S., Oriol L., and Villard J.-F., Rev. Sci. Instr., Vol. 82, Issue 033504, Pg. 1-7, (2011).

[Gio96] Giomataris Y., Rebourgeard Ph., Robert J. P., and Charpak G., Nucl. Instr. and Meth. A, Vol. 376, Pg. 29, (1996).

[Gle88] Glesius F. and Kniss T., IEEE Trans Nucl. Sci., Vol 35, Issue 1, Pg. 867, (1988).

[Gnu08] Gnuplot, *http://www.gnuplot.info/*, (2008).

[Gra10] Graphit Kropfmühl AG Company, *www.gk-graphite.de/graphite-supplier.html*, Germany, (2010).

[Ham06] Hamiltonian D., Neutron Interaction with Matter, European commission, institute for transuranium elements. Posfach 2340, 76125, Germany, (2006).

[Jia10] He J., Gao K., Vidali G., Bennett C. J., Kaiser R. I., The Astrophysical Journal, Vol. 721, Pg. 1656, (2010).

[Hum51] Hummel V. and Hamermesh B., Phys. Rev., Vol., 82, Issue 1, (1951).

[Hui04] Hussein Esam M. A., Handbook of Radiation Probing, Gauging, Imaging, and Analysis, Vol. I: Basics and Techniques and II: Application and Design, (2004).

[Ion04] Ion S., Nicholls D., Matzie R., and Matzner D., Pebble Bed Modular Reactor-The First Generation IV Reactor To Be Constructed, Nuclear Energy, Vol. 43, No. 1, (2004).

[Jon88] Jones D. T. L., Yudelev M., and Hendriks W. L. J., Radiat. Prot. Dosim., Vol. 23, Pg. 365, (1988).

[Jon92] Jones D. T. L., Symons J. E., Fulcher T. J., Brooks F. D., Nchodu M. R., Allie M. S., Buffler A., and Oliver M. J., Medical Physics, Vol. 19, No. 5, Pg. 1285, (1992).

[Kah65] Kahn S., Harman R., and Forgue V., Nucl. Sci. Eng., Vol. 23, Pg. 8, (1965).

[Hon07] Kim H. C., Kim S. Y., Kim J. K., and Noh J. M., Monte Carlo Benchmark Calculations for 400 MWth PBMR Core, *www.icenes2007.org/icenes...pdf/.../MONTE%20CARLO.pdf*

[Kno00] Knoll G. F., Radiation Detection and Measurement, 3rd edition, John Wiley & Sons, Inc., New York (2000).

[Kos03] Koster A., *et al.*, PBMR Design For The Future, Nuclear Engineering and Design 222, Pg. 231, (2003).

[Lam66] Lamarsh J. R., Introduction to Nuclear Reactor Theory, Addison-Wesley Publishing Company, Inc. USA, (1966).

[Lau09] Laurie M., Futterer M. A., Lapetite J. M., Fourrez S., and Morice R., Advanc. Nucl. Instr. Meas. Meth. and App. (ANIMMA), Pg. 1, (2009).

[Lee99] Lee W., Cho G., Kim K., Kim H. J., Choi Y., and Park M. K., Nucl. Sci. Symp., Vol. 2, Pg. 772, (1999).

[Liu01] Liu J. C., Bull J. S., Drozdoff J., May R., and Vylet V., Radiat. Prot. Dosim., Vol. 96, Pg. 333, (2001).

[Mad83] Madland D. G. and Nix J. R., Nucl. Sci. Eng., Vol. 81, Pg. 213, (1982).

[Man93] Manual on the use of Thermocouples in Temperature Measurements, ASTM committee E20 on Temperature Measurement, (1993).

[Mar00] Martin J. E., Physics for Radiation Protection, John Wiley & Sons, Inc., New York, USA (2000).

[Dou05] McGregor D. S., Ohmes M. F., Ortiz R. E., Ahmed A. S. M., and Shultis J. K., Nucl. Instr. and Meth. A, Vol. 554, Pg. 494, (2005).

[MCN09] Monte Carlo N-Particle transport code, MCNP 5 & MCNPX 2.6, *http://mcnp-green.lanl.gov/*, (2009).

[Mil86] Miller P. E. and Denton M. B., J. Chem. Educ., Vol. 63, No. 7, Pg. 617, (1986).

[Mil62] Mills Jr. W. R., Caldwell R. I., and Morgan I. L., Rev. Sci. Instr., Vol. 33, Pg. 866, (1962).

[Mon84] Montague R. G., Harrison M. F. A., and Smith A. C. H., J. Phys. B: At. Mol. Phys. Vol. 17, (1984).

[Bha05] Mukherjee B., Makowski D., and Simrock S., Nucl. Instr. and Meth. A, Vol. 545, Pg. 830, (2005).

[Nab84] Nabielek H., Kaiser G., Huschka H., Ragoss H., Wimmers M., and Theymann W., Fuel for Pebble-Bed HTRs. Nucl. Eng. Des., vol. 78, Pg. 155, (1984).

[NNDC] National Nuclear Data Center, Evaluated Nuclear Data File (ENDF-B), retrieval and plotting, *http://www.nndc.bnl.gov/sigma*.

[NTemp04] Neutron Flux with Maxwell Distribution, Chapter 5, *http://www.ansn-jp.org/item_file/2004-RP-01-5.pdf.*

[Nic96] Nicholls D. R., Utility Requirements for HTGRs, Technical Committee Meeting on High Temperature Cooled Reactor Technology Development, JHB South Africa, 13-15 Nov. (1996).

[Nic55] Nicholsonm K. P. and Snellingm G. F., Atomic Energy Research Establishment, Harwell, Berks, Br. J. Appl. Phys., Vol. 6, Pg. 104, (1955).

[Nis95] Nishikawa M., Uetake M., Tanaka K., and Shiraishi T., Fusion Technol., vol. 28, Pg. 717, (1995).

[NDS11] Nuclear data society, *www-nds.iaea.org/exfor/servlet/E4SMakeE4*, (2011).

[Nucl11] Nuclear Physics and Reactor Theory Fundamentals Handbook, Department of Energy, *www.scribd.com/doc/2324756/Handbook-Nuclear-Physics.*

[Ott85] Ott K. O. and Neuhold R. J., Introductory Nuclear Reactor Dynamics, American Nuclear Society, 555 North Kensington Avenue la grange Park, Illinois, 60525, United states of America, (1985).

[Pau58] Paul W., Reinhard H. P., and Von Zahn U., Z. Phys., Vol. 152, Pg. 143, (1958).

[Pan08] Pancin J., Andriamonje S., Aune S., Giganon A., Giomataris Y., Lecolley J. F., Riallot M., and Rosa R., Nucl. Instr. and Meth. A, Vol. 592, Pg. 104, (2008).

[Pfe10] Pfeiffer Balzers, Turbo-Molecular Pump TPH 170, TPU 170 Operation Instructions, 1st edition, 8610/N 2449.

[Pol91] Pollock D. D., Thermocouples: Theory and Properties, CRC Press, (1991).

[Pro06] Procter G., Proceedings HTR2006: 3rd International Topical Meeting on High Temperature Reactor Technology, JHB South Africa, Oct. 1-4 (2006).

[Rei79] Reily T. D., The Measurements of Leached Hulls, Los Alamos Scientific Laboratory Report LA-7784-MS, Pg. 57, (1979).

[Reu08] Reuss P., Nuclear Engineering Neutron Physics, EDP Science, France (2008).

[Rice74] Rice-Evans P., Spark, Streamer, Proportional, and Drift Chambers, The Richelieu press, London, (1974).

[Rin] Rinard P., Neutron Interactions with Matter, chapter 12. *www.fas.org/sgp/othergov/doe/lanl/lib-www/la.../00326407.pdf*, (1991).

[Rit68] Ritchie J. B. and Patterson J., Proc. Inst. Mech, Engrs., Vol. 69, Pg. 707, (1968).

[Sak80] Sakai E., Kubo K., and Yoshida H., IEEE Trans Nucl. Sci. NS-27(1), Pg. 776, (1980).

[Sak83] Sakai E., Usui S., Ohkado H., Hayashi Y., and Nakatani H., IEEE Trans. Nucl. Sci. NS-30(1), Pg. 802, (1983).

[Sha69] Shalev S., Fishelson Z., and Cuttler J. M., Nucl. Instr. Meth., Vol. 71, Pg. 292, (1969).

[Sla04] Slabber J., 2nd International Topical Meeting on High Temperature Reactor Technology, Beijing China, Paper B15, Pg. 1, (2004).

[Sob53] Soberman R. K., Korff S. A., Friedland S. S., and Katzenstein H. S., Rev. Sci. Instr. 24, 1058 (1953).

[Sen06] Sen S., Albornoz F., and Reitsma F., Proceedings HTR2006: 3rd International Topical Meeting on High Temperature Reactor Technology, JHB South Africa, 1-4 Oct. (2006).

[Su70] Su C. S. and Liu T. C., Nucl. Instr. and Meth., Vol. 89, Pg. 233, (1970).

[Sto66] Stokes A. J., Meal T. J., and Meyers J. E., Jr., IEEE Trans. Nucl. Sci. NS-13(1), Pg. 630, (1966).

[Syn04] Syntfeld A., *et al.*, Nuclear Science Symposium Conference Record, IEEE, Vol. 3, Pg. 1545, (2004).

[Tat09] Jevremovic T., Nuclear Principles in Engineering, 2nd edition, Springer Science+Business Media, LLC, New York, USA (2009).

[Tur95] Turner J. E., Atoms, Radiation, and Radiation Protection, 2nd edition, John Wiley & Sons, Inc., New York, USA (1995).

[Ued11] Ueda H., Tanaka H., Maruhashi A., Ono K., and Sakurai Y., Applied Radiation and Isotopes, Pg. 1, (2011).

[Val85] Valentine K. H., Kopp M. K., Allin G. W., Clay W. T., and Miller V. C., IEEE Trans Nucl. Sci., Vol. 32, Issue 1, Pg. 384, (1985).

[Joh11] Van Rooyen J., Transport and Shielding of Ionizing Shielding, unpublished.

[Ven05] Venter P. J., Mitchell M. N., and Fortier F., PBMR Reactor Design and Development, 18th Int. Conf. on Struct. Mch. in reactor Tchn. (2005).

[Vent05b] Venter P. J., Integrated Design Approach of the Pebble Bed Modular Using Models, 18th Int. Conf. on Struct. Mch. in reactor Tchn., SMiRT18-SO1-5, Pg. 4428, (2005).

[Ver74] Verghese K., Bohannon J. R., and Kowalczuk A. D., Nucl. Instr. and Meth., Vol. 74, Pg. 355, (1969).

[Wat52] Watt B. E., Phys. Rev., Vol. 87, Pg. 1037, (1952).

[Wiki11] Wikipedia cross-sectional cut of turbomolecular pump, *http://en.wikipedia.org/wiki/Turbomolecular_pump*, (2011).

[Wil50] Wilkinson D. H., Ionization Chambers and Counters, Cambridge University Press, Cambridge, Massachusetts, (1950).

[Wil94] Willms R. S., Taylor D. J., Enoeda M., and Okuno K., Fusion Eng. Des., 28 Proc. 3rd Int Symp. on Fusion Nuclear Technology, Los Angeles, CA, 1994 (5th edition), (1995).

[Yuk11] Yuki O., Takashi Y., Takurou M., Keisuke M., Kenji I., and Takahiro U., Prog. Nucl. Sci. and Tech., Vol. 1, Pg. 296, (2011).

[MCNP5] X-5 Monte Carlo Team, MCNP Ů A General Monte Carlo N-Particle Transport Code, Version 5 Manual, April 24, 2003 (Revised 2/1/2008).

[Zib10] Zibi Z., Benchmarking of MCNP Modeling of HTR Cores Against Experimental Data From The Astra Critical Facility, North West University, Potchefstroom South Africa, unpublished (2010).

[Zha02] Zha M., Zhong S., Chen R., and Li S., J. Nucl. Sci. and Tech., Vol. 39, Issue 1, Pg. 1086, (2002).

[Zam10] Zamonsky O. and Reistma F., PBMR Calculations, private communication, (2010).

[Zie97] Ziermann E. and Ivens G., Abschlussbericht *ü*ber den Leistungsbetrieb des AVR Versuchskernkraftwerks. FZ J*ü*lich Report Jul-3448, (1997).

[Zie08] Ziegler J. F., Ziegler M. D., and Biersack J. P., *http://www.srim.org*, (2008).